Advanced Modeling and Analysis of the Doubly-Fed Induction Generator Based Wind Turbines

von der Fakultät für Ingenieurwissenschaften der
Abteilung Elektrotechnik und Informationstechnik
Der Universität Duisburg-Essen

zur Erlangung des akademischen Grades eines
Doktors der Ingenieurwissenschaften

genehmigte Dissertation
von
Ahmed Kossay El-Naggar
aus
Alexandria, Ägypten

Tag der Einreichung: 28.10.2016
Tag der mündlichen Prüfung: 12.04.2017
Erstgutachter: Prof. Dr.-Ing. Habil. Istvan Erlich
Zweitgutachter: Univ.-Prof. Dr.-Ing. Wilfried Hofmann

"When you live through everything and endure it, when you rise again after hundreds of setbacks, when you reject false hopes and miseries and grit your teeth just to see the truth clearly and with your own eyes, when you understand that the only meaning of life is in the struggle against evil. In this struggle only little can be done, but it is the only thing you can do. Otherwise it is the eternal abyss"

Alija Izetbegović

Acknowledgment

In the Name of God, the Merciful, the Compassionate, and praise belongs to God, the lord of all being. Blessings and peace be upon the most noble of Messengers, the Prophet Mohammad and on his kinsman and disciples.

The work presented in this thesis was carried out at the Institute of Electrical Power System (EAN) of University of Duisburg-Essen and the supervision of Univ. Prof. Dr.-Ing. habil. István Erlich. The research started in 2012 and was funded through a Scholarship granted directly from EAN. The funding is highly acknowledged.

I would like to thank Univ. Prof. Dr.-Ing. habil. István Erlich for accepting me as a PhD student at his institute and for granting me the scholarship. His suggestions, criticism, advice and guidance were a key factor in the improvement of this work and making be a better researcher. Thanks also to all EAN members, Apl. Prof. Dr.-Ing. habil. Gerhard Krost, for his comments and support, Dr. Fekadu Shewarega for the technical and personal discussion that helped me improving my work and my character and Abdul Wahab Korai for his friendship and endless help.

During my time at EAN God has blessed me with kind people who represented a family to me in Germany that gave me all the spiritual and moral support I needed. Therefore, my special thanks to my friends in the North Rhine Westphalia, Mohamed Taha, Ahmed Mohsen, Ahmed Hossam, Abdul Rahman Shoukry, Mohammed Aly and Alaa Atia and his family. Also thanks to Aziza Farid, from Marburg, for the language proof of my thesis.

Special thanks to my parents, who supported me all the way long to achieve what I dreamed of despite the sojourning away of them and the long distances between us. Thanks to my brother and sister, whom I used to resort to in times of distress and stumbling, to comfort me.

Contents

List of Figures

List of Tables

Nomenclature

Notation	Definition
$\underline{y}^{*\angle}$	Conjugate space vector
$\Im$	Imaginary operator
s	Laplace operator
$\mathbf{M}$	Matrix
$\tilde{y}$	Oscillatory component
$\Re$	Real operator
$\underline{y}^{\angle}$	Space vector
$y(t)$	Time dependent component
$\underline{G}(s)$	Transfer function

Symbols	Definition	Unit
p	Active power	[p.u.]
ρ	Air density	[kg/m^3]
μ_0	Air permeability	[henry m^{-1}]
ω	Angular frequency	[p.u.]
A	Area	[m^2]
C	Capacitance	[Farad]
c	Capacitance	[p.u.]
c	Coefficient	
I	Current	[A]
i	Current	[p.u.]
α	Current coefficients	
ξ	Damping ratio	
D	Damping coefficient	
r	Distance	[m]
t_{el}	Electromagnetic torque	[p.u.]
F	Force	[N]
ψ	Flux	[p.u.]
f	Frequency	[Hz]

k	Gain	[p.u.]
s_G	Generator slip	
z	Impedance	[p.u.]
H	Inertia time constant	[s]
J	Inertia constant	[kg×m^2]
L	Inductance	[henry]
l	Inductance	[p.u.]
σ	Leakage coefficient	
m	Mass	[kg]
$\dot{m}$	Mass flow rate	[kg/s]
θ	Mechanical angle	[p.u.]
φ	Phase angle	[rad]
β	Pitch angle	[$^\circ$]
P	Power	[Watt]
x	Reactance	[p.u.]
Q	Reactive power	[Vars]
r	Resistance	[p.u.]
Ω	Rotational speed	[rad/s]
S	Short-circuit power	[VA]
K	Stiffness constant	
τ	Time constant	[s]
t	Time	[s]
λ	Tip speed ratio	
T	Torque	[N.m]
v	Velocity	[m/s]
V	Voltage	[V]
v	Voltage	[p.u.]
E	Work	[J]

Subscripts	**Definition**
0	Synchronous quantity
1	Positive sequence
2	Negative sequence
AC	Alternating component

CH	Chopper
d,q	Components of space vector in rotating reference frame
α, β	Components of space vector in stationary reference frame
dt	Dead time
DC	Direct component
dyn	Dynamic
FFI/V	Feed forward current/ voltage
G	Grid
init	Initial value
I	Integral
LSC	Line side converter
M	Main
MSC	Machine side converter
max	Maximum value
meas	Measurement
p	Peak value
abc	Phase number
P	Proportional
ref	Reference
resp	Response
R	Rotor
S	Stator
SS	Steady state
WT	Wind turbine

Superscripts	**Definition**
$\angle$	Arbitrary Coordinate system
*	Conjugated complex component
$\angle\omega_S$	Coordinate system rotating with stator frequency
$\angle-\omega_S$	Coordinate system rotating with negative stator frequency
$\angle v_{G1}$	Reference frame aligned to positive sequence grid voltage
$\angle v_{S1}$	Reference frame aligned to positive sequence stator voltage
$\angle 0$	Stationary reference frame

Abbreviations	**Definition**
AC	Alternating component
BJT	Bipolar junction transistor
CMV	Common mode voltage
CPWM	Continuous pulse width modulation
DFIG	Doubly-fed induction generator
DC	Direct component
DD	Direct-drive
DPWM	Discontinuous pulse width modulation
EESG	Electrically excited synchronous generator
EMT	Electro-magnetic transient
FFT	Fast Fourier transformation
FRT	Fault Ride-Through
FEM	Finite element model
FOM	Full order model
GTO	Gate turn-off thyristor
HV	High voltage
IGBT	Insulated gate bipolar transistor
IGCT	Integrated gate commutated thyristor
LSC	Line side converter
LV	Low voltage
MSC	Machine side converter
MVMO	Mean variance mapping optimization
MV	Medium voltage
MOSFET	Metal oxide semiconductor field effect transistor
PMSG	Permanent magnet synchronous generator
PLL	Phase locked loop
PCC	Point of common coupling
PI	Proportional integral
PWM	pulse width modulation
ROM	Reduced order models
RMS	Root mean square
SCR	Short-circuit ratio
STI	Short time interruption

SPWM	Space vector pulse width modulation
SCIG	Squirrel cage induction generator
TSO/ DSO	Transmission or distribution system operator
VSC	Voltage source converter
WRIG	Wound rotor induction generator
WPP	Wind power plants
WT	Wind turbine

1 Introduction

In the last few years there was a constant tendency regarding expansion in reliance on the renewable energy especially wind energy as a main source for generation of electrical energy. This tendency is expected to continue in the future in order to reduce the negative consequences of the combustion of fossil fuels, oils natural gases, etc…on the eco system. However, the large extension the wind power into the power system has changed its status to have the same status as a power plant which has to participate on the provision of grid services to guarantee stable operation of the grid. Such provisionally services are now formulated as a stipulated requirements in most of the grid codes all over the continent. Currently, most of the wind turbine technologies are equipped rather with a partially or fully rated frequency converter, which allows for fast active and reactive power control of the wind turbine as well as maximum energy yield through optimized speed operation.

The doubly fed induction generator based wind turbine (DFIG-WT) with a partially rated converter is currently the dominating concept on the market. However, it suffers from high short-circuit current and DC voltage magnitudes during symmetrical and unsymmetrical current faults. Such high current and voltage magnitudes can be of harmful nature to the frequency converter, which requires protection against them either through protective devices like chopper and crowbar or through full disconnection from the grid under severe fault conditions. This may consequently not subject the DFIG-WT to the requirements of the grid codes. Furthermore, such high short-circuit current magnitudes will eventually elevate the fault current levels in the grid. Therefore, a deep understanding of the dynamic response of the DFIG-WT during different types of fault is essential in assessing the fault ride through (FRT) capability of it. Additionally, it will help in the knowledge of the fault current magnitudes of the DFIG-WT, which is crucial for the proper design of the electric power system component (e.g. circuit breakers, bus-bars, etc..) and protective relays setting for selective disconnection. Finally, proper techniques can be proposed to reduce such high current and voltage magnitudes through the right understanding of the dynamic nature of the machine without exploiting its capability limits.

1.1 Thesis Objectives

Based on the brief description provided above about the challenges of DFIG-WT connection to the grid a very detailed analysis of the dynamic behavior of the DFIG-WT under different fault types. This analysis defines the following objectives of this thesis:

  - Detailed modelling of the individual components of the DFIG-WT, so that the simulation results reflect the actual behavior as close as possible. The modelling should not only consider the linear behavior of each component but also all system non-linearity.
- Developing of a controller structure for each of the turbine, the machine side converter and the line side converter. The controller design should allow for maximum energy yield, fast and accurate response, and a separate control of the positive and negative sequence component as well as selective frequency components.
- Developing a method to assess the stability of the DFIG-WT output currents and voltages considering different grid stiffness, different controller parameters, different operating condition and the grid filters. Furthermore, developing of new methods to assess the influence of system non- linearity such as converter voltage limits and magnetic saturation on the system stability.
- Detailed analysis of the symmetrical fault response of the DFIG-WT with a new approximate and accurate mathematical equations describing the short-circuit current parameters, like the transient impedance, time constants and eigen frequencies.
- Proposing new methods for reduction of the peak short-circuit current, that will result in the highest reduction without exploiting the converter voltage limits, or operating in over modulation or in wind turbine disconnection.
- Detailed analysis of the unsymmetrical fault response of the DFIG-WT under each control objective and proposing new approximate expressions that describes the negative sequence short-circuit current with the highest possible accuracy.
- Proposing new method to estimate an equivalent parameters of the DFIG-WT that can be used in fault current calculation in accordance with IEC-60909 with the aid of parameter identification and no load FRT test and without any knowledge of the controller configuration. Furthermore, proposing a new method to estimate the equivalent R/X ratio in meshed networks, which leads eventually in much higher accuracy in comparison to other methods proposed in IEC-60909.

1.2 Thesis Outlines

Followed by the general introduction of the thesis objectives in this chapter, a statement about the disaster episode in the ecosystem in **Chapter 2** is provided and how the renewable energy especially the wind energy is important in curbing such disasters. Additionally, a brief

introduction about the current status of the wind energy and the different technologies of the wind turbines available on the market is made.

Chapter 3 deals with the modelling of the DFIG-WT system. This includes the aerodynamics of the rotor blades, the mechanical shaft, semiconductor devices and generator.

Chapter 4 deals with the developing of the control system for the DFIG-WT, followed by new criterion to assess the DFIG-WT output currents and voltages under different grid and controller configuration and considering the system non-linarites.

After the modeling and stability assessment phase of the proposed system in **Chapter 5** a very detailed analysis of the DFIG-WT response during symmetrical faults is performed. A new set of mathematical expressions were provided describing the different parameters characterizing the transient currents that constructs the total short-circuit currents. Additionally, the influence of the magnetic saturation and the voltage limitation of the converter on the short-circuit current behavior were analyzed.

In **Chapter 6** new methods to reduce the peak short-circuit current were provided. The new methods tend to increase the rate of change of the internal transient voltage or virtually increase the transient impedance or increase the damping of the transient components. The new methods were designed based on the knowledge of the transfer function of the DFIG stator and rotor currents with and without the feed-forward decoupled control. In order to achieve the highest peak reduction with exploiting the converter voltage limits and running into over modulation or system disconnection the mean variance mapping optimization (MVMO), which is a new population-based stochastic optimization technique, was adapted to optimally tune the parameters of the transient impedance compensation.

The analysis of the unsymmetrical fault response of the DFIG-WT was provided in **Chapter 7.** Under unsymmetrical faults there are predefined controller objective which can be set one at a time. Therefore, the analysis for each controller objective was performed and new mathematical expressions describing the negative sequence current parameters were provided and validated. Finally, a modified pulsating torque suppression control was proposed that will result in much faster response and lower number of transient currents. Nevertheless, the influence of the negative sequence voltage limitation, which is more likely to happen during unsymmetrical faults, were assessed and a method to account for it in the provided mathematical model of the negative sequence current was proposed.

In **Chapter 8** a new method to estimate the equivalent parameters; the R/X ratio and the locked rotor current ratio of the DFIG-WT for calculating of the short-circuit current in a direct manner as measured according to IEC-60909. The new method does not require any previous

knowledge of the controller configuration and it utilize a parameter identification to estimate the transient impedance as well as the R/X ratio from the FRT test under no-load condition. Additionally, a new method to estimate the equivalent R/X ratio in meshed networks was proposed. The new method is based on linearizing the exponential decaying term and it gives a better interpretation of the R/X ratio meaning and it provides also higher accuracy compared to the methods found in IEC-60909.

Chapter 9 summarizes the main content and contribution of this work and how it could be utilized for further analysis of interconnection aspects of large scale integration and control of WTs.

2 Wind Energy and The Global Climate Change

For 650,000 years the concentration of carbon dioxide (CO2) in the atmosphere has never exceed 300 ppm [1]. However, since the beginning of the Industrial Revolution (in the year 1750) [2] the atmospheric concentration of CO2 has increased 40%, from 280 ppm in 1750 to 400 ppm in 2015 as shown in Figure 2-1 [3]. According to the Intergovernmental Panel on Climate Change (IPCC) there is a scientific consensus that human activities (e.g. combustion of fossil fuels, principally coal, oil, and natural gas, along with deforestation) are the main causes of greenhouse gases (H_2O, CO_2, CH_4, N_2O, O_3 and CFCs)[1] [4].

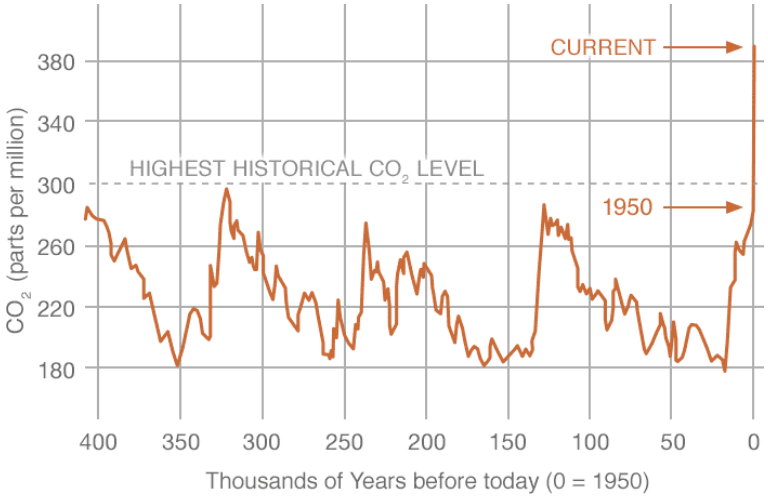

Figure 2-1 Concentration of mid-tropospheric CO_2 for thousands of years before today [1]

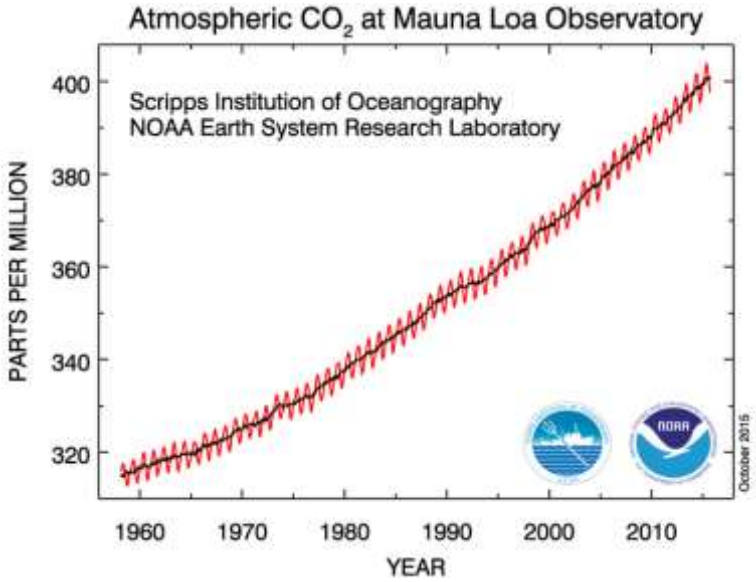

Figure 2-2 Atmospheric concentration of CO_2 in the last 50 years [3]

Greenhouse gases have a heat trapping nature, which was demonstrated by the physicist John Tyndall and the Swedish scientist Svante Arrhenius in the year 1860 and 1896, respectively [5].

[1] H_2O: Water, CO_2: Carbon Dioxide, CH_4: Methane, N_2O: Nitrous Oxide, O_3: Ozone, CFCs: Chlorofluorocarbons

Those gases accumulate in the Earth's atmosphere blocking heat radiating from earth toward space from escaping and causing surface air temperatures and subsurface ocean temperatures to rise as shown in Figure 2-2. This leads to an overall increase of the global temperature[6] [7] that is expected to reach 5.2 degrees Celsius by the year 2100 [8]. One way to reduce emission would be to replace fossil-fuel-based power by alternative sources of energy, such as solar and wind.

The global climate change has harmful effects on ecosystems, biodiversity and the livelihoods of people worldwide [9]. Despite the warning statements published by leading scientific organizations worldwide, which discuss the seriousness of the current situation [10], there are no signs of improvement, especially with the increasing significance of shale oil [11] and the expected failure of the United Nations Climate Change conference [12], which was held in Paris from November 30th to December 11th 2015 [13].

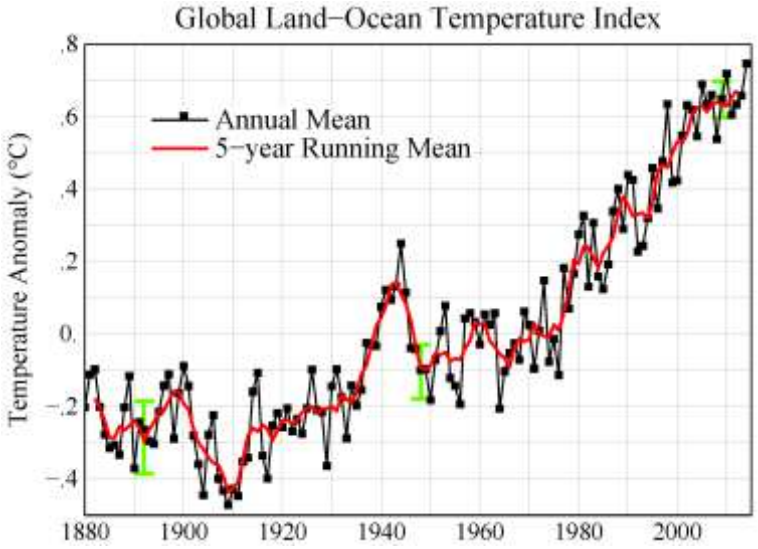

Figure 2-3 Global mean land-ocean temperature index from 1880 to present [8]

However, the increased public awareness and political pressure to tackle the climate problem have forced governments to pass laws that are geared towards reducing the problem and to develop plans to expand the reliance on renewable energy. In 2014, the number of countries focusing on renewable energy by pursuing environmental friendlier increased. Some of the ambitious targets include a rising number of countries with 100% renewable energy or electricity targets [14]. An example of this would be Denmark which has declared to achieve a 100% non-fossil based power generation system by 2050 [15]. As of early 2015, at least 164 countries have renewable energy targets as shown in Figure 2-4 [14], and an estimated number of 145 countries already have renewable energy support policies in place [16].

In terms of power generation wind energy is the least cost solution. Next to solar power, it is also the best leading technology regarding of dollars committed [16] [17]. According to various

studies wind energy has the potential to meet the world's energy demand while even generating surplus [18] [19] [20]. Additionally, the current wind energy technology has many environmental benefits, including the elimination of local air pollution, almost zero water consumption and operation without producing greenhouse gases. However, its greatest benefit is the reduction of CO_2 production of about 371 million tons in 2013. Further, this decline is expected to increase up to 899 million tons annually by the year 2020 and up to 1,521 million tons annually by the year 2030 [17].

Figure 2-4 Countries with renewable energy targets and policies [15]

2.1 Global Wind Power Status

Wind power has established itself as a main source for the generation of electricity in the past decade by delivering at least 3.4% of the world's electricity in 2014, a figure expected to increase to 6 -8% by 2020 and 8-17% by 2030 [17] [21]. Despite the dramatic decline of oil prices, wind power continued to grow in 2014 with a global installation of 51 GW and a total cumulative installed capacity of 372 GW. The offshore wind power represented 1.7 GW of the global total installed capacity in 2014 with a global cumulative of 7.5 GW, which accounts for 2% of the total wind capacity installed around the world [17] [22]. It is expected that the growth rate of wind power capacity will have grown 8.9% by the end of 2015, based on this figure, it is expected to reach 611-800 GW by 2020 and 964-1934 GW by 2030 [17], [21].

In 2014, the market growth was led by three countries accounting for 65% of the total installed capacity, China, Germany and the United States. The greatest expansion took place in China, where 23.3 GW of wind power was installed newly, which led to a total cumulative of 115 GW. In response to catastrophic rates of air pollution the Chinese government has announced new counter measures, relying on the expansion of wind power with an expected figure of 200 GW of wind power by 2020. Figure 2-5 shows the 10 leading countries of total installed wind power

capacity. In several countries such as Denmark, Nicaragua, Portugal and Spain, wind generates more than 20% of the electricity needed [21], [22].

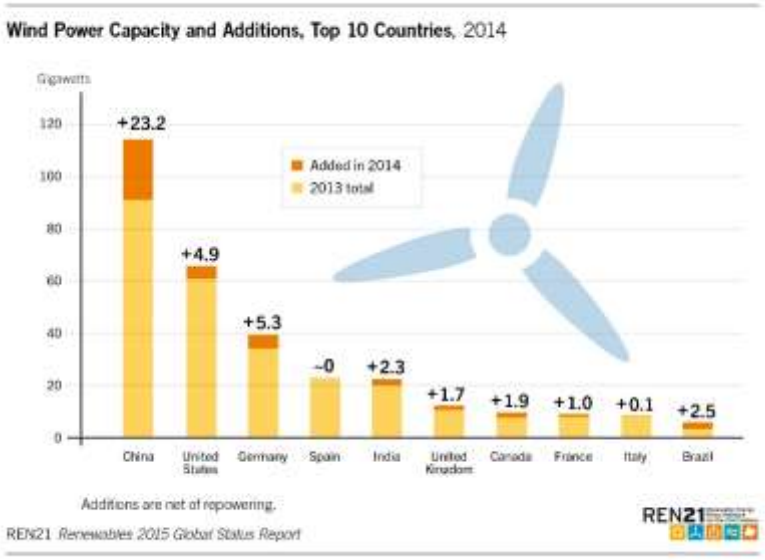

Figure 2-5 Top 10 leading countries with total installed wind power capacity [16]

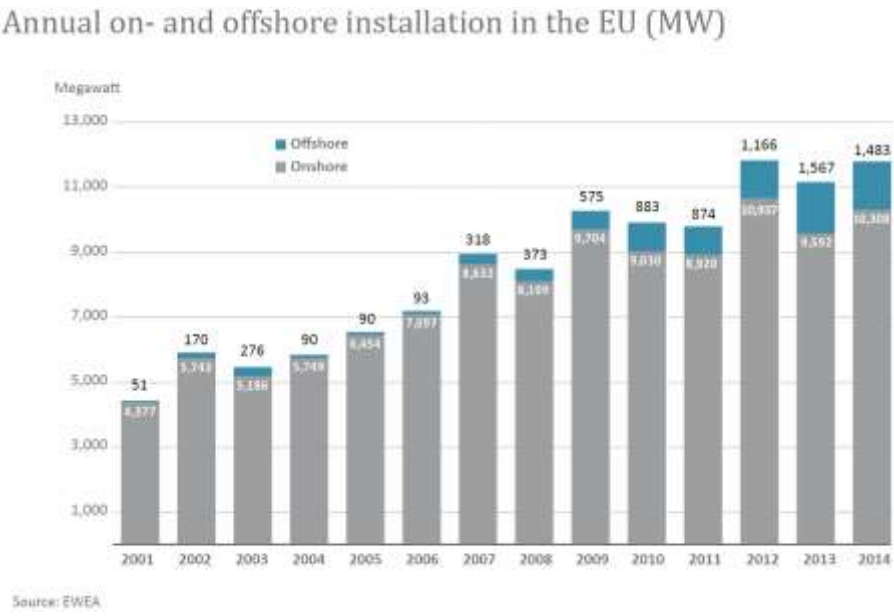

Figure 2-6 Annual wind power installation in Europe from 2001 to present [22]

The total installed wind power capacity in 2014 in the European Union added up to 11.8 GW showing a fall back to 11.9 GW in 2012 as shown in Figure 2-6 [22]. This figure is expected to reach 182-226 GW by 2020 and 253-389 by 2030 [17]. Germany leads the European market as shown in Figure 2-7and came second place globally concerning the newly installed capacity in the year 2014 with 5.3 GW representing a 58% increase in comparison to the previous year. Also Germany takes the third place globally regarding the total installed capacity of approximately 39 GW [16] [23]. The expansion of the German wind market is owed to its

parliament's decision to fully phase out nuclear energy by 2022 and to the amended Renewable Energy Sources Act (EEG), which came into force on 1 January 2012 [17] [22]. These decisions will have a significant impact on Germany's energy provision until and beyond 2020.

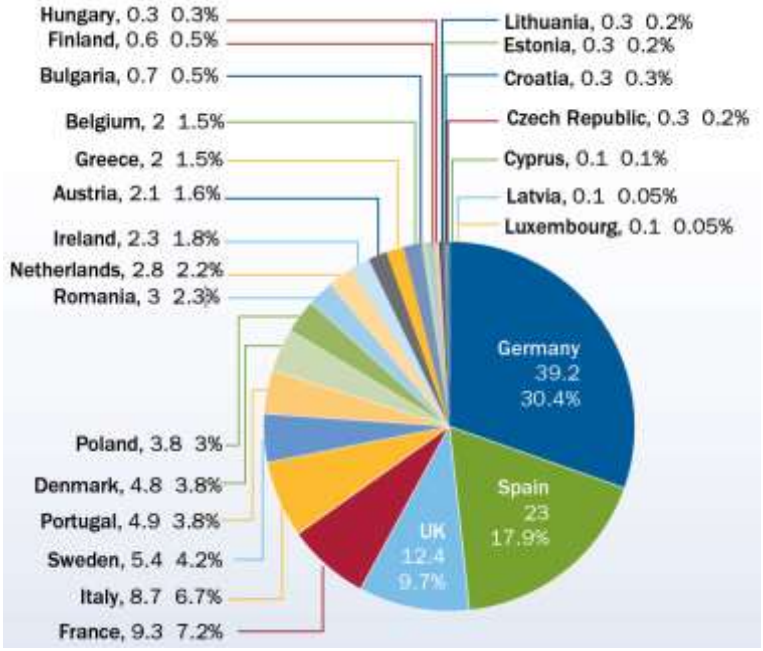

Figure 2-7 European wind market share for total installed capacity [23]

2.2 Wind Turbine Concepts

Till the year 1998 the majority of the installed wind turbines operated with fixed speed [24], [25]. It was a cheap and simple technology but inherited many disadvantages. Yet, these never created any unmanageable difficulties. However, since the establishment of grid codes the wind turbine technology has developed rapidly in order to match the stipulated requirements as well as to optimize energy yields, efficiency and overall costs. Based on rotation speed, the commercial wind turbine concepts can be classified into fixed speed, limited variable speed and variable speed. Wind turbines can be further classified into partial or full-scale power electronic converter and additionally into geared drive or direct-drive [24], [26].

2.2.1 Fixed Speed Wind Turbine

This type incorporate a three-stage gearbox and a squirrel cage induction generator (SCIG) as shown in Figure 2-8. The SCIG is directly connected to the stator with a capacitor bank for reactive power compensation and a soft-starter for smooth grid connection. A stall/ active stall control is integrated to allow for constant speed operation and to limit the speed and power output beyond the rated values [27]. In order to increase the energy yield and to reduce audible

noise a pole changeable generator with two stator windings that include different numbers of pole pairs is used. Thus, it enables operation at two rotational speeds [24], [26].

Despite being robust, easy and relatively cheap, the SCIG wind turbine also features many disadvantages. First, electromechanical torque variations due to wind speed fluctuations can result in mechanical stress and may eventually lead to swing oscillations between turbine and generator shaft. Further disadvantages are flickers, diminished aerodynamic efficiency, large mass and high costs due to the indispensable gearbox and the lack of voltage support capability.

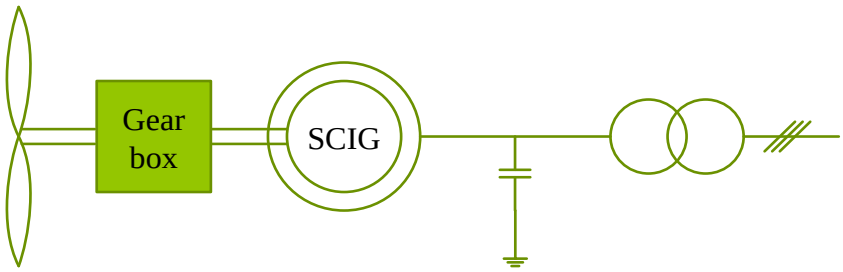

Figure 2-8 Layout of fixed speed SCIG-WT

2.2.2 Limited Variable Speed Wind Turbine

In order to increase the operational speed range, reduce the mechanical stress and to improve the power quality issues, the SCIG is replaced by a wound rotor induction generator (WRIG). The latter features variable rotor resistance by means of an optically controlled converter mounted on the rotor shaft, where the three-stage gearbox, capacitor bank and the soft-starter are still in place as shown in Figure 2-9 [28].

The energy extracted from the external power conversion is funneled as heat loss in the controllable resistance. Therefore, the speed range, which is dependent on the size of the variable resistance, is limited to 10% above the synchronous speed to reduce the heat loss.

2.2.3 Variable Speed Wind Turbine with Partial-Scale Converter

In this set-up a doubly-fed induction generator (DFIG) is used as shown in Figure 2-10, where the stator is directly connected to the grid and the rotor is linked through a partially scaled power electronic converter to enable variable speed operation. The dynamic speed range is dependent on the size of the frequency converter. A typical rating for the latter is 25-30% of the generator capacity leading to a typical speed range of ±30% around the synchronous speed [26]. The frequency converter also allows the rotor energy, to be fed into the grid instead of being dissipated. Moreover, this set-up can perform reactive power compensation and smooth grid connection.

The multi-stage gearbox as well as the slip-rings are still inevitable to have some drawbacks, such as heat dissipation from friction, regular maintenance and audible noise.

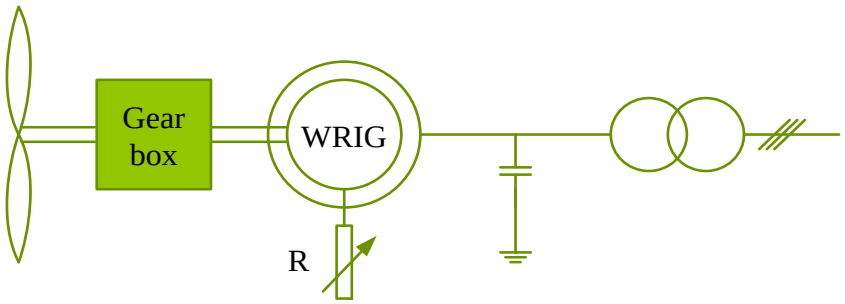

Figure 2-9 Layout of limited variable speed WRIG-WT

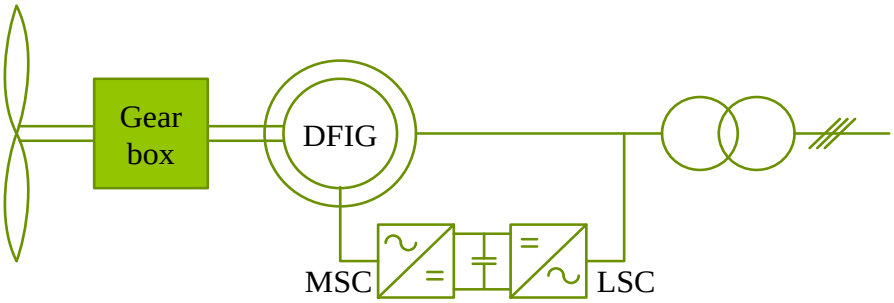

Figure 2-10 Layout of variable speed DFIG-WT

2.2.4 Variable Speed Wind Turbines with Full-Scale Converter

The generator types used in this set-up are connected to the grid through a full scale converter. The full-scale power converter performs reactive power compensation and smooth grid connection throughout the entire speed range. However, it has a higher cost and greater power losses. Three different types of drive-generator systems are combined within this concept. These are the direct-drive generator, the single-stage geared generator and the multiple-staged geared generator.

2.2.4.1 Direct-Drive Generator

The direct-drive (DD) generator rotates at a low speed, which results in the necessity of large size, large diameter for the implementation of a large number of poles with a reasonable pitch and large volume of the generator in order to produce high torques, limit the torque density, reduce weight and to keep winding losses small. A main advantage of this system is the absence of the gearbox and the brushes which consequently leads to less maintenance and lower costs. Still, the generator and the fully-scaled converter are rather large, heavy and expensive.

Figure 2-11 shows the configuration of a DDWT (the gearbox is omitted), where two types of generators are used. These are the electrically excited synchronous generator (EESG) and the

permanent magnet synchronous generator (PMSG) [24]. The latter is classified into radial flux, axial flux and transversal flux permanent magnet [26].

The EESG has lower iron losses when compared to the PMSG due to the exciter, which can control the excitation flux. However, it has a larger volume and weight and field losses of the exciter are inevitable. Yet, the PMSG is characterized by higher efficiency, lighter weight, better thermal characteristics and higher reliability in comparison to the EESG. Nevertheless, the PM materials are expensive and their availability is uncertain. Also, they demagnetize at high temperatures and require special corrosion protection when used in offshore wind farms [24], [26].

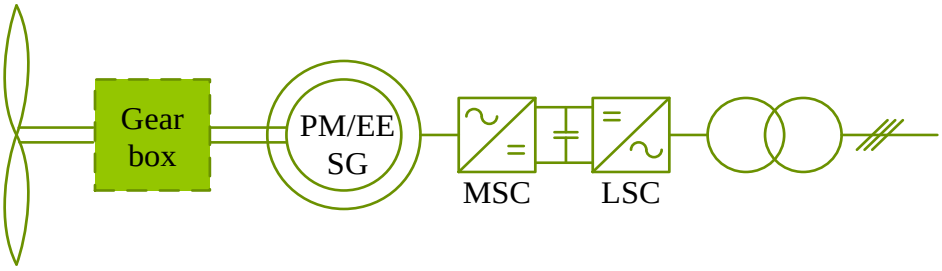

Figure 2-11 Layout of geared/gearless variable speed PM/EE SG-WT

2.2.4.2 Single-Stage Geared Generator

This set-up is a compromise between geared systems and DD systems, where a single-stage planter gearbox is used with the EESG or the PMSG to increase the speed roughly 10 times higher as shown in Figure 2-11. Consequently, the generator is much smaller, cheaper and more reliable.

2.2.4.3 Multiple-Stage Geared Generator

In order to reduce the generator's volume, improve its efficiency, obtain better fault-ride through capability than the DFIG and to dispense with the brushes, a multiple-gearbox is used with a PMSG or a SCIG as shown in Figure 2-12.

Figure 2-12 Layout of geared variable speed PMSG/ SCIG-WT

2.3 Latest Development of Wind Turbines

With the rising importance of wind power as a clean, safe and low cost option energy source, which consequently led to a steady increase of markets, larger and more efficient wind turbines are developed, especially for the offshore industry. The rate of increase of wind turbine size was slow beginning 1980 and early 2000. However, since 2001, when the first multi-megawatt offshore wind farm was commissioned [29], [30], the rate has risen especially due to the offshore industry, where operational restrictions and installation constraints are loose. Further, advance has been supported by developments in power electronics. Figure 2-13 shows the progress as well as the future expectations of the size and the rating of the WT and the role of power electronics.

Up to now, the largest commercial wind turbine is the V164-8.0 introduced by Vestas, the world's largest manufacturer of wind turbines. The V164-8.0 has a power rating of 8 MW and a rotor diameter of 164 m [31]. Table. 2-1 shows the world's largest wind turbine manufacturers and their largest wind turbine.

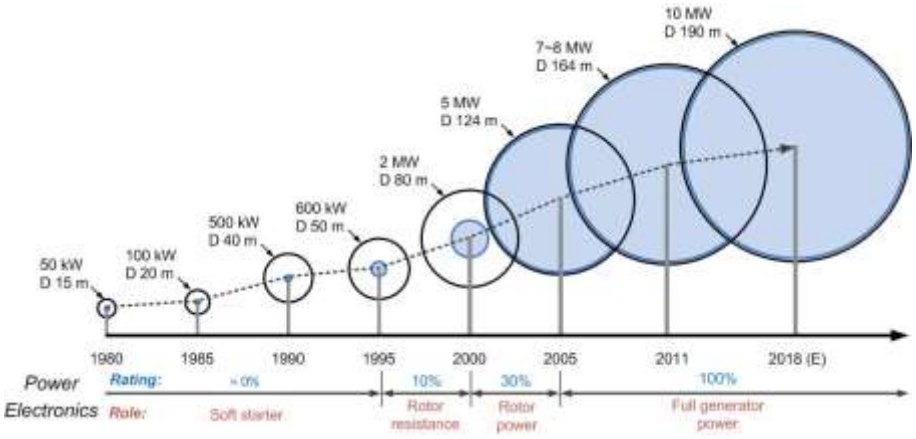

Figure 2-13 Evolution of wind turbine size and power electronics from 1980 until 2018 [15]

Currently, the DFIG-WT is the dominating concept [15]. However, manufacturers are looking for alternatives in order to get rid of the brushes. A promising alternative would be the brushless doubly-fed induction generator [32]. Additionally, with further developments in the power electronics sector and the decreasing prices and the availability of the materials for permanent magnet is guaranteed, the direct-drive turbines would be the most suitable generator, which currently makeup 27% of the global market [21]. There are further alternatives to avoid the use of power electronics. Such as the set-up proposed by Dewind, where a hydraulic torque replaced the power electronic converter connecting a synchronous machine directly to the grid in order to convert the variable speed into constant speed [24].

Table 2-1 Top 10 Wind turbine manufacturers[2]

Manufacturer	Market share	Country	Concept	Type name	kW
Vestas	11.6%	Denmark	PMSG-WT	V164-8.0	8000
Siemens	9.5%	Denmark	PMSG-WT	SWT-6.0-154	6000
Goldwind	9.0%	China	PMSG-WT	GW121/2500	2500
GE	8.7%	USA	DFIG-WT	GE 2.85-100	2850
Enercon	7.3%	Germany	EESG-WT	E-126	7580
Suzlon (Senvion)	5.5%	India (Germany)	DFIG-WT	6.2M152	6000
United Power	4.8%	China	DFIG-WT	UP6000-136	6000
Gamesa	4.5%	Spain	PMSG-WT	G132-5.0	5000
Mingyang	3.9%	China	PMSG-WT	SCD 3.0	3000
Envision	3.7%	China	DFIG-WT	4.0-136	4000

2.4 The Current Grid Codes

The increased penetration of the wind power into the power system has changed the status of wind power rather from being a passive energy source to have the same status as a power plant and to act like an active generation unit. In favor of that, the transmission system operators (TSOs) have issued grid codes and requirements that regulate the connection of the wind farms into the electrical grid and their operation during grid disturbances, with the objective to improve and stabilize wind turbine behavior, decrease the amounts of wind power lost following system disturbances and to provide the wind power stations with operational characteristics similar to those of the conventional power plants [33]. The grid codes stipulate the wind farm to adhere to the requirements regarding Fault Ride-Through (FRT), Reactive Current Supply, Active Power and Frequency Control, Voltage and Frequency Operating Range and Reactive Power Control and Voltage Regulation.

German Grid Codes

The first German grid codes that apply to networks with voltage levels 380, 220 and 110 kV was introduced in the year 2003 [34], and was later reformed in the year 2006 [35] based on the recommendations of the so-called “dena-study”, a study conducted in 2005 by the German

[2] Data is based on the specifications mentioned on the manufacturer’s website

transmission system operators in collaboration with the wind turbine manufactures and several research institutes [36]. In the year 2008, Germany was the first and only country to issue a separate grid code for offshore wind farms specifying 155 kV for grid connection point [37].

FRT Requirements

Figure 2-14 shows the required FRT according to E. ON grid code. The wind turbine should not trip during operation in area 1 and after fault clearance the active power must increase with a rate of 20% of the rated power per 1 second. In area 2, short time interruption (STI) is allowed only to prevent instability and after fault clearance resynchronization should take place within 2 second and active power must increase with a rate of 10% of rated power per 1 second. STI is only allowed in area 3 and after fault clearance the resynchronization can be longer than 2 s and the active power increase rate can be less than 10%/second. In area 4, the disconnection is performed through the supervisory grid protection. According to the FRT requirements, the wind turbine should ride through 100% voltage drop at the connection point (HV side) for a duration of 150 ms.

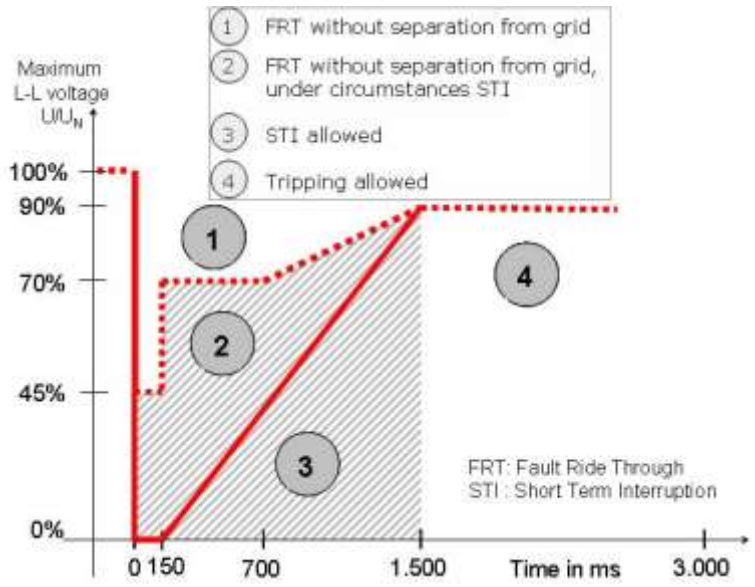

Figure 2-14 FRT requirements [35]

Reactive Current Supply During Voltage Drop Requirements

The E. ON grid code specifies that the wind turbine must support the grid voltage by injecting a reactive current in accordance to the stipulations shown in Figure 2-15. The voltage grid support must take place within 20 ms after fault recognition and the reactive current should be at least 2% of the rated current per 1% voltage dip.

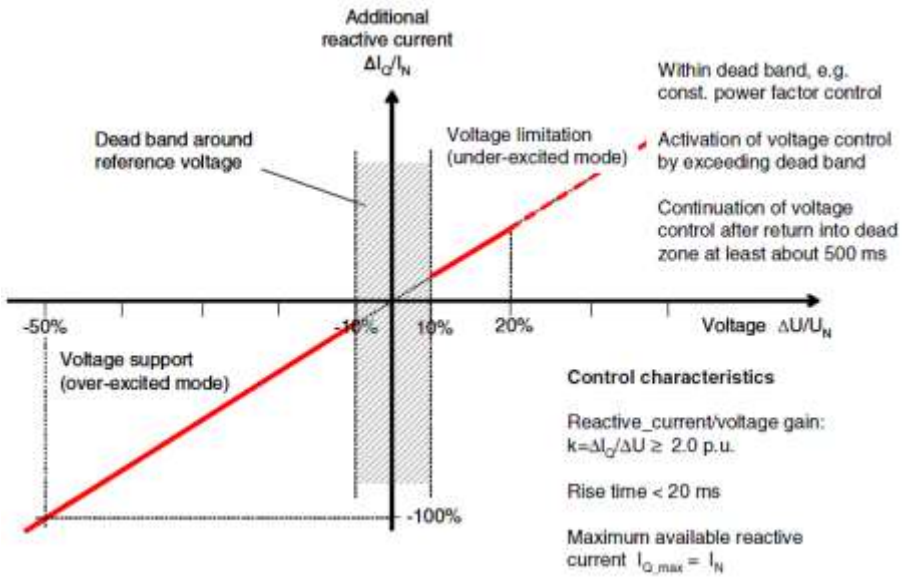

Figure 2-15 Voltage support requirements [35]

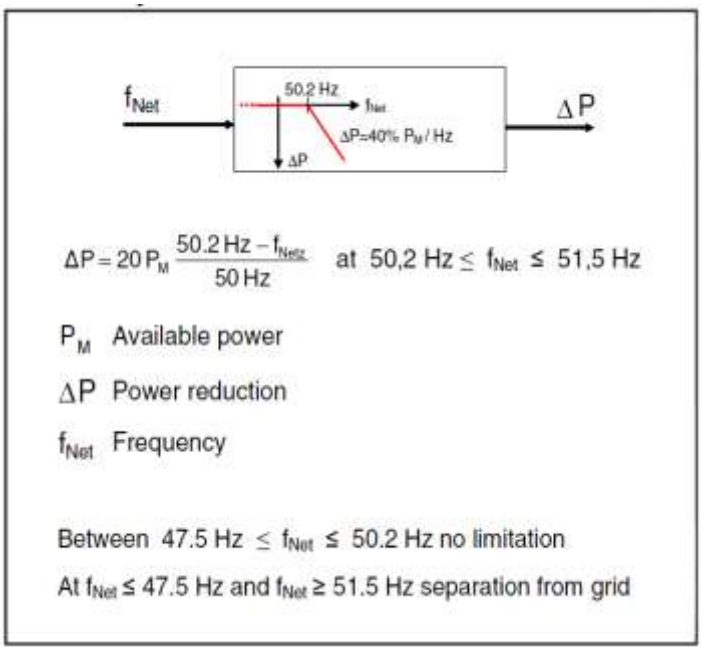

Figure 2-16 Active power reduction with over frequency requirements [35]

Active Power and Frequency Control

The wind farms are required to participate in the generation management in order to ensure a reliable operation, in which it should be possible to reduce the power output to a new set point value which corresponds to a percentage value referred to the grid connection capacity. The wind farm must have the ability to reduce its power output to the new set point with a gradient of 10 % of the grid capacitance per minute without being disconnected. When the frequency exceeds 50.2 Hz the wind turbine must reduce its active power by a gradient of 40% of the available power per minute.

Voltage and Frequency Operating Range

The wind turbine must operate continuously within the voltage frequency range indicated in Figure 2-17. Outside the frequency range of 47.5-51.5 Hz the wind turbine should disconnect immediately and in the frequency range of 50.25-51.5 Hz the active power must be limited with the frequency rise.

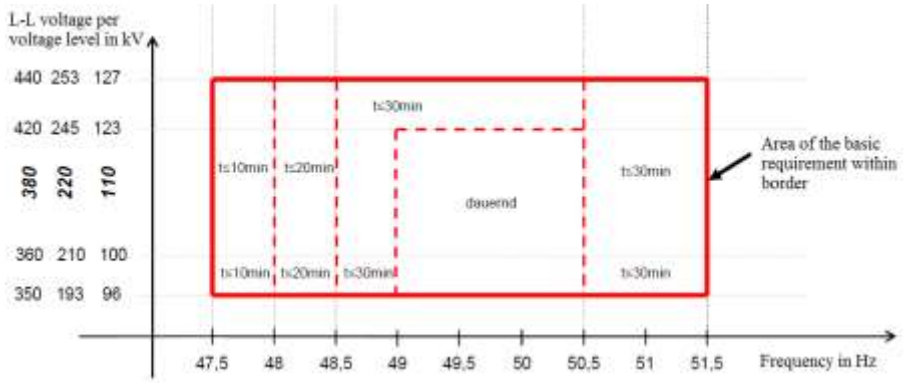

Figure 2-17 Voltage/frequency operating range requirements [35]

Reactive Power Control and Voltage Regulation

The wind turbines must fulfill the range of reactive power provision without limiting the active power output as displayed in Figure 2-18. The operating point for the steady-state reactive power can be defined by referring either to power factor, or to reactive power level (Q in Mvar) or to voltage level (V in kV).

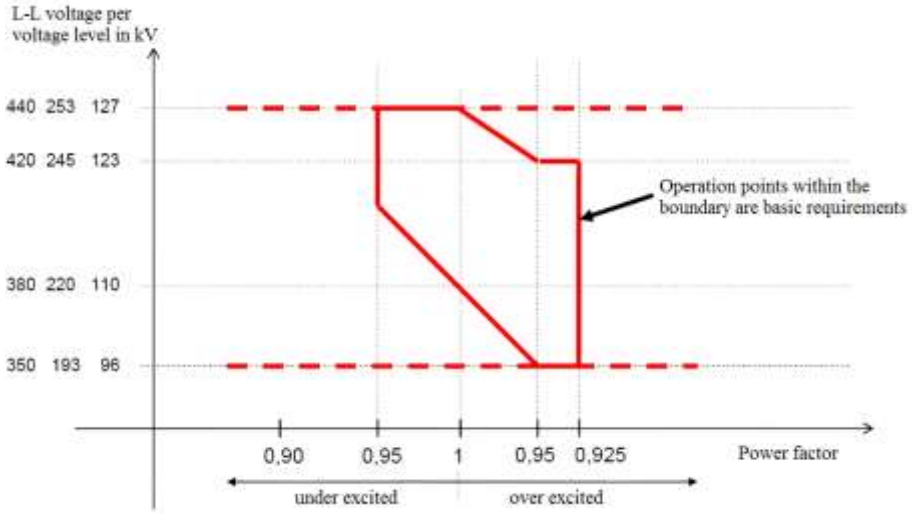

Figure 2-18 Reactive power provision during normal operation requirements [35]

3 Modeling of a Wind Turbine System

A detailed dynamic response analysis of the DFIG-WT requires appropriate modelling of the wind turbine system. The degree of modelling depends on the intended type of study. Therefore; in this study a very detailed model of wind and aerodynamics as presented in [38] [39] would be irrelevant. Instead less detailed models are implemented. The DFIG-WT system structure used in this work is shown in Figure 3-1 [40] [41].

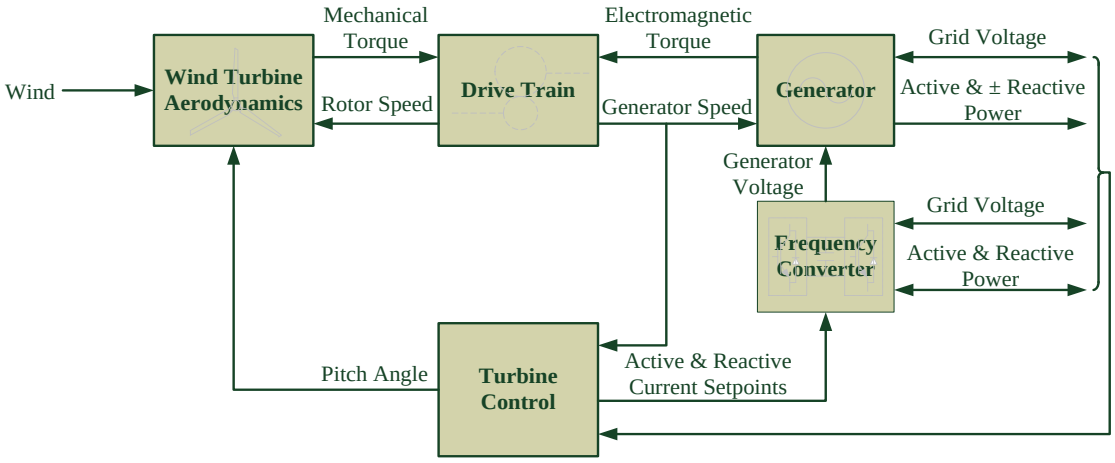

Figure 3-1 Wind Turbine system model

The *Wind Turbine Aerodynamics* block represents the process of energy extraction and conversion of the wind by the rotor blades to mechanical energy. It includes the aerodynamic model of the rotor blades and the pitch drive.

The *Drive Train* block represents the mechanical shaft that couples the rotor hub with the generator. The mechanical shaft consists of slow and fast shafts. The slow shaft is linked to the hub and to the low speed side of the gearbox. The gearbox multiplies the rotational speed of the fast shaft, which is linked to the generator.

The *Generator* block represents the electric generator, which in this case is the DFIG. The generator transforms the mechanical power into electric power as a function of the grid voltage.

The *Frequency Converter* block represents the voltage source converter (VSC) including the grid side converter, machine side converter and the DC link. The VSC generates the required generator output voltage in relation to the feed in control signals.

The *Turbine Control* block represents the control that is responsible for adjusting the rotor speed and generator's active and reactive power.

3.1 Wind Turbine Aerodynamics

The kinetic energy of any moving object with a constant mass *m*, that is moving in a straight line with speed *v* is given by:

$$E_k = \frac{1}{2} m v^2 \tag{3.1}$$

Assuming a uniform stream tube around a rotor plane as shown in Figure 3-2. The upstream, stream and downstream wind speed are designated as v_1, v_2 and v_3 respectively, and the upstream, rotor and downstream cross sectional area are designated as A_1, A_2 and A_3 respectively. If the air density is assumed as constant and the air flow is incompressible, the continuity equation can be written as:

$$\dot{m} = \rho A_1 v_1 = \rho A_2 v_2 = \rho A_3 v_3 = \text{constant} \tag{3.2}$$

where $\dot{m}$ is the flow rate and ρ is the air density.

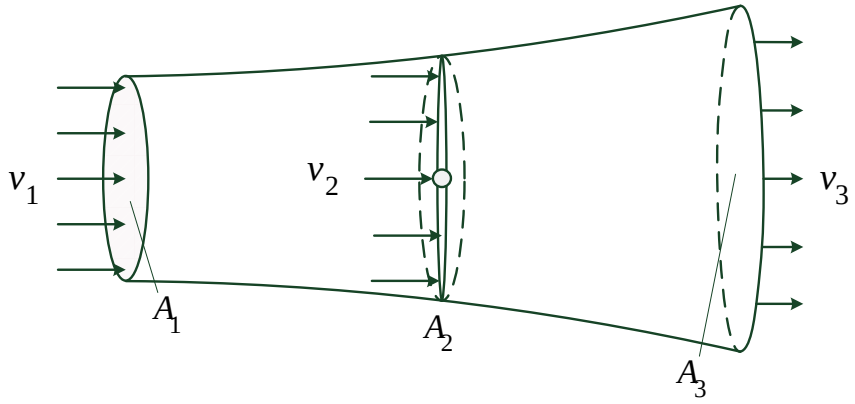

Figure 3-2 Stream tube model around wind turbine rotor

According to Euler's pump equation, the force exerted by the wind on the rotor is given by [42]:

$$F = \rho A_2 v_2 \left(v_1 - v_3 \right) \tag{3.3}$$

Applying Bernoulli's equation, assuming constant gravitational potential energy, yields the net work done on the rotor as [43]:

$$E_w = \frac{1}{2} m \left(v_1^2 - v_3^2 \right) \tag{3.4}$$

Finally, the power extracted from the wind is calculated as follow:

$$P_w = \dot{E}_w = F \dot{x} \tag{3.5}$$

Substituting eq. (3.3) and (3.4) in eq. (3.5) and considering eq. (3.2) yields:

$$P_w = \underbrace{\frac{1}{2}\rho A_2 v_1^3}_{\text{wind power}} \underbrace{\left[\frac{1}{2}(1+b)\left(1-b^2\right)\right]}_{\text{power coefficient}} = \frac{1}{2}\rho A_2 v_1^3 c_P \qquad (3.6)$$

where $b = \frac{v_3}{v_1}$ is the interference factor.

The power coefficient term (C_p) in eq. (3.6) represents a dimensionless ratio of the extractable power to the available kinetic power in the wind, which is a measure of the wind turbine's efficiency. The maximum value of the power coefficient is found by differentiating C_p with respect to *b* which yields a value of 0.59 (59.3%) at $b = 1/3$ [44]. This value is named after the German physicist Albert Betz, known as Betz limit and is applied to all wind turbine designs. The Betz limit is only a theoretical value and rather a lower value between 35%-40% can be achieved in modern wind turbines because of frictional losses, blade surface roughness and mechanical imperfections [42].

3.1.1 Rotor Blades Aerodynamics

As stated earlier the wind flow applies a force on the rotor blade. According to the Blade Element Momentum Theory (BEM) this force decomposes into axial F_x and tangential F_θ forces, which are determined by the lift C_L and drag C_D coefficients [44]. Those forces are examined along the blade profile by dividing the blade into *N* number of sections as shown in Figure 3-3 (usually from 10 to 20) and equating the force at each segment. Later on, numerical integration is performed along the blade span to determine the blade power coefficient [43].

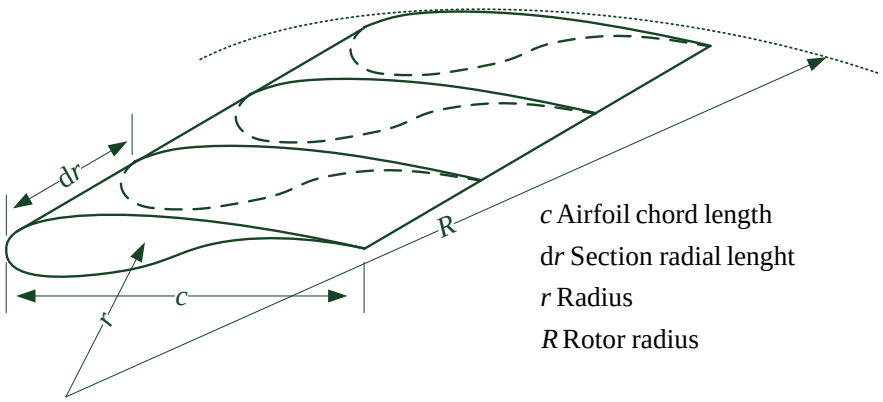

Figure 3-3 Schematic of the blade element model

The force profile on a rotor segment is shown in Figure 3-4. From this the following can be derived [44] [43]:

$$
\begin{aligned}
\mathrm{d}F_L &= \frac{1}{2}\rho v_{\mathrm{wi}}^2\, c\,\mathrm{d}r\, c_{\mathrm{L}} \\
\mathrm{d}F_D &= \frac{1}{2}\rho v_{\mathrm{wi}}^2\, c\,\mathrm{d}r\, c_{\mathrm{D}} \\
\mathrm{d}F_x &= \mathrm{d}F_L \sin\varphi + \mathrm{d}F_D \cos\varphi \\
\mathrm{d}F_\theta &= \mathrm{d}F_L \cos\varphi - \mathrm{d}F_D \sin\varphi
\end{aligned}
\qquad (3.7)
$$

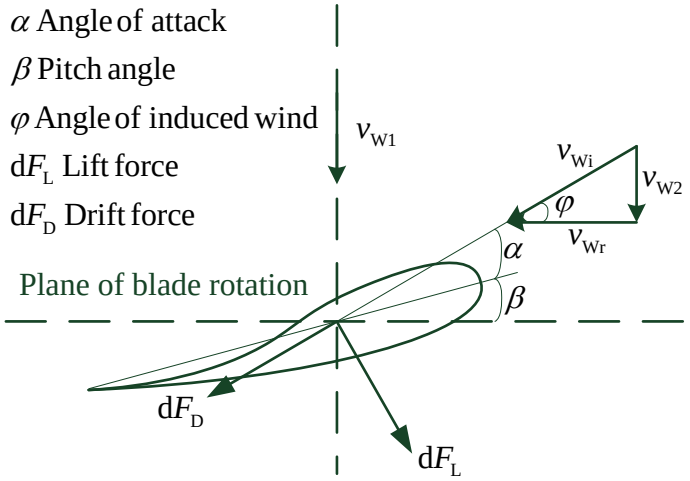

Figure 3-4 Force profile on an airfoil

The differential torque due to the tangential force at a distance *r*, with *B* as the number of blades, is given by:

$$\mathrm{d}T = \frac{1}{2} B\rho v_{\mathrm{wi}}^2\, c\, r\, \mathrm{d}r \left(c_{\mathrm{L}} \cos\varphi - c_{\mathrm{D}} \sin\varphi\right) \qquad (3.8)$$

and the power extracted by each segment is calculated as:

$$\mathrm{d}P = \Omega \mathrm{d}T = \frac{1}{2}\Omega B\rho v_{\mathrm{wi}}^2 cr\mathrm{d}r \left(c_{\mathrm{L}} \cos\varphi - c_{\mathrm{D}} \sin\varphi\right) \qquad (3.9)$$

where **Ω** is the rotational speed.

The overall rotor power coefficient can be calculated based on eq.(3.9) from the following:

$$c_{\mathrm{P}} = \frac{\int_{r_{\mathrm{h}}}^{R} \mathrm{d}P\mathrm{d}r}{P_{\mathrm{wind}}} = \frac{8}{\lambda^2} \int_{\lambda_{\mathrm{h}}}^{\lambda} c_{\mathrm{F}} \lambda_{\mathrm{R}}^3 a'\left(1-a\right)\left[1 - \frac{c_{\mathrm{D}}}{c_{\mathrm{L}}} \tan\varphi\right] \mathrm{d}\lambda_{\mathrm{R}} \qquad (3.10)$$

where the suffix h refers to the hub, $a = \frac{v_1 - v_2}{v_1}$ is the axial induction factor, $a' = \frac{\omega}{2\Omega}$ is the angular induction factor, $\lambda = \frac{\Omega R}{v_1}$ is the tip speed ratio, and c_{F} is a factor representing the tip losses.

3.1.2 Power Coefficient Representation for Simulation

The expression of the power coefficient in eq. (3.10) agrees rather well with the measurement data. However, the simulation of such an expression would require a considerable computational effort. Therefore, an alternative method would be to refer to a $c_{\mathrm{P}}(\lambda,\beta)$ lookup table as the one shown in Figure 3-5.

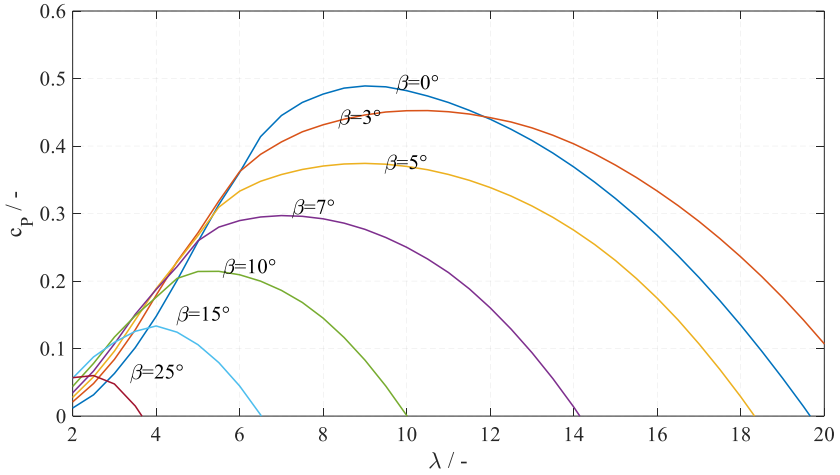

Figure 3-5 $c_{\mathrm{P}}(\lambda,\beta)$ *curves for pitch controlled wind turbine*

In order to avoid large memory use during simulation of a large number of machines and to avoid the interpolation process associated with a $c_{\mathrm{P}}(\lambda,\beta)$ lookup table, an alternative method would be a non-linear function in the form of [41]:

$$\begin{aligned} c_{\mathrm{P}}(\beta,\lambda) &= c_1\left(c_2/\lambda_{\mathrm{i}} - c_3\beta' - c_4\beta'^{C_5} - c_6\right)e^{c_7/\lambda_{\mathrm{i}}} \\ \frac{1}{\lambda_{\mathrm{i}}} &= \frac{1}{\lambda + c_8\beta} - \frac{c_9}{\beta^3+1} \\ \beta' &= c_{10}\beta \end{aligned} \tag{3.11}$$

or by a polynomial fit representation given by [45]:

$$c_{\mathrm{P}}(\beta,\lambda) = \sum_{i=1}^{n}\sum_{j=1}^{m}\alpha_{i,j}\beta^i\lambda^j \tag{3.12}$$

Another method presented in [41] based on the linearization of the aerodynamic model along the operating trajectory as shown in Figure 3-6 is given by:

$$\begin{aligned} P^*_{\mathrm{Aero}}(\beta,\Omega_{\mathrm{WR}},v_{\mathrm{w}}) \approx\ & P^*_{\mathrm{Aero}}(\beta_0,\Omega_{\mathrm{WR},0},v_{\mathrm{w},0}) + \left.\frac{\partial P^*_{\mathrm{Aero}}}{\partial\beta}\right|_{(\beta_0,\Omega_{\mathrm{WR},0},v_{\mathrm{w},0})}\Delta\beta + \\ & \left.\frac{\partial P^*_{\mathrm{Aero}}}{\partial\Omega_{\mathrm{WR}}}\right|_{(\beta_0,\Omega_{\mathrm{WR},0},v_{\mathrm{w},0})}\Delta\omega + \left.\frac{\partial P^*_{\mathrm{Aero}}}{\partial v_{\mathrm{w}}}\right|_{(\beta_0,\Omega_{\mathrm{WR},0},v_{\mathrm{w},0})}\Delta v_{\mathrm{w}} \end{aligned} \tag{3.13}$$

3.1.3 Pitch System

Wind turbines are designed to yield maximum energy extraction from wind to produce clean energy as cheaply as possible. Consequently, they are designed to operate at maximum wind speed not higher than 15 m/s, because wind speed beyond 15 m/s is rare, and to limit the mechanical stresses on the wind turbine structure and the power rating of the converter and the generator. Therefore, all wind turbines are designed with a power control strategy that limits the mechanical power input as well as the generator speed excursion during grid faults.

The mechanical power can be limited through three major methods, i.e., by using the aerodynamic characteristic of the rotor blade, which is referred to as stall control, by manipulating the C_p value through pitch angle, which is referred to as pitch control, or by using both the aerodynamic characteristic of the rotor blade and the pitch angle, which is referred to as active stall control or combi stall control [46].

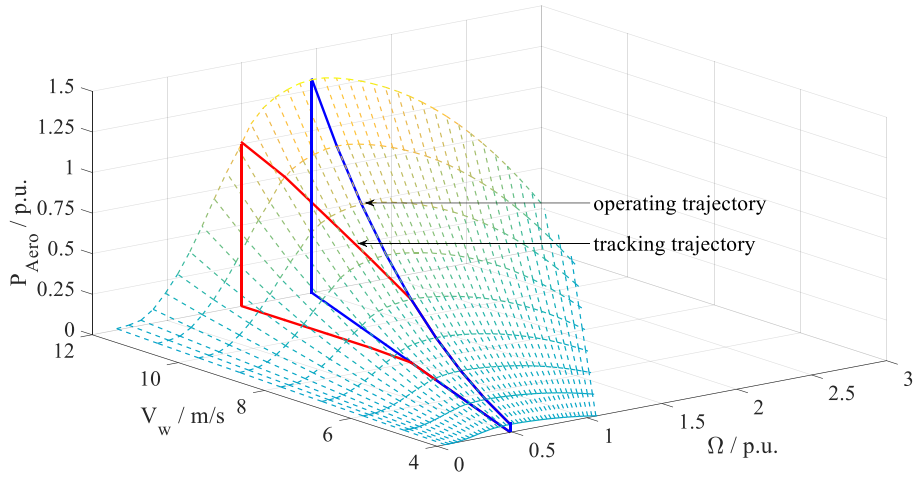

Figure 3-6 Rotor power operating trajectories

3.1.3.1 Stall Control

In stall control the rotor blades are bolted at a fixed angle to the hub, while the blades are aerodynamically designed so that turbulences are created behind the rotor blade in order to limit the lift force the moment the wind speed reaches its maximum value [47]. Additionally, the blade is twisted along its longitudinal axis to ensure that stalling occurs gradually and not abruptly.

The main advantage of the stall control is that it happens passively not requiring complex control and moving parts in the rotor. However, it represents a very complex aerodynamic design, there are design challenges in the structural dynamics of the wind turbine [40], as well as further power reduction as wind speed increases [27].

3.1.3.2 Pitch Control

In pitch control the power coefficient is reduced by pitching the blades out of the wind [47]. The pitch control requires sophisticated engineering to set the pitch angle as required and to avoid overlapping between pitch and torque controllers. However, pitch control ensures a simple, fast and reliable control and allows for smother control of the active power [27]. Therefore, pitch control is the most commonly used method implemented for power limitation in modern multi-MW wind turbines [46] [48]. It is also the method implemented in this work.

3.1.3.3 Active Stall Control

The active stall control resembles a combination between stall and pitch control, where the rotor blades go into deeper stall by pitching the rotor blade into the wind. In another sense the rotor blades will be moved in the opposite direction in contrast to the pitch control in order to increase the angle of attack. Thus, in contrast to stall control, the mechanical power is kept constant whenever the wind speed increases beyond its rated value [47] [46] [27]. The active stall control allows also for accurate power control to avoid power overshooting at the beginning of a gust wind [40].

Since the active stall machines have pitchable blades, it is rather an economic question whether it is worth to pay for the additional complexity of the blade design, when a pitch mechanism already exists.

3.2 Drive Train

The drive train represents the structural dynamics of the wind turbine's mechanical system, which, in addition to the tower, has a direct influence on the generator speed and consequently on the power output. The drive train consists of rotor blades, hub, low speed shaft, gearbox, high speed shaft, and generator rotor.

An accurate modelling of the mechanical system requires the employment of finite element models (FEM) [49] [41]. This type of modeling requires a thorough knowledge of the wind turbine structure, which is not available, and it introduces high levels of complexity that are unnecessary. Instead of using FEM, if only the dominant Eigen frequencies are to be considered, the drive train can be seen as a multi-mass system [47], which exhibits multi-torsional modes.

In [41] it was shown that the tower vibration has no remarkable influence on the generator speed or power output and could therefore be ignored, while the impact of rotor Eigen frequency and tower shadow can be ignored as proposed in [50] [41]. Additionally, the gearbox can be

considered as being flexible [49] [38] [27]. Accordingly, the drive train can be represented by a three-mass model with two torsional modes [49]. The first torsional mode describes the rotation of the rotor flexible blade inertia against the combined inertia of the hub and the rigid blade, while the second torsional mode describes the rotation of the combined inertia of the rigid rotor and hub against the inertia of the generator.

Two-Mass Model Representation

The three-mass model may not be suitable for the simulation of a large number of machines. Additionally, the low-frequency mode is only required for the stability study of the electrical system [49]. Therefore, the three-mass model can be reduced to an effective two mass model that gives an accurate representation of the low-frequency mode [51].

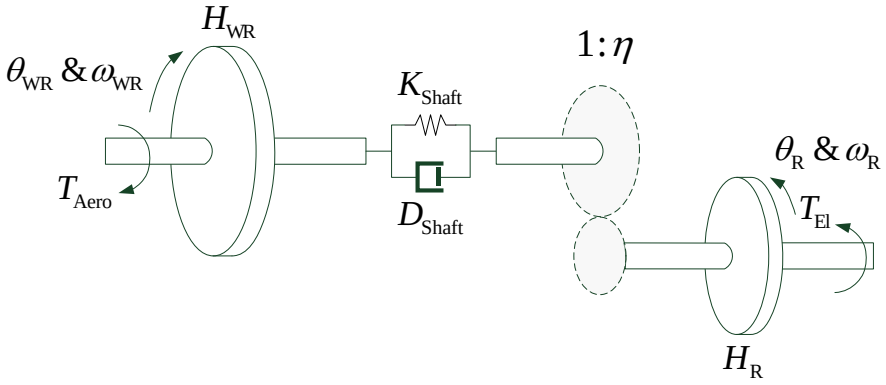

Figure 3-7 Two-mass model of the drive train

The two-mass model is characterized by a larger inertia, which represents the combined inertia of both rotor and hub, rotating against a much smaller inertia, which represents the generator as shown in Figure 3-7. The dynamic equations showing the two-mass model referred to the high speed side[3] are described by:

$$\begin{aligned} 2H'_{WR}\frac{d\omega'_{WR}}{dt} &= T'_{Aero} - D'_{Shaft}\left(\omega'_{WR} - \omega_R\right) - K'_{Shaft}\Delta\delta_{WG} \\ 2H_R\frac{d\omega_R}{dt} &= -T_{El} - D'_{Shaft}\left(\omega_R - \omega'_{WR}\right) + K'_{Shaft}\Delta\delta_{WG} \\ \frac{d\Delta\delta_{WG}}{dt} &= \omega'_{WR} - \omega_R \end{aligned} \qquad (3.14)$$

The derivation of the equivalent parameter of the two-mass model is achieved through estimating the value of the low-frequency mode with the aid of spectral analysis and solving the following set of equations [50] [51]:

[3] The referring of all terms to the high speed shaft is found in [38]

$$f_{\text{Shaft}} = \frac{1}{2\pi}\sqrt{\frac{K_{\text{shaft}}}{\left(\frac{1}{J_{\text{WR}}}+\frac{1}{\eta^2 J_{\text{R}}}\right)^{-1}}}$$

$$K_{\text{Shaft}} = \left(2\pi f_{\text{Shaft}}\right)^2 \frac{J_{\text{WR}}\eta^2 J_{\text{R}}}{\left(J_{\text{WR}}+\eta^2 J_{\text{R}}\right)} \qquad (3.15)$$

$$J_{\text{WR}} + \eta^2 J_{\text{R}} = J_{\text{total}}$$

The estimation of the damping coefficient is difficult due to the nonlinearities of the drive train. However, the damping coefficient can be calculated as presented in [38] by equating the logarithmic decrement from the amplitude of subsequent periods with the help of detailed simulation as follows:

$$\delta_{\text{s}} = \ln\left(\frac{a(t)}{a(t+t_{\text{p}})}\right) \qquad (3.16)$$

where a is the amplitude of the oscillation with a period t_{p} [38].

With the damping ratio defined as:

$$\xi = \frac{\delta_{\text{s}}}{\sqrt{\delta_{\text{s}}^2 + 4\pi^2}} \qquad (3.17)$$

The damping coefficient can then be calculated using the stiffness as follows:

$$D_{\text{Shaft}} = 2\xi\sqrt{K_{\text{Shaft}} J_{\text{WR}}} \qquad (3.18)$$

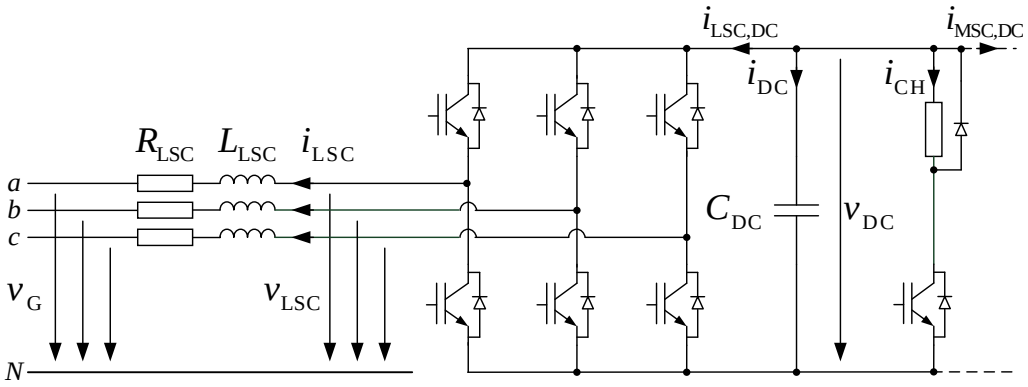

Figure 3-8 Two-level voltage source converter

3.3 Frequency Converter

Power electronics converters are used to control power flow in variable-speed drives during steady-state and dynamic periods. In DFIG-WT the back-to-back voltage source converter (VSC) is widely used. This is owed to its simplicity and the possibility of building redundancy into the string of series-connected switching devices [49]. Additionally, it allows power

generation in sub- and super synchronous modes, active and reactive power control and harmonic compensation [52].

The voltage level of the VSC used in a wind turbine application is classified into low voltage (400-690 V) and medium voltage (3- 6.6 kV) [53]. In DFIG-WT the low voltage two-level converter shown in Figure 3-8 is commonly used, while for medium voltage converter, the three-level NPC is the common topology.

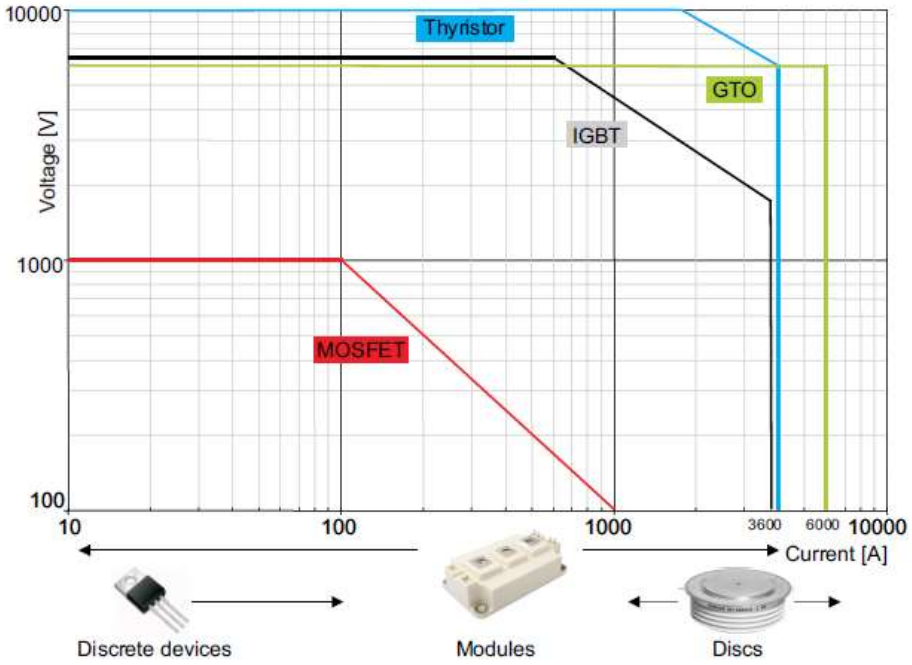

Figure 3-9 Current and voltage limits for semiconductor devices [54]

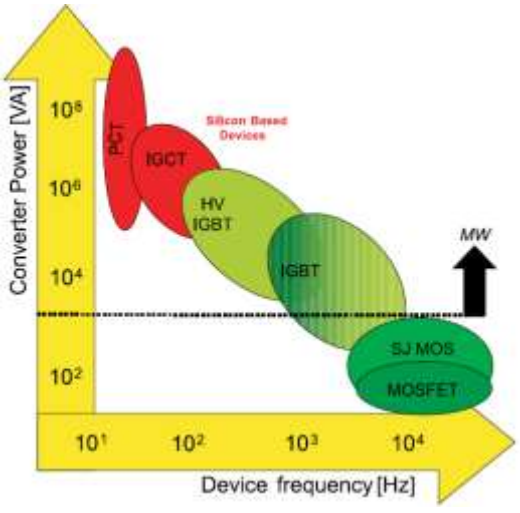

Figure 3-10 Switching frequency ranges for semiconductor devices [54]

3.3.1 Semiconductor Devices

There are several semiconductor devices on the market that can be used as switching devices in VSC, for example, a metal oxide semiconductor field effect transistor (MOSFET), an insulated gate bipolar transistor (IGBT), a gate turn-off thyristor (GTO), and an integrated gate

commutated thyristor (IGCT). The semiconductor devices are characterized based on their power rating and switching frequency as shown in Figure 3-9.

The IGBT is the dominating semiconductor device used in converter systems for DFIG-WT with voltage ratings of up to 6.5 kV and DC current ratings of up to 3.6 kA commercially available on the market. The IGBT offers turn-on and off capability, thus, allowing full controllability over a wide range of switching frequencies. The switching frequency is determined by the switching losses, which define the upper limit at approximately 5kHz, and the harmonic generation, which defines the lower limit at approximately 500 Hz as depicted in Figure 3-10.

The IGBT is developed by combining both a bipolar junction transistor (BJT) and a MOSFET, monolithically on the same silicon wafer in order to combine the qualities of both devices [55].

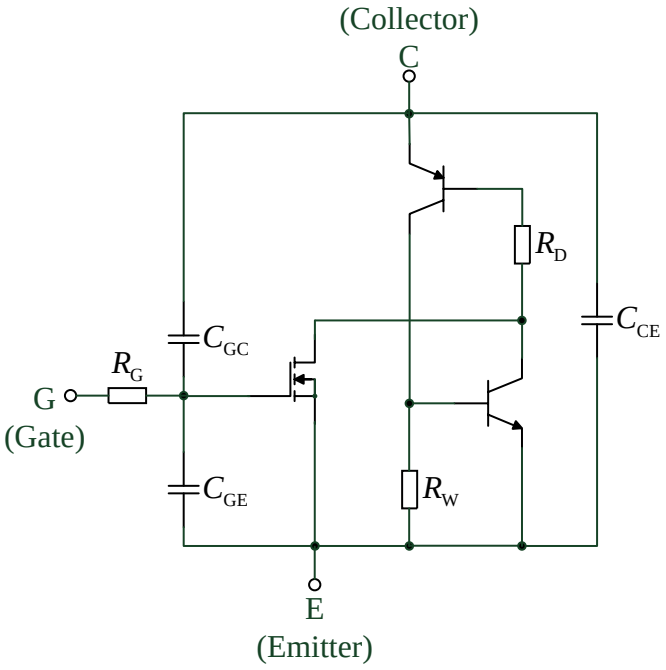

Figure 3-11 IGBT equivalent circuit diagram [54]

Therefore, the IGBT can be modeled as a BJT driven by a MOSFET, where the IGBT properties are influenced by the parasitic elements of the IGBT structure as shown in the equivalent circuit of Figure 3-11. The physical interpretation and designation of the parasitic elements of the IGBT equivalent circuit are evident in Table 3-1 [54].

The switching behavior of an IGBT under hard switching in the test circuit shown in Figure 3-12 is presented in Figure 3-13. When the IGBT is turned on at t_1, a gate current starts flowing and charges the gate-emitter capacitance C_{GE}; the gate-emitter voltage V_{GE} rises with a time constant dependent on the gate resistance and the input capacitance.

Since V_{GE} is still below the threshold value $V_{GE(th)}$, no collector current I_C will flow during this time interval, referred to as turn-on delay time $t_{d(on)}$, till the threshold value is reached at t_2.

Table 3-1 Physical interpretation of IGBT parasitic elements [54]

Symbol	Designation	Physical interpretation
C_{GE}	Gate-emitter capacitance	Overlapping gate and source metallization; dependent on gate-emitter voltage; independent of collector-emitter voltage
C_{GC}	Gate-collector capacitance	Miller capacitance; generated by overlapping of gate and n^- -drift area
C_{CE}	Collector-emitter capacitance	Junction capacitance between n^- - drift area and p-well; dependent on cell surface, breakdown voltage and collector-emitter voltage
R_W	Lateral resistance of the p-well	Base-emitter resistance of the parasitic bipolar NPN transistor
R_D	Drift resistance	Resistance of the n - region (base resistance of the PNP transistor)
R_G	Internal gate resistance	Polysilicon gate resistance; additional series resistors are often needed in modules with several transistor chips to minimize oscillations between chips

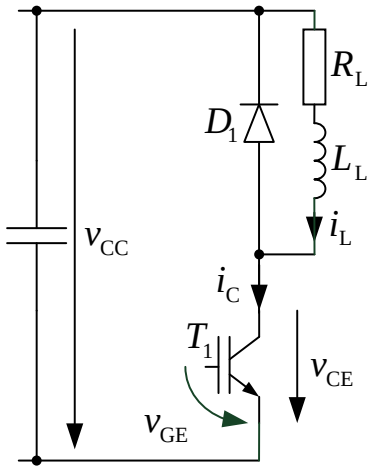

Figure 3-12 Test circuit for IGBT hard switching

After reaching the threshold voltage the collector current will start to rise and reach its nominal value in a time interval denoted by the rise time t_r, which is dependent on the load and the IGBT's transconductance. Due to the current flow a voltage drop will occur in the collector-emitter voltage V_{CE} due to the stray inductance L_σ[4]. When I_C reaches the full load current (1

[4] There was no data regarding stray inductance and its value was assumed in the range of nH

p.u.) the diode will start to turn-off. However, I_C will keep on rising, until the diode internal storage charge is discharged which causes the diode current to flow in reverse direction.

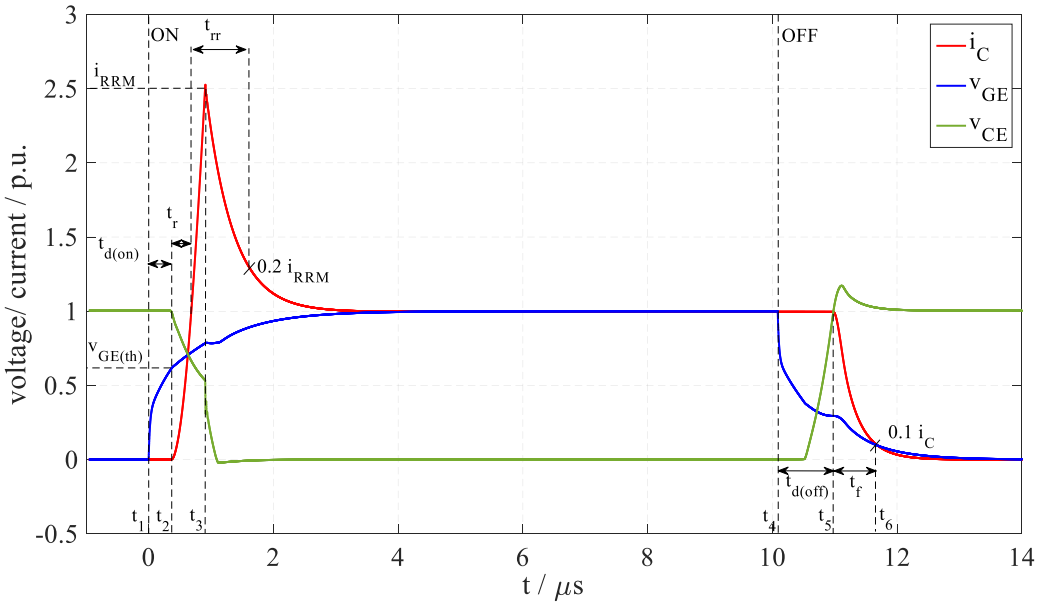

Figure 3-13 Switching behavior of IGBT

The collector current will increase beyond the load current till it reaches the diode's maximum reverse recovery current I_{RRM} at t_3 when the pn-junction in the diode becomes free of charge carriers. After that I_C declines to the load current value (diode current declines to the reverse current) and V_{CE} drops steeply. This time period when the load current is fully commutated by the IGBT (diode forward current reaches zero) till the diode current reaches its reverse value is referred to as transient recovery time t_{rr}.

At t_4 when the IGBT is turned off the process described above is reversed and V_{GE} falls to a value determined by the internal capacitance at t_5 in a time interval designated as turn-off delay time $t_{d(off)}$. After that, when the internal capacitances are recharged to such an extent that the charge carrier influence in the channel area vanishes, I_C drops steeply to 10% at t_6 in the time interval designated as the fall time t_f, which is mainly dependent on the IGBT technology and the doping concentration.

It is clear that the switching dynamics of the IGBT are very fast, which requires very small simulation time steps (~0.1-1 ns) to achieve high accuracy in the results. Such small simulation time step will result in high computational effort for the simulation of a full wind turbine system or even wind farms. An alternative method to increase the simulation time step and to reduce the computational effort is to replace the semiconductor devices by ideal switches. The implementation of ideal switches allows for investigating the harmonic generation and

interactions with the filter circuits. This can be ascertained by the voltage and current waves of a load fed by a single-phase full-bridge inverter using PWM switching technique and 4.5 kHz carrier frequency shown in Figure 3-14. The voltage and current wave forms shown in Figure 3-15 are highly symmetrical to each other, but with small voltage over-shoots in the detailed model due to the IGBT parasitic inductance as explained earlier. Additionally, the FFT spectrum is almost identical. However, the magnitudes of the harmonic contents of the detailed model voltage and current waves are a bit higher due to the dead-time implemented in the controller to avoid complementary switching of one arm due to the storage effect as already explained earlier.

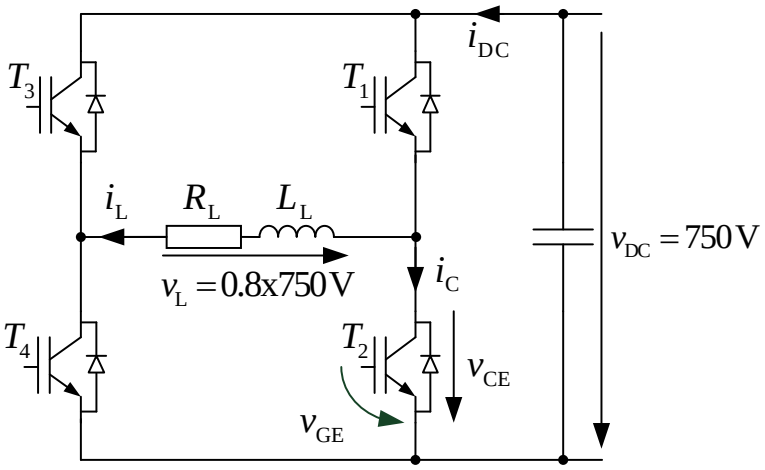

Figure 3-14 Single-phase full-bridge inverter for PWM pattern investigation

3.3.2 Switching Strategy

The quality of the converter voltage and current outputs are mainly dependent on the switching strategy used. In modern VSC applications the pulse width modulation (PWM) is the standard switching technique used, in which the state of the switching device changes rapidly between on and off so that the output filters average or filter out the switched signal.

The PWM types are classified into continuous PWM (CPWM) and discontinuous PWM (DPWM). The CPWM includes ¼ sinusoidal PWM (SPWM4), 1/6 sinusoidal PWM (SPWM6) and triangular PWM (TPWM), while DPWM includes DPWM0, DPWM1, DPWM2, DPWM3, DPWMMAX and DPWMMIN [56]. The main difference between CPWM and DPWM types is the generation of the common mode voltage (CMV) as shown in Figure 3-16. The CMV is usually injected into the reference signal to increase the modulation index up to 1.155 to better utilize the DC voltage.

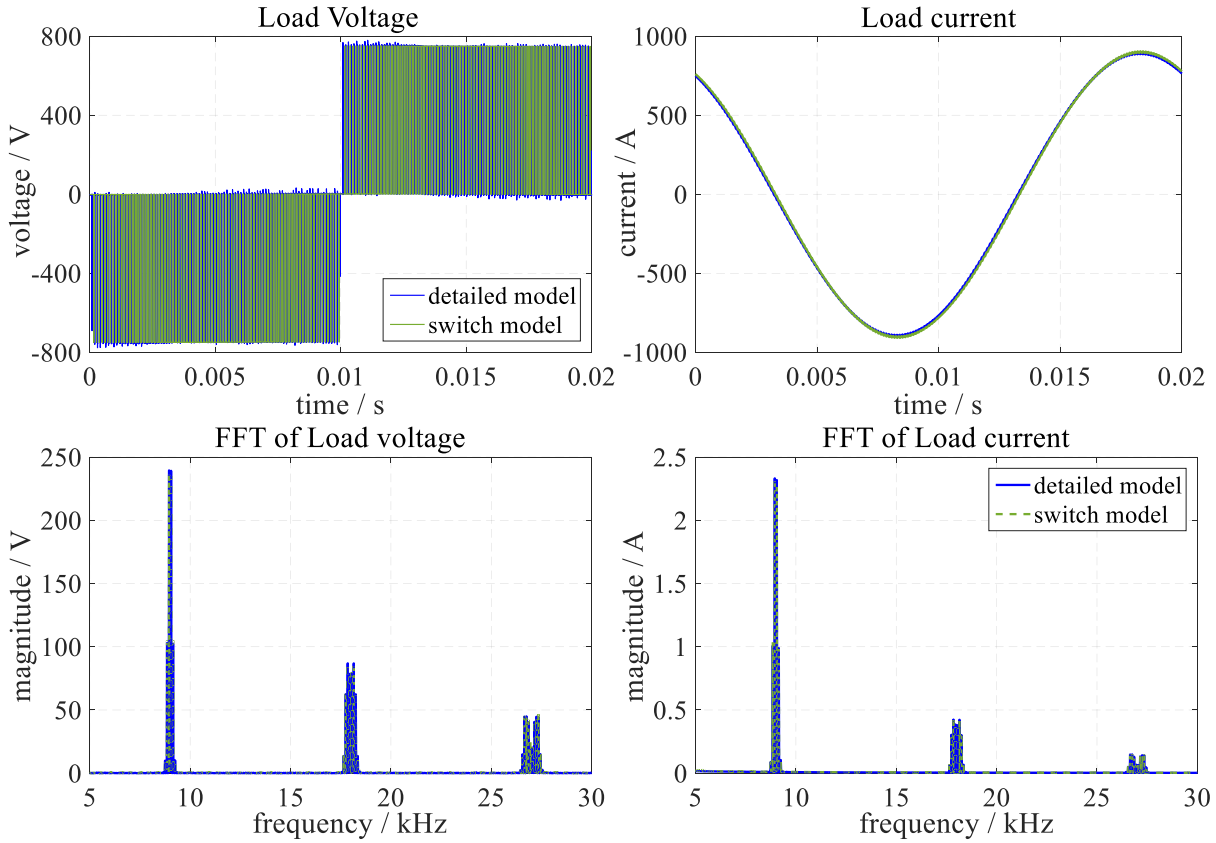

Figure 3-15 Voltage and current wave forms and their FFT spectrum of single-phase full bridge inverter using the detailed and switch models of IGBT

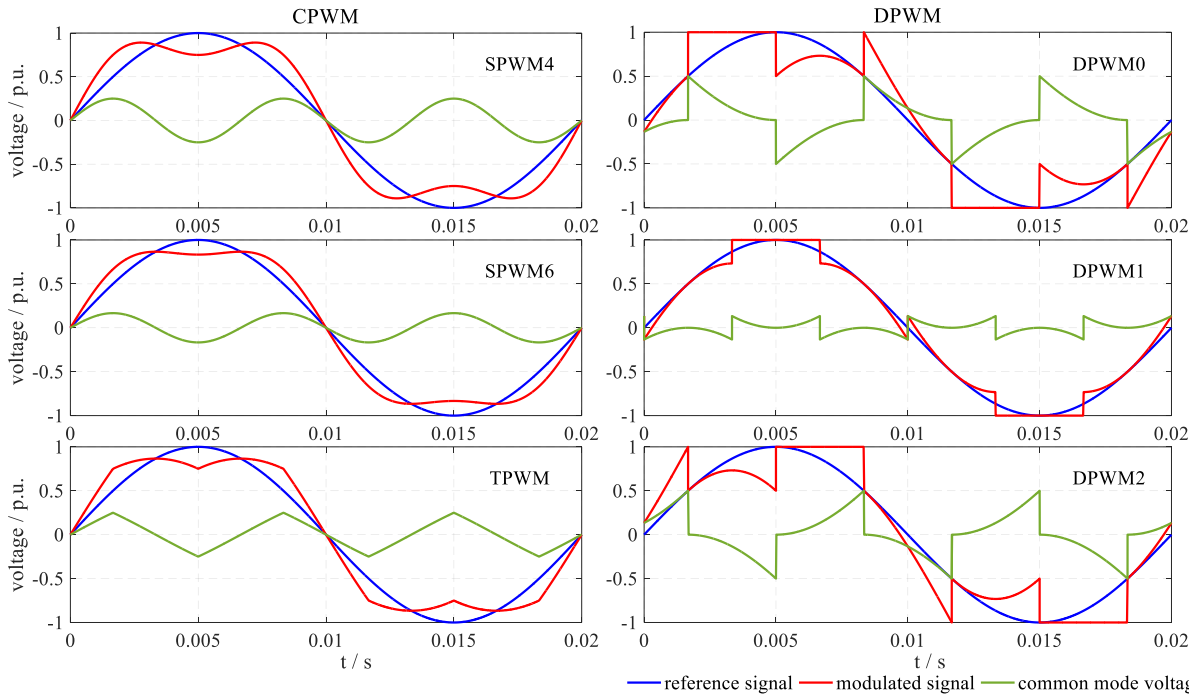

Figure 3-16 CPWM and DPWM signal generation

Another difference between CPWM and DPWM is seen in the generated switching instants, which are produced in accordance with Figure 3-17. In CPWM the switching instants occur continually within each period of the carrier wave, while in the DPWM some switches are not

operated for a certain time within the carrier period as shown in Figure 3-18. This leads to the finding that the CPWM yields higher switching losses than the DPWM. On the other hand, the DPWM will render a higher distortion of the output current than will the CPWM.

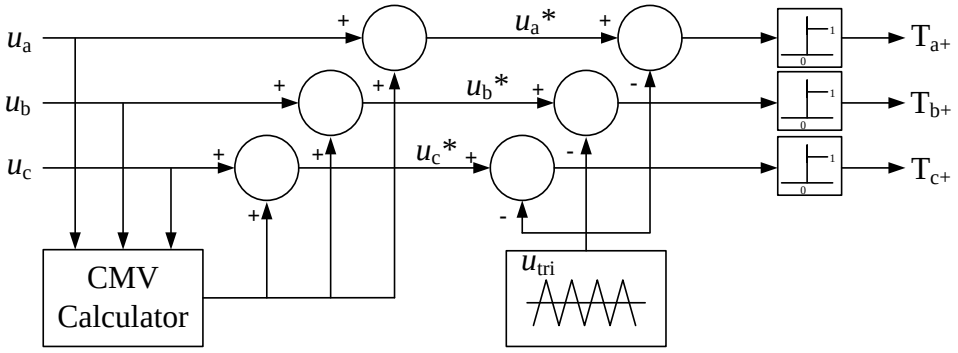

Figure 3-17 PWM switching instants generation

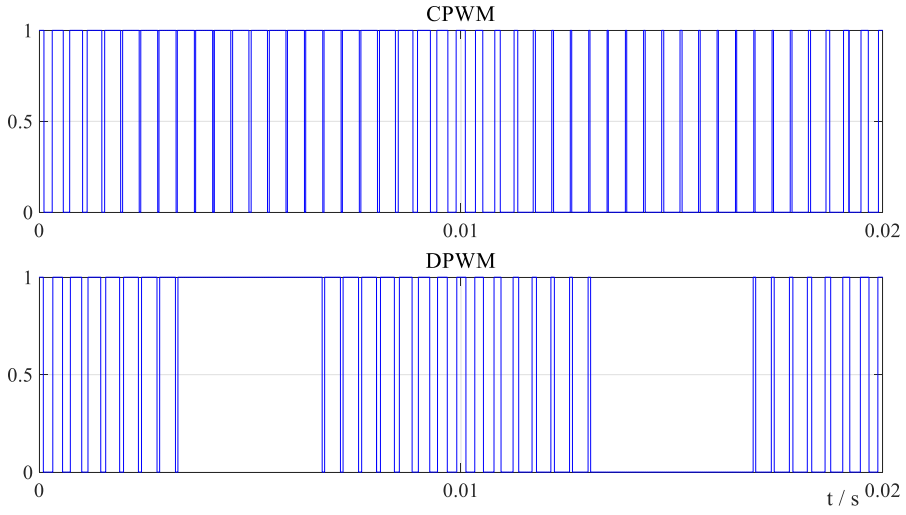

Figure 3-18 Switching patterns of the CPWM and the DPWM

3.3.3 Output Filters

The output waveforms of carrier based PWM converters contain harmonics which are concentrated at the carrier frequency, its sidebands, its multiples, and the sidebands of its multiples. Usually, the carrier frequency is chosen high enough to push the harmonics in the high bands as illustrated in the FFT spectrum in Figure 3-15, but not too high to limit the switching losses.

Harmonic filters are used to minimize the differential mode currents that occur in the cables due to the switching of the IGBTs and diodes, and to minimize the common mode currents that are generated by the high dv/dt of the power electronic components and the coupling capacitors. The filter includes primarily a dv/dt filter, an output choke and a high pass filter. The dv/dt filter is used to reduce voltage spikes in long conductors in order to reduce the stresses on the insulation. However, in wind turbine the converter is placed near the generator and there is no

need for such filter, and the choke, which is used to reduce the output current ripple and to achieve a smooth output current, would be enough, while the high pass filter is used to attenuate high order harmonics.

3.3.4 DC Circuit

The DC circuit as shown in Figure 3-8 consists of a DC capacitor and a braking chopper. The DC capacitor is used to suppress the interfering voltages originating from the rectification process and to prevent fast and large oscillations in the DC voltages. The braking chopper is used to protect the IGBT against high DC bus over voltages that may occur during fault conditions. The value of the DC capacitor is chosen based on the time constant required to charge the capacitor from zero to the rated voltage if supplied by the nominal active power. This time constant is given by:

$$\tau = \frac{1}{2}\frac{C_{\mathrm{DC}} V_{\mathrm{DC,N}}^2}{S_{\mathrm{N}}} \tag{3.19}$$

The DC capacitor time constant is usually set between 5 and 10 ms to satisfy low ripple and overvoltage in the DC voltage and to allow for fast active and reactive power.
The differential equation describing the DC voltage neglecting the losses is given by:

$$\frac{\mathrm{d}v_{\mathrm{DC}}}{\mathrm{d}t} = \frac{1}{c_{\mathrm{DC}}} \cdot i_{\mathrm{DC}} = \frac{1}{c_{\mathrm{DC}}}\left(-i_{\mathrm{LSC,DC}} - i_{\mathrm{MSC,DC}} - i_{\mathrm{CH}}\right) = \frac{1}{c_{\mathrm{DC}} \cdot v_{\mathrm{DC}}}\left(-p_{\mathrm{LSC}} - p_{\mathrm{MSC}} - p_{\mathrm{CH}}\right) \tag{3.20}$$

where,

$$p_{\mathrm{CH}} = \begin{cases} 0 & \text{, if chopper off} \\ \dfrac{v_{\mathrm{DC}}^2}{r_{\mathrm{CH}}} & \text{, if chopper on} \end{cases} \tag{3.21}$$

3.4 Generator

The main focus in this thesis is the DFIG, and only the model of this generator will be introduced. The DFIG is an induction machine type, in which the rotor is wound for the same number of poles as that of the stator and the terminals of the rotor conductor are connected to a set of slip rings that are fed by a power source.

3.4.1 Full Order Model

The voltage equation of the DFIG in the machine variables shown in Figure 3-19 , assuming identical stator and rotor windings, sinusoidal distributed windings, displaced 120°, and considering generation orientation, may be expressed as:

$$\begin{bmatrix} v_{\mathrm{S,abc}} \\ v_{\mathrm{R,abc}} \end{bmatrix} = -\begin{bmatrix} r_{\mathrm{S,abc}} & 0 \\ 0 & r_{\mathrm{R,abc}} \end{bmatrix} \begin{bmatrix} i_{\mathrm{S,abc}} \\ i_{\mathrm{R,abc}} \end{bmatrix} - \frac{\mathrm{d}}{\mathrm{d}t} \begin{bmatrix} \psi_{\mathrm{S,abc}} \\ \psi_{\mathrm{R,abc}} \end{bmatrix} \tag{3.22}$$

The flux linkages may be expressed for a magnetically linear system as:

$$\begin{bmatrix} \psi_{\mathrm{S,abc}} \\ \psi_{\mathrm{R,abc}} \end{bmatrix} = \begin{bmatrix} l_{\mathrm{S,abc}} & l_{\mathrm{M,abc}} \\ l_{\mathrm{M,abc}} & l_{\mathrm{R,abc}} \end{bmatrix} \begin{bmatrix} i_{\mathrm{S,abc}} \\ i_{\mathrm{R,abc}} \end{bmatrix} \tag{3.23}$$

All the relations stated in eq, (3.22) and (3.23) are given in p.u quantities, where all the parameters and variables are normalized to the machine's base power and voltage as given in Appendix. Additionally, all the rotor variables are referred to the stator windings by the stator rotor turns ratio. The assumption that the machine is linear and identical is a simplification that is not adequate for all types of studies. However, it is adequate for the prediction of their behavior in most of the applications [57]. Also, methods of modeling such effects will be introduced and discussed later.

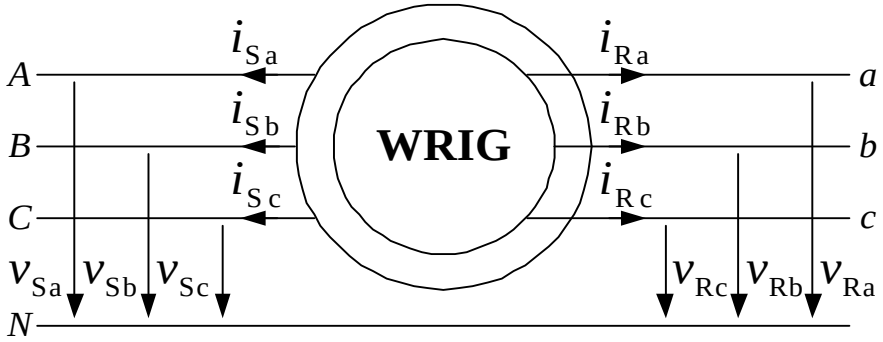

Figure 3-19 Wound rotor induction generator with measured quantities

It is usually desirable to express the machine variables as a space vector in an arbitrary reference frame. Using the transformation relations described in Appendix it yields the space vector model of the DFIG in a fixed reference frame as follows:

Voltage equations:

$$\begin{aligned} \underline{v}_{\mathrm{S1,2}}^{\angle 0} &= -r_{\mathrm{S}}\,\underline{i}_{\mathrm{S1,2}}^{\angle 0} - s\underline{\psi}_{\mathrm{S1,2}}^{\angle 0} \\ \underline{v}_{\mathrm{R1,2}}^{\angle 0} &= -r_{\mathrm{R}}\,\underline{i}_{\mathrm{R1,2}}^{\angle 0} - \left(s \mp \mathrm{j}\omega_{\mathrm{R}}\right)\underline{\psi}_{\mathrm{R1,2}}^{\angle 0} \end{aligned} \tag{3.24}$$

Flux equations:

$$\begin{aligned} \underline{\psi}_{\mathrm{S1,2}}^{\angle 0} &= l_{\mathrm{S}}\,\underline{i}_{\mathrm{S1,2}}^{\angle 0} + l_{\mathrm{M}}\,\underline{i}_{\mathrm{R1,2}}^{\angle 0} \\ \underline{\psi}_{\mathrm{R1,2}}^{\angle 0} &= l_{\mathrm{R}}\,\underline{i}_{\mathrm{R1,2}}^{\angle 0} + l_{\mathrm{M}}\,\underline{i}_{\mathrm{S1,2}}^{\angle 0} \end{aligned} \tag{3.25}$$

Electromagnetic torque

$$t_{\mathrm{el}} = \mathrm{Im}\left\{\underline{\psi}_{\mathrm{S1,2}} \cdot \underline{i}_{\mathrm{S1,2}}^{*}\right\} = \mathrm{Im}\left\{\underline{\psi}_{\mathrm{R1,2}} \cdot \underline{i}_{\mathrm{R1,2}}^{*}\right\} \tag{3.26}$$

Equation of motion

$$2H_{\mathrm{R}}\frac{\mathrm{d}\omega_{\mathrm{R}}}{\mathrm{d}t}=t_{\mathrm{m}}-t_{\mathrm{el}} \tag{3.27}$$

where the subscript 1 and 2 refer to positive and negative sequence respectively. It can be observed that the operator of the rotor speed is positive in the negative sequence model. This occurs due to the fact that the negative sequence model is the conjugate of the positive sequence. Equations (3.24) to (3.27) constitute the full order model (FOM) of the DFIG used for dynamic simulations.

The analysis of the transient response as well as of the control of the DFIG requires the transfer function of the DFIG currents, which can be derived from FOM after some mathematical manipulations as follows:

Stator current:

$$\begin{aligned}\underline{i}_{\mathrm{S1,2}}^{\angle 0}&=\frac{-\left(r_{\mathrm{R}}+\left(s\mp\mathrm{j}\omega_{\mathrm{R}}\right)l_{\mathrm{R}}\right)\underline{v}_{\mathrm{S1,2}}^{\angle 0}+sl_{\mathrm{M}}\underline{v}_{\mathrm{R1,2}}^{\angle 0}}{s^2\sigma l_{\mathrm{S}}l_{\mathrm{R}}+s\left(l_{\mathrm{R}}r_{\mathrm{S}}+l_{\mathrm{S}}r_{\mathrm{R}}\mp\mathrm{j}\omega_{\mathrm{R}}\sigma l_{\mathrm{S}}l_{\mathrm{R}}\right)+r_{\mathrm{S}}\left(r_{\mathrm{R}}\mp\mathrm{j}\omega_{\mathrm{R}}l_{\mathrm{R}}\right)}\\&=\underline{G}_{\mathrm{SZ1,2}}\underline{v}_{\mathrm{S1,2}}^{\angle 0}+\underline{G}_{\mathrm{SW1,2}}\underline{v}_{\mathrm{R1,2}}^{\angle 0}\end{aligned} \tag{3.28}$$

Rotor current:

$$\begin{aligned}\underline{i}_{\mathrm{R1,2}}^{\angle 0}&=\frac{\left(s\mp\mathrm{j}\omega_{\mathrm{R}}\right)l_{\mathrm{M}}\underline{v}_{\mathrm{S1,2}}^{\angle 0}-\left(r_{\mathrm{S}}+sl_{\mathrm{S}}\right)\underline{v}_{\mathrm{R1,2}}^{\angle 0}}{s^2\sigma l_{\mathrm{S}}l_{\mathrm{R}}+s\left(l_{\mathrm{R}}r_{\mathrm{S}}+l_{\mathrm{S}}r_{\mathrm{R}}\mp\mathrm{j}\omega_{\mathrm{R}}\sigma l_{\mathrm{S}}l_{\mathrm{R}}\right)+r_{\mathrm{S}}\left(r_{\mathrm{R}}\mp\mathrm{j}\omega_{\mathrm{R}}l_{\mathrm{R}}\right)}\\&=\underline{G}_{\mathrm{RZ1,2}}\underline{v}_{\mathrm{S1,2}}^{\angle 0}+\underline{G}_{\mathrm{RW1,2}}\underline{v}_{\mathrm{R1,2}}^{\angle 0}\end{aligned} \tag{3.29}$$

where $\sigma=1-\frac{l_{\mathrm{M}}^2}{l_{\mathrm{S}}l_{\mathrm{R}}}$ is the leakage coefficient.

The frequency response of stator and rotor currents are shown in Figure 3-19 and 3-20 respectively with $\omega_{\mathrm{R}}=1.2\omega_{\mathrm{S}}$. As illustrated, both magnitudes of positive and negative sequence responses are a reflection of each other in opposite frequency ranges[5], while the angels are the conjugate of each other. In the low frequency range (0-1 Hz) the response to stator voltage shows a high magnitude for both the positive and the negative sequence, while the response to the rotor voltage shows negative magnitudes for both the positive and the negative sequence. This is because in the low frequency range (substituting the Laplace operator by zero) the rotor circuit is close circuited when seen from the stator side and the stator impedance becomes purely resistive, while the rotor impedance becomes infinite when seen from the rotor. Yet, in the frequency range around the rotor speed (substituting the Laplace operator by

[5] Negative frequency refers to the rotation of the space vector in the opposite direction

$j\omega_R = j1.2\omega_S$) this phenomenon is reversed. The rotor is open circuited when seen from the stator side while the rotor impedance becomes purely resistive when seen from the rotor.

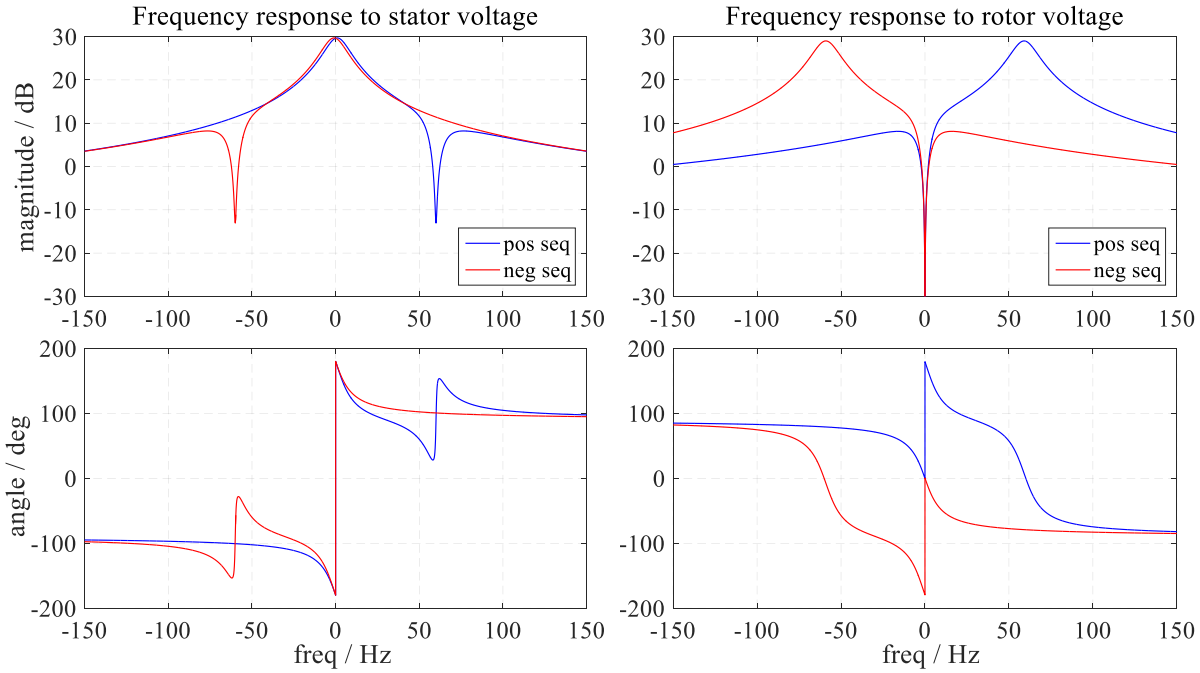

Figure 3-20 DFIG stator current frequency response

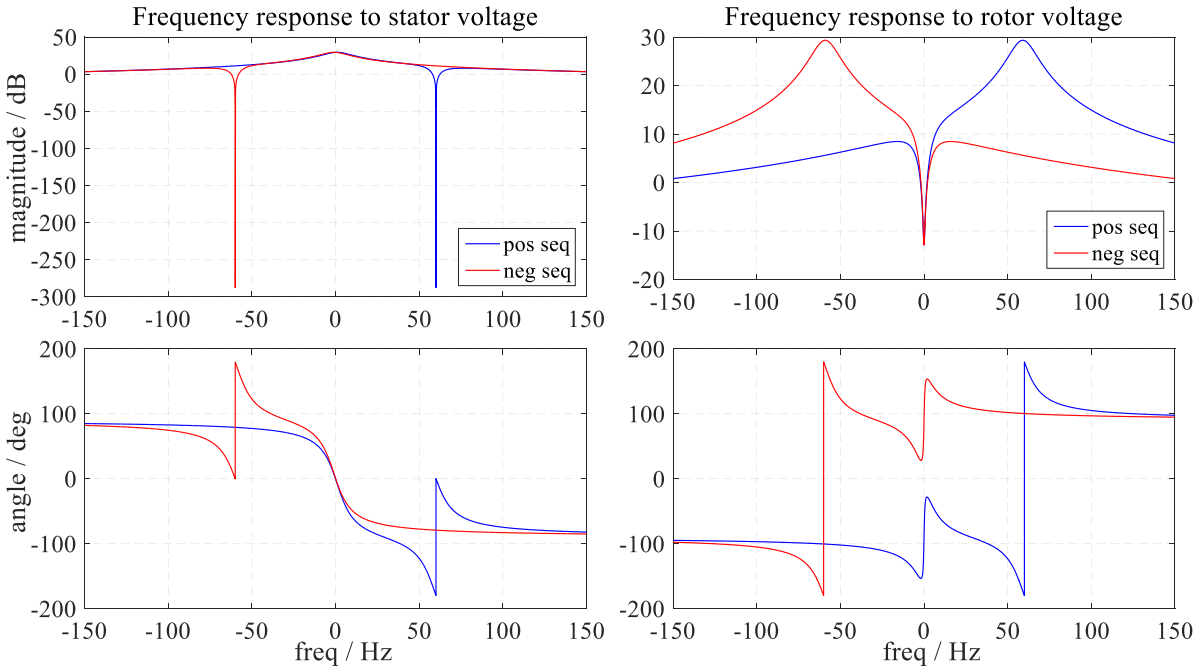

Figure 3-21 DFIG rotor current frequency response

3.4.2 Modeling of Nonlinearities

3.4.2.1 Magnetic Saturation

Magnetic saturation usually occurs due to the nonlinearity of material permeability, where a further increase in the magnetic field's intensity wouldn't lead to a further increase in the flux density and rather levels off. The saturation has a remarkable influence on the performance of the machine and therefore requires an adequate representation [58].

For the DFIG saturation occurs in the main flux and leakage flux paths [59]. The main flux saturation is primarily dependent on the magnetizing current as well as on the load [60], while the leakage flux saturation is dependent on the slot geometry [61] and the magnitude of the phase current. Additionally, there is a cross-saturation between main and leakage flux which is mainly related to the non-linearity of the air-gab and the skewed rotor slots [62].

There are several approaches for modeling the saturation of the DFIG found in literature, which offer high accuracy [61]–[64]. However, they even require knowledge of the machine's physical structure or inherit rigorous and complex set of mathematical equations. A direct method of representing both main and leakage flux saturation while also considering the effect of cross saturation is represented in [59] [60], where the current and the fluxes are measured at different operating points and corresponding saturation curves are obtained by the use of identification tools. Furthermore, polynomial functions or look-up tables are used to modify the inductances online.

3.4.2.2 Skin Effect

The skin effect is a phenomenon that occurs in conductors carrying AC currents, where the magnetic field produced by the AC current induces eddy currents that oppose the main AC current at the conductor center. As a result the AC current is forced to conduct between the conductor surface and a level called skin depth. This implies that the effective cross sectional area of the conductor becomes smaller and consequently the conductor's effective resistance increases while its inductance decreases.

In the DFIG the bottom part of the rotor conductor is linked by a greater slot leakage flux than the top part and the current tends to crowd towards the top of the bar near the air gap and its density decreases exponentially with depth. The skin depth, which is dependent on the slot shape, for a rectangular slot is given by:

$$\delta = \frac{1}{\sqrt{\pi f \mu_0 \gamma}} \tag{3.30}$$

where μ_0 is the air permeability and $\gamma = \rho^{-1}$ is the conductivity coefficient of the bar.

Due to the skin effect the effective rotor resistance and leakage inductance should be modified accordingly as follows:

$$r_{\mathrm{AC}} = \xi \frac{\sinh 2\xi + \sin 2\xi}{\cosh 2\xi - \cos 2\xi} r_{\mathrm{DC}} = \kappa_{\mathrm{r}} r_{\mathrm{DC}}$$
$$l_{\sigma,\mathrm{AC}} = \frac{3}{2\xi} \frac{\sinh 2\xi - \sin 2\xi}{\cosh 2\xi - \cos 2\xi} l_{\sigma,\mathrm{DC}} = \kappa_{\mathrm{l}} l_{\sigma,\mathrm{DC}} \qquad (3.31)$$

where $\xi = h_r \sqrt{\pi f \mu_0 \sigma \frac{b_r}{b_s}}$, h_r, b_r and σ are the rotor conductor's high, width, and conductivity respectively and b_s is the rotor slot width.

3.4.3 High Frequency Models

The increased switching frequency of the VSC leads to an increased parasitic current injection, which, in turn, leads to high shaft voltages, bearing currents and conducted and radiated noises. Such high frequency phenomena cannot be captured by the presented model due to the absence of parasitic components in the model's equations.

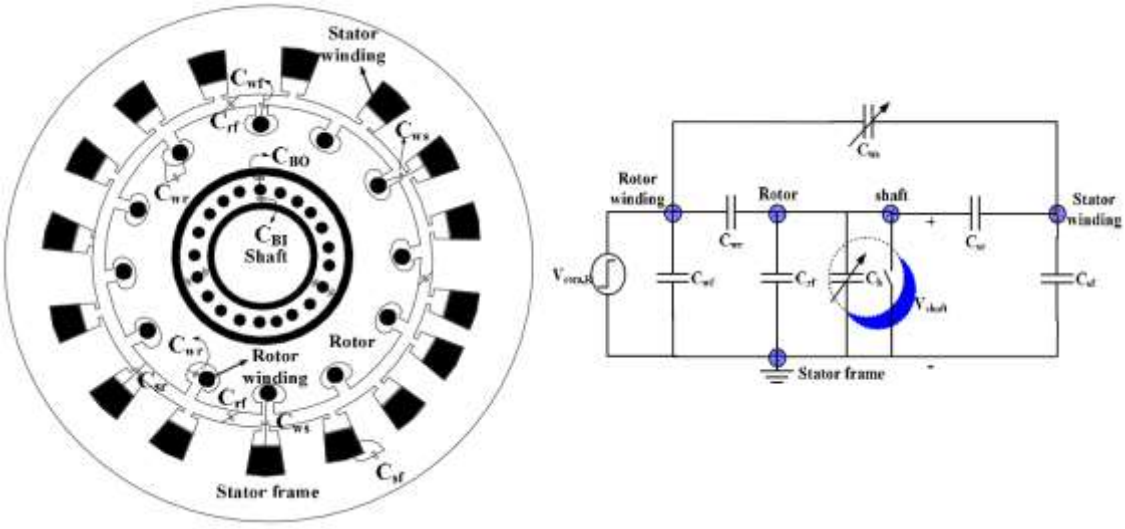

Figure 3-22 DFIG high frequency parasitic capacitances [71]

There are several machine models considering this phenomena found in literature. Those models vary between distributed machine parameter models as in [65]–[67] and lumped machine parameter models as in [68], [69]. A brief and comprehensive review regarding all high frequency models of induction machine can be found in [70]. It can be concluded that the difference between the proposed models is in the details of modeling the parasitic capacitances shown in Figure 3-22 [71], and the range of the targeted frequencies to be captured.

In the low frequency ranges (0-500 Hz) the parasitic capacitances have no remarkable influence on the machine's dynamics except during the starting phase. For the sake of simplicity this can be ignored for the intended study. This becomes evident in [70], where there is an obvious trend to become capacitive only in high frequency ranges.

3.4.4 Reduced Order Models (ROM)

As already noted, the computational costs associated with the performance of the FOM limits their practical applications especially when a wind park with considerable number of units is subjected to power system dynamic stability studies. Therefore, a suitable model is required that makes compromises between the accuracy, for considering relevant dynamic interactions between grid and WT, and the simplicity required for the simulation of large systems.

The simulation tools for stability studies use reduced order models (ROM) of the power system in order to increase the required simulation time step in the range of ms. There are several techniques applied for the model reduction of power systems such as Modal based techniques [72], [73], Balanced Reduction technique [74], optimal Henkel –norm approximation [75] and Integral Manifold theory [76]. However, Singular perturbation technique is the most prominent reduction technique applied to the power system, because it provides a tool to over-come the lack of provision and to improve the quasi-steady-state approximation that characterizes other reduction- order techniques (except Integral Manifold technique) [77], [78].

According to Singular perturbation, the dynamic system can be modeled as a fast and slow system according to the following equations:

$$\begin{aligned} \frac{\mathrm{d}x}{\mathrm{d}t} &= f\left(x,z,u,t,\varepsilon\right), \quad x\left(t_0\right)=x_0 \\ \varepsilon\frac{\mathrm{d}z}{\mathrm{d}t} &= g\left(x,z,u,t,\varepsilon\right), \quad z\left(t_0\right)=z_0 \end{aligned} \tag{3.32}$$

where ε is a small positive parameter that denotes how fast the fast system reaches its steady state. Accordingly, setting $\varepsilon = 0$ imposes that the speed of z is infinite and its transient is instantaneous.

Applying Singular perturbation to the DFIG setting $\underline{\psi}_{\mathrm{S1,2}}^{\angle \pm \omega_{\mathrm{S}}}$ as the fast state-variable and neglecting its derivative to the much faster frequency components results in an algebraic equivalent circuit shown in Figure 3-23, where the transient impedance is defined as:

$$\underline{z}'_{\mathrm{S1,2}} = r_{\mathrm{S}} + \mathrm{j}\omega_{\mathrm{S}}\sigma l_{\mathrm{S}} \tag{3.33}$$

and the Thevenin voltage source behind the impedance is defined as a function of the state variable rotor flux:

$$\underline{v}'_{1,2} = \mathrm{j}\omega_0 l_\mathrm{M} \underline{\psi}_{\mathrm{R1,2}}^{\angle \pm \omega_\mathrm{S}} \tag{3.34}$$

The state variable rotor flux is found by solving the following differential equation:

$$\dot{\underline{\psi}}_{\mathrm{R1,2}}^{\angle \pm \omega_\mathrm{S}} = -r_\mathrm{R} \frac{l_\mathrm{M}}{l_\mathrm{R}} \underline{i}_{\mathrm{S1,2}}^{\angle \pm \omega_\mathrm{S}} - \left(\frac{r_\mathrm{R}}{l_\mathrm{R}} + \mathrm{j}\left(\omega_\mathrm{S} \mp \omega_\mathrm{R}\right) \right) \underline{\psi}_{\mathrm{R1,2}}^{\angle \pm \omega_\mathrm{S}} - \underline{v}_{\mathrm{R1,2}}^{\angle \pm \omega_\mathrm{S}} \tag{3.35}$$

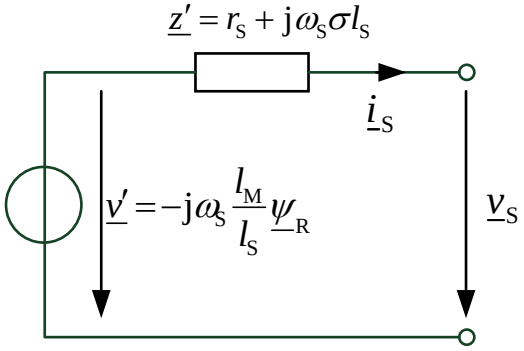

Figure 3-23 DFIG ROM equivalent circuit

3.4.4.1 Extended ROM (ROM/E)

Neglecting the derivative of the stator flux leads to the inclusion of the rotating dynamics and the exclusion of the stationary dynamics. In other words, the DC decaying components of fluxes and consequently their currents will be missing. The absence of the DC components results in ill attendance of the protection system, because they create an alternating active power resulting in a fast rise of the DC-link voltage and subsequently can lead to chopper operation. Also, it increases the rotor current magnitude and may lead to the blocking of the MSC [79]. Additionally, the short backward movement of the rotor angle, called “back-swing-effect”, which occurs directly after the fault, will be missing [80].

For this purpose an enhanced model was proposed in [79] and [81] that allows for the use of the ROM, but activates an additional differential equation of the stator flux that accounts for the DC-components when required. This differential equation is given by:

$$\dot{\tilde{\underline{\psi}}}_\mathrm{S}^{\angle \omega_\mathrm{S}} = -\left(\frac{r_\mathrm{S} + r_\mathrm{N}}{l_\mathrm{S} + l_\mathrm{N}} + \mathrm{j}\omega_\mathrm{S} \right) \left(\tilde{\underline{\psi}}_\mathrm{S}^{\angle \omega_\mathrm{S}} - \underline{\psi}_\mathrm{S}^{\angle \omega_\mathrm{S}^{ROM}} \right) \tag{3.36}$$

where the superscript “ROM” signifies the slow ROM solution, and r_N and l_N represent the network resistance and inductance.

Equation (3.36) is valid when assuming that $\underline{\psi}_\mathrm{R} \approx \underline{\psi}_\mathrm{R}^{ROM}$ and $\underline{v}_\mathrm{S} = \underline{v}_\mathrm{S}^{ROM}$. The first assumption is nearly fulfilled when the crowbar is switched off. Yet, it is less tenable with the presence of the crowbar in the circuit but still acceptable, while the second assumption presupposes that the stator terminal is extended up to the Thevenin equivalent voltage of the grid. In this case, the

stator's parameters must also be modified to include the network impedance. However, it should be emphasized that it is not necessary to know specifics for the assumption to be, in principle, possible. It is obvious that the suggested extension of the stator circuits to a virtual voltage source corresponds with the assumptions used for the standard short-circuit current calculation. Still, the approach presupposes constant equivalent grid impedance. Therefore, the simulation is restricted to cases where the impedance is not significantly affected by the grid fault.

To account for the full extent of the interaction between the DFIG and the rotor side converter, one has to distinguish between four operating modes, they are:

Mode 1) Normal mode. Rotor current and rotor voltage are controlled by the IGBTs

Mode 2) Crowbar mode. Rotor side IGBT-converter switched off, crowbar switched on. When the crowbar is on, the DFIG equations have to be solved with $\underline{v}_\mathrm{R} = 0$ and $r_\mathrm{R} \rightarrow r_\mathrm{R} + r_\mathrm{CR}$. The rotor side converter controller is stopped and reset in this mode.

Mode 3) No load mode; rotor side IGBT-converter switched off and rotor-current $\underline{i}_\mathrm{R} = 0$.

Mode 4) Deactivated IGBT-converter mode current); generator rotor windings are fed by anti-parallel diodes of rotor side converter. Fast rise of the dc-link voltage is possible. In this mode the DFIG can be described by the same equations as used for normal mode. However, the absolute value of the rotor voltage is determined by the dc-link voltage only

$$\underline{v}_\mathrm{R} = -\frac{2}{w\pi} v_\mathrm{dc} e^{\mathrm{j}\arg(\underline{i}_\mathrm{R})} \tag{3.37}$$

where w considers the turns ratio between the reference values of v_dc and $\underline{v}_\mathrm{R}$.

3.4.4.2 Modified ROM (ROM/M)

Another approach to consider the DC decaying components is to directly estimate their values from the ROM. In synchronous rotating frame fluxes responses can be divided into fast response representing the DC component and slow response representing the AC components. Following from this and from the fact that the stator voltage contains only AC component, the fast system can be derived from eq. (3.24) by ignoring $\dot{\underline{\psi}}_\mathrm{R}$ as:

$$\begin{aligned}
\Delta\underline{v}_\mathrm{S}^{\angle\omega_\mathrm{S}} e^{-\mathrm{j}\omega_\mathrm{S} t} &= -\left(s + \frac{r_\mathrm{S}}{\sigma l_\mathrm{S}} \right) \Delta\underline{\psi}_\mathrm{S,DC}^{\angle 0} + \frac{r_\mathrm{S} l_\mathrm{M}}{\sigma l_\mathrm{S} l_\mathrm{R}} \Delta\underline{\psi}_\mathrm{R,DC}^{\angle 0} \\
\Delta\underline{v}_\mathrm{R}^{\angle\omega_\mathrm{S}} e^{-\mathrm{j}\omega_\mathrm{S} t} &= -\left(\frac{r_\mathrm{R}}{\sigma l_\mathrm{R}} + \mathrm{j}\left(\omega_\mathrm{S} - \omega_\mathrm{R}\right) \right) \Delta\underline{\psi}_\mathrm{R,DC}^{\angle 0} + \frac{r_\mathrm{R} l_\mathrm{M}}{\sigma l_\mathrm{S} l_\mathrm{R}} \Delta\underline{\psi}_\mathrm{S,DC}^{\angle 0}
\end{aligned} \tag{3.38}$$

Rearranging eq. (3.38) yields the fluxes DC components:

$$\Delta\underline{\psi}_{\mathrm{S,DC}}^{\angle 0} = \frac{-\Delta\underline{v}_{\mathrm{S}}^{\angle\omega_{\mathrm{S}}} e^{-\mathrm{j}\omega_{\mathrm{S}}t} + \dfrac{r_{\mathrm{S}} l_{\mathrm{M}}}{\sigma l_{\mathrm{S}} l_{\mathrm{R}}} \underline{\psi}_{\mathrm{R,DC}}^{\angle 0}}{s + \dfrac{r_{\mathrm{S}}}{\sigma l_{\mathrm{S}}}}$$

$$\Delta\underline{\psi}_{\mathrm{R,DC}}^{\angle 0} = \frac{-\Delta\underline{v}_{\mathrm{R}}^{\angle\omega_{\mathrm{S}}} e^{-\mathrm{j}\omega_{\mathrm{S}}t} + \dfrac{r_{\mathrm{R}} l_{\mathrm{M}}}{\sigma l_{\mathrm{S}} l_{\mathrm{R}}} \underline{\psi}_{\mathrm{S,DC}}^{\angle 0}}{\dfrac{r_{\mathrm{R}}}{\sigma l_{\mathrm{R}}} + \mathrm{j}\left(\omega_{\mathrm{S}} - \omega_{\mathrm{R}}\right)} \qquad (3.39)$$

As given in the previous equation the stator flux DC component can be calculated using a PT1 element with the stator time constant, while the rotor flux DC component can be directly calculated from the rotor voltage which is decided by the controller. Figure 3-24 shows the implementation of eq. (3.39) to estimate the DC components of the fluxes and currents, where it is clear that a specific knowledge of the network parameters is not required.

The same modes described for ROM/E are also valid for this method, but for Mode 4 the rotor voltage would be given by:

$$\Delta\underline{v}_{\mathrm{R}} = -2 r_{\mathrm{CH}} \underline{i}_{\mathrm{R}} \qquad (3.40)$$

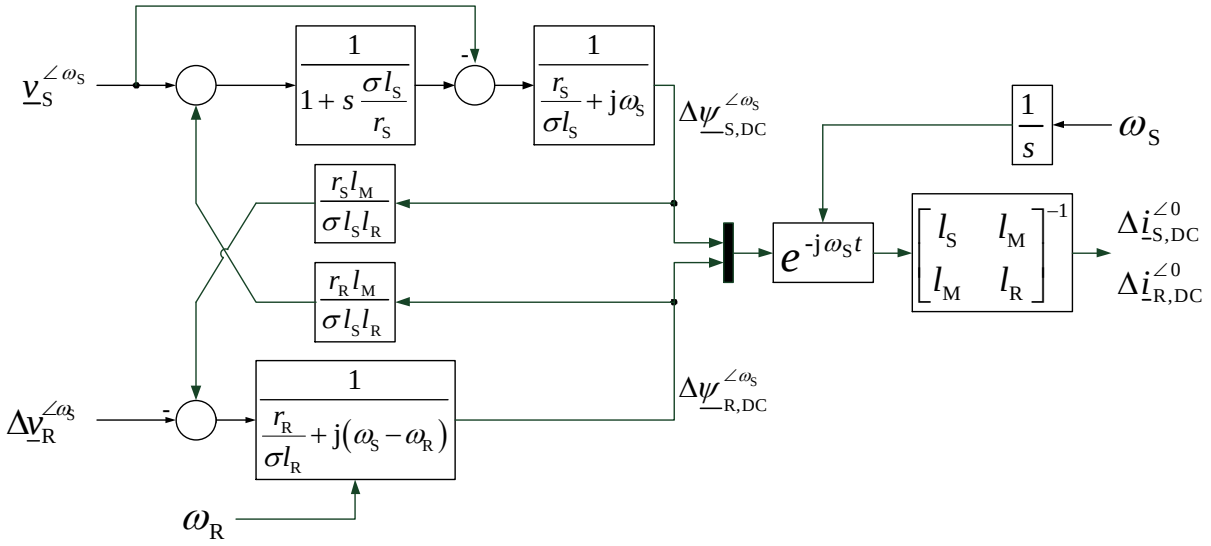

Figure 3-24 Modified DFIG ROM to estimate the DC components

3.4.5 Steady State Model

The steady-state model of the DFIG is required for the load flow calculation and for the design of the MSC converter. The steady-state model is derived from the vector model in eq. (3.24) by replacing the Laplace operator by the operating frequency:

$$\underline{v}_{\mathrm{S1,2}} = -r_{\mathrm{S}} \underline{i}_{\mathrm{S1,2}} - \mathrm{j}\omega_{\mathrm{S}} \underline{\psi}_{\mathrm{S1,2}}$$
$$\underline{v}_{\mathrm{R1,2}} = -r_{\mathrm{R}} \underline{i}_{\mathrm{R1,2}} - \mathrm{j}\left(\omega_{\mathrm{S}} \mp \omega_{\mathrm{R}}\right) \underline{\psi}_{\mathrm{R1,2}} \qquad (3.41)$$

Eliminating the fluxes yields:

$$\begin{aligned}
\underline{v}_{S1,2} &= -r_S \underline{i}_{S1,2} - \mathrm{j}\omega_S \left(l_S \underline{i}_{S1,2} + l_M \underline{i}_{R1,2} \right) = -r_S \underline{i}_{S1,2} - \mathrm{j}x_S \underline{i}_{S1,2} - \mathrm{j}x_M \underline{i}_{R1,2} \\
\frac{\underline{v}_{R1,2}}{s_{G1,2}} &= -\frac{r_R}{s_{G1,2}} \underline{i}_{R1,2} - \mathrm{j}\omega_S \left(l_R \underline{i}_{R1,2} + l_M \underline{i}_{S1,2} \right) = -\frac{r_R}{s_{G1,2}} \underline{i}_{R1,2} - \mathrm{j}x_R \underline{i}_{R1,2} - \mathrm{j}x_M \underline{i}_{S1,2}
\end{aligned} \qquad (3.42)$$

with the slip $s_{G1,2} = \dfrac{\omega_S \mp \omega_R}{\omega_S}$.

The equivalent circuit of the DFIG based on eq. (3.42) is shown in Figure 3-25.

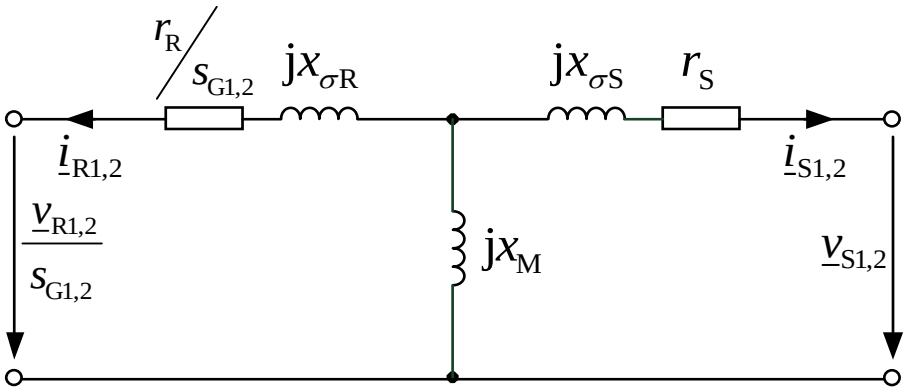

Figure 3-25 DFIG steady-state equivalent circuit

4 Control Design of DFIG-WT

The control of wind turbines can be divided into two hierarchical control tasks which are; supervisory wind farm control and in place wind turbine control. The task of the wind farm control is to determine the individual V/Q set points for each individual WT based as well as for the compensation units based on the commands communicated from the transmission or distribution system operator (TSO/ DSO), in order to fulfill the required control objectives at the point of common coupling (PCC). The task of the wind turbine control is to maximize and optimize the energy capture from the wind, provision of ancillary services, i.e frequency control and reactive power control, ride through of faults, interact with the wind farm control, WT protection and start-up/ shut-down of WT. In this sense the wind turbine control is divided into three control loops which are: turbine control, MSC control and LSC control. Figure 4-1 illustrates the structure of the hierarchical control of the WT in a wind farm and the different control loops and the assigned objectives. It should be noted that the wind farm control will not be discussed because it is not part of this work. However, a detailed discussion related to it can be found in [41]. P_S

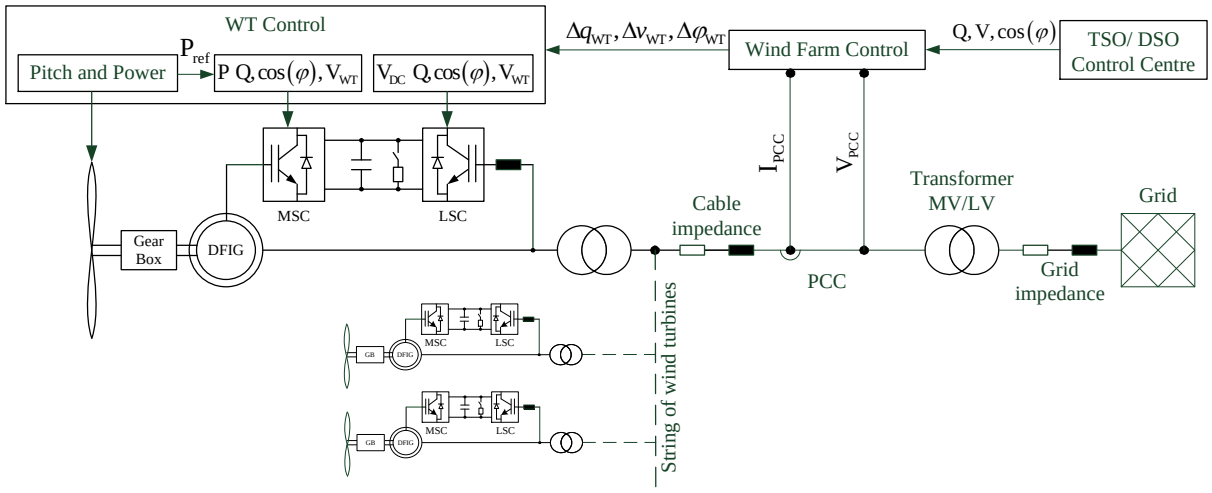

Figure 4-1 Structure of the WT's hierarchical control and its assigned objectives

4.1 Turbine Control

The turbine control fulfills two main tasks namely the power-speed control and the pitch control. The objective of the first task is to maximize energy yields from the wind by adjusting the rotational speed in accordance to the tracking curve, while the objective of the second task is to maintain the rotational speed and limit the turbine power during high wind speed and wind gusts periods. According to this it can be concluded that the power-speed control is only active below the rated turbine speed and the pitch control is active beyond the rated speed. However,

a conflict between the two controllers may occur at the rated speed because the speed will fluctuate around the rated speed as a result of gusts [41].

4.1.1 Power-Speed Control

The turbine speed is limited between the two speeds illustrated in Figure 4-2 within the power-speed control functions. The cut-in speed limit is set so that the energy yield from wind would cover the overall losses of the system with a surplus, while the cut-out speed is set in accordance to the structural and design limitations and the acoustic impact.

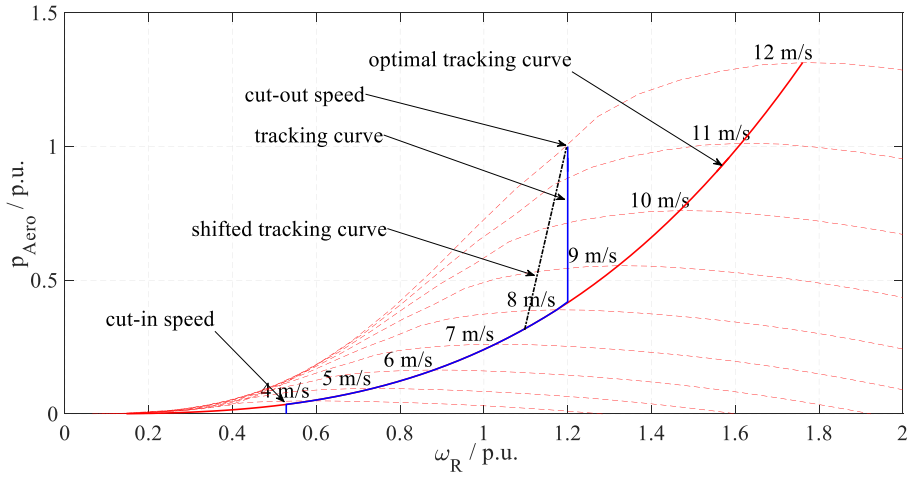

Figure 4-2 Power-speed tracking curve of DFIG-WT

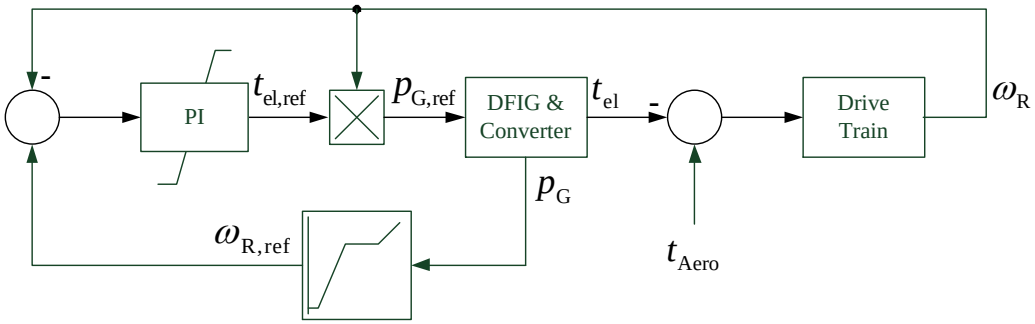

Figure 4-3 Power-speed controller of DFIG-WT

The tracking curve represents a relationship between the measured power and the reference speed. Around the rated speed the power curve is deviated to avoid any conflict with the pitch controller and avoid over speed tripping. The tracking curve can be interpreted by a look-up table in the controller, from which the reference speed is selected and with the aid of a PI-controller the reference power set-point can be estimated. Figure 4-3 shows the schematic representation of the power-speed controller, where the measured power rather than the wind speed is utilized to determine the reference speed in order to avoid distortions and inaccuracies accompanied with the measurement of wind speed. Such arrangement offers an easy and

straight forward method for power and speed control in contrast to other strategies based on nonlinear control or search algorithms that require extensive knowledge of the turbine structure.

4.1.2 Pitch Control

Beyond the rated wind speed the aerodynamic torque as well as the turbine speed should be limited to their rated values. As already mentioned, this is achieved by the pitch controller which manipulate the aerodynamic coefficient through changing the pitch angle. The pitch angle is adjusted by means of a servo-mechanism, which is modeled as a PT1 element of a time delay equal to the servo time constant and with a rate and output limitation.

The pitch angle is controlled by a PI-controller that generates the reference pitch angle based on the error difference between the measured and the rated speed as follows:

$$\beta_{\text{ref}} = k_{\text{P}}\left(1+\frac{1}{s\tau_{\text{I}}}\right)\left(\omega_{\text{R,ref}}-\omega_{\text{R}}\right) \tag{4.1}$$

The gain of the PI-controller is expressed as a static gain times the reciprocal of aerodynamic sensitivity of the system in order to counteract any variation. The static gain and time integral are designed considering the system behavior of a second order system, which yields the following expression [50]:

$$k_{\text{P}} \cong \frac{2\xi k_{\text{Shaft}}\omega_{\text{R,ref}}}{\omega_0}\left[-\frac{\text{d}P}{\text{d}\theta}\right]^{-1},\ \tau_{\text{I}} = \frac{2\xi}{\omega_0} \tag{4.2}$$

where $\text{d}P/\text{d}\theta$ is the aerodynamic sensitivity and ξ and ω_0 are the controller design parameters with typical values of 0.66 and 0.6 respectively.

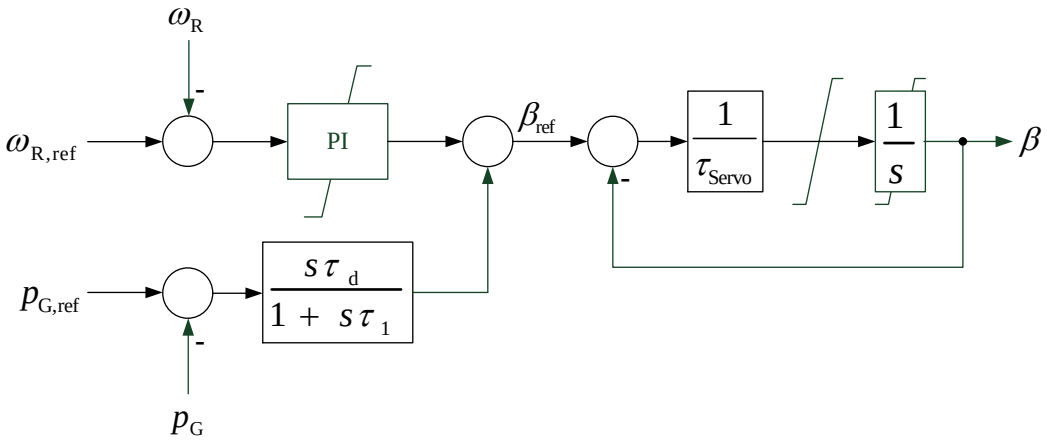

Figure 4-4 Pitch control system

In addition to the pitch controller a pitch booster is included to ensure a fast reaction to power changes caused by a voltage drop or strong wind gusts. The overall schematic of the pitch controller is shown in Figure 4-4.

4.2 Converters Control

The frequency converter of the DFIG contains two independent controllers, one assigned to the LSC and one to the MSC as demonstrated in Figure 4-1. The design of both controllers is the key factor for the safe and stable operation of the DFIG for different grid conditions. Additionally, they determine whether or not the DFIG is subjected to the grid codes requirements. Therefore, the controllers design will be discussed in detail. First of all, the procedure for sequence separation will be introduced, because it is a common component in both controllers and it offers different control options and the ability for the objectives' selection and prioritization. Later on, the LSC and MSC control will be derived and the current and voltage limitation strategies will be discussed. Finally, the stability of both LSC and MSC controllers will be investigated considering the influence of the DFIG non-linarites.

4.2.1 Positive and Negative Sequence Components Separation Methods

Sequence detection can be thought as a subset of the synchronization problem, which is closely related to the estimation of the fundamental frequency. A fast and accurate tracking of the positive sequence fundamental grid voltage frequency and magnitude is required for the synchronization of the converters with the grid. Additionally, it enhances the network stability through appropriate active and reactive power provision performed by the converter during and post grid faults. There are widespread separation techniques available, for instance delay signal cancellation (DSC), a double second order generalized integrator (DSOGI), a decoupled double synchronous reference frame (DDSRF), etc. A review regarding the available detection techniques and their performances can be found in [82]. Although these techniques have been shown to be accurate, their performances may be severely affected by harmonics especially by low order harmonics and sub harmonics. Furthermore, due to the complexity of the resulting nonlinear closed loop scheme, it is difficult to design the parameters in order to ensure stability or some desired transient performance.

Negative sequence detection according to Lê

A fast and accurate method for negative sequence detection was introduced in 1989 by Lê.[83]. According to Fortescue the complex conjugate space vector of the negative sequence component assuming a harmonic free three-phase system can be written as [84]:

$$\underline{y}_2^{*\angle 0} = \frac{1}{2}\left(\underline{y}^{\angle 0} - \mathrm{j} \cdot \underline{y}^{\angle 0} e^{\mathrm{j}\frac{\pi}{2}} \right) \tag{4.3}$$

Based on the fact stated in eq. (4.3), Lê has utilized a PT1 element and two gain factors to realize the 90 lead phase shift in the input space vector and consequently facilitate the extraction of the negative sequence space vector as shown in Figure 4-5. The time constants and gain factors are given by:

$$\tau_{\mathrm{Lê}} = \frac{1}{k_2 \omega_0} \tag{4.4}$$

$$k_1 = 1 + \frac{1}{k_2^2} \tag{4.5}$$

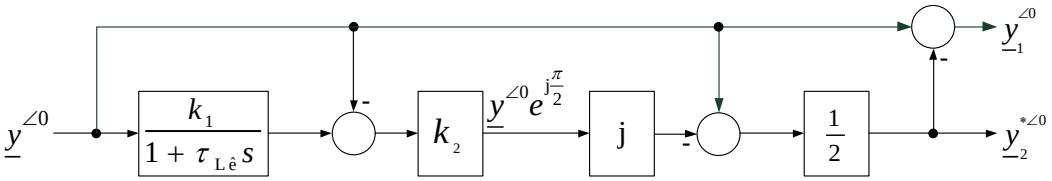

Figure 4-5 Positive and negative sequence detection according to Lê

The transfer function of the Lê filter would then be given by:

$$\underline{G}_{\mathrm{Lê}} = \frac{1}{2} + \frac{1}{2} k_2 \left(1 - \mathrm{j} \frac{k_1}{1 + s\tau_{\mathrm{Lê}}} \right) \tag{4.6}$$

The frequency loci of the negative sequence space vector as well as the step response according to eq. (4.6) for different k_2 values are shown in Figure 4-6 and 4-7 respectively. It is clear that the filter offers a unity gain without phase shift to the negative sequence component, and full rejection of the positive sequence component. However, the main disadvantages are the high reinforcement of the high order harmonics as well as the high dynamic over-shoots that increase with the k_2 value.

In order to reduce the gain in the high frequency range as well as the dynamic over-shoot a low-pass filter can be adapted to the negative sequence component as represented in Figure 4-8. In this process the negative sequence component is detected according to Lê and then transformed to its rotating coordinate, where a low-pass filter can be applied to filter out any unwanted harmonics and finally transform them back. The time constant of the low-pass filter is chosen such that it would not extend the response time significantly and reduces the gain of the nearest high frequency.

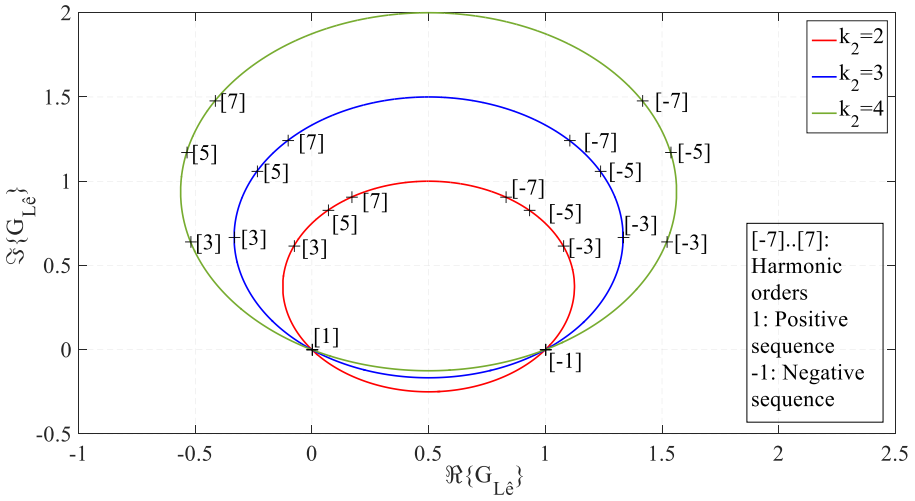

Figure 4-6 Frequency response locus of the negative sequence component according to Lê

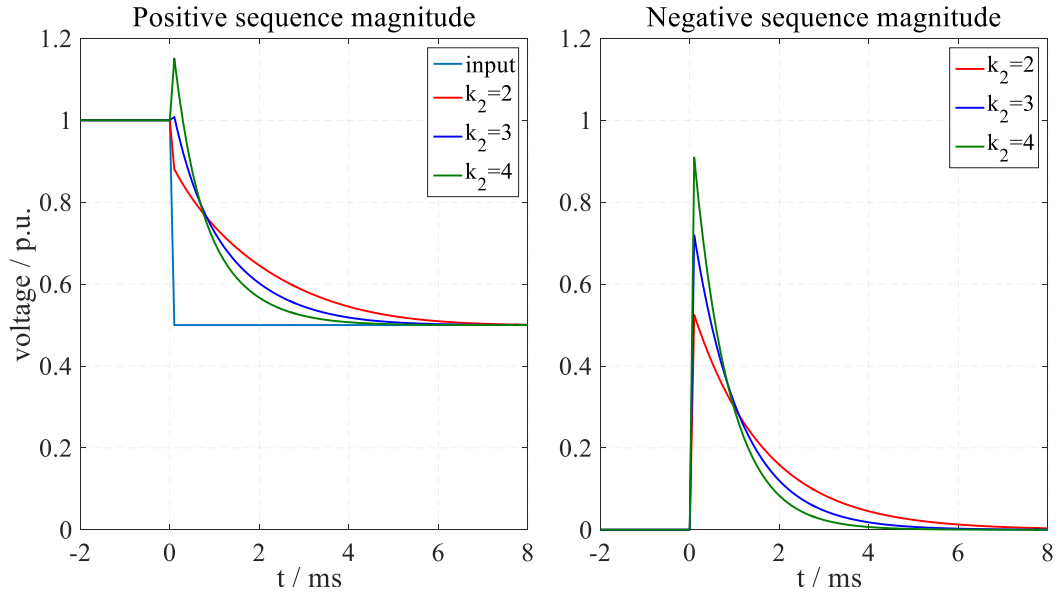

Figure 4-7 Step response of the Lê filter transfer function

The frequency loci of the negative sequence space vector and the step response of the modified method are shown in Figure 4-9 and 4-10 respectively. It is obvious how the modified method successfully reduces the high frequency gains and the over-shoot without significantly increasing the response time.

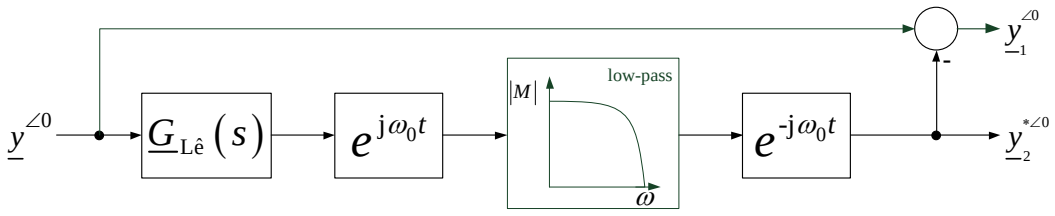

Figure 4-8 Modified Lê filter structure

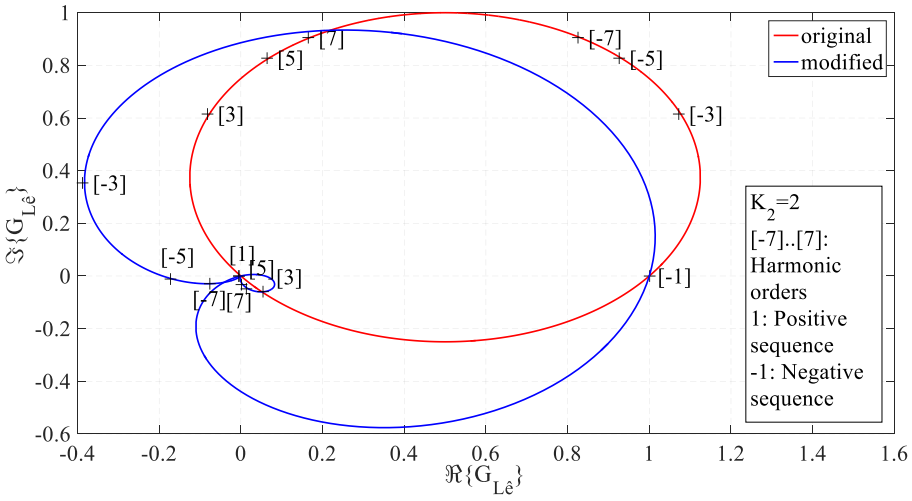

Figure 4-9 Frequency response locus of the modified Lê filter

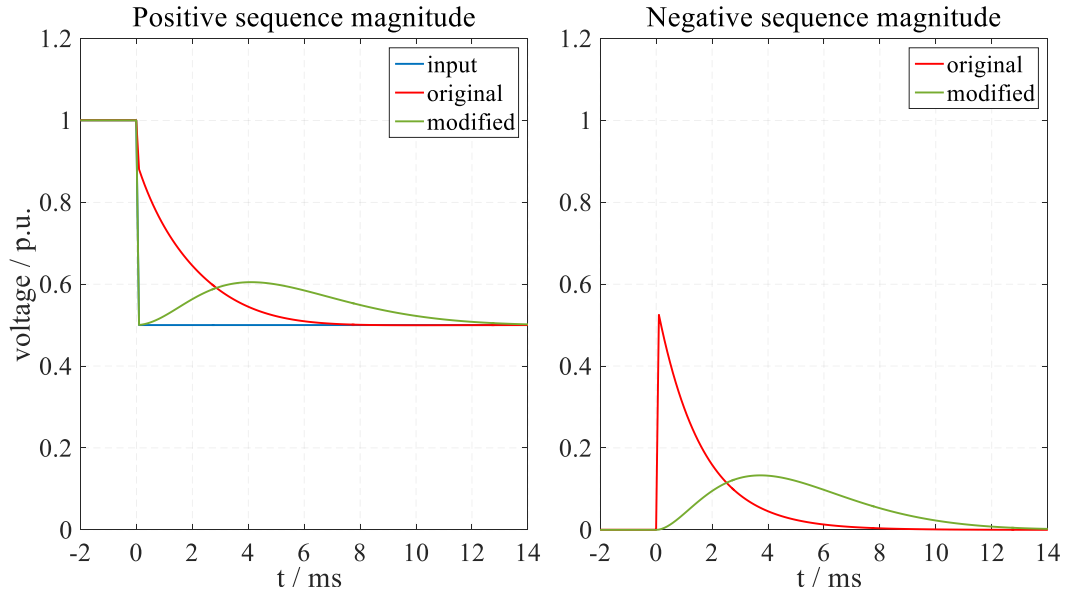

Figure 4-10 Step response of the modified Lê filter

4.2.2 Stability Criterion for Grid-Connected Inverters

The increased penetration of converter based renewable energy sources into the electrical power system has raised concerns regarding the effects of grid impedance on the converter's control performance and stability. The grid impedance has a great influence on the current control loop stability and in case of a weak grid connection the controller may be destabilized and which might lead to sustained harmonic resonance. In addition, the non-linear behavior of the grid operation requires an adequate design of the current control loop as well as grid filters to satisfy a very large set of grid impedance [85], [86].

The stability analysis of such an interconnected system is performed by using the impedance-based stability criterion, in which the system's stability is guaranteed when the ratio of the source output impedance to the load input impedance satisfies the Nyquist stability criterion

[87]. In the system shown in Figure 4-11, under the assumption of the small-signal model, the current flowing is given by:

$$\underline{i}_s(s) = \frac{\underline{v}_s(s)}{\underline{z}_l(s)} \cdot \frac{1}{1+\frac{\underline{z}_s(s)}{\underline{z}_l(s)}} \tag{4.7}$$

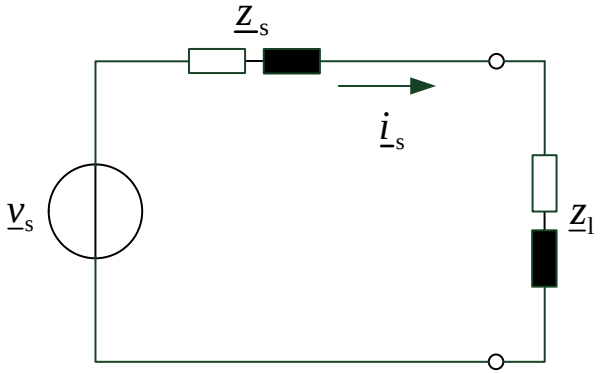

Figure 4-11 Small-signal representation of a voltage source

Under the assumption that the source voltage and the load admittance are stable, the source current is stable if and only if the locus of the open-loop transfer function $h(s) = \underline{z}_s(s)/\underline{z}_l(s)$ encircles -1+j0 counterclockwise N times equal to the number of poles of $h(s)$ in the right-half *s* plane.

It will be shown later that the grid connected inverter tends to act as a current source with the output current as a function of both the internal reference set-point currents and the terminal/grid voltage. Therefore, applying the existing impedance-based stability criterion would lead to misleading results. As a result, another method should be adapted to offer a comprehensive insight of the controller's stability.

Rewriting the inverter output current as a function of both the reference current and the terminal voltage yields:

$$\underline{i}_s(s) = \underline{G}_{ref}(s)\underline{i}_{ref}(s) + \underline{G}_s(s)\underline{v}_s(s) \tag{4.8}$$

Based on eq. (4.8) the inverter equivalent circuit would match Figure 4-12 provided that:

$$\begin{aligned} \underline{z}_s(s) &= -\frac{1-\underline{G}_{ref}(s)}{\underline{G}_s(s)} \\ \underline{y}_{ref}(s) &= -\frac{\underline{G}_s(s)}{\underline{G}_{ref}(s)} \end{aligned} \tag{4.9}$$

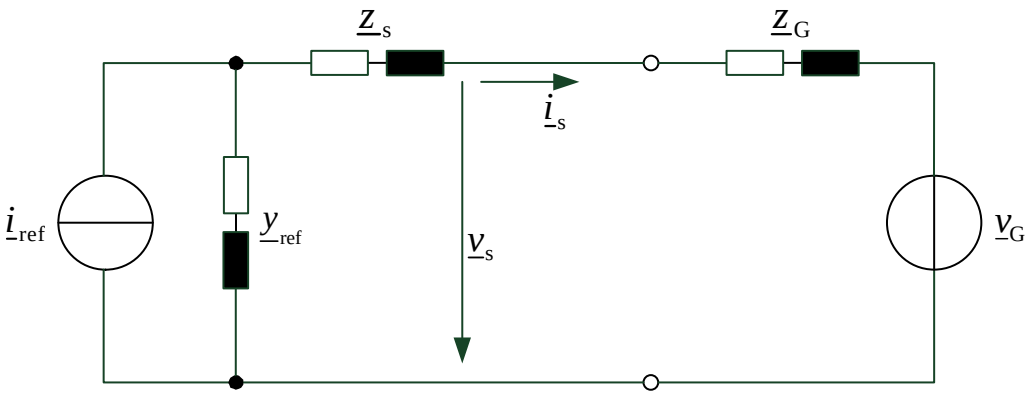

Figure 4-12 Equivalent circuit of a grid-connected inverter

With the given arrangement the controller's stability should be investigated in two modes of operation. The first mode is the floating mode, where the inverter's output current stability is investigated when the inverter does not inject a current into the grid as shown in Figure 4-13. In this case the inverter output current is given by:

$$\underline{i}_s(s) = \frac{\underline{v}_G(s)}{\underline{z}_G(s)} \cdot \frac{1}{1+\dfrac{\underline{z}_s(s)+\underline{z}_{ref}(s)}{\underline{z}_G(s)}} \tag{4.10}$$

Then, the inverter's output current is stable if and only if the open-loop transfer function $h_I(s) = \left(\underline{z}_s(s)+\underline{z}_{ref}(s)\right)\big/\underline{z}_G(s)$ is stable.

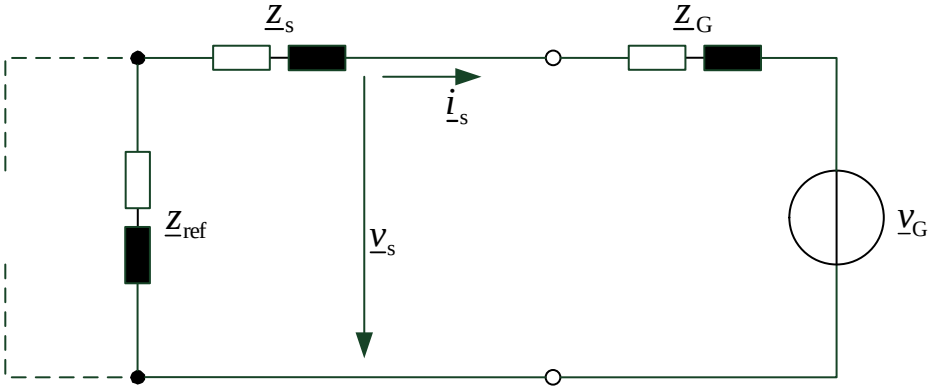

Figure 4-13 Equivalent circuit for inverter output voltage stability investigation

The second mode is the stand alone mode, where the inverter output voltage stability is investigated when the load is fed only through the inverter as shown in Figure 4-14. In this case the inverter's output voltage is given by:

$$\underline{v}_s(s) = \frac{\underline{i}_{ref}(s)}{\underline{y}_G(s)} \cdot \frac{1}{1+\underline{y}_{ref}(s)\left(\dfrac{1}{\underline{y}_G(s)}+\dfrac{1}{\underline{y}_s(s)}\right)} \tag{4.11}$$

Consequently, the inverter's output voltage is stable if and only if the open-loop transfer function $h_{\mathrm{V}}(s) = \underline{y}_{\mathrm{ref}}(s)\left(1/\underline{y}_{\mathrm{G}}(s) + 1/\underline{y}_{\mathrm{s}}(s)\right)$ is stable.

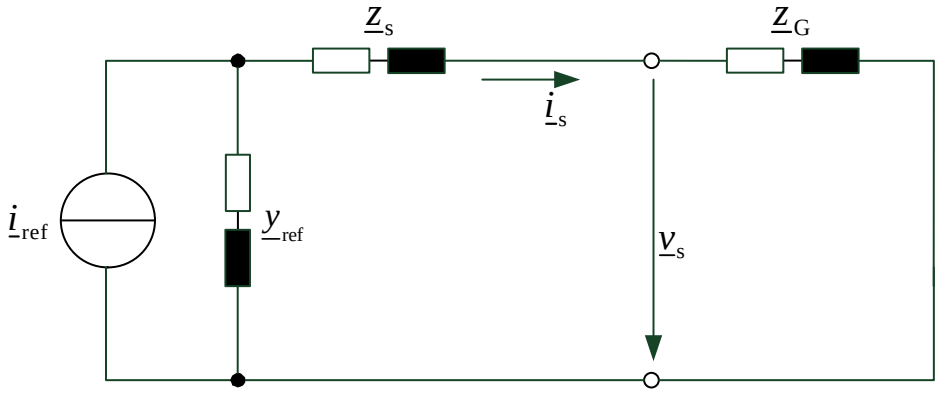

Figure 4-14 Equivalent circuit for inverter output current stability investigation

4.2.3 Line-Side Converter Control

The main objective of the LSC is to maintain the DC voltage and provide reactive power support during different grid operating conditions. Recalling the LSC circuit diagram from the last chapter, the LSC voltage can be rewritten in grid positive voltage coordinates as follows:

$$\underline{v}_{\mathrm{LSC}}^{\angle v_{\mathrm{G1}}} = \underline{v}_{\mathrm{G}}^{\angle v_{\mathrm{G1}}} + (r_{\mathrm{LSC}} + (s + \mathrm{j}\omega_0) l_{\mathrm{LSC}}) \cdot \underline{i}_{\mathrm{LSC}}^{\angle v_{\mathrm{G1}}} \tag{4.12}$$

The inner current control loop of the LSC is derived by setting eq. (4.12) in steady-state by replacing the Laplace operator with zero and considering a standard PI-controller to compensate for measurement uncertainties, which results in the following controller equation:

$$\underline{v}_{\mathrm{LSC,ref}}^{\angle v_{\mathrm{G1}}} = \underline{v}_{\mathrm{G}}^{\angle v_{\mathrm{G1}}} + (r_{\mathrm{LSC}} + \mathrm{j}\omega_0 l_{\mathrm{LSC}}) \cdot \underline{i}_{\mathrm{LSC}}^{\angle v_{\mathrm{G1}}} + \underline{v}_{\mathrm{LSC,C}}^{\angle v_{\mathrm{G1}}} \tag{4.13}$$

where $\underline{v}_{\mathrm{LSC,C}}^{\angle v_{\mathrm{G1}}}$ is the PI-controller's output and is given by:

$$\underline{v}_{\mathrm{LSC,C}}^{\angle v_{\mathrm{G1}}} = \left(k_{\mathrm{P,i}} + \frac{k_{\mathrm{I,i}}}{s}\right) \cdot \left(\underline{i}_{\mathrm{LSC,ref}}^{\angle v_{\mathrm{G1}}} - \underline{i}_{\mathrm{LSC}}^{\angle v_{\mathrm{G1}}}\right) \tag{4.14}$$

The feed-forward terms of the voltage and current allow for a fast response of the converter, for the PI-controller to only compensate for errors in the system's parameters and to provide a fast transition of the current to the perspective new set point values.

In the outer control loop the reference currents are based on the state of the DC and Grid voltages. Recalling the differential equation describing the DC voltage from the last chapter and replacing the Laplace operator(variable) by zero yields:

$$-p_{\mathrm{LSC}} = v_{\mathrm{DC}} \cdot i_{\mathrm{DC}} + p_{\mathrm{MSC}} \tag{4.15}$$

With the power input of the LSC in a gird voltage oriented reference frame ($v_{\mathrm{G1d}}^{\angle v_{\mathrm{G1}}} = |\underline{v}_{\mathrm{G1}}|, v_{\mathrm{G1q}}^{\angle v_{\mathrm{G1}}} = 0$) ignoring the choke resistance:

$$p_{\mathrm{LSC}} = \Re\{\underline{v}_{\mathrm{G1}} \cdot \underline{i}_{\mathrm{LSC1}}\} = |\underline{v}_{\mathrm{G1}}| \cdot i_{\mathrm{LSCd}}^{\angle v_{\mathrm{G1}}} \tag{4.16}$$

$$q_{\mathrm{LSC}} = \Im\{\underline{v}_{\mathrm{G1}} \cdot \underline{i}_{\mathrm{LSC1}}\} = -|\underline{v}_{\mathrm{G1}}| \cdot i_{\mathrm{LSCq}}^{\angle v_{\mathrm{G1}}} \tag{4.17}$$

By equating eq. (4.15) with (4.16) the DC voltage can be controlled by adjusting the d-axis current. As a result, the corresponding set-point for the d-axis current is given as follows:

$$\underline{i}_{\mathrm{LSCd,ref}}^{\angle v_{\mathrm{G1}}} = -\frac{v_{\mathrm{DC}} \cdot i_{\mathrm{DC}} + p_{\mathrm{MSC}}}{|\underline{v}_{\mathrm{G}}|} \tag{4.18}$$

On the other hand, the q-axis current can be used for reactive power provision with its set-point given by:

$$\underline{i}_{\mathrm{LSCq,ref}}^{\angle v_{\mathrm{G1}}} = -\frac{q_{\mathrm{LSC}}}{|\underline{v}_{\mathrm{G1}}|} \tag{4.19}$$

Instead of directly measuring the DC charging current a PI-controller can be used to estimate the DC circuit power and to compensate for measurement uncertainties as well as to ensure accurate control, while the q-axis current can be directly estimated from eq. (4.19). Accordingly, the LSC reference currents are calculated as:

$$\underline{i}_{\mathrm{LSCd,ref}}^{\angle v_{\mathrm{G1}}} + \mathrm{j}\underline{i}_{\mathrm{LSCq,ref}}^{\angle v_{\mathrm{G1}}} = -\left(k_{\mathrm{P,v}} + \frac{k_{\mathrm{I,v}}}{s}\right) \cdot \left(v_{\mathrm{DC,ref}} - v_{\mathrm{DC}}\right) - \frac{p_{\mathrm{MSC}} + \mathrm{j}q_{\mathrm{LSC}}}{|\underline{v}_{\mathrm{G}}|} \tag{4.20}$$

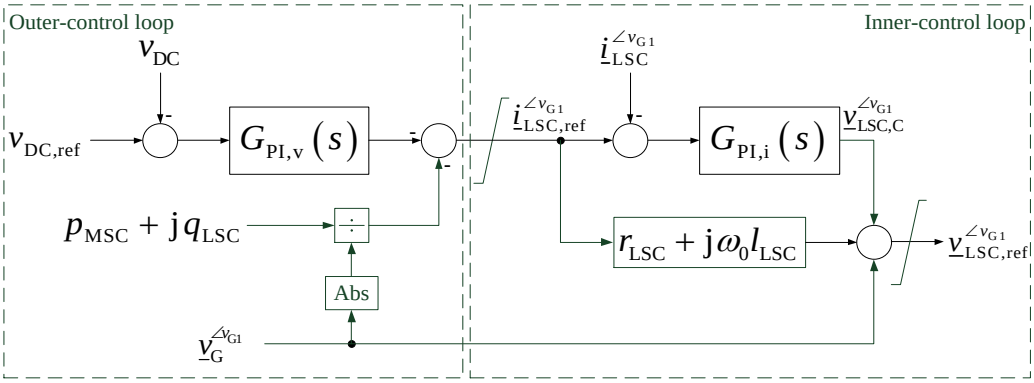

Figure 4-15 LSC overall control loops

The full LSC control loop is shown in Figure 4-15. It should be noted that the feed-forward term of the MSC power enhances the dynamic response of the DC voltage controller, although it could be omitted and the error will be the compensated by the PI-controller.

4.2.3.1 LSC Harmonic Currents Control

As already mentioned in the previous chapter the inverter output filters are used to filter out high current harmonics that reside at the side bands of the switching frequency and its multiples. The output filters should have resonance frequencies lower than the switching frequency of the inverter; otherwise the filter effectiveness will be reduced. However, the resonance frequencies should also be high enough to limit harmonic propagation and to avoid inductance saturation [86].

The output filter has a limited damping ratio in the frequency range below 750 Hz, therefore active damping is required to enhance the power quality. The important harmonics to be damped are the 5th, 7th, 11th and 13th. The targeted harmonics can be decoupled from the measured signal using a multi-frequency decomposition filter (MFDF) [88].

The MFDF is a fast multi band-pass filter that is developed from the idea of the Lê filter. It is assumed that the measured signal contains the aforementioned harmonic orders in addition to the negative sequence component and DC component, which can be expressed as:

$$\underline{y}^{\angle 0} = \underline{y}_{\mathrm{DC}} + \underline{y}_1 e^{\mathrm{j}\omega_0 t} + \underline{y}_2^{*} e^{-\mathrm{j}\omega_0 t} + \sum_{n=5}^{n=13} \underline{y}_n e^{\mathrm{j}n\omega_0 t} \tag{4.21}$$

If the measured signal is passed through *m*-1 PT1 elements, with *m* the number of the required harmonics for extraction, the output of each PT1 element can then be given by:

$$\begin{bmatrix} \underline{y}^{\angle 0} \\ \underline{y}_{\mathrm{PT1},1}^{\angle 0} \\ \vdots \\ \underline{y}_{\mathrm{PT1},m\text{-}1}^{\angle 0} \end{bmatrix} = \begin{bmatrix} 1 & \cdots & \cdots & 1 \\ \vdots & \dfrac{1}{1+\mathrm{j}\omega_0\tau_1} & \cdots & \vdots \\ \vdots & \vdots & \ddots & \vdots \\ 1 & \cdots & \cdots & \dfrac{1}{1+\mathrm{j}n_{13}\omega_0\tau_{m-1}} \end{bmatrix} \begin{bmatrix} \underline{y}_{\mathrm{DC}} \\ \underline{y}_1 e^{\mathrm{j}\omega_0 t} \\ \vdots \\ \underline{y}_{n_{13}} e^{\mathrm{j}n_{13}\omega_0 t} \end{bmatrix} = \mathbf{M}_{\mathrm{MFDF}} \begin{bmatrix} \underline{y}_{\mathrm{DC}} \\ \underline{y}_1 e^{\mathrm{j}\omega_0 t} \\ \vdots \\ \underline{y}_{n_{13}} e^{\mathrm{j}n_{13}\omega_0 t} \end{bmatrix} \tag{4.22}$$

with

$$\tau_{1\to m-1} = \frac{1}{\omega_0 k_{1\to m-1}} \tag{4.23}$$

where $k_{1\to m-1} = 1, 2, \ldots$ is the filter gain factor.

From eq. (4.21) the harmonic components can be extracted by multiplying the inverse of the gain matrix $\mathbf{M}_{\mathrm{MFDF}}$ with the measured signal and the output of the PT1 elements.

Each individual harmonic current can be transformed into its rotating reference frame using the positive sequence voltage angle multiplied by the respective harmonic order. A PI-controller

can be later applied with a reference current value set to zero for each individual harmonic current component as shown in Figure 4-16.

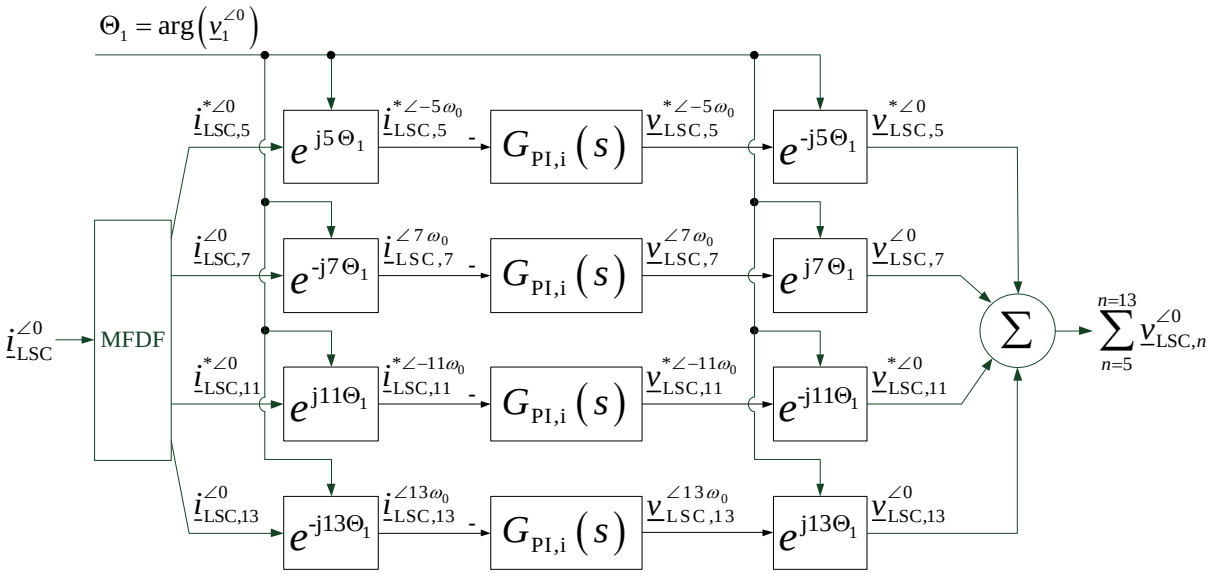

Figure 4-16 LSC harmonic currents control loop

4.2.3.2 LSC Current Limitation

The magnitude of the current flowing through the IGBT should be such that the IGBT's junction temperature does not exceed the maximum junction temperature. The junction temperature is dependent on the conduction and switching losses, thermal resistance, heat sink, cooling process and ambient temperature [52]. The maximum current allowed is later calculated based on the power loss curves supplied by the semiconductor manufacturer and interpreted by the polynomial equation in the controller [48].

During wind gusts or grid faults the LSC currents may exceed the maximum value and they must be limited to avoid any damage or derating of the semiconductor devices that may lead to violation of the grid code requirements. In order to perform an adequate current limitation a prioritization of the different current components should be defined. For LSC the current limitation is performed according to the following hierarchal priorities:

1. LSC positive sequence active current
2. LSC positive sequence reactive current
3. LSC negative sequence currents
4. LSC harmonic currents

The highest priority is usually set to the positive sequence active current to avoid high voltages in the DC circuit. Consequently, the maximum current of the positive sequence reactive current is:

$$i_{\max,q} = \sqrt{i_{\max}^2 - i_{LSC,d}^2} \qquad (4.24)$$

A straight forward limitation of the negative sequence currents that is used is:

$$i_{\max,2} = i_{\max} - \left|\underline{i}_{\mathrm{LSC},1}\right| \tag{4.25}$$

However, an advanced limitation that would result in 15.4% higher current limitation is adapted. This limitation is based on [89], where the maximum phase currents are:

$$\begin{aligned} i_{a,\max} &= \sqrt{i_1^2 + i_2^2 + 2i_1 i_2 \cos(\alpha)} \\ i_{b,\max} &= \sqrt{i_1^2 + i_2^2 + 2i_1 i_2 \cos\left(\alpha - \frac{2\pi}{3}\right)} \\ i_{c,\max} &= \sqrt{i_1^2 + i_2^2 + 2i_1 i_2 \cos\left(\alpha + \frac{2\pi}{3}\right)} \end{aligned} \tag{4.26}$$

where $\alpha = \arg\left(\underline{i}_{\mathrm{LSC},1}\right) + \arg\left(\underline{v}_{\mathrm{G},1}\right) - \arg\left(\underline{i}_{\mathrm{LSC},2}\right) + \arg\left(\underline{v}_{\mathrm{G},2}\right)$.

Based on eq. (4.26) the current limitation for the negative sequence current is [88]:

$$\begin{aligned} i_{2,\max} = \sqrt{i_1^2 \left[\max\left\{ \left(\cos(\alpha), \cos\left(\alpha + \frac{2\pi}{3}\right), \cos\left(\alpha - \frac{2\pi}{3}\right) \right)^2 \right\} - 1 \right] + i_{\max}^2} \\ - \left|\underline{i}_1\right| \cdot \max\left\{ \cos(\alpha), \cos\left(\alpha + \frac{2\pi}{3}\right), \cos\left(\alpha - \frac{2\pi}{3}\right) \right\} \end{aligned} \tag{4.27}$$

Figure 4-17 shows that the current limitation for the negative sequence current for different values of α. It is obvious that the maximum current limitation is achieved for $\alpha = \pi/3, \pi, 5\pi/3$ and that the advanced current limitation method allows for an increase in current limitation.

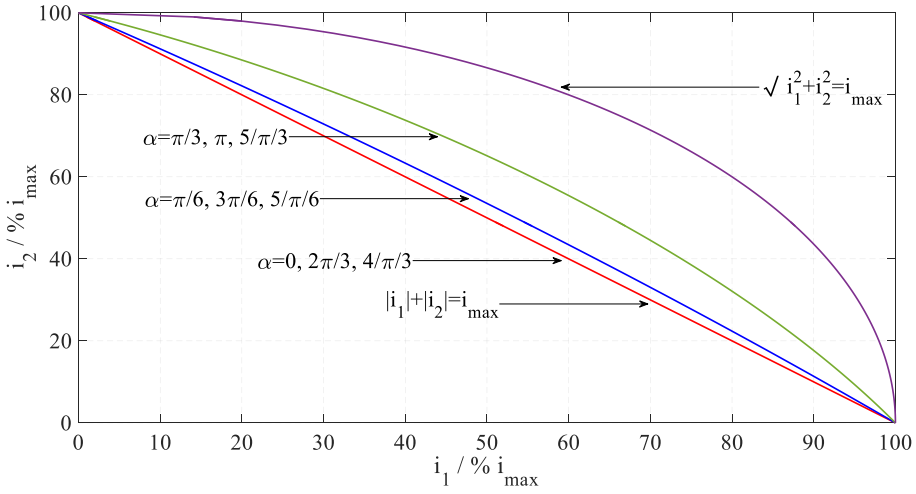

Figure 4-17 Current limitation for the negative sequence current

4.2.3.3 LSC Voltage Limitation

As already discussed earlier the maximum modulation index achieved with CPWM or DPWM is $2/\sqrt{3}$. Consequently, the maximum LSC output voltage magnitude is:

$$\hat{V}_{\mathrm{LSC,max}} = \frac{V_{\mathrm{DC}}}{\sqrt{3}} \tag{4.28}$$

The required LSC voltage may exceed the maximum value during over-voltage grid operation. Therefore, an adequate voltage limitation strategy should be applied in order to prevent the converter running into over-modulation, which leads to increased harmonic generation and an overloading of the filter circuit.

The voltage limitation should be performed in accordance with the current prioritization explained above. Figure 4-18 shows an example of voltage limitation through the provision of an under excited reactive current, where the d component of the LSC voltage was reduced to limit the magnitude of the LSC voltage. From this it follows that the highest voltage priority is set to the q component of the voltage in contrast to the current in order to guarantee a full control effort of the DC link voltage. The voltage limitation of the LSC voltage then becomes:

$$\begin{aligned} v_{\mathrm{LSCq}} &= v_{\mathrm{LSC,max}} \\ v_{\mathrm{LSCd}} &= \sqrt{v_{\mathrm{LSC,max}}^2 - v_{\mathrm{LSCq}}^2} \end{aligned} \tag{4.29}$$

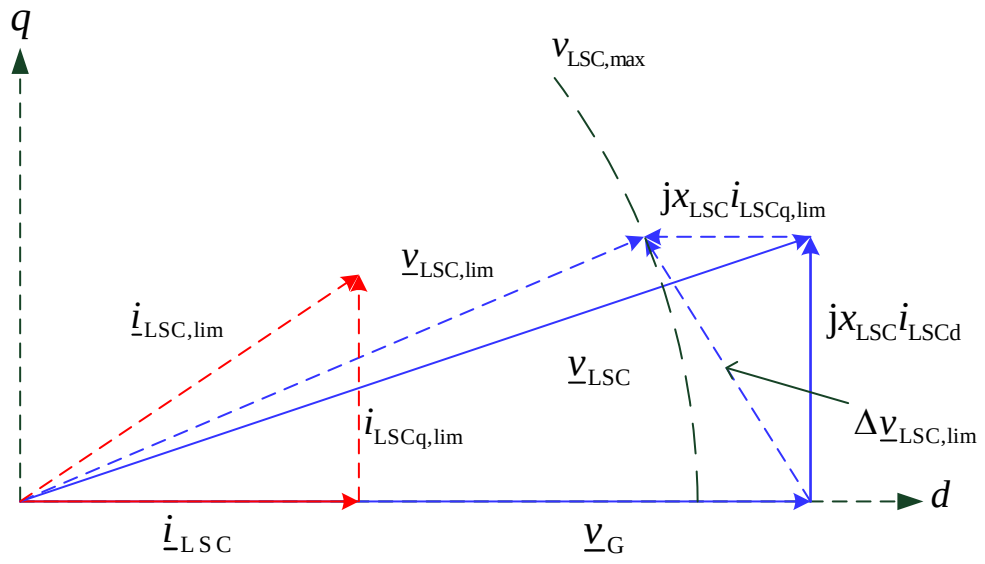

Figure 4-18 Vector diagram of the LSC with voltage limitation

The voltage limitation for the negative sequence voltage is performed in an opposite manner to the current, where the priority is set to the negative sequence voltage over the positive sequence voltage in order to mitigate the negative sequence currents to avoid any conflict with the current

priorities. Again, the priority is set to the q component of the negative sequence voltage in the same manner as for the positive sequence voltage. Accordingly, it follows:

$$v_{1,\max} = \sqrt{v_{G2}^2\left[\max\left\{\left(\cos(\alpha),\cos\left(\alpha+\frac{2\pi}{3}\right),\cos\left(\alpha-\frac{2\pi}{3}\right)\right)^2\right\}-1\right]+v_{\max}^2} \\ -|\underline{v}_{G2}|\cdot\max\left\{\cos(\alpha),\cos\left(\alpha+\frac{2\pi}{3}\right),\cos\left(\alpha-\frac{2\pi}{3}\right)\right\} \tag{4.30}$$

4.2.4 LSC Stability Analysis

The LSC control is based on the instantaneous values of voltages and currents. Therefore, the transfer function of the output currents should consider the gain and the phase errors introduced by the measuring filters and the converter sampling. The measuring filter implemented is a 2nd order Bessel filter with a transfer function given by:

$$G_{\text{meas}} = \frac{1}{1+\frac{1.3617}{\omega_c}s+\frac{0.618}{\omega_c^2}s^2} \tag{4.31}$$

where ω_c is the cut-off frequency.

The magnitude and phase errors of the measuring filter can be compensated for by the targeted frequency component for a fast and accurate control. Consequently, the transfer function of the measuring filter for the fundamental frequency is:

$$\underline{G}_{\text{meas}}^{*} = \frac{1\pm \mathrm{j}\frac{1.3617\omega_0}{\omega_c}-0.618\left(\frac{\omega_0}{\omega_c}\right)^2}{1+\frac{1.3617}{\omega_c}s+\frac{0.618}{\omega_c^2}s^2} \tag{4.32}$$

The converter's sampling is modeled by a transpose delay:

$$G_{\text{dt}} = e^{-s\tau_{\text{dt}}} \tag{4.33}$$

The transfer function of the converter's sampling for the fundamental frequency is:

$$\underline{G}_{\text{dt}}^{*} = e^{-(s-\mathrm{j}\omega_0)\tau_{\text{dt}}} \tag{4.34}$$

The complete block diagram of the LSC system is shown in Figure 4-19, from which the transfer function of the LSC output currents is derived:

$$\underline{i}_{\text{LSC}}^{\angle 0} = \frac{\underline{G}_{\text{dt}}^{*}(s)\cdot(\underline{G}_{\text{PI}}^{*}(s)+\underline{z}_{\text{LSC}})\ \underline{i}_{\text{LSC,ref}}^{\angle 0}+\left(\underline{G}_{\text{dt}}^{*}(s)\cdot\underline{G}_{\text{meas}}^{*}(s)-1\right)\underline{v}_{\text{G}}^{\angle 0}}{G_{\text{LSC}}^{-1}(s)+\underline{G}_{\text{dt}}^{*}(s)\cdot\underline{G}_{\text{meas}}^{*}(s)\cdot\underline{G}_{\text{PI}}^{*}(s)} \tag{4.35}$$

where $\underline{z}_{\mathrm{LSC}} = r_{\mathrm{LSC}} + \mathrm{j}\omega_0 l_{\mathrm{LSC}}$ and $\underline{G}^*_{\mathrm{PI}}(s) = G_{\mathrm{PI}}(s \mp \mathrm{j}\omega_0) = k_{\mathrm{P}} + k_{\mathrm{I}}/s \mp \mathrm{j}\omega_0$.

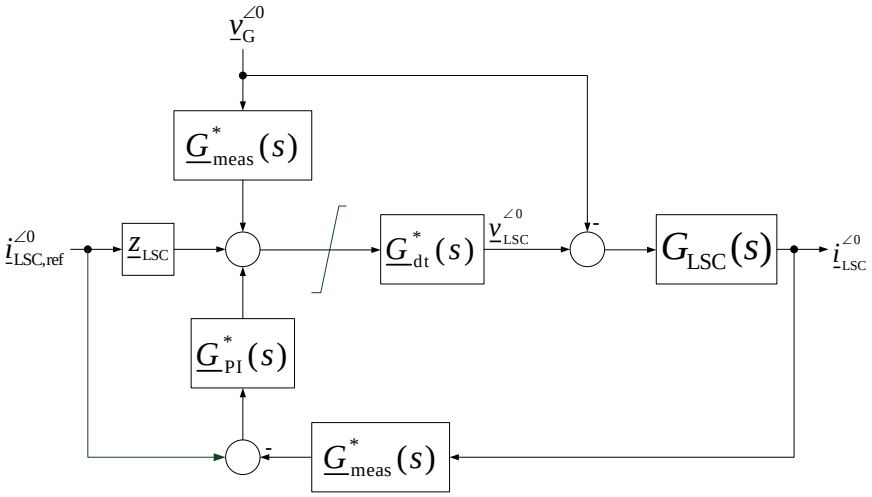

Figure 4-19 LSC closed-loop transfer function

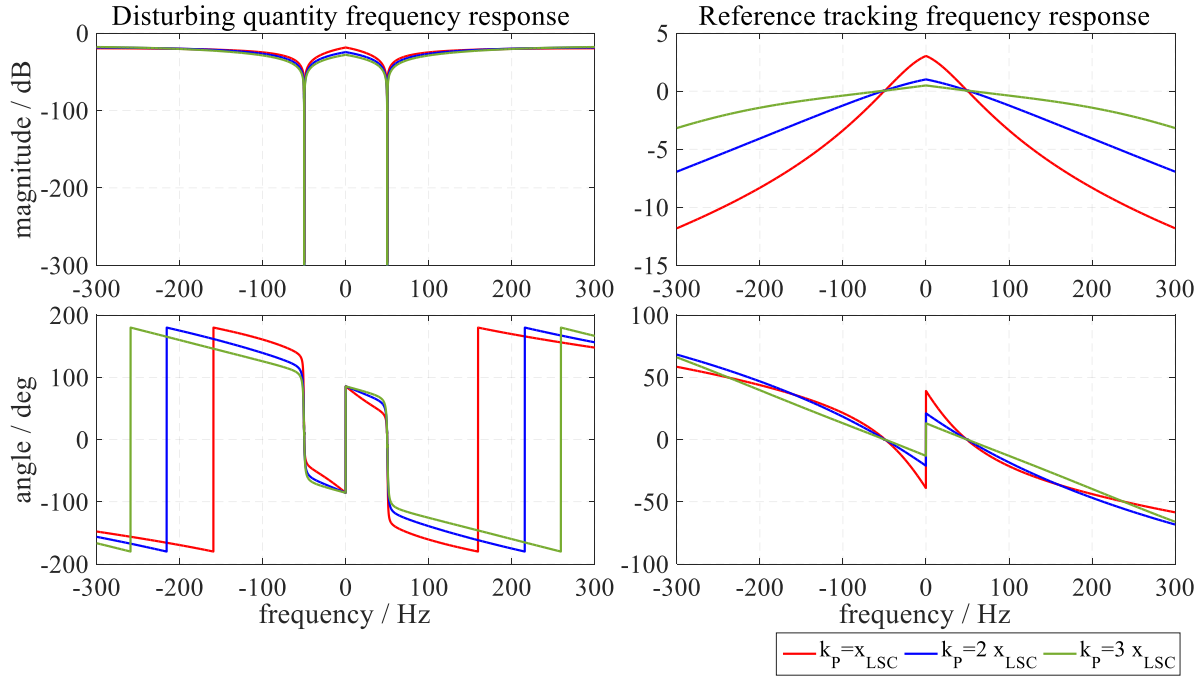

Figure 4-20 Frequency response of the LSC transfer function for different proportional gain values

The frequency response of the LSC transfer function for different values of PI-controller proportional gain is shown in Figure 4-20. From this it can be concluded that the feed-forward decoupled control offers a high rejection gain for the disturbing quantity, zero gain for the reference tracking quantity and zero phase shifts for both quantities at the fundamental frequency. This implies that the LSC features a current source with a very high input impedance ($|y_{\mathrm{ref}}| \ll$). Additionally, the proportional gain does not change the gains and the phase shifts at the fundamental frequency. However, it increases the bandwidth of the PI-controller, which in turns decreases the rejection gain in the frequency range beyond the fundamental frequency.

4.2.4.1 Influence of Grid Stiffness

In order to account for the influence of the grid stiffness on the LSC output current the transfer function should be extended by a term representing the grid impedance. The influence of the grid impedance on the LSC output current can be expressed by:

$$\underline{v}'^{\angle 0}_{\mathrm{G}} = \underline{v}^{\angle 0}_{\mathrm{G}} + G_{\mathrm{Grid}}(s) \cdot \underline{i}^{\angle 0}_{\mathrm{LSC}} \tag{4.36}$$

where $G_{\mathrm{Grid}} = r_{\mathrm{G}} + sl_{\mathrm{G}}$.

The block diagram of the LSC system would be modified as shown in Figure 4-21 and the resulting transfer function then is:

$$\underline{i}^{\angle 0}_{\mathrm{LSC}} = \frac{\underline{G}^{*}_{\mathrm{dt}}(s) \cdot (\underline{G}^{*}_{\mathrm{PI}}(s) + \underline{z}_{\mathrm{LSC}})\ \underline{i}^{\angle 0}_{\mathrm{LSC,ref}} + \left(\underline{G}^{*}_{\mathrm{dt}}(s) \cdot \underline{G}^{*}_{\mathrm{meas}}(s) - 1\right) \underline{v}^{\angle 0}_{\mathrm{G}}}{G^{-1}_{\mathrm{LSC}}(s) + \underline{G}^{*}_{\mathrm{dt}}(s) \cdot \underline{G}^{*}_{\mathrm{meas}}(s) \cdot \left(\underline{G}^{*}_{\mathrm{PI}}(s) - G_{\mathrm{Grid}}(s)\right) + G_{\mathrm{Grid}}(s)} \tag{4.37}$$

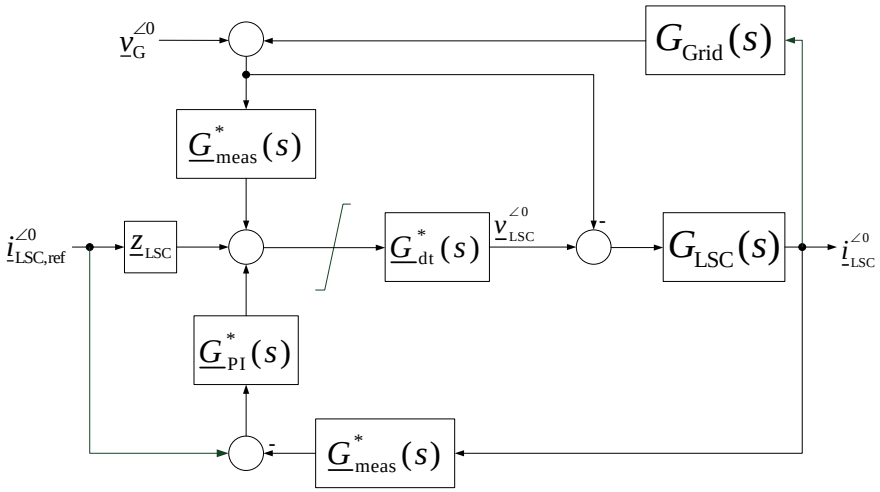

Figure 4-21 LSC closed-loop transfer function considering grid stiffness

The frequency response of the LSC transfer function given by eq. (4.33) for different short-circuit ratios (SCR) of the grid is shown in Figure 4-22. The frequency response shows that the grid impedance has no significant influence in the frequency range -100 to 100 Hz. Beyond this range the grid impedance has an opposite effect to that of the PI-controller, whereas the grid impedance increases the rejection gain increases. This is attributed to the fact that the grid reactance increases proportionally to the frequency and therefore its admittance decreases and tends to tighten the bandwidth of the LSC output current.

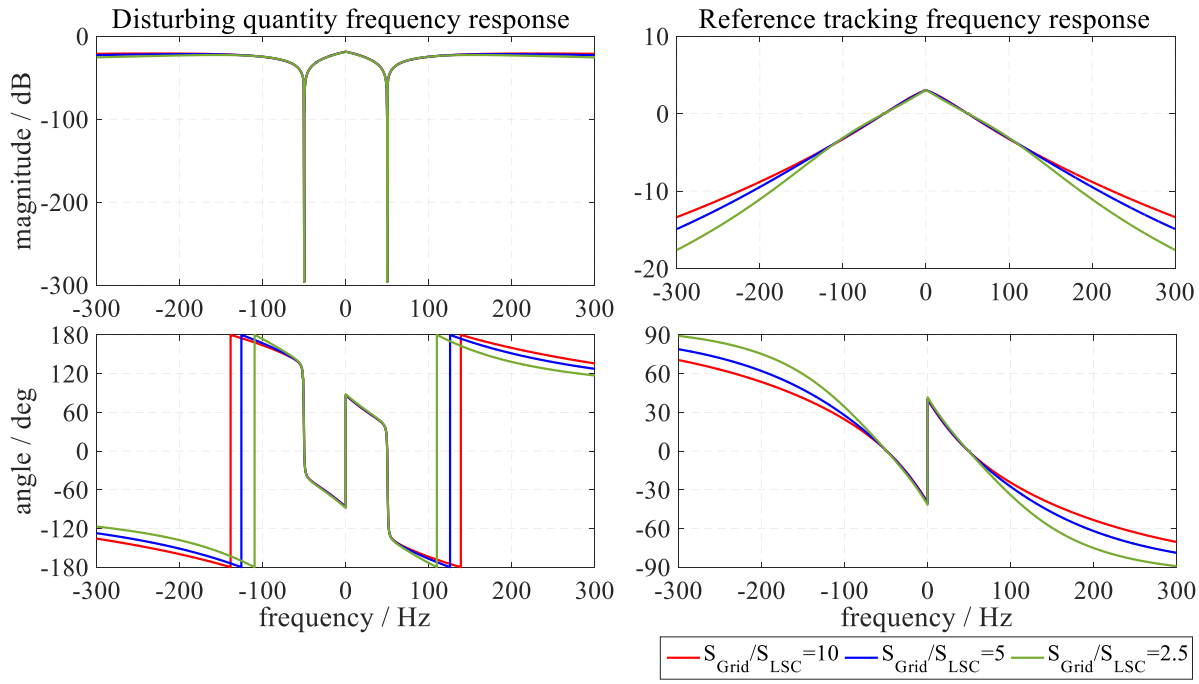

Figure 4-22 Frequency response of the LSC transfer function for different grid SCRs

Recalling the stability criterion for the inverter output currents and voltages, eq. (4.33) can be rearranged to obtain the open-loop transfer functions for floating and standalone modes respectively as:

$$h_{\mathrm{I}}(s) = -\frac{G_{\mathrm{LSC}}^{-1}(s) + \underline{G}_{\mathrm{dt}}^{*}(s)\cdot\underline{G}_{\mathrm{meas}}^{*}(s)\cdot\underline{G}_{\mathrm{PI}}^{*}(s)}{G_{\mathrm{grid}}(s)\left(\underline{G}_{\mathrm{dt}}^{*}(s)\cdot\underline{G}_{\mathrm{meas}}^{*}(s)-1\right)} \tag{4.38}$$

$$h_{\mathrm{V}}(s) = -1-\frac{G_{\mathrm{LSC}}^{-1}(s) + \underline{G}_{\mathrm{dt}}^{*}(s)\cdot\underline{G}_{\mathrm{meas}}^{*}(s)\cdot\left(\underline{G}_{\mathrm{PI}}^{*}(s)-G_{\mathrm{grid}}(s)\right)+G_{\mathrm{grid}}(s)}{\underline{G}_{\mathrm{dt}}^{*}(s)\cdot(\underline{G}_{\mathrm{PI}}^{*}(s)+\underline{z}_{\mathrm{LSC}})} \tag{4.39}$$

The frequency response for $h_{\mathrm{I}}(s)$ and $h_{\mathrm{V}}(s)$ is shown in Figure 4-23 for different SCRs of the grid, where the circles shown indicate the cross-over frequencies and the boxes indicate the phase margins.

In the floating mode as the grid SCR increases the cross over frequency and the phase margin as well as the magnitude increase. This yields that as the grid SCR increases the LSC output current tends to be more stable and its magnitude increases as well. The opposite happens when the grid SCR decreases. Still, the grid SCR does not has a significant influence on the cross over frequency of the LSC output voltage in the standalone mode. However, the phase margin increases with the decrease of the grid SCR and the magnitude. The opposite happens when the grid SCR increases.

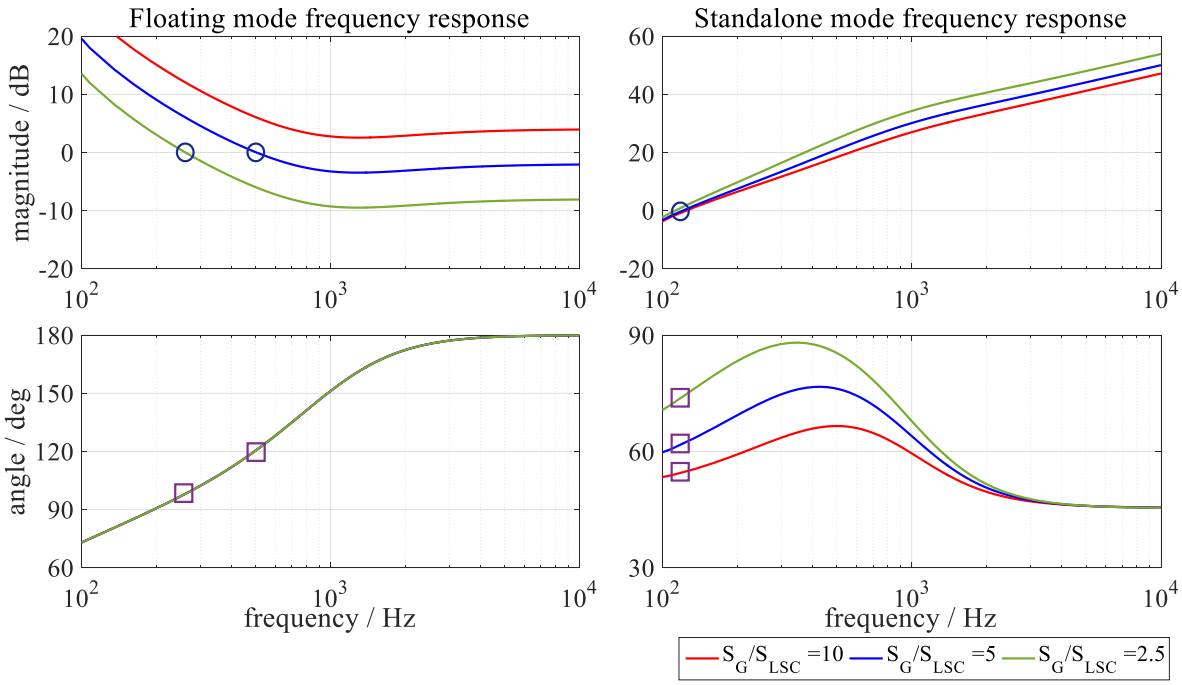

Figure 4-23 Frequency response of LSC open-loop transfer functions

4.2.4.2 Influence of LSC Filter

The LSC is equipped with a two notch filter tuned at the carrier frequency and its double and a high pass filter to filter out all higher harmonics beyond the notch filter. The filters will add more zeros and poles to the system and consequently will modify the resonance frequencies. Figure 4-24 shows the closed-loop transfer function including the LSC filters.

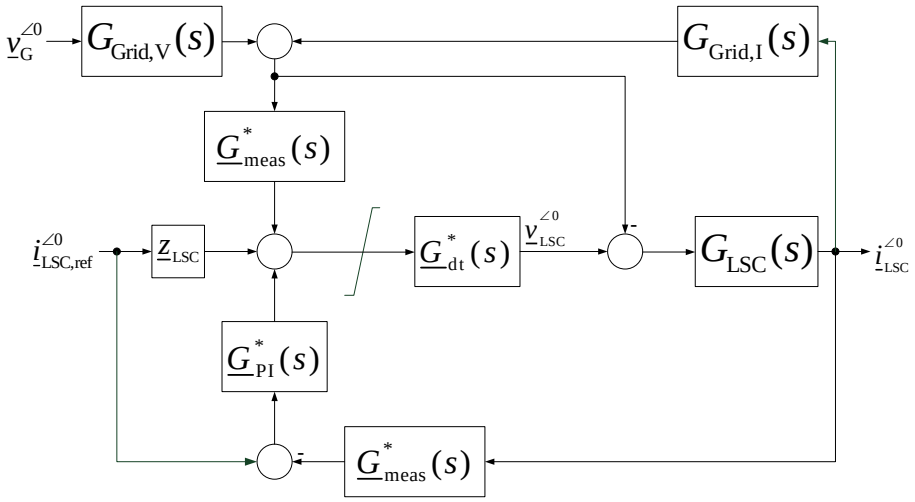

Figure 4-24 LSC closed-loop transfer function considering LSC filters

The transfer-function of the LSC current is accordingly:

$$\underline{i}^{\angle 0}_{\mathrm{LSC}} = \frac{\underline{G}^*_{\mathrm{dt}}(s)\cdot(\underline{G}^*_{\mathrm{PI}}(s)+\underline{z}_{\mathrm{LSC}})\ \underline{i}^{\angle 0}_{\mathrm{LSC,ref}} + G_{\mathrm{Grid,V}}(s)\cdot\left(\underline{G}^*_{\mathrm{dt}}(s)\cdot\underline{G}^*_{\mathrm{meas}}(s)-1\right)\underline{v}^{\angle 0}_{\mathrm{G}}}{G^{-1}_{\mathrm{LSC}}(s)+\underline{G}^*_{\mathrm{dt}}(s)\cdot\underline{G}^*_{\mathrm{meas}}(s)\cdot\left(\underline{G}^*_{\mathrm{PI}}(s)-G_{\mathrm{Grid,I}}(s)\right)+G_{\mathrm{Grid,I}}(s)} \tag{4.40}$$

where,

$$G_{\mathrm{Grid,V}}(s)=\frac{G_{\mathrm{Filter}}(s)}{G_{\mathrm{Filter}}(s)+G_{\mathrm{Grid}}(s)} \tag{4.41}$$

$$G_{\mathrm{Grid,I}}(s)=G_{\mathrm{Grid}}(s)\cdot G_{\mathrm{Grid,V}}(s) \tag{4.42}$$

The frequency response of the LSC current is shown in Figure 4-25 for different grid SCRs. Again, the filters do not have a remarkable influence in the frequency range between -100 Hz to 100 Hz. Beyond this range a notch frequency dependent on the grid impedance is found. This notch represents the highest gain in the response of the disturbing quantity, which shows that such a resonance is triggered by the grid voltage. Although the gains at the notch frequency are still low, the resultant current cannot be controlled by the LSC because a high rejection gain in the reference tracking quantity at the resonance frequencies is found. This fact necessitates the need of active damping to mitigate any sustained oscillation that may occur in the system in the frequency range between the 5$^{\mathrm{th}}$ and the 13$^{\mathrm{th}}$ order.

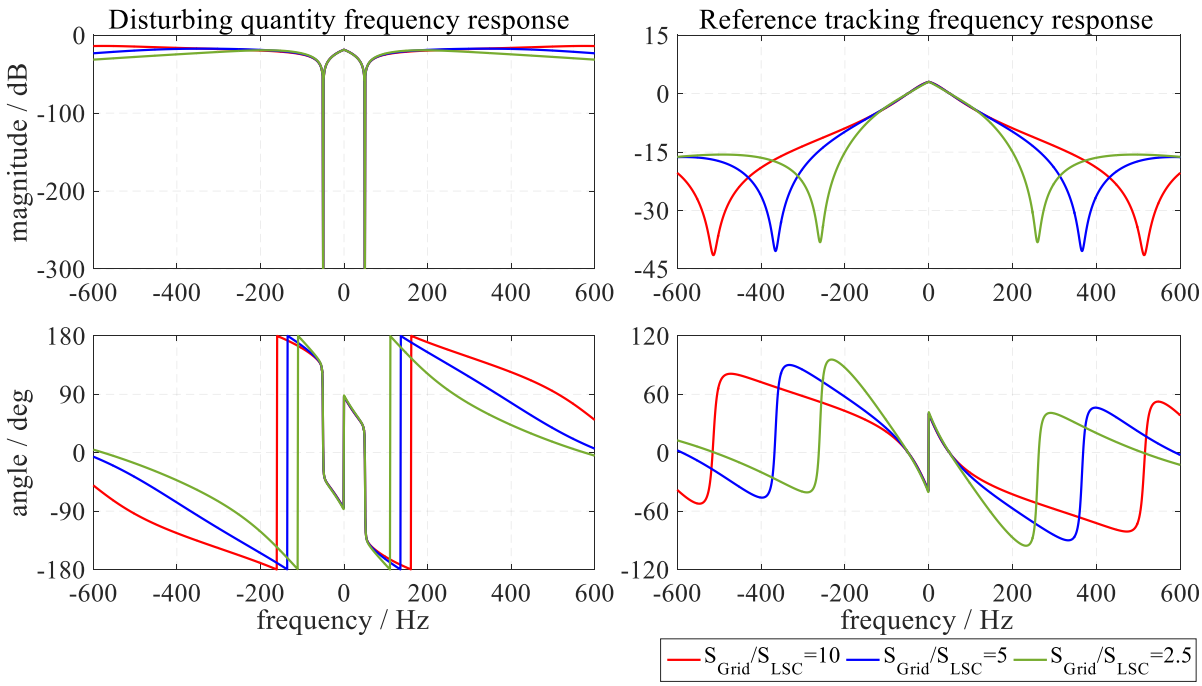

Figure 4-25 Frequency response of the LSC transfer function including output filters

The open-loop transfer functions are given by:

$$h_{\mathrm{I}}(s)=\frac{G_{\mathrm{Filter}}(s)}{G_{\mathrm{Grid}}(s)}\left(1-\frac{G_{\mathrm{LSC}}^{-1}(s)+\underline{G}_{\mathrm{dt}}^{*}(s)\cdot\underline{G}_{\mathrm{meas}}^{*}(s)\cdot\underline{G}_{\mathrm{PI}}^{*}(s)}{G_{\mathrm{Filter}}(s)\left(\underline{G}_{\mathrm{dt}}^{*}(s)\cdot\underline{G}_{\mathrm{meas}}^{*}(s)-1\right)}\right) \tag{4.43}$$

$$h_{\mathrm{V}}(s)=-1-\frac{G_{\mathrm{LSC}}^{-1}(s)+\underline{G}_{\mathrm{dt}}^{*}(s)\cdot\underline{G}_{\mathrm{meas}}^{*}(s)\cdot\left(\underline{G}_{\mathrm{PI}}^{*}(s)-G_{\mathrm{Grid,I}}(s)\right)+G_{\mathrm{Grid,I}}(s)}{\underline{G}_{\mathrm{dt}}^{*}(s)\cdot(\underline{G}_{\mathrm{PI}}^{*}(s)+\underline{z}_{\mathrm{LSC}})} \tag{4.44}$$

The frequency response of the open-loop transfer functions is shown in Figure 4-26. As illustrated in the floating mode the cross-over frequency increases with the grid SCR, while the

phase margin decreases. This is related to the fact that the current magnitude increases as the grid impedance decreases. At the cross over frequency the grid experiences its lowest impedance. However, the values of the cross over frequencies for the standalone mode remain almost the same as before, which leads to the conclusion that the current control loop always remains stable.

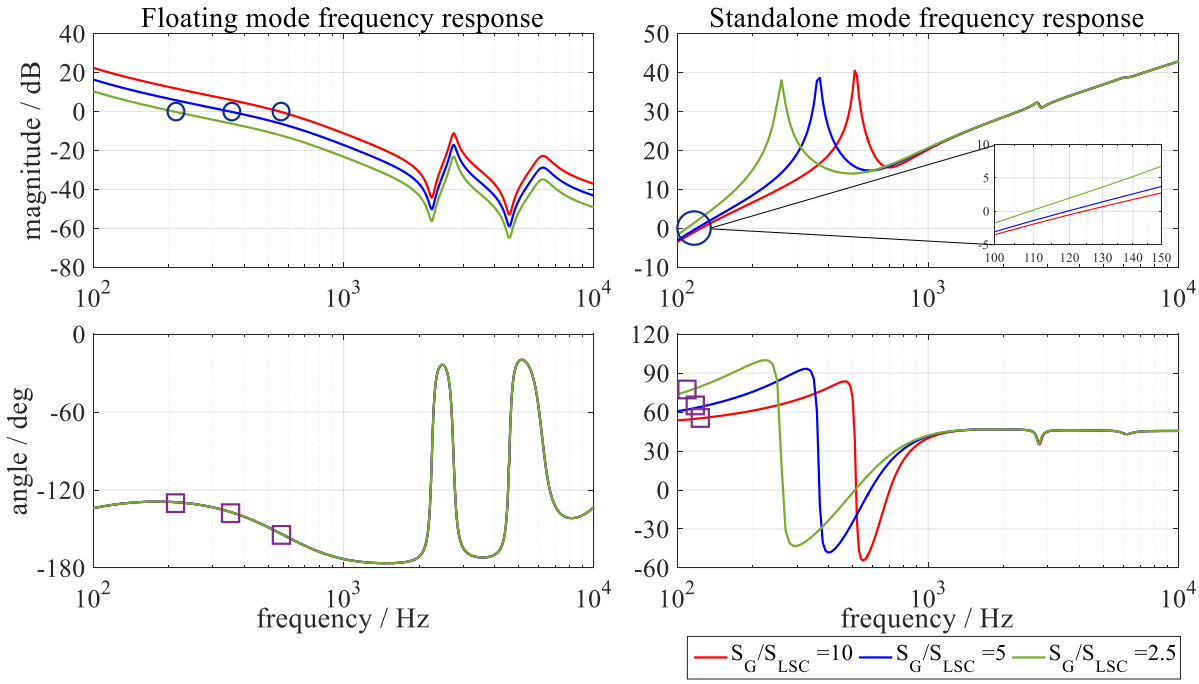

Figure 4-26 Frequency response of LSC open-loop transfer functions including output filters

4.2.4.3 Influence of Active Damping

The influence of active damping is considered by incorporating the harmonic currents' control-loop shown in Figure 4-16 in the transfer function. Therefore, the phase and gain errors introduced by the measurement and converter should be compensated for each desired frequency to achieve fast and accurate control. Accordingly, the transfer functions given by eq. (4.28) and (4.30) are rewritten as:

$$\underline{\boldsymbol{G}}^{*}_{\text{meas}} = \begin{bmatrix} G^{-1}_{\text{meas}}\big|_{s\to \text{j}\omega_0} & \cdots & 0 \\ \vdots & \ddots & \vdots \\ 0 & \cdots & G^{-1}_{\text{meas}}\big|_{s\to \text{j}13\omega_0} \end{bmatrix} \cdot G_{\text{meas}} \tag{4.45}$$

$$\underline{\boldsymbol{G}}^{*}_{\text{dt}} = \begin{bmatrix} G^{-1}_{\text{dt}}\big|_{s\to \text{j}\omega_0} & \cdots & 0 \\ \vdots & \ddots & \vdots \\ 0 & \cdots & G^{-1}_{\text{dt}}\big|_{s\to \text{j}13\omega_0} \end{bmatrix} \cdot G_{\text{dt}} \tag{4.46}$$

The transfer function of the PI-controller is also modified to include the PI-controller of each frequency component controller as follows:

$$\underline{\boldsymbol{G}}_{\mathrm{PI}}^{*}(s)=k_{\mathrm{P}}\cdot\begin{bmatrix}1\\ \vdots\\ 1\end{bmatrix}+k_{\mathrm{I}}\cdot\begin{bmatrix}\dfrac{1}{s-\mathrm{j}\omega_0}\\ \vdots\\ \dfrac{1}{s-\mathrm{j}13\omega_0}\end{bmatrix} \tag{4.47}$$

The closed-loop transfer function and the transfer function of the LSC current as well as the open-loop transfer functions remain the same as before but with the modified transfer functions in eq. (4.45) to (4.47).

The frequency response of the LSC current transfer function is shown in Figure 4-27. It is clear that there is a very high rejection gain at the targeted harmonic components in both responses and unity gain and zero phase shift at the fundamental frequency to the reference tracking quantity. This points to the fact that the harmonic current components are fully mitigated and the output current will track perfectly the values of the reference current.

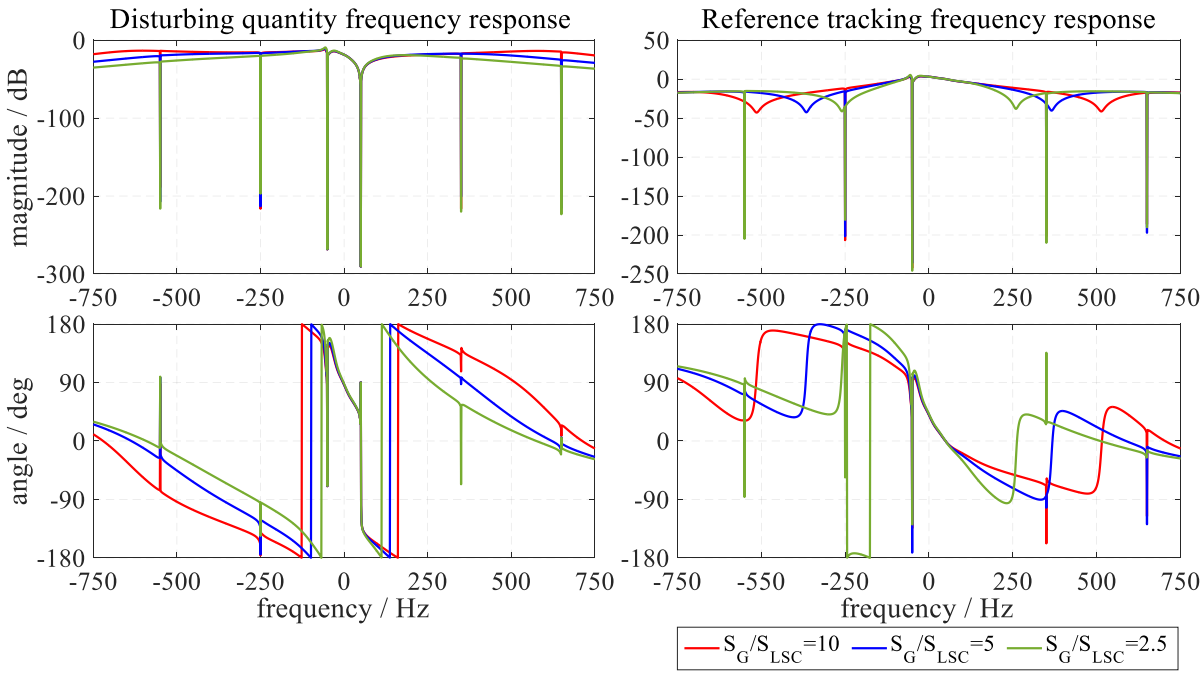

Figure 4-27 Frequency response of the LSC transfer function including active damping

Figure 4-28 shows the corresponding frequency response of the open-loop transfer functions. As shown the cross over-frequencies and phase margin are still the same for both responses. However, in the floating mode the 7th order harmonic coincides with the cross-over frequency when $S_{\mathrm{G}}/S_{\mathrm{LSC}}=5$ adding a positive phase margin to the response, which means that the harmonic controller increases the stability margin of the LSC at this frequency. From this fact

it can be concluded that the harmonic current controller should be tuned based on the cross-over frequency in order to increase the stability margin. Yet, the cross-over frequency itself is dependent on the grid impedance, which demonstrates a non-linear behavior requiring an adaptive type of harmonic controller.

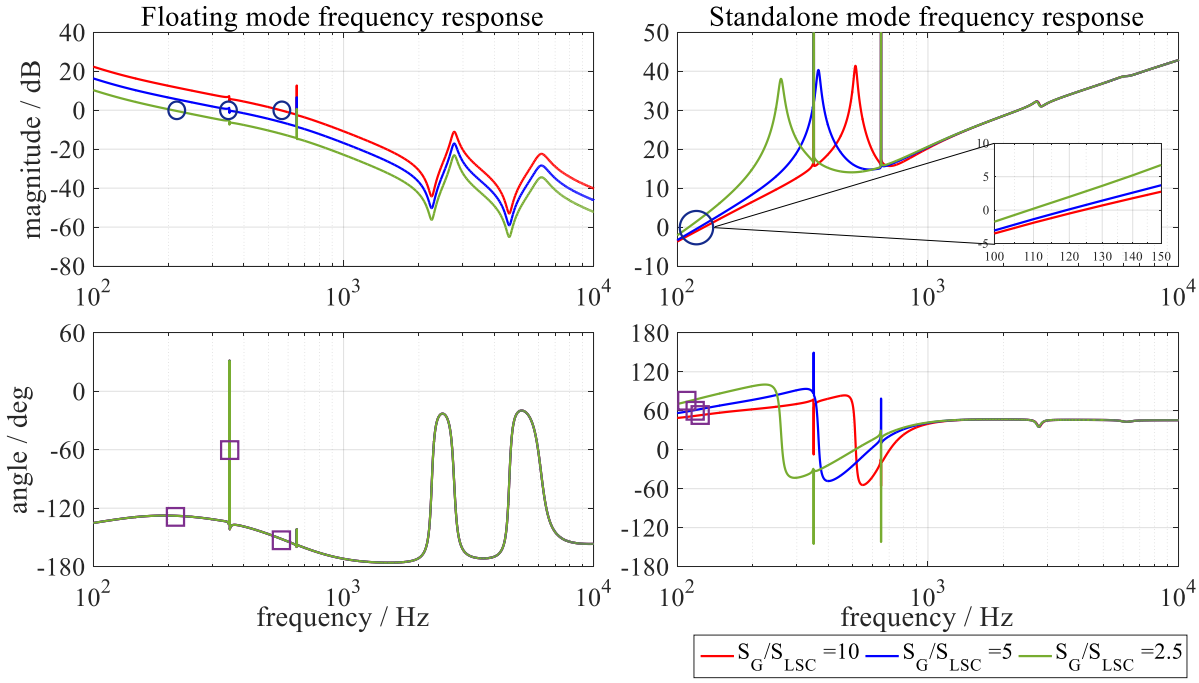

Figure 4-28 Frequency response of LSC open-loop transfer functions including active damping

4.2.4.4 Influence of LSC Voltage Limitation

In all the previous analyses it was assumed that the converter produces the required corresponding voltage. However, in a real environment the controller will limit the produced voltage within the converter voltage limits. Consequently, the dynamic state of the LSC will change and the response LSC output current will also change accordingly. In order to establish the response of the LSC under voltage limitation a trust-region method is used to minimize the non-linear equation described by [90]:

$$\min_x \begin{pmatrix} f_1\left(\dfrac{\underline{i}_{\mathrm{LSC}}^{\angle 0}}{\underline{v}_{\mathrm{G}}^{\angle 0}}\right)^2 \\ f_2\left(\dfrac{\underline{v}_{\mathrm{LSC}}^{\angle 0}}{\underline{v}_{\mathrm{G}}^{\angle 0}}\right)^2 \end{pmatrix} \& \min_x \begin{pmatrix} f_1\left(\dfrac{\underline{i}_{\mathrm{LSC}}^{\angle 0}}{\underline{i}_{\mathrm{LSC,ref}}^{\angle 0}}\right)^2 \\ f_2\left(\dfrac{\underline{v}_{\mathrm{LSC}}^{\angle 0}}{\underline{i}_{\mathrm{LSC,ref}}^{\angle 0}}\right)^2 \end{pmatrix} \tag{4.48}$$

and subjected to

$$\left|\underline{v}_{\mathrm{LSC}}^{\angle 0}\right| \le \frac{2}{\sqrt{3}} \tag{4.49}$$

Figure 4-29 and 4-30 show the frequency response of the LSC output voltage and the corresponding frequency response of the LSC current respectively for a grid SCR equal to 10. In the case of a high grid SCR the LSC voltage tracks the corresponding set-point in response to the disturbing quantity in the low frequency band between -55 and 150 Hz. This is related to the low voltage drop across the grid impedance that results in a high voltage at the LSC terminals. This will either lead to lower rejection gain or to different phase shifts in the response of the LSC current, which can be observed especially at the resonance frequencies. Still, in the response to the reference quantity the magnitude difference is low and the LSC voltage tracks the set-point with a slight magnitude error. This is related to the fact that the PI-controller only compensates for small errors, which will be reflected as small magnitude or phase differences in the response of the LSC current.

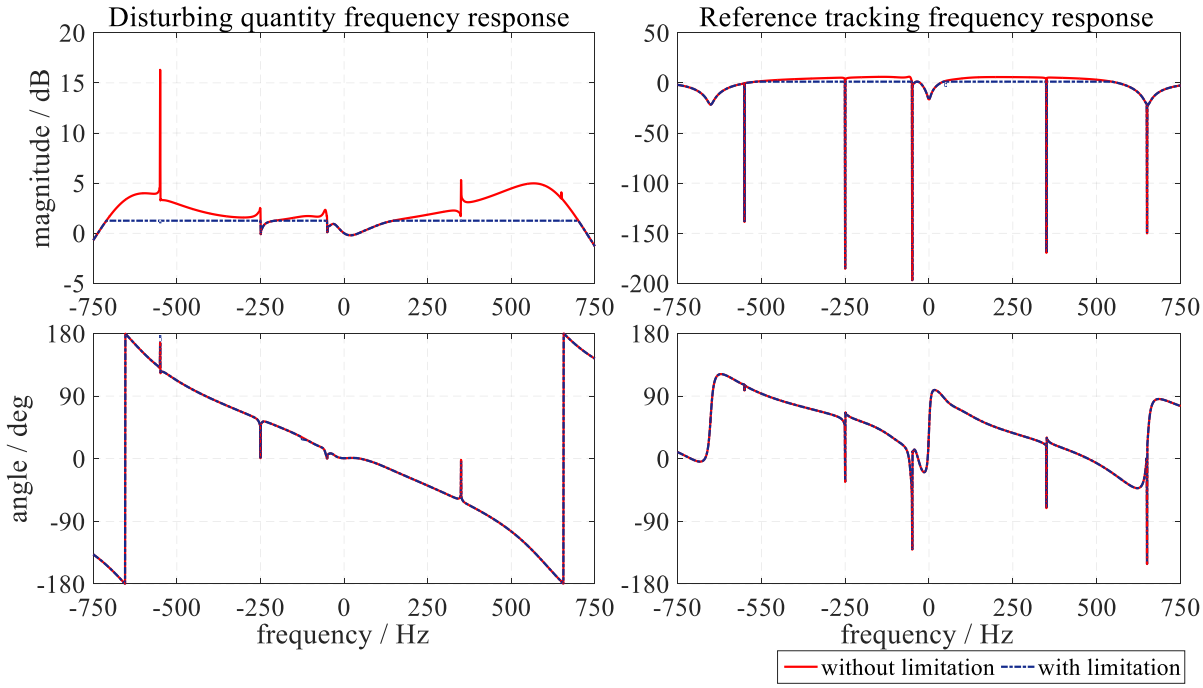

Figure 4-29 Frequency response of the LSC voltage considering voltage limitation

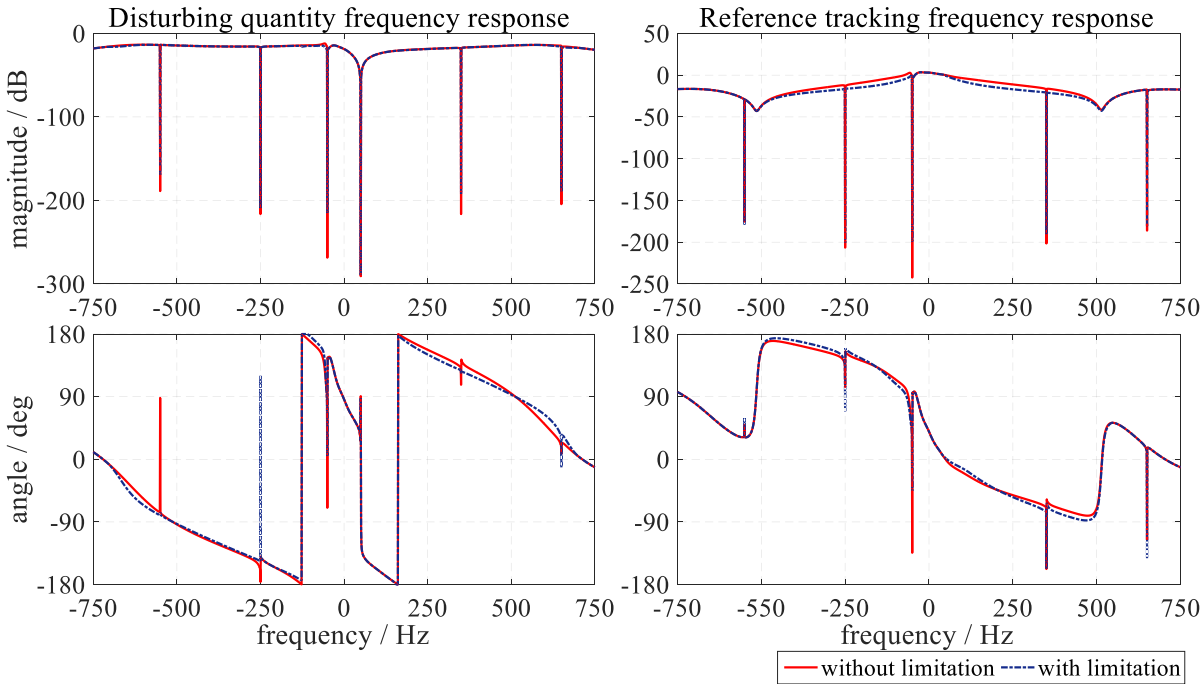

Figure 4-30 Frequency response of the LSC current considering voltage limitation

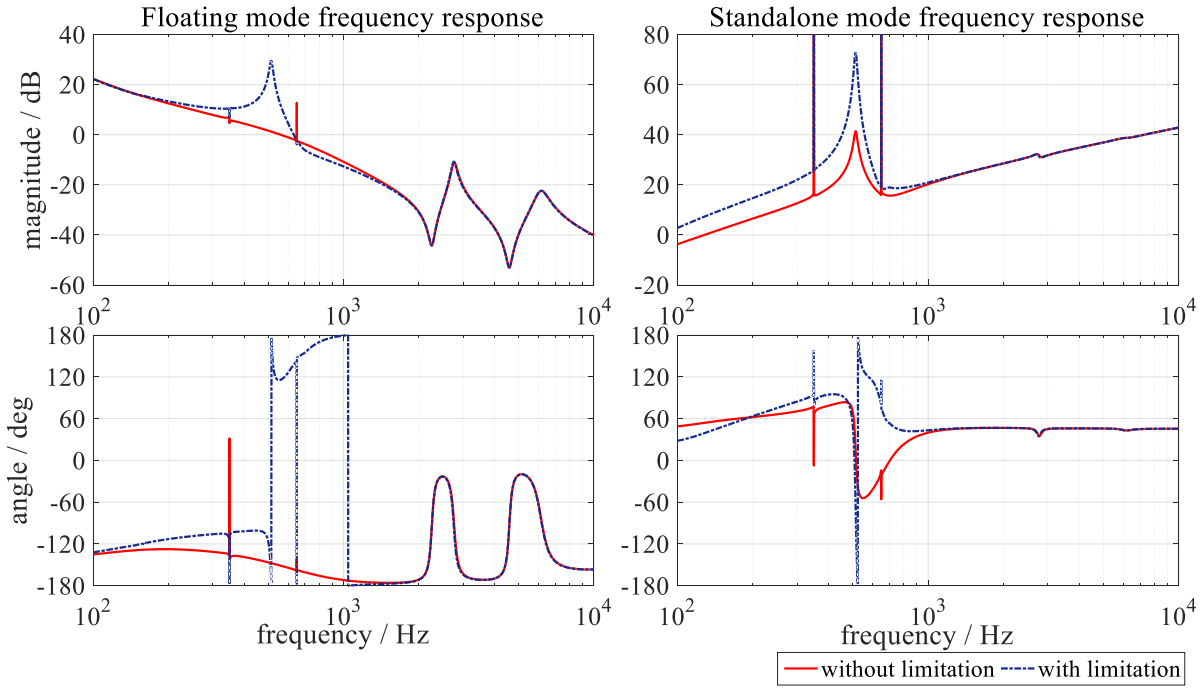

Figure 4-31 Frequency response of LSC open-loop transfer functions considering voltage limitation

The frequency response of the corresponding open-loop transfer functions is shown in Figure 4-31. The voltage limitation has a small influence on the cross-over frequency, where in the floating mode it is slightly increased and in the stand alone mode it shows a slight decrease. However, the voltage limitation has remarkably influenced the stability margin at the 13th order harmonic, where the phase margin is zero and the gain margin is near to zero. This means that in the case when the supply voltage contains a 13th order harmonic voltage, there will be a sustained high current magnitude that may destroy the converter.

4.2.5 Machine-Side Converter Control

The main task of the MSC is to control the DFIG output active and reactive power. The active power is set according to the tracking characteristic described earlier to gain optimum output power, while the reactive power set-point is set either externally, by the wind farm supervisory controller or operator, locally, by the local voltage controller, or both. The control of the MSC is designed in the same manner as for the LSC, where the control is performed in stator voltage coordinates and depends on a feed-forward term and a PI-controller to guarantee a fast and accurate response.

From the space vector model of the DFIG, the rotor voltage in stator voltage coordinate can be rewritten as:

$$\underline{v}_{\mathrm{R}}^{\angle \nu_{\mathrm{S1}}} = -r_{\mathrm{R}}\,\underline{i}_{\mathrm{R}}^{\angle \nu_{\mathrm{S1}}} - \left(s + \mathrm{j}s_{\mathrm{G1}}\omega_{\mathrm{S}}\right)\underline{\psi}_{\mathrm{R}}^{\angle \nu_{\mathrm{S1}}} \tag{4.50}$$

Replacing the Laplace operator by zero and considering a standard PI-controller to compensate for measurement uncertainties, and substituting the rotor flux with the currents yields the rotor current control equation:

$$\begin{aligned} \underline{v}_{\mathrm{R,ref}}^{\angle \nu_{\mathrm{S1}}} &= -\left(r_{\mathrm{R}} + \mathrm{j}s_{\mathrm{G1}}\omega_{\mathrm{S}}\frac{r_{\mathrm{S}}l_{\mathrm{R}} + \mathrm{j}\omega_{\mathrm{S}}\sigma l_{\mathrm{S}}l_{\mathrm{R}}}{r_{\mathrm{S}} + \mathrm{j}\omega_{\mathrm{S}}l_{\mathrm{S}}}\right)\underline{i}_{\mathrm{R}}^{\angle \nu_{\mathrm{S1}}} + \mathrm{j}s_{\mathrm{G1}}\omega_{\mathrm{S}}\frac{l_{\mathrm{M}}}{r_{\mathrm{S}} + \mathrm{j}\omega_{\mathrm{S}}l_{\mathrm{S}}}\underline{v}_{\mathrm{S}}^{\angle \nu_{\mathrm{S1}}} + \underline{v}_{\mathrm{R,C}}^{\angle \nu_{\mathrm{S1}}} \\ &\approx -\left(r_{\mathrm{R}} + \mathrm{j}s_{\mathrm{G1}}\omega_{\mathrm{S}}\sigma l_{\mathrm{R}}\right)\underline{i}_{\mathrm{R}}^{\angle \nu_{\mathrm{S1}}} + s_{\mathrm{G1}}\frac{l_{\mathrm{M}}}{l_{\mathrm{S}}}\underline{v}_{\mathrm{S}}^{\angle \nu_{\mathrm{S1}}} + \underline{v}_{\mathrm{R,C}}^{\angle \nu_{\mathrm{S1}}} \end{aligned} \tag{4.51}$$

where $\underline{v}_{\mathrm{R,C}}^{\angle \nu_{\mathrm{S1}}}$ is the PI-controller output and is given by:

$$\underline{v}_{\mathrm{R,C}}^{\angle \nu_{\mathrm{S1}}} = \left(k_{\mathrm{P,i}} + \frac{k_{\mathrm{I,i}}}{s}\right)\cdot\left(\underline{i}_{\mathrm{R,ref}}^{\angle \nu_{\mathrm{S1}}} - \underline{i}_{\mathrm{R}}^{\angle \nu_{\mathrm{S1}}}\right) \tag{4.52}$$

The reference value for the rotor current is determined from the total power of the DFIG-WT given by:

$$\begin{aligned} \underline{s}_{\mathrm{WT}} &= \underline{s}_{\mathrm{DFIG}} + \underline{s}_{\mathrm{LSC}} \\ &= \underline{v}_{\mathrm{S}} \cdot \underline{i}_{\mathrm{S}}^{*} + \underline{s}_{\mathrm{LSC}} \end{aligned} \tag{4.53}$$

From the steady-state generator equation, by substituting for the stator currents with rotor currents in eq. (4.48) the rotor current set-points are found as:

$$\underline{i}_{\mathrm{R,ref}} = \frac{\left(r_{\mathrm{S}} + \mathrm{j}x_{\mathrm{S}}\right)\left(\underline{s}_{\mathrm{ref}}^{*} - \underline{s}_{\mathrm{LSC}}^{*}\right) + \left|\underline{v}_{\mathrm{S}}\right|^{2}}{\mathrm{j}x_{\mathrm{M}}\underline{v}_{\mathrm{S}}} \tag{4.54}$$

The set-points given in eq. (4.49) depend on the machine parameters, which may vary during operation due to heating, saturation, and skin effect. Therefore, a PI-controller is considered to

compensate for measuring uncertainties and the final reference rotor current would be given by:

$$\underline{i}_{\mathrm{R,ref}} = \frac{l_{\mathrm{S}}}{l_{\mathrm{M}}}\left(\underline{s}^{*}_{\mathrm{ref}} - \underline{s}^{*}_{\mathrm{LSC}}\right) + \left(k_{\mathrm{P,s}} + \frac{k_{\mathrm{I,s}}}{s}\right)\cdot\left(\underline{s}^{*}_{\mathrm{ref}} - \underline{s}^{*}_{\mathrm{LSC}} - \underline{s}^{*}_{\mathrm{S}}\right) - \mathrm{j}\frac{\underline{v}_{\mathrm{S}}}{x_{\mathrm{M}}} \tag{4.55}$$

The MSC overall controller is shown in Figure 4-32. It should be noted that the feed-forward terms guarantee a fast response of the controller. Therefore; the PI-controllers should be tuned to act slowly in order to avoid fast windup and conflicts between subordinate loops.

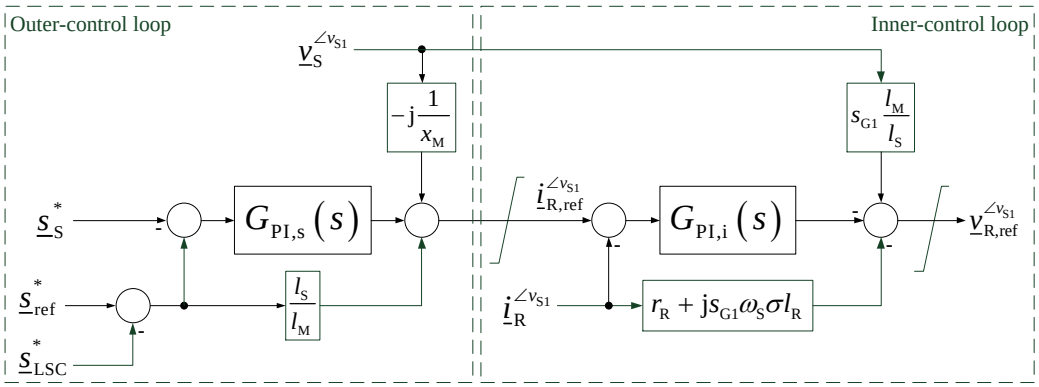

Figure 4-32 MSC overall control loops

4.2.5.1 MSC Current Limitation

The current limitation of the MSC is performed in the same manner as for the LSC. However, the priorities for the MSC may change during the operation. During normal operation the highest priority is set to the positive sequence active current to allow for optimum tracking, while during symmetrical grid faults the priority is set to the positive sequence reactive current to allow voltage support according to the grid codes requirements.

For unsymmetrical grid faults the negative slip is usually higher than 2 in the super-synchronous mode, which requires a high rotor voltage to allow for full control of the negative sequence rotor current. Therefore, under severe unsymmetrical fault conditions the MSC cannot fully compensate for the rotor negative sequence current. Consequently, the positive sequence current limit has to be reduced to:

$$i_{\mathrm{MSC,max1}} = \sqrt{i^{2}_{\mathrm{MSC,max}} - i^{2}_{\mathrm{MSC,2}}} \tag{4.56}$$

There are different control objectives for negative sequence components. Each of them requires different limitation strategies. These limitation strategies will not be discussed here, but a detailed discussion can be found in [48].

4.2.5.2 MSC Voltage Limitation

It is very likely that the MSC operates at its voltage limits during high voltage periods especially in the super-synchronous mode when the slip reaches its maximum value. Also, this may happen during unsymmetrical grid faults and therefore the voltage limitation process should be coordinated with the current limitation. Usually, the highest priority is set to the positive sequence to ensure full controllability of the positive sequence current. However, when full compensation of pulsating torques is required during unsymmetrical grid faults the required negative sequence rotor voltage will attain high magnitudes, as will be shown later, and therefore the highest priority may change to the negative sequence voltage.

The maximum value of the negative sequence voltage cannot be estimated in the same manner as for LSC because the sequence components of the rotor voltage have different frequencies. Therefore, the maximum value is calculated directly by:

$$v_{\mathrm{MSC,max2}} = v_{\mathrm{MSC,max}} - v_{\mathrm{MSC,1}} \tag{4.57}$$

4.2.6 MSC Stability Analysis

The control of the MSC is based also on the instantaneous values of voltage and current. However, the compensation of the phase and magnitude errors introduced by the measuring filters and converter sampling should also consider the rotor slip. Consequently, the transfer function for the measuring filter of the stator voltage remains as in eq. (4.32), while for the rotor current measuring filter and converter sampling they are:

$$\underline{G}^{*}_{\mathrm{meas}}\left(s-\mathrm{j}\omega_{\mathrm{R}}\right)=\frac{1+\dfrac{1.3617}{\omega_{\mathrm{c}}}\mathrm{j}\left(\omega_{\mathrm{S}}-\omega_{\mathrm{R}}\right)+\dfrac{0.618}{\omega_{\mathrm{c}}^{2}}\mathrm{j}\left(\omega_{\mathrm{S}}-\omega_{\mathrm{R}}\right)^{2}}{1+\dfrac{1.3617}{\omega_{\mathrm{c}}}\left(s-\mathrm{j}\omega_{\mathrm{R}}\right)+\dfrac{0.618}{\omega_{\mathrm{c}}^{2}}\left(s-\mathrm{j}\omega_{\mathrm{R}}\right)^{2}} \tag{4.58}$$

$$\underline{G}^{*}_{\mathrm{dt}}\left(s-\mathrm{j}\omega_{\mathrm{R}}\right)=\frac{e^{-\left(s-\mathrm{j}\omega_{\mathrm{R}}\right)\tau_{\mathrm{dt}}}}{e^{-\mathrm{j}\left(\omega_{\mathrm{S}}-\omega_{\mathrm{R}}\right)\tau_{\mathrm{dt}}}}=e^{-\left(s-\mathrm{j}\omega_{\mathrm{S}}\right)\tau_{\mathrm{dt}}} \tag{4.59}$$

The complete block diagram of the MSC controller is shown in Figure 4-33. From this the transfer function of the stator currents is derived as:

$$\underline{i}_{\mathrm{S}}^{\angle 0}=\frac{\left(\underline{N}_{\mathrm{S}}(s)-\underline{D}_{\mathrm{S}}(s)\cdot\left(\underline{G}_{\mathrm{DVS}}(s)-\underline{G}_{\mathrm{DVR}}(s)\right)\right)\underline{v}_{\mathrm{S}}^{\angle 0}+\underline{G}^{*}_{\mathrm{PI}}(s)\cdot\underline{G}^{*}_{\mathrm{dt}}\left(s-\mathrm{j}\omega_{\mathrm{R}}\right)\cdot\underline{G}_{\mathrm{SW}}(s)\underline{i}_{\mathrm{R,ref}}^{\angle 0}}{1-\underline{D}_{\mathrm{S}}(s)} \tag{4.60}$$

where

$$\underline{N}_{\mathrm{S}}(s)=\underline{G}_{\mathrm{SW}}(s)\cdot\left(\underline{G}_{\mathrm{DVS}}(s)+\underline{G}^{*}_{\mathrm{meas}}(s)\cdot\underline{G}^{*}_{\mathrm{dt}}\left(s-\mathrm{j}\omega_{\mathrm{R}}\right)\cdot\underline{G}_{\mathrm{FFV}}\right) \tag{4.61}$$

$$\underline{D}_{\mathrm{S}}(s)=\underline{G}_{\mathrm{dt}}^{*}\left(s-\mathrm{j}\omega_{\mathrm{R}}\right)\cdot\underline{G}_{\mathrm{meas}}^{*}\left(s-\mathrm{j}\omega_{\mathrm{R}}\right)\cdot\underline{G}_{\mathrm{RW}}(s)\cdot\left(\underline{G}_{\mathrm{PI}}^{*}(s)-\underline{G}_{\mathrm{FFI}}\right) \tag{4.62}$$

$$\underline{G}_{\mathrm{FFV}}=s_{\mathrm{G1}}\frac{l_{\mathrm{M}}}{l_{\mathrm{S}}},\underline{G}_{\mathrm{FFI}}=r_{\mathrm{R}}+\mathrm{j}s_{\mathrm{G1}}\omega_{\mathrm{S}}\sigma l_{\mathrm{R}} \tag{4.63}$$

$$\underline{G}_{\mathrm{DVS}}(s)=\frac{\underline{G}_{\mathrm{SZ}}}{\underline{G}_{\mathrm{SW}}},\underline{G}_{\mathrm{DVR}}(s)=\frac{\underline{G}_{\mathrm{RZ}}}{\underline{G}_{\mathrm{RW}}} \tag{4.64}$$

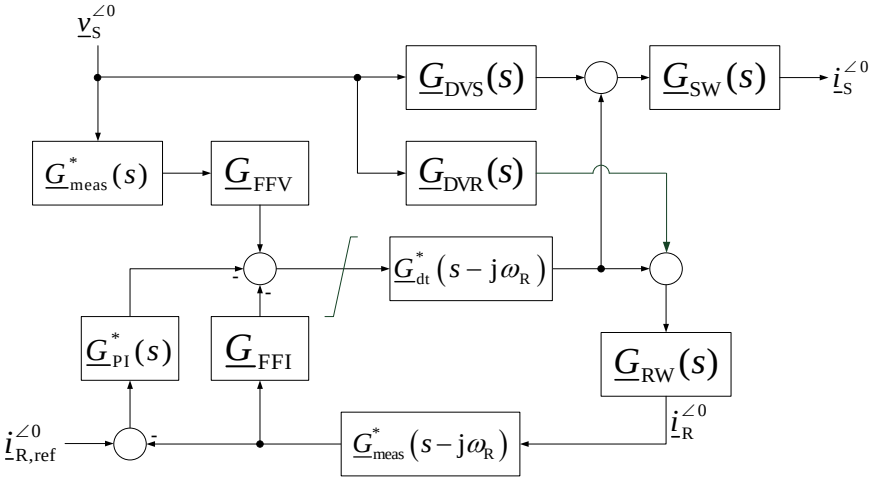

Figure 4-33 MSC closed-loop transfer function

The frequency response of the stator current for different rotor speeds is shown in Figure 4-34. The PI-controller settings are $k_{\mathrm{P}}=0.07$ and $\tau_{\mathrm{I}}=10\,\mathrm{ms}$. The response is almost identical for the different speeds, which indicates the functionality of the speed decoupling approach proposed for the controller. However, as the rotor speed increases the magnitude of the low Eigen frequency increases as well. This indicates that the magnitude of the transient response produced by this pole will increase with the rotor speed. This statement will be proven later, and in order to reduce such effects the proportional gain should be increased. At the operating frequency (50 Hz) there is a rejection gain in the response to the disturbing quantity and the gain in response to the reference tracking equals to $\underline{i}_{\mathrm{S}}^{\angle 0}\big|_{\underline{v}_{\mathrm{S}}=0}\approx-l_{\mathrm{M}}/l_{\mathrm{S}}\cdot\underline{i}_{\mathrm{R,ref}}^{\angle 0}$. This shows that the stator current tracks the reference current regardless of the value of the stator voltage.

Unlike the rotor speed, the variation of the PI-controller's proportional gain has a remarkable effect on the stator's current response especially on the response to the reference tracking quantity as depicted in Figure 4-35. From the response to the reference tracking it becomes clear that the gains at the eigen frequencies decrease with every increase in the proportional gain while the bandwidth increases. In the response of the disturbing quantity this fact can also be observed. Yet, its impact is smaller and the rejection bandwidth increases with the proportional gain. One important observation here is the gain at the slow pole. It becomes clear how the gain increases remarkably with the proportional gain. It can be concluded from the

previous discussion that as the proportional gain increases the damping at the fast poles increases as well while it decreases remarkably at the slow pole.

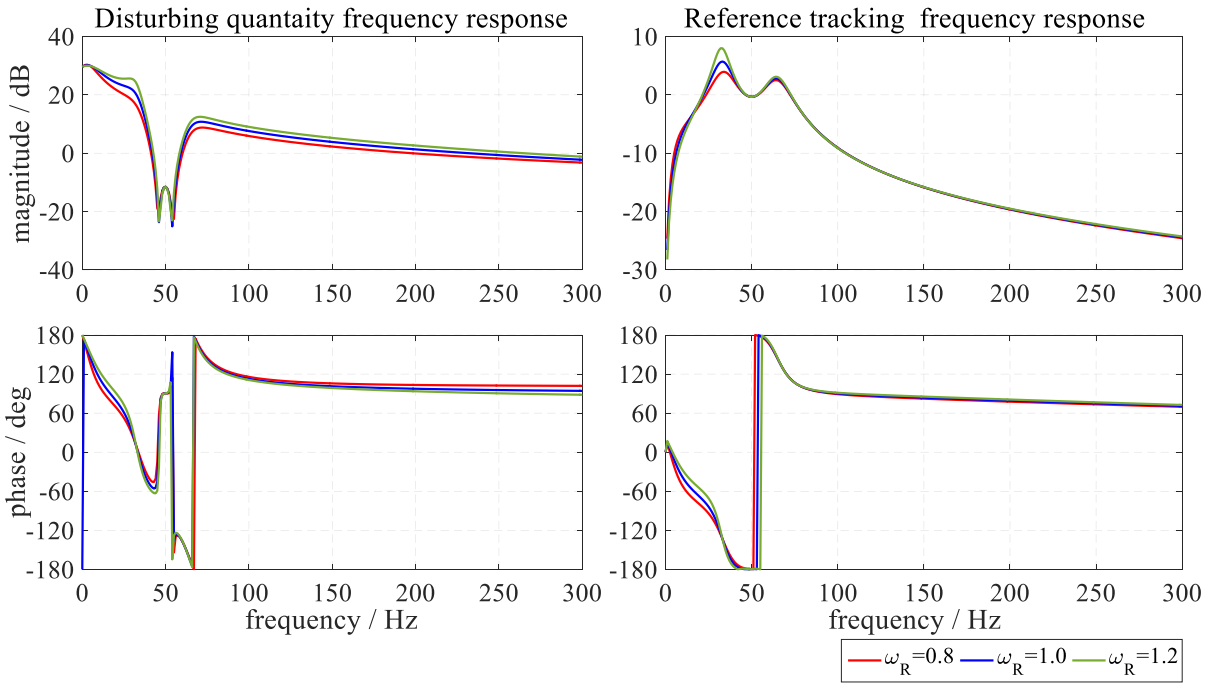

Figure 4-34 Frequency response of the DFIG stator's current for different rotor speeds

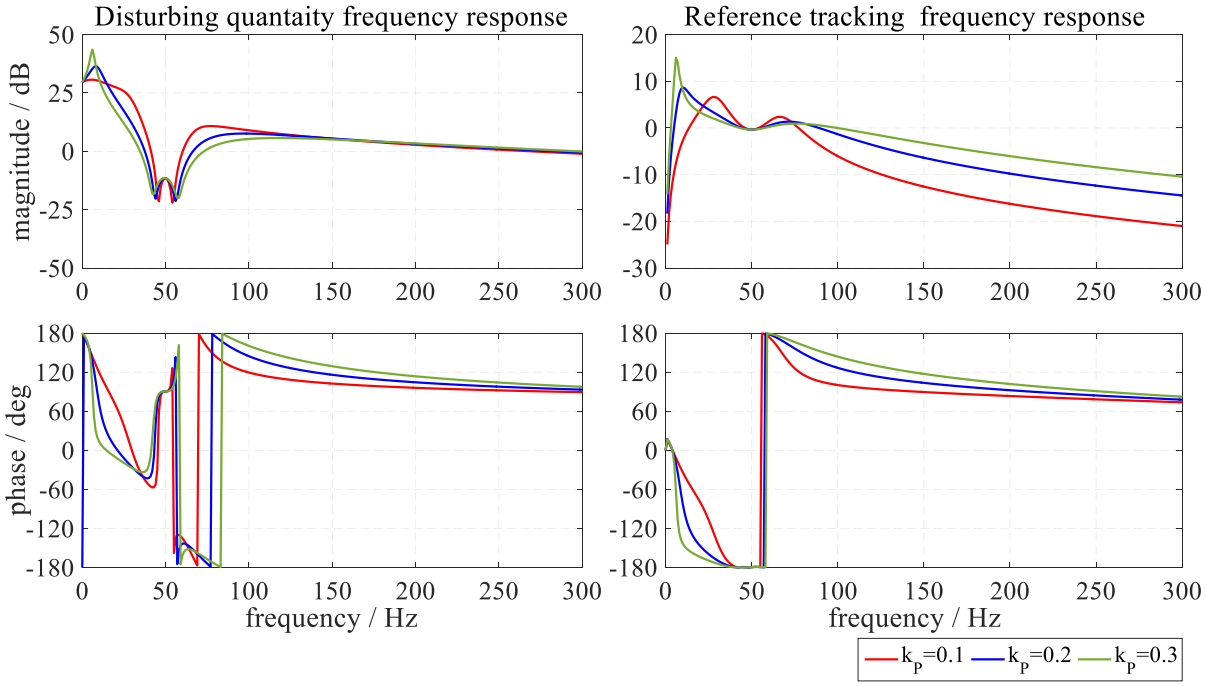

Figure 4-35 Frequency response of the DFIG stator's current for different proportional gain values

4.2.6.1 Influence of Grid Stiffness

The impact of grid stiffness on the DFIG stator's current can be evaluated in the same manner as for LSC by using the following equation:

$$\underline{v}_{\mathrm{S}}^{\angle 0} = \underline{v}_{\mathrm{G}}^{\angle 0} + G_{\mathrm{Grid}}(s) \cdot \underline{i}_{\mathrm{S}}^{\angle 0} \tag{4.65}$$

The modified structure of the MSC control system under consideration of the grid impedance is shown in Figure 4-36.

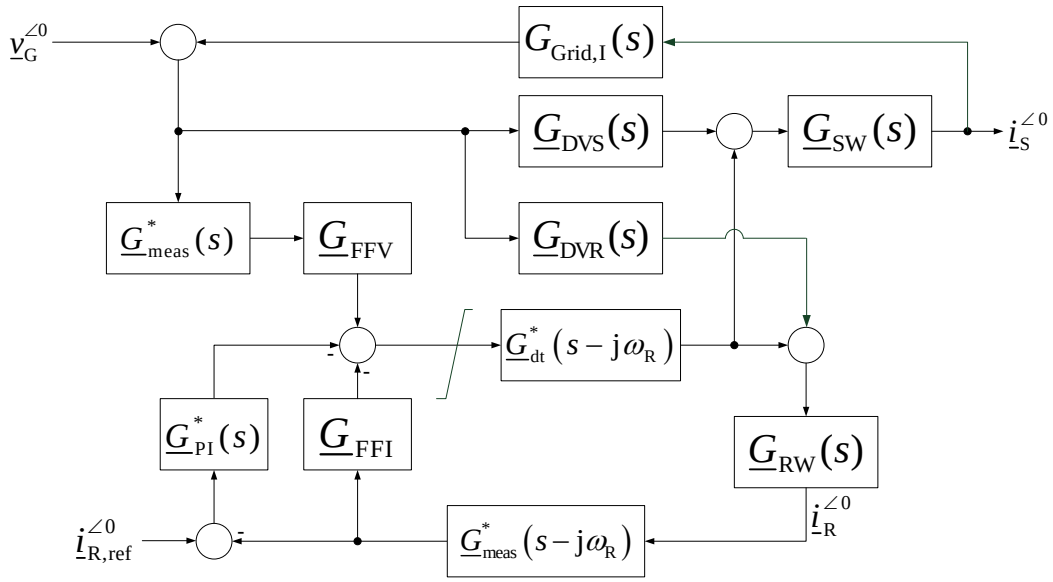

Figure 4-36 MSC closed-loop transfer function considering grid stiffness

The resultant DFIG stator's current transfer function is then:

$$\underline{i}_{\mathrm{S}}^{\angle 0} = \frac{\left(\underline{N}_{\mathrm{S}}(s) - \underline{D}_{\mathrm{S}}(s) \cdot \left(\underline{G}_{\mathrm{DVS}}(s) - \underline{G}_{\mathrm{DVR}}(s)\right)\right)\underline{v}_{\mathrm{G}}^{\angle 0} + \underline{G}_{\mathrm{PI}}^{*}(s) \cdot \underline{G}_{\mathrm{dt}}^{*}(s - \mathrm{j}\omega_{\mathrm{R}}) \cdot \underline{G}_{\mathrm{SW}}(s)\underline{i}_{\mathrm{R,ref}}^{\angle 0}}{1 - \underline{D}_{\mathrm{S}}(s) - G_{\mathrm{Grid}}(s) \cdot \left(\underline{N}_{\mathrm{S}}(s) - \underline{D}_{\mathrm{S}}(s) \cdot \left(\underline{G}_{\mathrm{DVS}}(s) - \underline{G}_{\mathrm{DVR}}(s)\right)\right)} \tag{4.66}$$

The frequency response of the stator's current given in eq. (4.61) is shown in Figure 4-37. It is clear that the magnitude in both responses decreases as the grid SCR decreases. An exception to this is in the narrow band around the operating frequency where the gains are almost identical. This can be easily justified by the increased value of the grid impedance which results in lower current magnitudes.

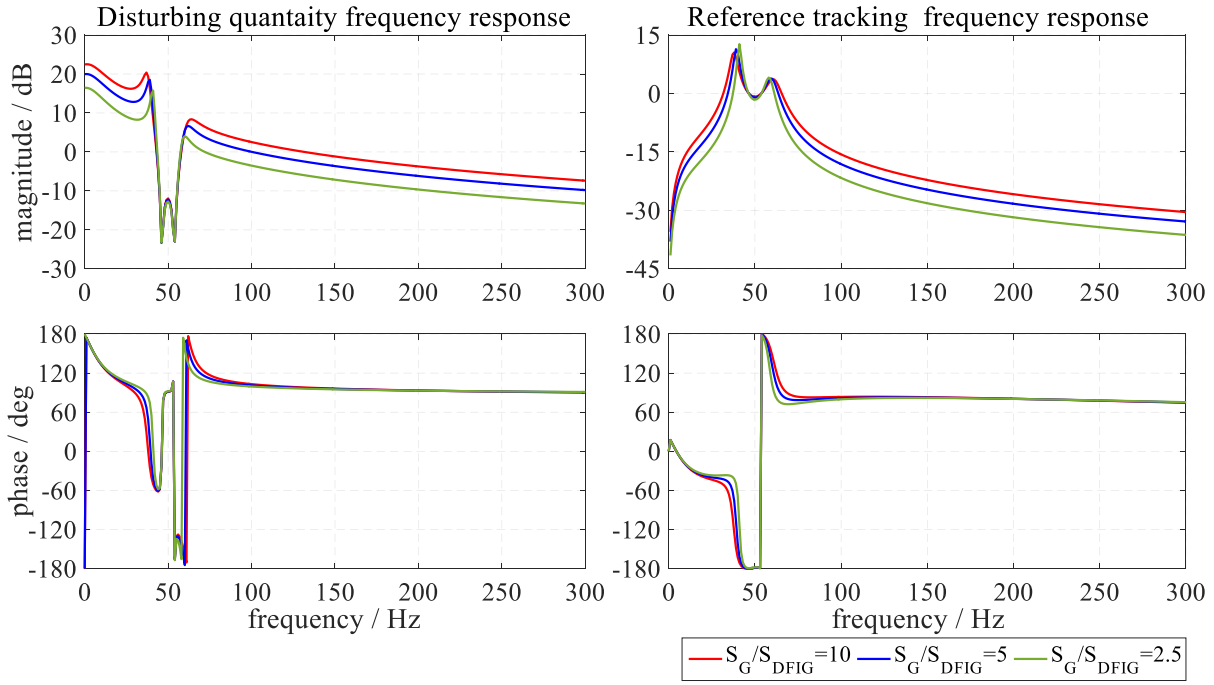

Figure 4-37 Frequency response of the DFIG stator's current for different grid SCRs

Recalling the stability criterion the open-loop transfer functions for floating and standalone modes respectively are expressed as:

$$h_{\mathrm{I}}(s) = -\frac{1-\underline{D}_{\mathrm{S}}(s)}{G_{\mathrm{Grid}}(s)\cdot\left(\underline{N}_{\mathrm{S}}(s)-\underline{D}_{\mathrm{S}}(s)\cdot\left(\underline{G}_{\mathrm{DVS}}(s)-\underline{G}_{\mathrm{DVR}}(s)\right)\right)} \tag{4.67}$$

$$h_{\mathrm{V}}(s) = -1-\frac{G_{\mathrm{Grid}}(s)\cdot\left(\underline{N}_{\mathrm{S}}(s)-\underline{D}_{\mathrm{S}}(s)\cdot\left(\underline{G}_{\mathrm{DVS}}(s)-\underline{G}_{\mathrm{DVR}}(s)\right)\right)-1+\underline{D}_{\mathrm{S}}(s)}{\underline{G}^{*}_{\mathrm{PI}}(s)\cdot\underline{G}^{*}_{\mathrm{dt}}\left(s-\mathrm{j}\omega_{\mathrm{R}}\right)\cdot\underline{G}_{\mathrm{SW}}(s)} \tag{4.68}$$

The frequency response of the open-loop transfer functions is shown in Figure 4-38. There is only one cross-over frequency of 385 Hz in the floating mode and with a high phase margin for the highest grid SCR. For other grid conditions the magnitude tends to be constant throughout the high frequency region while the phase shifts start at almost -15° and settle at zero degree. In the standalone mode there are no cross-over frequencies, where the magnitudes keep on increasing with the frequency, while the phase shifts increase with the frequency from -90° onwards and finally settle at zero degrees for the frequencies beyond 10 kHz. It can then be concluded that the DFIG stator's current and voltage are always stable regardless of the grid condition provided that the grid voltage is stable.

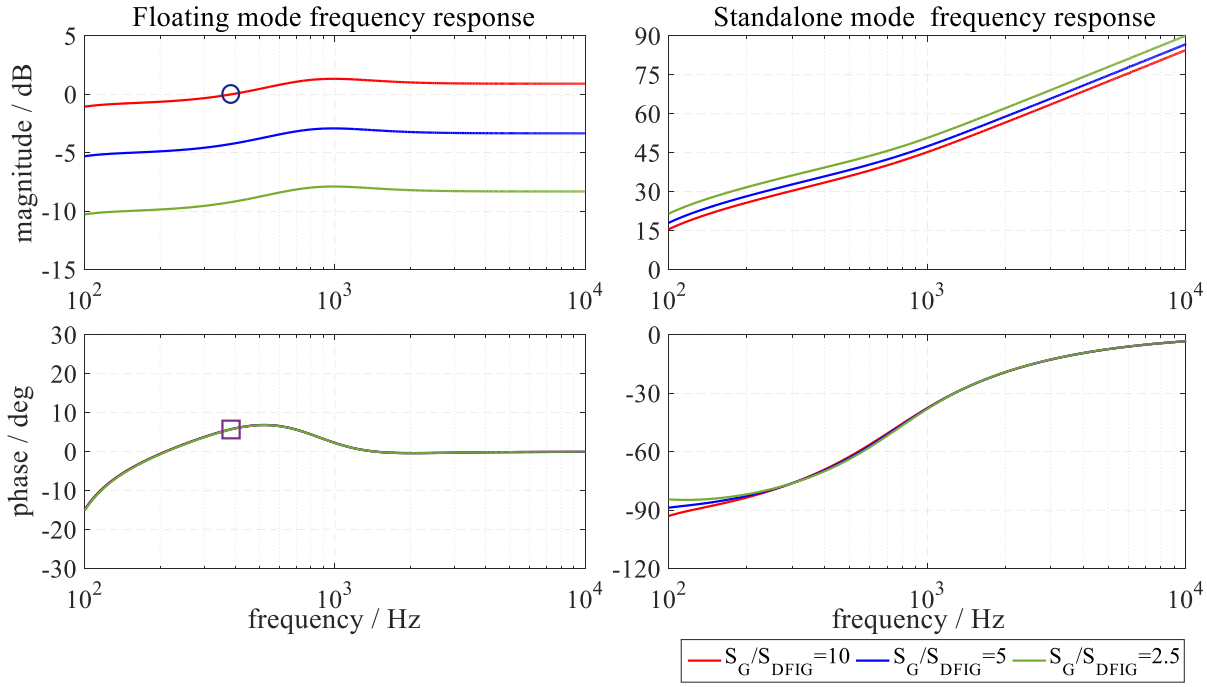

Figure 4-38 Frequency response of MSC open-loop transfer functions for different grid SCRs

4.2.6.2 Influence of Stator Filter

In DFIG harmonic currents are generated in both stator and rotor circuits. These harmonics are impressed by the grid, machine asymmetry, wind speed fluctuations and shadowing effects, rotor eccentricity, magnetic saturation and the converter. Considering the fundamental field of the current components, the harmonic currents generated will propagate from rotor to stator and vice versa according to [91]:

$$\omega_{S,harm} = \omega_{R,harm} + \omega_{mech} \tag{4.69}$$

$$\omega_{R,harm} = \omega_{S,harm} + \omega_{mech} \tag{4.70}$$

According to eq. (4.69) and (4.70) the main harmonic currents with the carrier frequency and its multiple generated by converter switching propagate from the rotor circuit as an interharmonics in the stator circuit. This leads to the assumption that the design of the DFIG filter is not simple because the harmonic order varies with the rotor speed. However, the harmonic order will vary in a band of $(1+s_G)\omega_S$ around the carrier frequency and its multiple. Therefore, the stator notch filters can still be tuned at the carrier frequency and its multiple. Additionally, a high-pass filter with a cut-off frequency greater than the notch filter is implemented to filter out all other higher harmonics. Also an additional notch filter tuned to a frequency much lower than the carrier frequency to filter out the slot harmonics.

The impact of the stator's filter on the stator current is considered by using the following equation:

$$\underline{v}_{\mathrm{S}}^{\angle 0} = G_{\mathrm{Grid,V}}(s)\cdot\underline{v}_{\mathrm{G}}^{\angle 0} + G_{\mathrm{Grid,I}}(s)\cdot\underline{i}_{\mathrm{S}}^{\angle 0} \tag{4.71}$$

The MSC control system with the stator filter is shown in Figure 4-39. The resultant stator current transfer function is then given by:

$$\begin{aligned}\underline{i}_{\mathrm{S}}^{\angle 0} = &\frac{G_{\mathrm{Grid,V}}(s)\cdot\left(\underline{N}_{\mathrm{S}}(s)-\underline{D}_{\mathrm{S}}(s)\cdot\left(\underline{G}_{\mathrm{DVS}}(s)-\underline{G}_{\mathrm{DVR}}(s)\right)\right)}{1-\underline{D}_{\mathrm{S}}(s)-G_{\mathrm{Grid,I}}(s)\cdot\left(\underline{N}_{\mathrm{S}}(s)-\underline{D}_{\mathrm{S}}(s)\cdot\left(\underline{G}_{\mathrm{DVS}}(s)-\underline{G}_{\mathrm{DVR}}(s)\right)\right)}\underline{v}_{\mathrm{G}}^{\angle 0}\\ &+\frac{\underline{G}_{\mathrm{PI}}^{*}(s)\cdot\underline{G}_{\mathrm{dt}}^{*}\left(s-\mathrm{j}\omega_{\mathrm{R}}\right)\cdot\underline{G}_{\mathrm{SW}}(s)}{1-\underline{D}_{\mathrm{S}}(s)-G_{\mathrm{Grid,I}}(s)\cdot\left(\underline{N}_{\mathrm{S}}(s)-\underline{D}_{\mathrm{S}}(s)\cdot\left(\underline{G}_{\mathrm{DVS}}(s)-\underline{G}_{\mathrm{DVR}}(s)\right)\right)}\underline{i}_{\mathrm{R,ref}}^{\angle 0}\end{aligned} \tag{4.72}$$

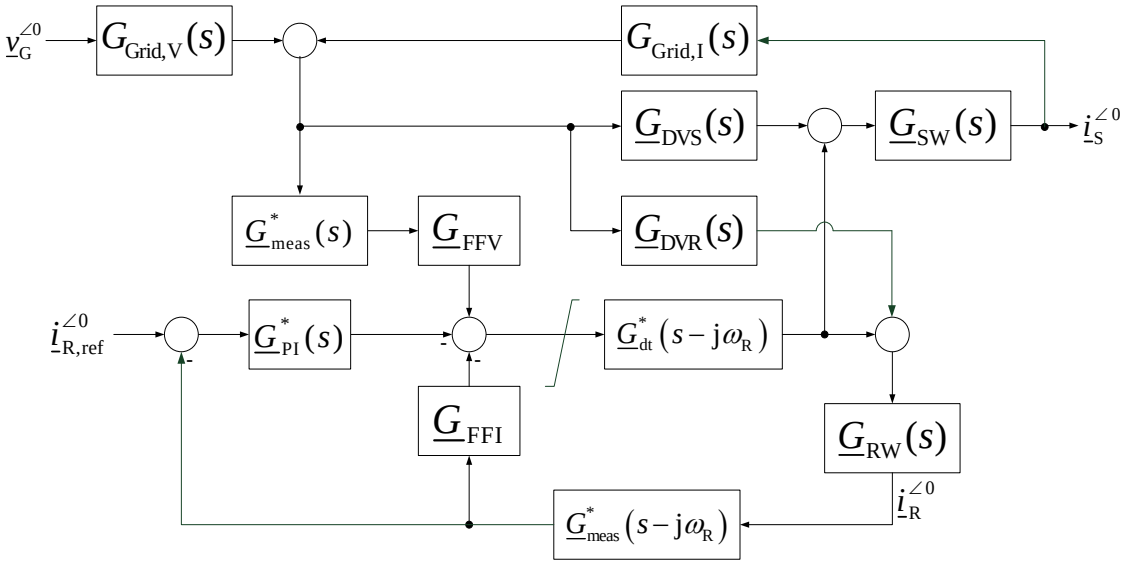

Figure 4-39 MSC closed-loop transfer function considering stator filters

The open-loop transfer functions considering the stator filter are found to be:

$$h_{\mathrm{I}}(s) = -\frac{\dfrac{G_{\mathrm{Filter}}(s)}{G_{\mathrm{Grid}}(s)}}{G_{\mathrm{Filter}}(s)\cdot\left(\dfrac{\underline{N}_{\mathrm{S}}(s)-\underline{D}_{\mathrm{S}}(s)\cdot\left(\underline{G}_{\mathrm{DVS}}(s)-\underline{G}_{\mathrm{DVR}}(s)\right)}{1-\underline{D}_{\mathrm{S}}(s)}\right)-1} \tag{4.73}$$

$$h_{\mathrm{V}}(s) = -1-\frac{G_{\mathrm{Grid,I}}(s)\cdot\left(\underline{N}_{\mathrm{S}}(s)-\underline{D}_{\mathrm{S}}(s)\cdot\left(\underline{G}_{\mathrm{DVS}}(s)-\underline{G}_{\mathrm{DVR}}(s)\right)\right)-1+\underline{D}_{\mathrm{S}}(s)}{G_{\mathrm{PI}}^{*}(s)\cdot\underline{G}_{\mathrm{dt}}^{*}\left(s-\mathrm{j}\omega_{\mathrm{R}}\right)\cdot\underline{G}_{\mathrm{SW}}(s)} \tag{4.74}$$

The frequency response of the stator's current described by eq. (4.72) is shown in Figure 4-40. It is obvious that the filter circuit does not change the gains in the frequency range up to 300 Hz because it is supposed that the filter has a very high impedance in this range. However, beyond this range the filter results in a high gain in the response of the disturbing quantity at frequencies equal to 738 Hz, 805 Hz, and 890 Hz for SCR values of 10, 5, and 2.5 respectively. Still, the rejection gain at those frequencies in response to reference tracking has remarkably increased for SCR values of 10 and 5, while the gain for the SCR value of 2.5 changes to a positive value. Yet, the filter significantly increases the rejection gain in the response of the

reference tracking at frequencies equal to 400 Hz, 530 Hz, and 670 Hz for SCR values 10, 5, and 2.5 respectively.

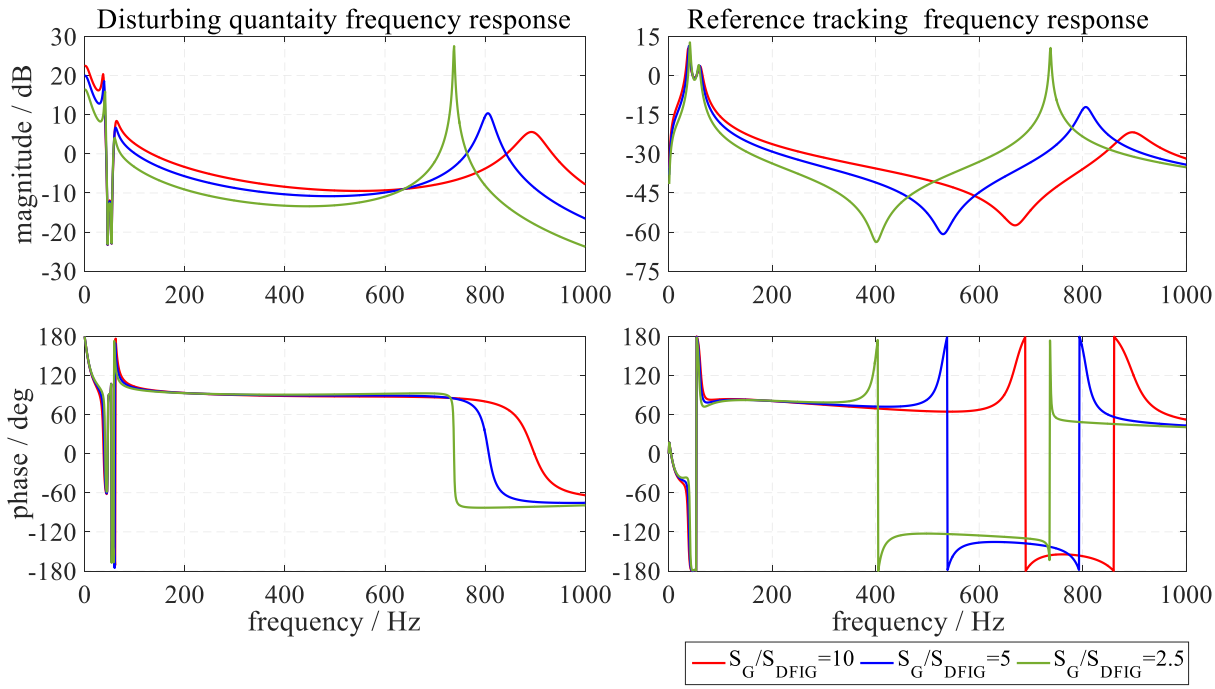

Figure 4-40 Frequency response of the DFIG stator's current including stator filters

The frequency response of the open-loop transfer functions shown in Figure 4-41 illustrates how the filter influences the stability margins. In the floating mode a two cross-over frequencies exist. At the low cross-over frequency the phase margin reaches high value of almost 180°, which means that the stator's current is stable. However, at the high cross-over frequency, which equals the notch frequencies described in the frequency response of the stator's current, the phase-margin is too small. Its value equals 0.6° for a SCR value of 2.5 and reaches 7° for a SCR value of 10. This means that at this frequency the stator current reaches high values especially for low SCR values of the grid which may lead to the disconnection of the DFIG.

In the standalone mode there is no cross-over frequency highlighting that the output voltage is be stable in the whole frequency range. However, the gain margins at the notch frequencies described earlier are low especially at the lowest SCR value, where the gain margin equals 4 dB. Consequently, at low SCR values the DFIG output voltage at this frequency may reach high values that can also lead to the disconnection from the grid.

From the discussion above it can be concluded that the filter design of the stator's circuit is critical and requires a sophisticated engineering design to avoid system instability and to increase the system's stability margins.

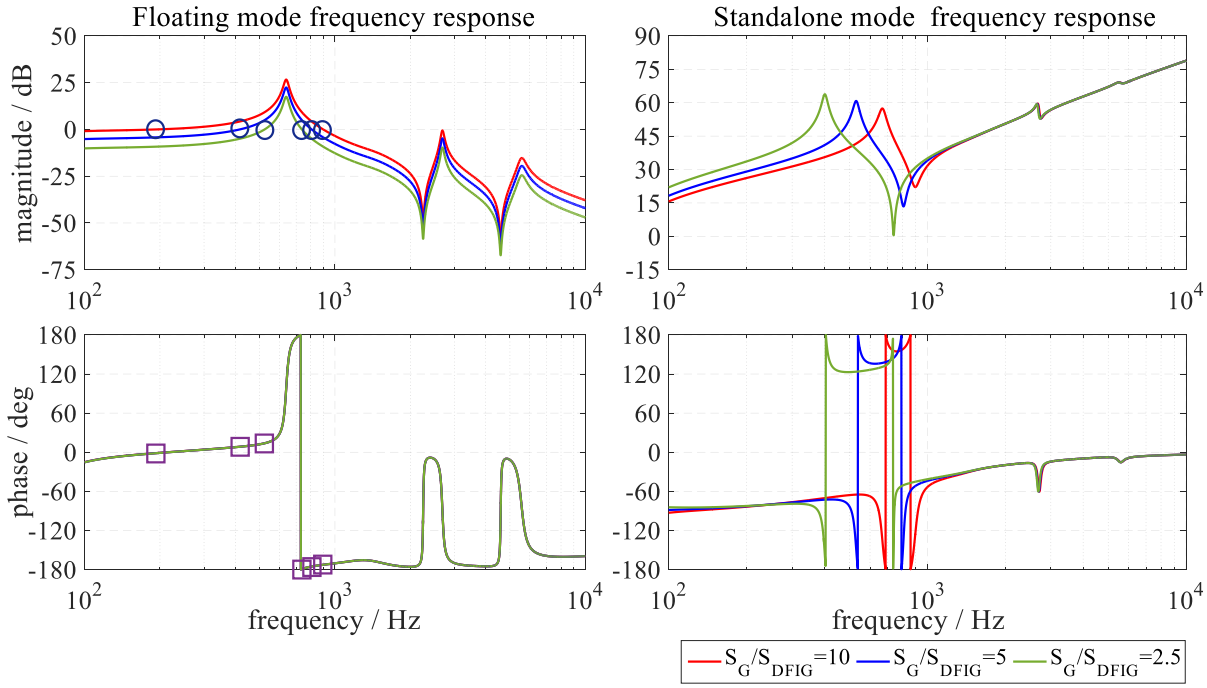

Figure 4-41 Frequency response of MSC open-loop transfer functions including stator filters

4.2.6.3 Influence of Magnetic Saturation

The values of the machine inductances strongly influence the location of the zeros and poles. The values of the machine inductances are not a time invariant and rather change non-linearly with the operating point. Due to the lack of data, only the influence of the main flux saturation on the machine's stability will be discussed.

The value of the main inductance depends on the magnitude of the main current, which is defined by the operating point. The main inductance value is measured at different operating points and a polynomial curve fitting is applied to define a mathematical interpretation of the measured data. Figure 4-42 shows the measured data of the main inductance at different values of the main current and the fitted data. The polynomial function defining the non-linear relation between the main current and main inductance is of the third order and is given by:

$$l_{\mathrm{M}} = 7.315 \cdot \left|\underline{i}_{\mathrm{M}}\right|^3 + 5.54 \cdot \left|\underline{i}_{\mathrm{M}}\right|^2 - 13.23 \cdot \left|\underline{i}_{\mathrm{M}}\right| + 6.767 \qquad (4.75)$$

where the main current $\left|\underline{i}_{\mathrm{M}}\right| = \left|\underline{i}_{\mathrm{S}} + \underline{i}_{\mathrm{R}}\right|$ is the algebraic sum of both the rotor and the stator currents.

In the same manner as before a trust-region method is used to solve the set of non-linear equations described by:

$$\min_x \begin{pmatrix} f_1\left(\dfrac{\underline{i}_S^{\angle 0}}{\underline{v}_G^{\angle 0}}\right)^2 \\ f_2\left(\dfrac{\underline{i}_R^{\angle 0}}{\underline{v}_G^{\angle 0}}\right)^2 \\ f_3\left(\dfrac{l_M}{\underline{v}_G^{\angle 0}}\right)^2 \end{pmatrix} \& \min_x \begin{pmatrix} f_1\left(\dfrac{\underline{i}_S^{\angle 0}}{\underline{i}_{R,ref}^{\angle 0}}\right)^2 \\ f_2\left(\dfrac{\underline{i}_R^{\angle 0}}{\underline{i}_{R,ref}^{\angle 0}}\right)^2 \\ f_3\left(\dfrac{l_M}{\underline{i}_{R,ref}^{\angle 0}}\right)^2 \end{pmatrix} \tag{4.76}$$

and subjected to

$$l_M \le 6.767 \tag{4.77}$$

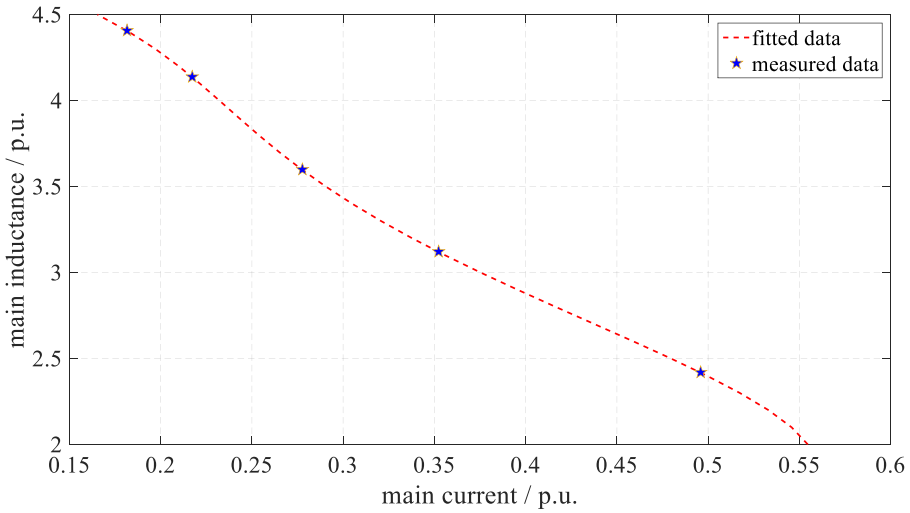

Figure 4-42 DFIG main inductance value at different operating points

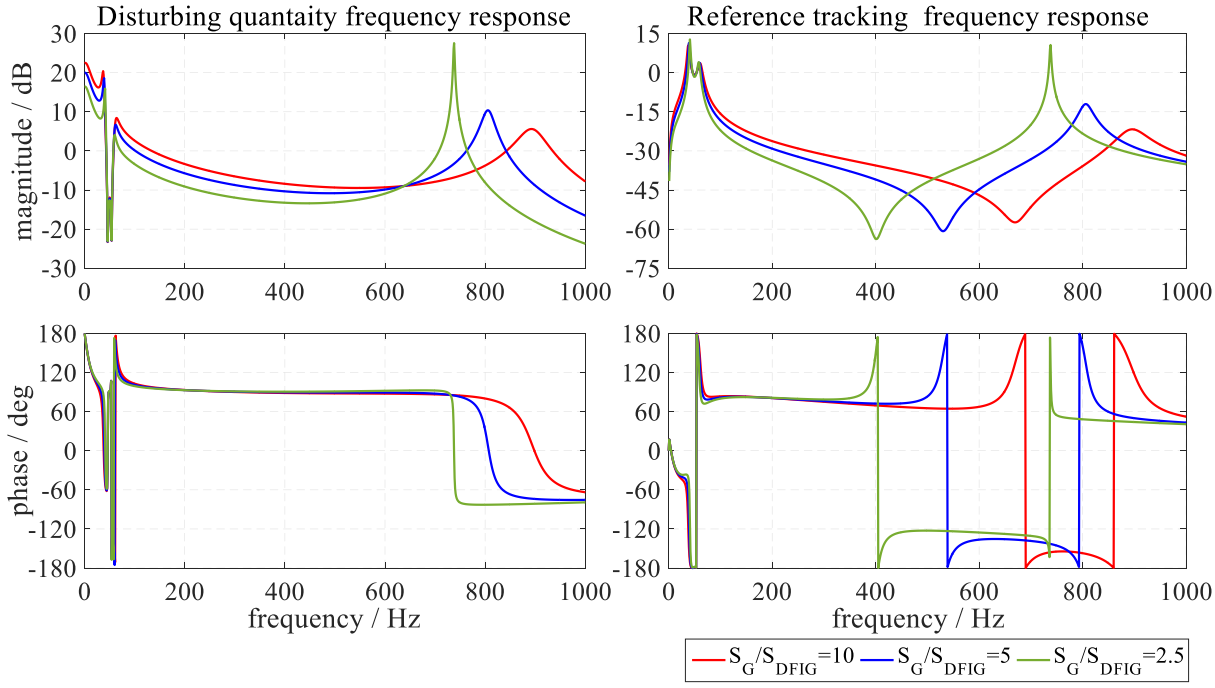

Figure 4-43 Frequency response of the DFIG stator's current considering magnetic saturation

The frequency response of the DFIG stator's current and MSC open-loop transfer functions considering magnetic saturation for different grid SCR values is shown in Figure 4-43 and Figure 4-44 respectively. The resemblance between the frequency responses in this case and in the case without the influence of the magnetic saturation shown in Figure 4-40 and Figure 4-41 can be observed easily.

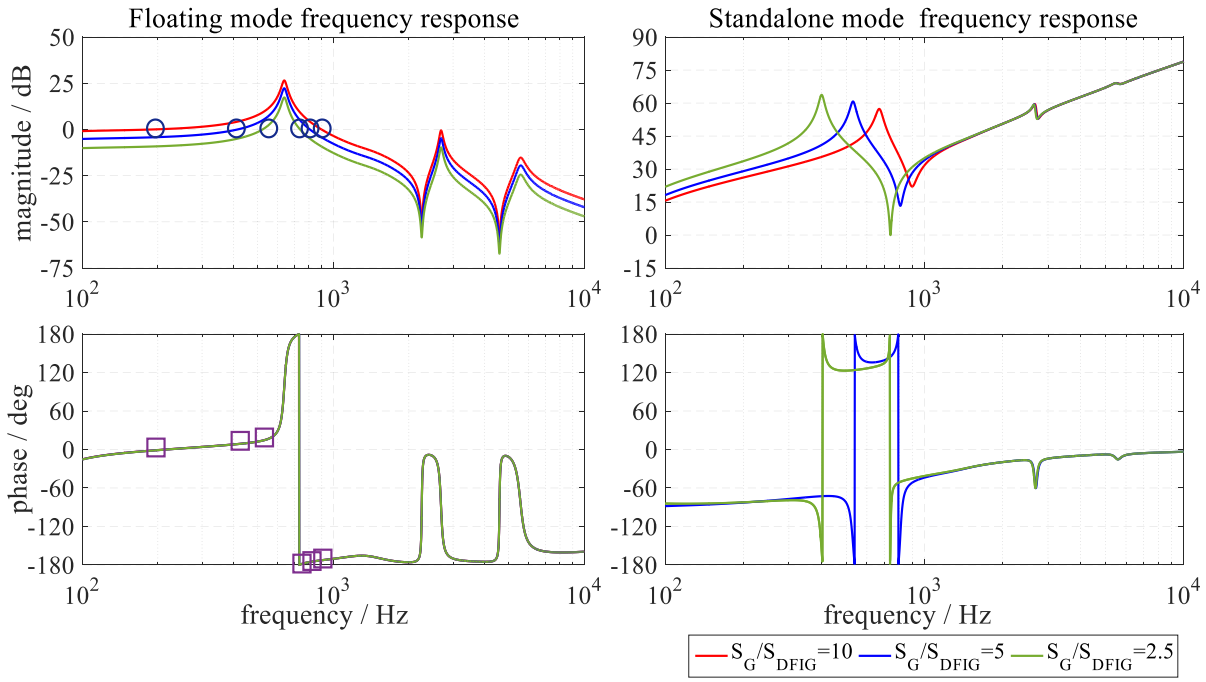

Figure 4-44 Frequency response of MSC open-loop transfer functions considering magnetic saturation

The magnetizing current is the main reason there is no remarkable difference between the two cases. The difference between the magnetizing current magnitudes under rated conditions (rated stator voltage and power output) with and without consideration of the magnetic saturation is shown in Figure 4-45. It is clear that the difference between the two cases is not significant and exists mostly in a frequency band around the operating frequency. That is why this similarity between the two cases are found.

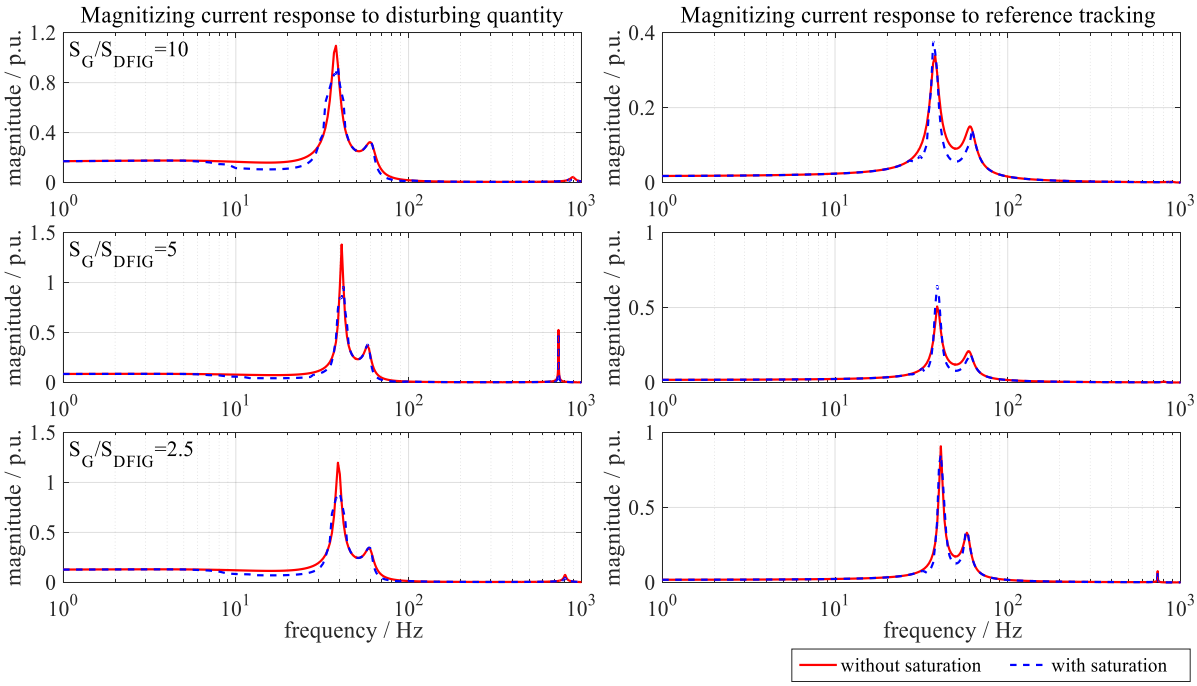

Figure 4-45 Magnetizing current magnitudes under rated conditions

4.2.6.4 Influence of MSC Voltage Limitation

The maximum modulation index which is achieved in the manner already discussed earlier equals $2/\sqrt{3}$. Under such conditions and under consideration of a safety factor the maximum available steady-state voltage MSC can generate is 0.45 p.u. In order to account for the MSC voltage limitation the problem described in eq. (4.76) is modified to display the influence of the rotor voltage on the frequency response:

$$\min_x \begin{pmatrix} f_1\left(\dfrac{\underline{i}_S^{\angle 0}}{\underline{v}_G^{\angle 0}}\right)^2 \\ f_2\left(\dfrac{\underline{i}_R^{\angle 0}}{\underline{v}_G^{\angle 0}}\right)^2 \\ f_3\left(\dfrac{l_M}{\underline{v}_G^{\angle 0}}\right)^2 \\ f_4\left(\dfrac{\underline{v}_R^{\angle 0}}{\underline{v}_G^{\angle 0}}\right)^2 \end{pmatrix} \& \min_x \begin{pmatrix} f_1\left(\dfrac{\underline{i}_S^{\angle 0}}{\underline{i}_{R,ref}^{\angle 0}}\right)^2 \\ f_2\left(\dfrac{\underline{i}_R^{\angle 0}}{\underline{i}_{R,ref}^{\angle 0}}\right)^2 \\ f_3\left(\dfrac{l_M}{\underline{i}_{R,ref}^{\angle 0}}\right)^2 \\ f_2\left(\dfrac{\underline{v}_R^{\angle 0}}{\underline{i}_{R,ref}^{\angle 0}}\right)^2 \end{pmatrix} \qquad (4.78)$$

and subjected to

$$l_M \le 6.767 \,\&\, |v_R| \le 0.45 \qquad (4.79)$$

The frequency response of the rotor voltage to the disturbing quantity and reference tracking considering the MSC voltage limitation is shown in Figure 4-46 and 4-47 respectively. It can

be observed that there are no differences between the phase angle for the two cases with and without limitation and that the magnitude is limited to -6.9357 dB ($=20\log_{10}(0.45)$). According to the response to the disturbing quantity the voltage limitation is critical in the frequency region <44 Hz for high SCR values of the grid, while there is no voltage limitation performed in this frequency region in response to the reference tracking. The highest rotor voltage gains are located at the low eigen frequency (38, 39 and 41 Hz for SCR 10, 5, and 2.5 respectively) in both responses, at the high eigen frequency (738,807 and 897 Hz for SCR 2.5, 5, and 10) in the response to the disturbing quantity for all SCR values and only for the lowest SCR value in response to the reference tracking. It is clear that the gain increases strongly as the SCR decreases due to the low impedance value at the eigen frequencies.

The MSC voltage limitation will consequently reduce the gains of the stator current especially at the eigen frequencies. This can be observed in the frequency response of the DFIG stator's current shown in Figure 4-48. For high SCR values the gain is reduced in the frequency region of <40 Hz in the response to the disturbing quantity, and the rejection gain is increased especially at the eigen frequencies around the operating frequency. Furthermore, the gain is reduced at the high eigen frequency especially for low SCR. The gain at the low eigen frequency is reduced in the response to reference tracking especially for the low SCR value, and it is reduced as well at the high eigen frequency for the low SCR value.

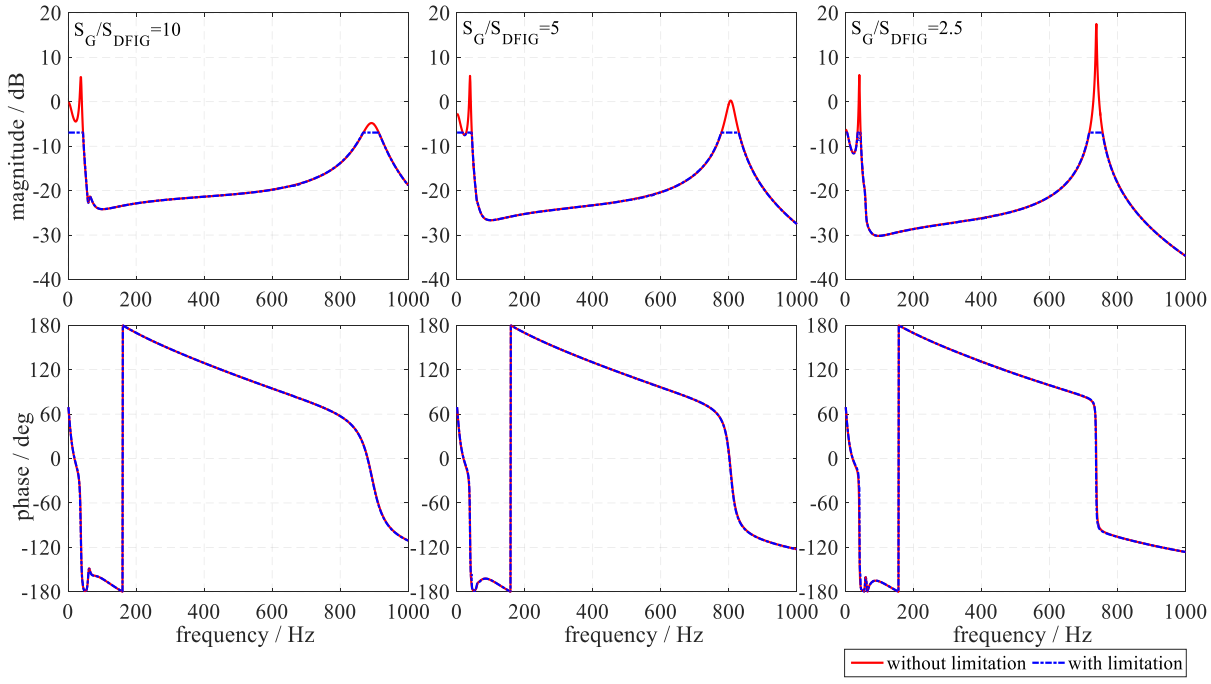

Figure 4-46 Frequency response of the rotor voltage to the disturbing quantity

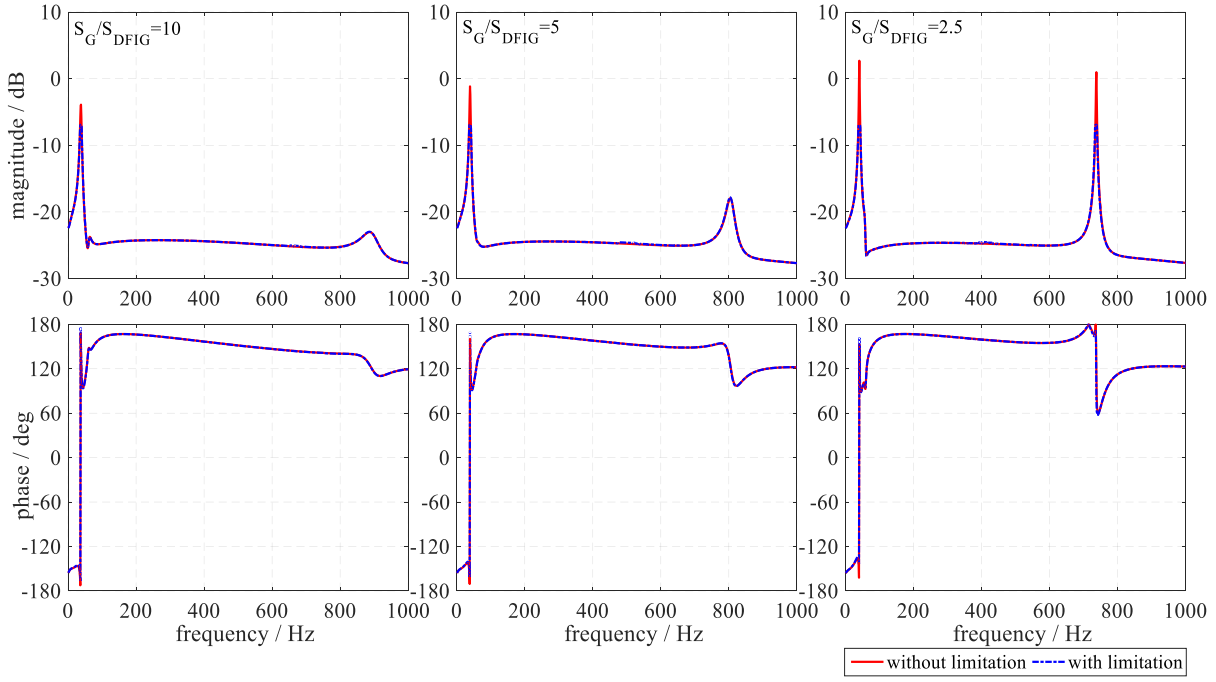

Figure 4-47 Frequency response of the rotor voltage to reference tracking

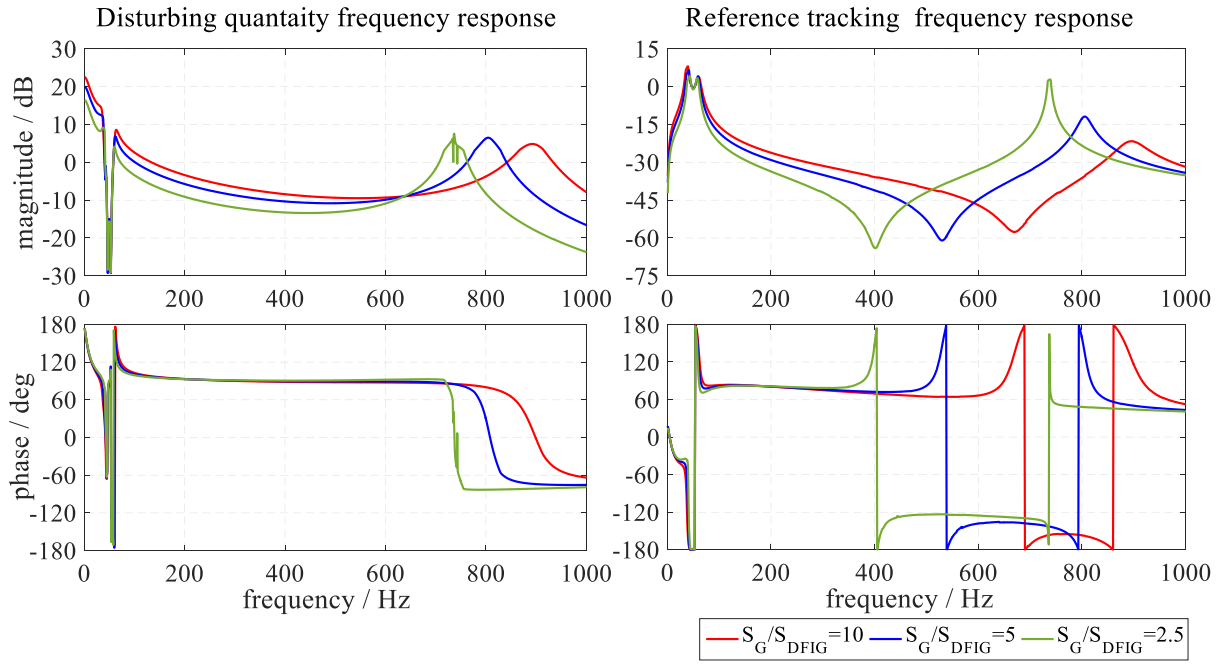

Figure 4-48 Frequency response of the DFIG stator's current considering voltage limitation

The frequency response of MSC open-loop transfer functions are shown in Figure 4-49. The voltage limitation enhances the stability margins of the floating mode, where only one cross-over frequency at 100 Hz exists for a SCR value of 10. This is because the voltage limitation increases the machine's output impedance by reducing the machine's stator current gains. In the standalone mode the voltage limitation does not change the stability margin because, as already shown in Figure 4-48, the gain of the stator's current in response to the reference tracking is slightly reduced only for a small SCR value.

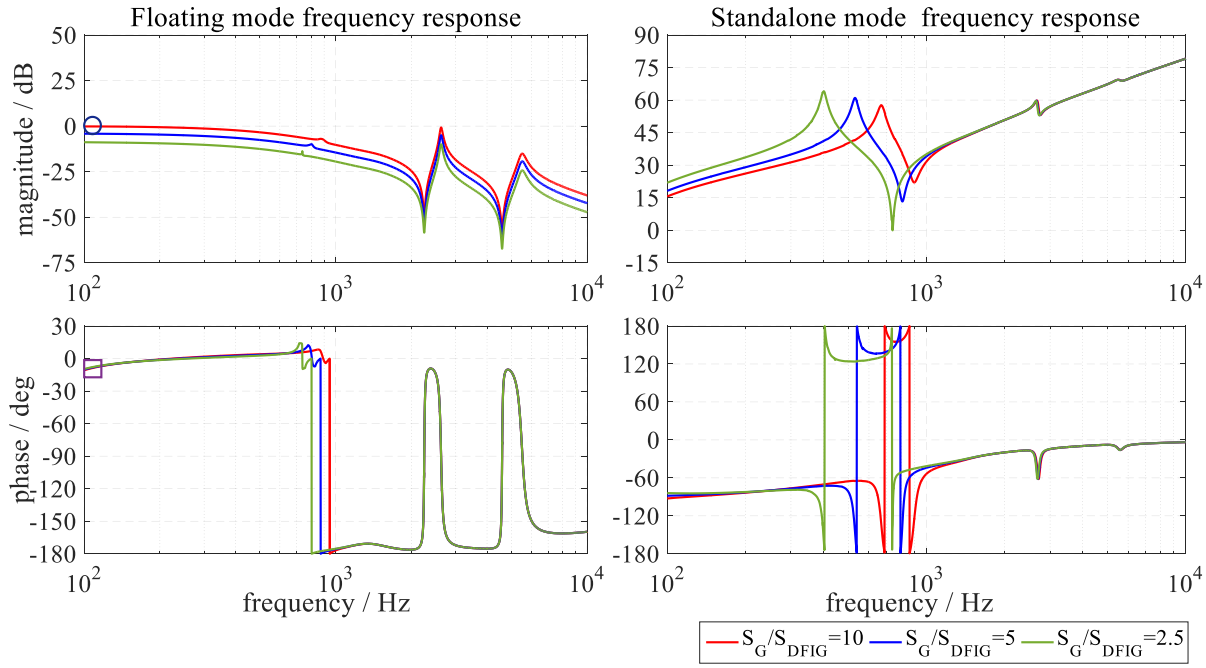

Figure 4-49 Frequency response of MSC open-loop transfer functions considering voltage limitation

5 Analysis of the Symmetrical Fault Response

The detailed modeling and control of the DFIG-WT regarding the interconnection aspects and stability criterion with the grid have been introduced in the previous chapters. From this it can be concluded that the fault response of the DFIG-WT is dictated by a combination of factors, including the electrical parameters of the machine and the controller configuration of the converters, which make it imperative to take into account all of these factors in order to provide a much deeper and clearer analysis of the fault current contribution of the DFIG-WT.

With the increased incorporation of the wind power plants (WPP) into the power system the knowledge of their fault current contribution became crucial for the power system component design, e.g. circuit breakers, bus-bars, etc., and protective relays settings for selective disconnection. However, the fault current contribution has not been thoroughly addressed in the literature, the most have concerned only with the behavior under crowbar operation [92]. Nonetheless, the crowbar protection circuit is currently marginal in the modern DFIG-WT, because during crowbar operation the DFIG behaves like a conventional IG absorbing reactive power from the gird consequently the DFIG is not compatible with the grid codes requirements anymore. Additionally, the analysis of the DFIG-WT fault current contribution with the crowbar is a trivial matter as will be shown later [88].

So far, there are not any sufficient studies that address the influence of the controller and system nonlinearities on the fault response. The only analysis that however only considers the controller configuration is given in [88], but the provided mathematical expressions that describe the short-circuit current behavior were complex and some unjustified approximations were made. Also the influence of nonlinearities as well as the converter blocking were not considered. Therefore, in this chapter a very detailed analysis of the DFIG-WT short-circuit current under symmetrical fault is introduced. The analysis will consider the configuration of the converter controller and the system's nonlinearities, and approximations will be made, which can be justified by the fact that it provides simple and useful expressions of the short-circuit current components.

5.1 LSC Symmetrical Fault Response Analysis

Rewriting the voltage equation of the LSC converter in a fixed reference frame yields[6]:

$$\underline{v}_{\mathrm{LSC}}^{\angle 0} = \underline{v}_{\mathrm{G}}^{\angle 0} + (r_{\mathrm{LSC}} + sl_{\mathrm{LSC}}) \cdot \underline{i}_{\mathrm{LSC}}^{\angle 0} \qquad (5.1)$$

[6] The subscript "1" referring to the sequence component is omitted for simplicity

Rearranging eq. (5.1) will result in the LSC current transfer function:

$$\underline{i}_{\mathrm{LSC}}^{\angle 0}=\frac{\underline{v}_{\mathrm{LSC}}^{\angle 0}-\underline{v}_{\mathrm{G}}^{\angle 0}}{r_{\mathrm{LSC}}+sl_{\mathrm{LSC}}}=G_{\mathrm{LSC}}(s)\cdot\left(\underline{v}_{\mathrm{LSC}}^{\angle 0}-\underline{v}_{\mathrm{G}}^{\angle 0}\right) \tag{5.2}$$

The response of the LSC current to step change in the grid voltage ($\Delta\underline{v}_{\mathrm{G}}^{\angle 0}/s$), which leads consequently to a step change in the LSC voltage ($\Delta\underline{v}_{\mathrm{LSC}}^{\angle 0}/s$), according to eq. (5.2) in the time domain is given by:

$$\underline{i}_{\mathrm{LSC}}^{\angle 0}(t)=\frac{\Delta\underline{v}_{\mathrm{LSC}}^{\angle 0}-\Delta\underline{v}_{\mathrm{G}}^{\angle 0}}{r_{\mathrm{LSC}}+\mathrm{j}\omega_0 l_{\mathrm{LSC}}}e^{-\frac{t}{\tau_{\mathrm{LSC}}}}+\underline{i}_{\mathrm{LSC,ss}}^{\angle 0} \tag{5.3}$$

where $\tau_{\mathrm{LSC}}=l_{\mathrm{LSC}}/r_{\mathrm{LSC}}$ is the choke time constant and $\underline{i}_{\mathrm{LSC,ss}}^{\angle 0}$ is the LSC steady-state fault current. The short-circuit current of the LSC according to eq. (5.3) consists of a dc decaying transient component, whose magnitude is dependent on the change in the grid and the LSC voltage and the value of the LSC choke. It decays with the choke time constant. Since the change in the grid voltage is determined by the fault location, the change in the LSC voltage and the value of the steady-state fault current is dictated by the controller. Therefore, the controller equation should be inserted into eq. (5.3) for a full analysis of the LSC fault current.

Fault Response of the LSC Current with a Feed-Forward Decoupled Control

Considering the inner-current control loop of the LSC the transfer function of the current is described by eq. (4.31). For the sake of the dynamic analysis the transfer function representing the converter switching in eq. (4.30) will be replaced by a first-order Padé approximation [93] as follows:

$$\frac{-s\tau_{\mathrm{dt}}\left(2+\mathrm{j}\omega_0\tau_{\mathrm{dt}}\right)+2\left(2+\mathrm{j}\omega_0\tau_{\mathrm{dt}}\right)}{s\tau_{\mathrm{dt}}\left(2-\mathrm{j}\omega_0\tau_{\mathrm{dt}}\right)+2\left(2-\mathrm{j}\omega_0\tau_{\mathrm{dt}}\right)} \tag{5.4}$$

The characteristic polynomial of the LSC current transfer function is of the fifth order. According to Galois' Theory [94] some of the quantic equations can be solved in radicals. However, to date there is no general formula that could be applied. Although some methods have been proposed for solving the solvable quantic in [95] and [96], the resultant expressions would be very complex and impractical.

Taking into consideration that the time constants τ_{dt} and $\tau_{\mathrm{meas}}=1/1.1\omega_{\mathrm{c}}$ are in the range of hundreds μsec, while the choke and PI-controller time constants are in the range of tens *m*sec, the transfer functions $G_{\mathrm{dt}}^{*}(s)$ and $G_{\mathrm{meas}}^{*}(s)$ can be neglected by replacing them with the static

gain of one without loss of accuracy. The negligence will result in a full rejection of the disturbing quantity $\Delta\underline{v}_{\mathrm{G}}^{\angle 0}$ and to a reduced order transfer function of the current given by:

$$\underline{i}_{\mathrm{LSC}}^{\angle 0} = \frac{(s - \mathrm{j}\omega_0)(\frac{1}{\tau_{\mathrm{kp}}} + \mathrm{j}\omega_0) + \frac{1}{\tau_{\mathrm{ki}}}}{s^2 + s(\frac{1}{\tau_{\mathrm{kp}}} - \mathrm{j}\omega_0) + \frac{1}{\tau_{\mathrm{ki}}} - \mathrm{j}\frac{\omega_0}{\tau_{\mathrm{kp}}}} \underline{i}_{\mathrm{LSC,ref}}^{\angle 0} \tag{5.5}$$

where $\tau_{\mathrm{kp}} = \dfrac{l_{\mathrm{LSC}}}{r_{\mathrm{LSC}} + k_{\mathrm{P}}}$, $\tau_{\mathrm{ki}} = \dfrac{l_{\mathrm{LSC}}}{k_{\mathrm{I}}}$ and $k_{\mathrm{I}} = \dfrac{k_{\mathrm{P}}}{\tau_{\mathrm{I}}}$.

Figure 5-1 shows the current component resultant from a step change in the grid voltage, while Figure 5-2 shows the difference between the full short-circuit current response and the short-circuit current response neglecting both $G_{\mathrm{dt}}^{*}(s)$ and $G_{\mathrm{meas}}^{*}(s)$ referred to by an approximate. It can be concluded from both figures that negligence is justified and does not yield a significant difference.

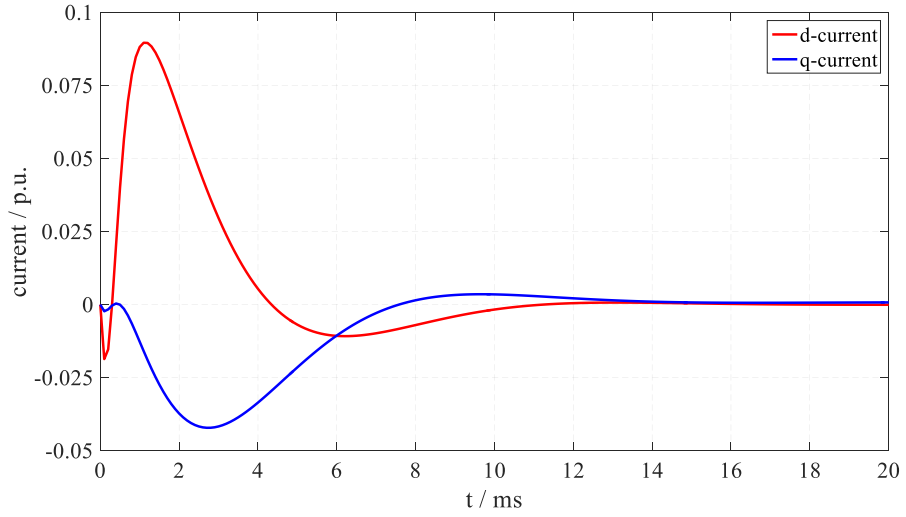

Figure 5-1 LSC current response to step change in the grid voltage

According to eq. (5.5) any step change in the reference current $\Delta\underline{i}_{\mathrm{LSC,ref}}^{\angle 0}$ will result in two transient current decaying components. These currents decay with time constants and frequencies found by solving the general quadratic formula of the characteristic polynomial [97], which results in the following expressions:

$$-\frac{1}{\tau_{\mathrm{DC}}} + \mathrm{j}\omega_{\mathrm{DC}} = -\frac{1}{2\tau_{\mathrm{kp}}} + \mathrm{j}\frac{\omega_0}{2} - \sqrt{(\frac{1}{2\tau_{\mathrm{kp}}} + \mathrm{j}\frac{\omega_0}{2})^2 - \frac{1}{\tau_{\mathrm{ki}}} + \mathrm{j}\frac{\omega_0}{\tau_{\mathrm{kp}}}} \tag{5.6}$$

$$-\frac{1}{\tau_{\mathrm{AC}}} + \mathrm{j}\omega_{\mathrm{AC}} = -\frac{1}{2\tau_{\mathrm{kp}}} + \mathrm{j}\frac{\omega_0}{2} + \sqrt{(\frac{1}{2\tau_{\mathrm{kp}}} + \mathrm{j}\frac{\omega_0}{2})^2 - \frac{1}{\tau_{\mathrm{ki}}} + \mathrm{j}\frac{\omega_0}{\tau_{\mathrm{kp}}}} \tag{5.7}$$

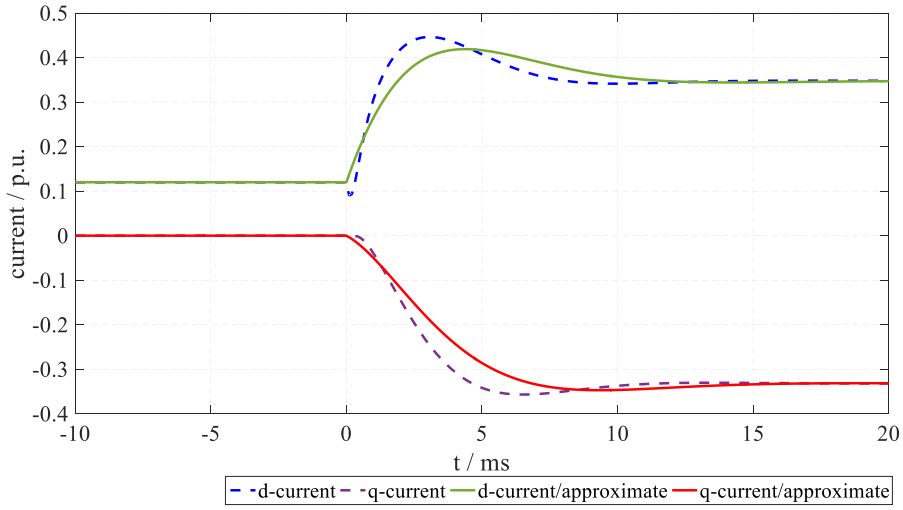

Figure 5-2 Influence of measurement delays and converter switching on the LSC short-circuit current

Usually the PI-controller is tuned empirically. However, the circuit parameters of the LSC are well known and the PI-controller can only compensate for a small error. Therefore, the PI-controller parameters can be tuned according to the following rules without violating the maximum modulation index:

$$k_{\mathrm{P}} \geq x_{\mathrm{LSC}},\ \tau_{\mathrm{I}} \geq \frac{l_{\mathrm{LSC}}}{r_{\mathrm{LSC}}} \tag{5.8}$$

If the PI-controller parameters were tuned according to eq. (5.8), the resultant system would have a damping ratio appreciably greater than unity $\zeta > 1$, yielding an overdamped system [87]. This means that one of the system poles would lie far away from the origin yielding a very fast decaying transient current. The other pole would lie very close to the system's zero yielding very small magnitudes. Figure 5-3 shows the resultant transient current components to the step change in the reference current, where it is clear that the AC transient current has a negligible magnitude and the DC transient current decayed in one cycle.

Based on this conclusion the LSC short-circuit current can be described in time domain by:

$$\underline{i}_{\mathrm{LSC}}^{\angle 0}(t) \approx \Delta \underline{i}_{\mathrm{LSC,ref}}^{\angle 0} e^{-\left(\frac{1}{\tau_{\mathrm{DC}}} - \mathrm{j}\omega_{\mathrm{DC}}\right)t} + \underline{i}_{\mathrm{LSC,ref}}^{\angle 0} \tag{5.9}$$

and the DC time constant and the associated frequency can be further reduced to:

$$-\frac{1}{\tau_{\mathrm{DC}}} + \mathrm{j}\omega_{\mathrm{DC}} \approx -\frac{1}{\tau_{\mathrm{kp}}} + \mathrm{j}\frac{1}{\omega_0 \tau_{\mathrm{ki}}} \tag{5.10}$$

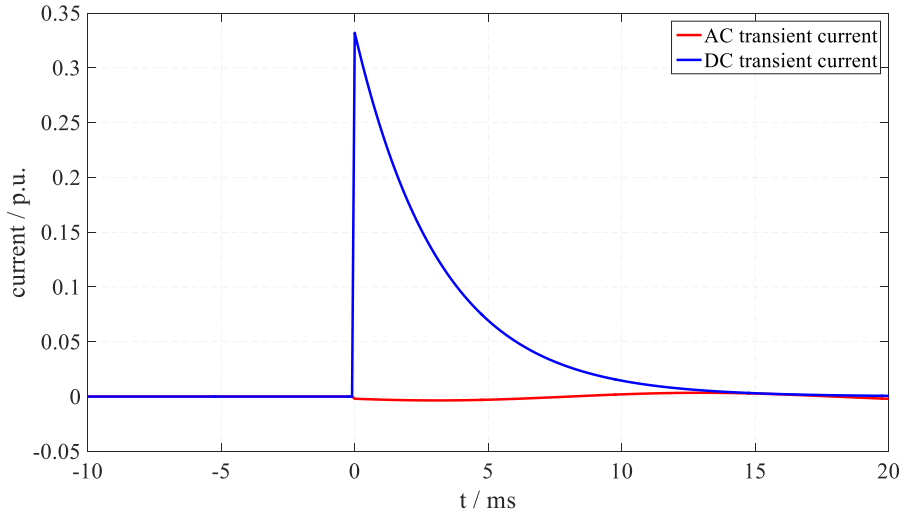

Figure 5-3 LSC transient current components

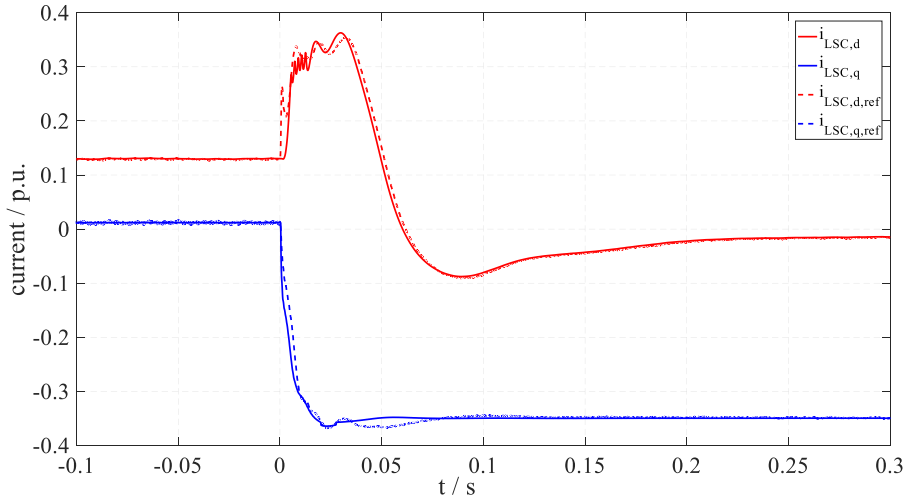

Figure 5-4 LSC current tracking behavior during 80% voltage drop

In a real controller environment there would be no step jumps in the reference currents, especially in the d-component, because the reference current is dependent on the dynamic behavior of the DFIG and the DC circuit as well as the measurement delays introduced to the grid voltage that determines the required reactive power provision. Accordingly, it may be assumed that the LSC output current immediately tracks the reference current and that the LSC behaves like a current source with the reference current as a set-point. Figure 5-4 shows the tracking behavior of the LSC output current to the reference current during a voltage drop of 80%, where it becomes obvious that the LSC current tracks the reference current with small deviations that can be neglected.

5.2 DFIG Symmetrical Fault Response

The characteristic polynomial of the DFIG stator current transfer function described in eq. (3.27) is of the second order. Hence, the roots are found by solving the general quadratic formula of the characteristic polynomial that yields the following relations:

$$\frac{1}{\tau_{\mathrm{DC}}}+\mathrm{j}\omega_{\mathrm{DC}}=\frac{1}{2}\left(\frac{1}{\sigma\tau_{\mathrm{S}}}+\frac{1}{\sigma\tau_{\mathrm{R}}}-\mathrm{j}\omega_{\mathrm{R}}\right)-\frac{1}{2}\sqrt{\left(\frac{1}{\sigma\tau_{\mathrm{S}}}+\frac{1}{\sigma\tau_{\mathrm{R}}}-\mathrm{j}\omega_{\mathrm{R}}\right)^{2}-\frac{4}{\sigma\tau_{\mathrm{S}}\tau_{\mathrm{R}}}+\mathrm{j}\omega_{\mathrm{R}}\frac{4}{\sigma\tau_{\mathrm{S}}}} \tag{5.12}$$

$$\frac{1}{\tau_{\mathrm{AC}}}+\mathrm{j}\omega_{\mathrm{AC}}=\frac{1}{2}\left(\frac{1}{\sigma\tau_{\mathrm{S}}}+\frac{1}{\sigma\tau_{\mathrm{R}}}-\mathrm{j}\omega_{\mathrm{R}}\right)+\frac{1}{2}\sqrt{\left(\frac{1}{\sigma\tau_{\mathrm{S}}}+\frac{1}{\sigma\tau_{\mathrm{R}}}-\mathrm{j}\omega_{\mathrm{R}}\right)^{2}-\frac{4}{\sigma\tau_{\mathrm{S}}\tau_{\mathrm{R}}}+\mathrm{j}\omega_{\mathrm{R}}\frac{4}{\sigma\tau_{\mathrm{S}}}} \tag{5.13}$$

with the stator and rotor time constants:

$$\tau_{\mathrm{S}}=\frac{l_{\mathrm{S}}}{r_{\mathrm{S}}} \tag{5.14}$$

$$\tau_{\mathrm{R}}=\frac{l_{\mathrm{R}}}{r_{\mathrm{R}}} \tag{5.15}$$

The expressions of the time constants and eigen frequencies given in eq. (5.12) and (5.13) are too complex to proceed with, and a more relaxed expression would be beneficial to drive the dynamic response of the stator current with sufficient accuracy. If the dynamic response of the DFIG is separated into fast and slow responses as described in Chapter 3, the transfer functions of the stator current for both slow and fast responses can be expressed as:

$$\underline{i}_{\mathrm{S,DC}}^{\angle 0}=\frac{-\left(r_{\mathrm{R}}-\mathrm{j}\omega_{\mathrm{R}}l_{\mathrm{R}}\right)\underline{v}_{\mathrm{S}}^{\angle 0}+sl_{\mathrm{M}}\underline{v}_{\mathrm{R}}^{\angle 0}}{sl_{\mathrm{S}}\left(r_{\mathrm{R}}-\mathrm{j}\omega_{\mathrm{R}}\sigma l_{\mathrm{R}}\right)+r_{\mathrm{S}}\left(r_{\mathrm{R}}-\mathrm{j}\omega_{\mathrm{R}}l_{\mathrm{R}}\right)} \tag{5.16}$$

$$\underline{i}_{\mathrm{S,AC}}^{\angle 0}=\frac{-\left(r_{\mathrm{R}}+\left(s-\mathrm{j}\omega_{\mathrm{R}}\right)l_{\mathrm{R}}\right)\underline{v}_{\mathrm{S}}^{\angle 0}+\mathrm{j}\omega_{0}l_{\mathrm{M}}\underline{v}_{\mathrm{R}}^{\angle 0}}{sl_{\mathrm{R}}\left(r_{\mathrm{S}}+\mathrm{j}\omega_{0}\sigma l_{\mathrm{S}}\right)-\mathrm{j}\omega_{\mathrm{R}}l_{\mathrm{R}}\left(r_{\mathrm{S}}+\mathrm{j}\omega_{0}\sigma l_{\mathrm{S}}\right)+r_{\mathrm{R}}\left(r_{\mathrm{S}}+\mathrm{j}\omega_{0}l_{\mathrm{S}}\right)} \tag{5.17}$$

From the equations above the time constants and eigen frequencies can be simplified to:

$$\frac{1}{\tau_{\mathrm{DC}}}+\mathrm{j}\omega_{\mathrm{DC}}\approx\frac{r_{\mathrm{S}}\left(r_{\mathrm{R}}-\mathrm{j}\omega_{\mathrm{R}}l_{\mathrm{R}}\right)}{l_{\mathrm{S}}\left(r_{\mathrm{R}}-\mathrm{j}\omega_{\mathrm{R}}\sigma l_{\mathrm{R}}\right)} \tag{5.18}$$

$$\frac{1}{\tau_{\mathrm{AC}}}+\mathrm{j}\omega_{\mathrm{AC}}\approx\frac{r_{\mathrm{R}}\left(r_{\mathrm{S}}+\mathrm{j}\omega_{0}l_{\mathrm{S}}\right)}{l_{\mathrm{R}}\left(r_{\mathrm{S}}+\mathrm{j}\omega_{0}\sigma l_{\mathrm{S}}\right)}-\mathrm{j}\omega_{\mathrm{R}} \tag{5.19}$$

Consequently, the different current components forming the total DFIG stator short-circuit current are expressed as:

The DC transient current is:

$$\Delta \underline{i}_{\mathrm{S,DC}}^{\angle 0}(t) = \underline{y}_{\mathrm{S,DC}} \left(\Delta \underline{v}_{\mathrm{S}}^{\angle 0} + \frac{l_{\mathrm{M}} r_{\mathrm{S}}}{l_{\mathrm{S}} \left(r_{\mathrm{R}} - \mathrm{j}\omega_{\mathrm{R}} \sigma l_{\mathrm{R}} \right)} \Delta \underline{v}_{\mathrm{R}}^{\angle 0} \right) e^{-\left(\frac{1}{\tau_{\mathrm{DC}}} + \mathrm{j}\omega_{\mathrm{DC}} \right) t} \tag{5.20}$$

where,

$$\underline{y}_{\mathrm{S,DC}} = \frac{\left(r_{\mathrm{R}} - \mathrm{j}\omega_{\mathrm{R}} l_{\mathrm{R}} \right)}{r_{\mathrm{S}} \left(r_{\mathrm{R}} - \mathrm{j}\omega_{\mathrm{R}} l_{\mathrm{R}} \right) + \mathrm{j}\omega_{\mathrm{S}} l_{\mathrm{S}} \left(r_{\mathrm{R}} - \mathrm{j}\omega_{\mathrm{R}} \sigma l_{\mathrm{R}} \right)} \tag{5.21}$$

The AC transient current is:

$$\Delta \underline{i}_{\mathrm{S,AC}}^{\angle 0}(t) = \underline{y}_{\mathrm{S,AC}} \left(\Delta \underline{v}_{\mathrm{S}}^{\angle 0} - \frac{\mathrm{j}\omega_{\mathrm{S}} l_{\mathrm{M}} \left(r_{\mathrm{S}} + \mathrm{j}\omega_{\mathrm{S}} \sigma l_{\mathrm{S}} \right)}{\mathrm{j}\omega_{\mathrm{S}} \left(\sigma - 1 \right) r_{\mathrm{R}} l_{\mathrm{S}}} \Delta \underline{v}_{\mathrm{R}}^{\angle 0} \right) e^{-\left(\frac{1}{\tau_{\mathrm{AC}}} + \mathrm{j}\omega_{\mathrm{AC}} \right) t} \tag{5.22}$$

where,

$$\underline{y}_{\mathrm{S,AC}} = \frac{r_{\mathrm{R}} \left(1 - \dfrac{\left(r_{\mathrm{S}} + \mathrm{j}\omega_{\mathrm{S}} l_{\mathrm{S}} \right)}{\left(r_{\mathrm{S}} + \mathrm{j}\omega_{\mathrm{S}} \sigma l_{\mathrm{S}} \right)} \right)}{r_{\mathrm{R}} \left(r_{\mathrm{S}} + \mathrm{j}\omega_{\mathrm{S}} l_{\mathrm{S}} \right) + \mathrm{j}\left(\omega_{\mathrm{S}} - \omega_{\mathrm{R}} \right) l_{\mathrm{R}} \left(r_{\mathrm{S}} + \mathrm{j}\omega_{\mathrm{S}} \sigma l_{\mathrm{S}} \right)} \tag{5.23}$$

Finally, the steady-state current is:

$$\underline{i}_{\mathrm{S,SS}}^{\angle 0} = \frac{-\left(r_{\mathrm{R}} + \mathrm{j}\left(\omega_{\mathrm{S}} - \omega_{\mathrm{R}} \right) l_{\mathrm{R}} \right) \underline{v}_{\mathrm{S}}^{\angle 0} + \mathrm{j}\omega_{\mathrm{S}} l_{\mathrm{M}} \underline{v}_{\mathrm{R}}^{\angle 0}}{r_{\mathrm{R}} \left(r_{\mathrm{S}} + \mathrm{j}\omega_{\mathrm{S}} l_{\mathrm{S}} \right) + \mathrm{j}\left(\omega_{\mathrm{S}} - \omega_{\mathrm{R}} \right) l_{\mathrm{R}} \left(r_{\mathrm{S}} + \mathrm{j}\omega_{\mathrm{S}} \sigma l_{\mathrm{S}} \right)} \tag{5.24}$$

Finally, the DFIG stator short-circuit space vector current is given by:

$$\underline{i}_{\mathrm{S}}^{\angle 0}(t) = \Delta \underline{i}_{\mathrm{S,DC}}^{\angle 0}(t) + \Delta \underline{i}_{\mathrm{S,AC}}^{\angle 0}(t) + \underline{i}_{\mathrm{S,SS}}^{\angle 0} \tag{5.25}$$

and the phase current will be given by:

$$i_{\mathrm{Sa}}(t) = \Re \left\{ \Delta \underline{i}_{\mathrm{S,DC}}^{\angle 0}(t) + \Delta \underline{i}_{\mathrm{S,AC}}^{\angle 0}(t) + \underline{i}_{\mathrm{S,SS}}^{\angle 0} \right\} \tag{5.26}$$

Figure 5-5 shows the actual behavior and the approximated behavior of the natural fault response of the DFIG stator current. There is a strong resemblance between both behaviors, which proves the validity and accuracy of the derived approximated expressions given in eq. (5.18) to (5.24).

5.2.1 Fault Response of the DFIG with Feed-Forward Decoupled Control

The closed-loop decoupled control of the DFIG was discussed in detail in the previous chapter. It can be deduced from the transfer function of the stator current in eq. (4.55), replacing the dead-time transfer function with the first order Padé approximation for the LSC. The characteristic polynomial is of the 8$^{\mathrm{th}}$ order. It is already known that the quartic equation is the highest degree polynomial that can be solved in radicals. Therefore, the roots of the

characteristic polynomial can be only solved by numerical methods, for instance the Newton-Raphson method [98].

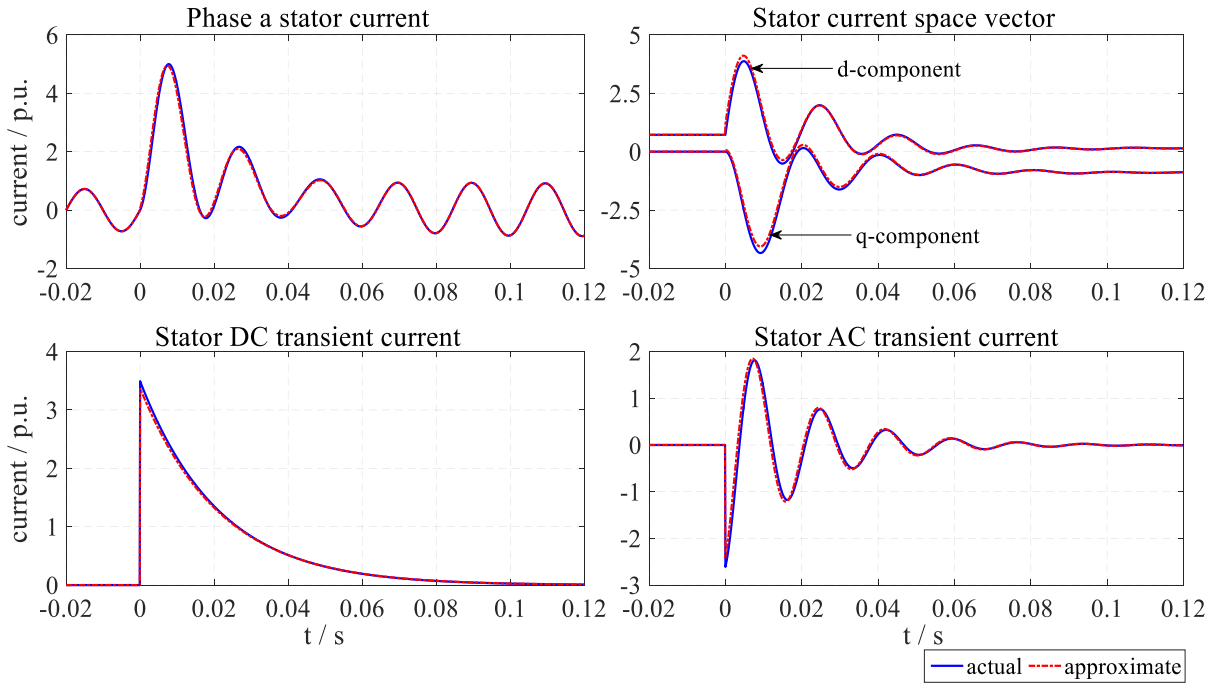

Figure 5-5 Natural fault response of the DFIG stator current

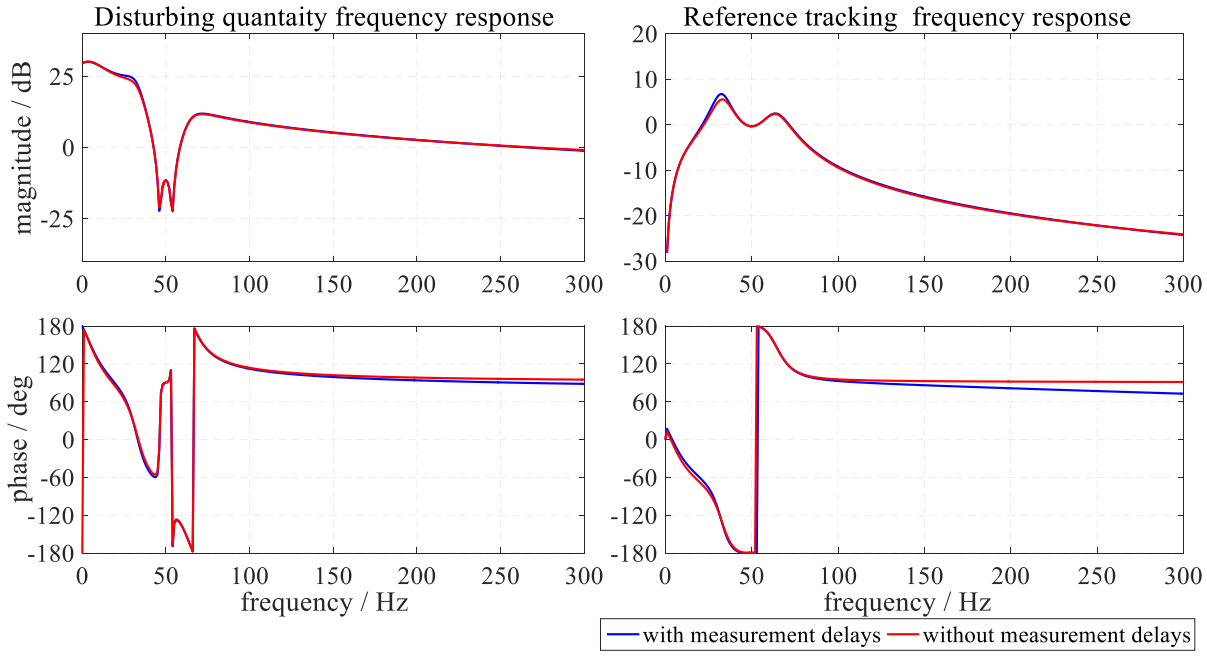

Figure 5-6 Influence of measurement delays exclusion on DFIG stator current frequency response

The multi megawatt scale DFIG is usually characterized by a natural time response that is in the range of tens *m*sec, which is much larger than the time delays introduced by the measurement filter and the converter sampling. Figure 5-6 shows the frequency response of the DFIG stator current transfer function with and without considering the transfer functions $G_{dt}^{*}(s)$

and $\underline{G}^{*}_{\mathrm{meas}}(s)$, where there is a small gain difference at the lower eigen frequency and a remarkable phase difference in the response to the reference tracking beyond 150 Hz. This indicates that excluding $\underline{G}^{*}_{\mathrm{dt}}(s)$ and $\underline{G}^{*}_{\mathrm{meas}}(s)$ will not have a significant influence on the dynamic response. This fact can be observed in Figure 5-7 that shows the short-circuit stator current with and without considering the measurement delays, where the difference between the two responses is insignificant.

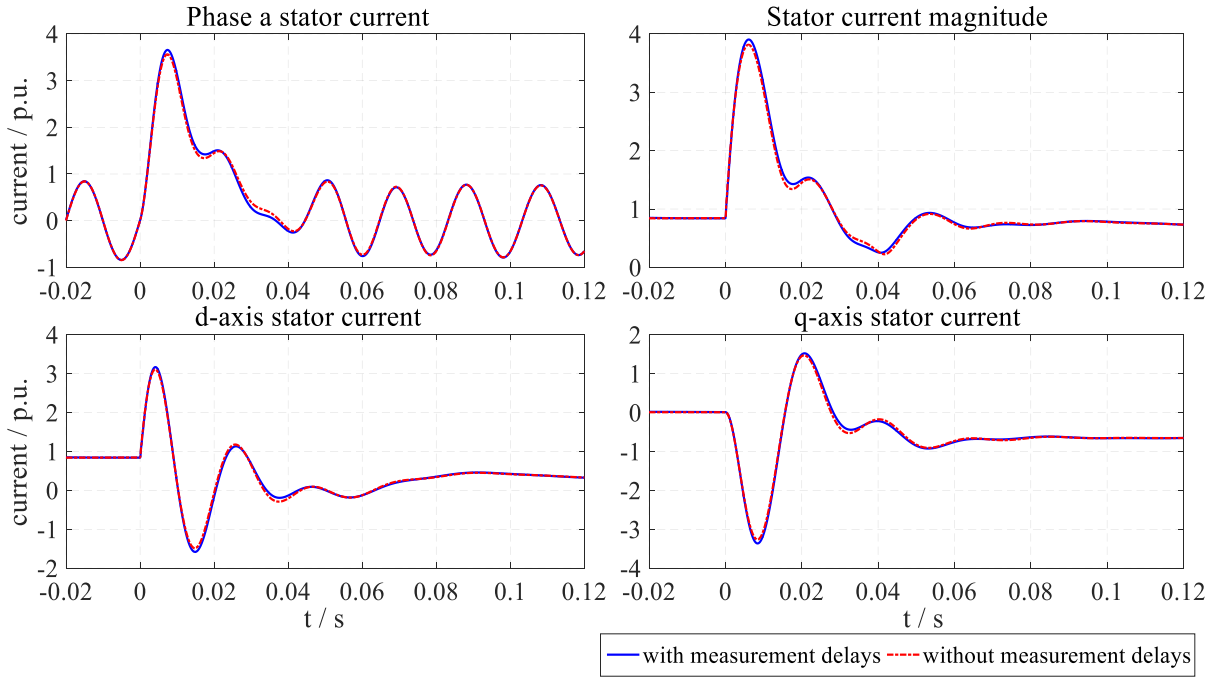

Figure 5-7 Influence of measurement delays exclusion on DFIG stator short-circuit current

By excluding both $G^{*}_{\mathrm{dt}}(s)$ and $G^{*}_{\mathrm{meas}}(s)$ the transfer function of the DFIG stator current is reduced to a third-order transfer function given by:

$$\underline{i}_{\mathrm{S}}^{\angle 0} = \frac{\left(b_2 s^2 + \underline{b}_1 s + \underline{b}_0\right)\underline{v}_{\mathrm{S}}^{\angle 0} + s l_{\mathrm{M}}\left(k_{\mathrm{P}}\left(s - \mathrm{j}\omega_{\mathrm{S}}\right) + k_{\mathrm{I}}\right)\underline{i}_{\mathrm{R,ref}}^{\angle 0}}{a_3 s^3 + \underline{a}_2 s^2 + \underline{a}_1 s + \underline{a}_0} \tag{5.27}$$

where

$$a_3 = -\sigma l_{\mathrm{S}} l_{\mathrm{R}} \tag{5.28}$$

$$\underline{a}_2 = -r_{\mathrm{S}} l_{\mathrm{R}} - k_{\mathrm{P}} l_{\mathrm{S}} + \mathrm{j}\sigma l_{\mathrm{S}} l_{\mathrm{R}}\left(\omega_{\mathrm{S}} + \omega_{\mathrm{R}} + \mathrm{j}s_{\mathrm{G}}\omega_{\mathrm{S}}\right) \tag{5.29}$$

$$\underline{a}_1 = \omega_{\mathrm{S}}^2 \sigma l_{\mathrm{S}} l_{\mathrm{R}} - k_{\mathrm{P}}\left(r_{\mathrm{S}} - \mathrm{j}\omega_{\mathrm{S}} l_{\mathrm{S}}\right) - k_{\mathrm{I}} l_{\mathrm{S}} + \mathrm{j}r_{\mathrm{S}} l_{\mathrm{R}}\left(\omega_{\mathrm{S}} + \omega_{\mathrm{R}} + \sigma s_{\mathrm{G}}\omega_{\mathrm{S}}\right) \tag{5.30}$$

$$\underline{a}_0 = r_{\mathrm{S}}\left(\mathrm{j}\omega_{\mathrm{S}}\left(k_{\mathrm{P}} - l_{\mathrm{R}}\left(\omega_{\mathrm{R}} + \sigma\omega_{\mathrm{S}} s_{\mathrm{G}}\right)\right) - k_{\mathrm{I}}\right) \tag{5.31}$$

$$b_2 = s_{\mathrm{G}}\frac{l_{\mathrm{M}}^2}{l_{\mathrm{S}}} + l_{\mathrm{R}} \tag{5.32}$$

$$\underline{b}_1 = -\omega_S s_G \frac{l_M^2}{l_S} - k_P - \mathrm{j} l_R \left(\omega_S \left(1+\sigma s_G\right) + \omega_R\right) \tag{5.33}$$

$$\underline{b}_0 = k_I - \omega_S l_R \left(\omega_R + s_G \omega_S \sigma\right) + \mathrm{j}\omega_S k_P \tag{5.34}$$

According to eq. (5.27) the short-circuit current of the DFIG stator has three transient components, whose magnitudes, decaying time constants and frequencies are dependent on machine electrical parameters, controller parameters and steady-state current. Figure 5.8 shows the different current components of the DFIG stator short-circuit current derived from the simulation results and from eq. (5.27).

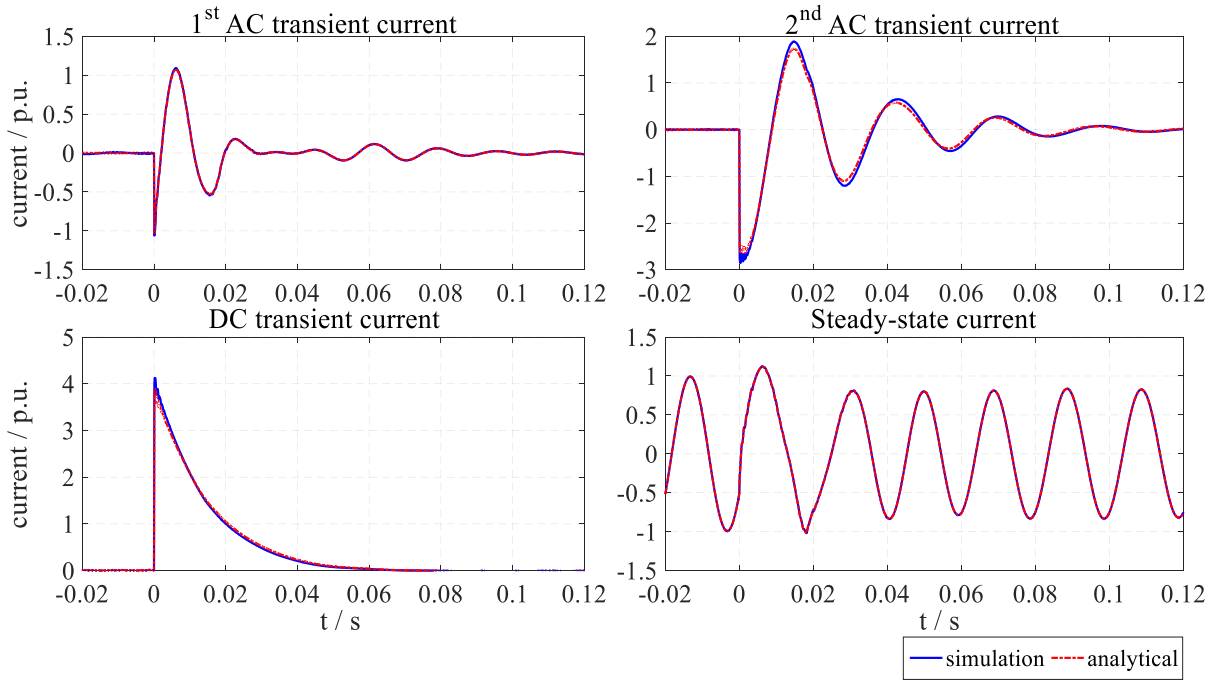

Figure 5-8 DFIG stator short-circuit current components

5.2.2 Estimation of Short-Circuit Parameters

The time constants and eigen frequencies of the different short-circuit current components can be found by finding the roots through solving the general cubic formula of the characteristic polynomial in eq. (5.27) as follows [97]:

$$-\frac{1}{\tau_{DC}} + \mathrm{j}\omega_{DC} = -2\sqrt{\underline{Q}}\cos\left(\frac{\cos^{-1}\left(\underline{R}\Big/\sqrt{\underline{Q}^3}\right)}{3}\right) - \frac{1}{3\sigma\tau_{kp}} - \frac{\underline{\nu}_S}{3\sigma} - \mathrm{j}\omega_S \tag{5.35}$$

$$-\frac{1}{\tau_{AC1,2}} + \mathrm{j}\omega_{AC1,2} = -2\sqrt{\underline{Q}}\cos\left(\frac{\cos^{-1}\left(\underline{R}\Big/\sqrt{\underline{Q}^3}\right) \pm 2\pi}{3}\right) - \frac{1}{3\sigma\tau_{kp}} - \frac{\underline{\nu}_S}{3\sigma} - \mathrm{j}\omega_S$$

(5.36)

where

$$\underline{Q} = \frac{1}{3\sigma}\left(\frac{1}{\tau_{\mathrm{ki}}} + \frac{\underline{\nu}_{\mathrm{S}}}{\tau_{\mathrm{kp}}}\right)\left(\frac{1}{3\sigma\tau_{\mathrm{kp}}} + \frac{\underline{\nu}_{\mathrm{S}}}{3\sigma} - 1\right) \tag{5.37}$$

$$\underline{R} = \frac{1}{6\sigma}\left(\underline{\nu}_{\mathrm{S}} + \frac{1}{\tau_{\mathrm{kp}}}\right)\left(\frac{1}{9\sigma^2}\left(\underline{\nu}_{\mathrm{S}} + \frac{1}{\tau_{\mathrm{kp}}}\right)^2 - \left(\frac{1}{\tau_{\mathrm{ki}}} + \frac{\underline{\nu}_{\mathrm{S}}}{\tau_{\mathrm{kp}}}\right)\right) + \frac{\underline{\nu}_{\mathrm{S}}}{2\sigma\tau_{\mathrm{ki}}} \tag{5.38}$$

$$\underline{\nu}_{\mathrm{S}} = \frac{1}{\tau_{\mathrm{S}}} + \mathrm{j}\omega_{\mathrm{S}},\ \tau_{\mathrm{kp}} = \frac{l_{\mathrm{R}}}{k_{\mathrm{P}}},\ \tau_{\mathrm{ki}} = \frac{l_{\mathrm{R}}}{k_{\mathrm{I}}} \tag{5.39}$$

Again the expressions in eq. (5.35) and (5.36) are too complex to derive a simple mathematical interpretation of the DFIG fault current. Following the same procedure as before and separating the DFIG dynamic response into fast and slow, with the following assumption for the sake of simplicity:

$$s_{\mathrm{G1}}\frac{l_{\mathrm{M}}}{l_{\mathrm{S}}}\underline{v}_{\mathrm{S}}^{\angle 0} - \mathrm{j}s_{\mathrm{G1}}\omega_{\mathrm{S}}\sigma l_{\mathrm{R}}\underline{i}_{\mathrm{R}}^{\angle 0} \approx -\mathrm{j}\left(\omega_{\mathrm{S}} - \omega_{\mathrm{R}}\right)\underline{\psi}_{\mathrm{R}}^{\angle 0} \tag{5.40}$$

will result in the following transfer functions:

$$\underline{i}_{\mathrm{S,DC}}^{\angle 0} = \frac{-\left(ss_{\mathrm{G}}\frac{l_{\mathrm{M}}^2}{l_{\mathrm{S}}} + \mathrm{j}\omega_{\mathrm{R}}l_{\mathrm{R}} + \mathrm{j}s_{\mathrm{G}}\omega_{\mathrm{S}}\sigma l_{\mathrm{R}} - k_{\mathrm{P}} - \mathrm{j}\frac{k_{\mathrm{I}}}{\omega_{\mathrm{S}}}\right)\underline{v}_{\mathrm{S}}^{\angle 0} + sl_{\mathrm{M}}\left(k_{\mathrm{P}} + \mathrm{j}\frac{k_{\mathrm{I}}}{\omega_{\mathrm{S}}}\right)\underline{i}_{\mathrm{R,Ref}}^{\angle 0}}{-sl_{\mathrm{S}}\left(k_{\mathrm{P}} + \mathrm{j}\frac{k_{\mathrm{I}}}{\omega_{\mathrm{S}}} - \mathrm{j}\omega_0\sigma l_{\mathrm{R}}\right) + r_{\mathrm{S}}\left(\mathrm{j}\omega_{\mathrm{R}}l_{\mathrm{R}} + \mathrm{j}s_{\mathrm{G}}\omega_{\mathrm{S}}\sigma l_{\mathrm{R}} - k_{\mathrm{P}} - \mathrm{j}\frac{k_{\mathrm{I}}}{\omega_{\mathrm{S}}}\right)} \tag{5.41}$$

$$\underline{i}_{\mathrm{S,AC}}^{\angle 0} = \frac{\left(l_{\mathrm{R}}s^2 + \underline{b}_1 s + \underline{b}_0\right)\underline{v}_{\mathrm{S}}^{\angle 0} + \mathrm{j}\omega_0 l_{\mathrm{M}}\left(k_{\mathrm{P}}\left(s - \mathrm{j}\omega_{\mathrm{S}}\right) + k_{\mathrm{I}}\right)\underline{i}_{\mathrm{R,ref}}^{\angle 0}}{\underline{a}_2 s^2 + \underline{a}_1 s + \underline{a}_0} \tag{5.42}$$

where

$$\underline{a}_2 = l_{\mathrm{R}}\left(r_{\mathrm{S}} + \mathrm{j}\omega_{\mathrm{S}}\sigma l_{\mathrm{S}}\right) \tag{5.43}$$

$$\underline{a}_1 = \left(r_{\mathrm{S}} + \omega_{\mathrm{S}}l_{\mathrm{S}}\right)\left(k_{\mathrm{P}} - \mathrm{j}\sigma s_{\mathrm{G}}\omega_{\mathrm{S}}l_{\mathrm{R}}\right) - \mathrm{j}\left(\omega_{\mathrm{S}} + \omega_{\mathrm{R}}\right)\left(r_{\mathrm{S}} + \mathrm{j}\omega_{\mathrm{S}}\sigma l_{\mathrm{S}}\right)l_{\mathrm{R}} \tag{5.44}$$

$$\underline{a}_0 = -\omega_{\mathrm{S}}\omega_{\mathrm{R}}l_{\mathrm{R}}\left(r_{\mathrm{S}} + \mathrm{j}\omega_{\mathrm{S}}\sigma l_{\mathrm{S}}\right) + \left(r_{\mathrm{S}} + \mathrm{j}\omega_{\mathrm{S}}l_{\mathrm{S}}\right)\left(k_{\mathrm{I}} - \mathrm{j}\omega_{\mathrm{S}}\left(k_{\mathrm{P}} - \mathrm{j}s_{\mathrm{G1}}\omega_{\mathrm{S}}\sigma l_{\mathrm{R}}\right)\right) \tag{5.45}$$

$$\underline{b}_1 = k_{\mathrm{P}} - \mathrm{j}\omega_{\mathrm{S}}s_{\mathrm{G}}\left(\frac{l_{\mathrm{M}}^2}{l_{\mathrm{S}}} + \sigma l_{\mathrm{R}}\right) - \mathrm{j}\left(\omega_{\mathrm{S}} + \omega_{\mathrm{R}}\right)l_{\mathrm{R}} \tag{5.46}$$

$$\underline{b}_0 = k_{\mathrm{I}} - \omega_{\mathrm{S}}^2 s_{\mathrm{G}}\left(\frac{l_{\mathrm{M}}^2}{l_{\mathrm{S}}} + \sigma l_{\mathrm{R}}\right) - \mathrm{j}\omega_{\mathrm{S}}\left(k_{\mathrm{P}} - \mathrm{j}\omega_{\mathrm{R}}l_{\mathrm{R}}\right) \tag{5.47}$$

Neglecting σs_{G} will reduce both eq. (5.41) and (5.42) into:

$$\underline{i}_{\mathrm{S,DC}}^{\angle 0}=\frac{-\left(ss_{\mathrm{G}}\frac{l_{\mathrm{M}}^{2}}{l_{\mathrm{S}}}+\mathrm{j}\omega_{\mathrm{R}}l_{\mathrm{R}}-k_{\mathrm{P}}-\mathrm{j}\frac{k_{\mathrm{I}}}{\omega_{\mathrm{S}}}\right)\underline{v}_{\mathrm{S}}^{\angle 0}+sl_{\mathrm{M}}\left(k_{\mathrm{P}}+\mathrm{j}\frac{k_{\mathrm{I}}}{\omega_{\mathrm{S}}}\right)\underline{i}_{\mathrm{R,Ref}}^{\angle 0}}{-sl_{\mathrm{S}}\left(k_{\mathrm{P}}+\mathrm{j}\frac{k_{\mathrm{I}}}{\omega_{\mathrm{S}}}-\mathrm{j}\omega_{\mathrm{S}}\sigma l_{\mathrm{R}}\right)+r_{\mathrm{S}}\left(\mathrm{j}\omega_{\mathrm{R}}l_{\mathrm{R}}-k_{\mathrm{P}}-\mathrm{j}\frac{k_{\mathrm{I}}}{\omega_{\mathrm{S}}}\right)} \tag{5.48}$$

$$\underline{i}_{\mathrm{S,AC}}^{\angle 0}=\frac{-\left(\left(s-\mathrm{j}\omega_{\mathrm{S}}\right)^{2}l_{\mathrm{R}}+\left(k_{\mathrm{P}}\left(s-\mathrm{j}\omega_{\mathrm{S}}\right)+k_{\mathrm{I}}\right)\right)\underline{v}_{\mathrm{S}}^{\angle 0}-\mathrm{j}\omega_{\mathrm{S}}l_{\mathrm{M}}\left(k_{\mathrm{P}}\left(s-\mathrm{j}\omega_{\mathrm{S}}\right)+k_{\mathrm{I}}\right)\underline{i}_{\mathrm{R,Ref}}^{\angle 0}}{\left(\left(s-\mathrm{j}\omega_{\mathrm{S}}\right)^{2}l_{\mathrm{R}}+\left(k_{\mathrm{P}}\left(s-\mathrm{j}\omega_{\mathrm{S}}\right)+k_{\mathrm{I}}\right)\right)\left(r_{\mathrm{S}}+\mathrm{j}\omega_{\mathrm{S}}l_{\mathrm{S}}\right)-\mathrm{j}\omega_{\mathrm{S}}l_{\mathrm{M}}^{2}\left(s-\mathrm{j}\omega_{\mathrm{S}}\right)^{2}} \tag{5.49}$$

Based on eq. (5.48) and (5.49) the time constants and eigen frequency can be simply derived as:

$$\frac{1}{\tau_{\mathrm{DC}}}+\mathrm{j}\omega_{\mathrm{DC}}\approx\frac{r_{\mathrm{S}}\left(-\omega_{\mathrm{S}}\left(k_{\mathrm{P}}-\mathrm{j}\omega_{\mathrm{R}}l_{\mathrm{R}}\right)-\mathrm{j}k_{\mathrm{I}}\right)}{l_{\mathrm{S}}\left(-\omega_{\mathrm{S}}\left(k_{\mathrm{P}}-\mathrm{j}\omega_{\mathrm{S}}\sigma l_{\mathrm{R}}\right)-\mathrm{j}k_{\mathrm{I}}\right)} \tag{5.50}$$

$$-\frac{1}{\tau_{\mathrm{AC1,2}}}+\mathrm{j}\omega_{\mathrm{AC1,2}}\approx-\frac{k_{\mathrm{P}}\left(r_{\mathrm{S}}+\mathrm{j}\omega_{\mathrm{S}}l_{\mathrm{S}}\right)}{2l_{\mathrm{R}}\left(r_{\mathrm{S}}+\mathrm{j}\omega_{\mathrm{S}}\sigma l_{\mathrm{S}}\right)}+\mathrm{j}\omega_{0}\pm\sqrt{\frac{k_{\mathrm{P}}\left(r_{\mathrm{S}}+\mathrm{j}\omega_{\mathrm{S}}l_{\mathrm{S}}\right)}{l_{\mathrm{R}}\left(r_{\mathrm{S}}+\mathrm{j}\omega_{\mathrm{S}}\sigma l_{\mathrm{S}}\right)}\left(\frac{k_{\mathrm{P}}\left(r_{\mathrm{S}}+\mathrm{j}\omega_{\mathrm{S}}l_{\mathrm{S}}\right)}{4l_{\mathrm{R}}\left(r_{\mathrm{S}}+\mathrm{j}\omega_{\mathrm{S}}\sigma l_{\mathrm{S}}\right)}-\frac{k_{\mathrm{I}}}{k_{\mathrm{P}}}\right)} \tag{5.51}$$

From eq. (5.51) two facts can be deduced. Firstly, for the machine to operate in a stable mode the following always need to be satisfied:

$$\Re\left\{\sqrt{\frac{k_{\mathrm{P}}\left(r_{\mathrm{S}}+\mathrm{j}\omega_{\mathrm{S}}l_{\mathrm{S}}\right)}{l_{\mathrm{R}}\left(r_{\mathrm{S}}+\mathrm{j}\omega_{\mathrm{S}}\sigma l_{\mathrm{S}}\right)}\left(\frac{k_{\mathrm{P}}\left(r_{\mathrm{S}}+\mathrm{j}\omega_{\mathrm{S}}l_{\mathrm{S}}\right)}{4l_{\mathrm{R}}\left(r_{\mathrm{S}}+\mathrm{j}\omega_{\mathrm{S}}\sigma l_{\mathrm{S}}\right)}-\frac{k_{\mathrm{I}}}{k_{\mathrm{P}}}\right)}\right\}<\Re\left\{\frac{k_{\mathrm{P}}\left(r_{\mathrm{S}}+\mathrm{j}\omega_{\mathrm{S}}l_{\mathrm{S}}\right)}{2l_{\mathrm{R}}\left(r_{\mathrm{S}}+\mathrm{j}\omega_{\mathrm{S}}\sigma l_{\mathrm{S}}\right)}\right\} \tag{5.52}$$

If this condition is not met, especially for small values of proportional gain, one of the roots will be positive leading to unstable behavior. Therefore, eq. (5.52) can be utilized to tune the PI-controller parameters in the initial design phase. Secondly, for larger machines characterized by $r_{\mathrm{S}}<<x_{\mathrm{S}}$, eq. (5.51) can be further reduced to:

$$-\frac{1}{\tau_{\mathrm{AC1,2}}}+\mathrm{j}\omega_{\mathrm{AC1,2}}\approx-\frac{k_{\mathrm{P}}}{2\sigma l_{\mathrm{R}}}+\mathrm{j}\omega_{\mathrm{S}}\pm\sqrt{\left(\frac{k_{\mathrm{P}}}{2\sigma l_{\mathrm{R}}}\right)^{2}-\frac{k_{\mathrm{I}}}{\sigma l_{\mathrm{R}}}} \tag{5.53}$$

The current components constituting the short-circuit current of the DFIG stator with full decoupled control can now be found as follows:

The DC transient current is:

$$\Delta\underline{i}_{\mathrm{S,DC}}^{\angle 0}\left(t\right)\approx\frac{\Delta\underline{v}_{\mathrm{S}}^{\angle 0}}{\underline{z}'_{\mathrm{S}}}e^{-\left(\frac{1}{\tau_{\mathrm{DC}}}+\mathrm{j}\omega_{\mathrm{DC}}\right)t} \tag{5.54}$$

where $\underline{z}'_{\mathrm{S}}$ is the transient impedance and is given by:

$$\underline{z'}_{\mathrm{S}} \approx r_{\mathrm{S}} + \mathrm{j}\omega_{\mathrm{S}} l_{\mathrm{S}} \frac{\left(k_{\mathrm{P}} + \mathrm{j}\frac{k_{\mathrm{I}}}{\omega_{\mathrm{S}}} - \mathrm{j}\omega_{\mathrm{S}}\sigma l_{\mathrm{R}} \right)}{\left(k_{\mathrm{P}} + \mathrm{j}\frac{k_{\mathrm{I}}}{\omega_{\mathrm{S}}} - \mathrm{j}\omega_{\mathrm{S}} l_{\mathrm{R}} \right)} \tag{5.55}$$

The AC transient currents is:

$$\Delta \underline{i}_{\mathrm{S,AC}}^{\angle 0}(t) \approx \left(\frac{\Delta \underline{v}_{\mathrm{S}}^{\angle 0}}{\underline{z'}_{\mathrm{S}}} - \frac{\mathrm{j}\omega_{\mathrm{S}} l_{\mathrm{M}}}{r_{\mathrm{S}} + \mathrm{j}\omega_{\mathrm{S}} l_{\mathrm{S}}} \Delta \underline{i}_{\mathrm{R,Ref}}^{\angle 0} \right) \left(\underline{\alpha}_{\mathrm{AC1}} e^{-\left(\frac{1}{\tau_{\mathrm{AC1}}} - \mathrm{j}\omega_{\mathrm{AC1}} \right) t} + \underline{\alpha}_{\mathrm{AC2}} e^{-\left(\frac{1}{\tau_{\mathrm{AC2}}} - \mathrm{j}\omega_{\mathrm{AC2}} \right) t} \right) \tag{5.56}$$

where

$$\underline{\alpha}_{\mathrm{AC1}} = \frac{1}{2} - \frac{1}{2\sqrt{1 - 4\dfrac{r_{\mathrm{S}} + \mathrm{j}\omega_{\mathrm{S}}\sigma l_{\mathrm{S}}}{\tau_{\mathrm{PI}}\tau_{\mathrm{kp}}\left(r_{\mathrm{S}} + \mathrm{j}\omega_{\mathrm{S}} l_{\mathrm{S}} \right)}}} \tag{5.57}$$

$$\underline{\alpha}_{\mathrm{AC2}} = \frac{1}{2} + \frac{1}{2\sqrt{1 - 4\dfrac{r_{\mathrm{S}} + \mathrm{j}\omega_{\mathrm{S}}\sigma l_{\mathrm{S}}}{\tau_{\mathrm{PI}}\tau_{\mathrm{kp}}\left(r_{\mathrm{S}} + \mathrm{j}\omega_{\mathrm{S}} l_{\mathrm{S}} \right)}}} \tag{5.58}$$

The steady-state current is:

$$\underline{i}_{\mathrm{S,SS}}^{\angle 0} = \frac{-\underline{v}_{\mathrm{S}}^{\angle 0} + \mathrm{j}\omega_{\mathrm{S}} l_{\mathrm{M}} \underline{i}_{\mathrm{R,Ref}}^{\angle 0}}{r_{\mathrm{S}} + \mathrm{j}\omega_{\mathrm{S}} l_{\mathrm{S}}} \tag{5.59}$$

Finally, the DFIG stator short-circuit space vector current with fully decoupled control is given by:

$$\underline{i}_{\mathrm{S}}^{\angle 0}(t) = \Delta \underline{i}_{\mathrm{S,DC}}^{\angle 0}(t) + \Delta \underline{i}_{\mathrm{S,AC}}^{\angle 0}(t) + \underline{i}_{\mathrm{S,SS}}^{\angle 0} \tag{5.60}$$

and the phase current will be given by:

$$i_{\mathrm{Sa}}(t) = \Re\left\{ \Delta \underline{i}_{\mathrm{S,DC}}^{\angle 0}(t) + \Delta \underline{i}_{\mathrm{S,AC}}^{\angle 0}(t) + \underline{i}_{\mathrm{S,SS}}^{\angle 0} \right\} \tag{5.61}$$

5.2.3 Validation of Short-Circuit Parameters

In order to validate the different expressions derived above describing the short-circuit parameters of the DFIG stator with full decoupled control, the real parameters should be extracted from the simulated signals. According to eq. (5.61) the phase current can be rewritten, assuming the short-circuit was applied at the zero crossing of the stator voltage, as:

$$\begin{aligned} i_{\mathrm{Sa}}(t) = &\left|i_{\mathrm{S,ss}}\right|\sin\left(\omega_{\mathrm{S}}t+\varphi_{\mathrm{S}}\right)+\left|i_{\mathrm{DC}}\right|e^{-\frac{t}{\tau_{\mathrm{DC}}}}\sin\left(\omega_{\mathrm{DC}}t-\varphi_{\mathrm{DC}}\right) \\ &+\left|i_{\mathrm{AC1}}\right|e^{-\frac{t}{\tau_{\mathrm{AC1}}}}\sin\left(\omega_{\mathrm{AC1}}t+\varphi_{\mathrm{AC1}}\right)+\left|i_{\mathrm{AC2}}\right|e^{-\frac{t}{\tau_{\mathrm{AC2}}}}\sin\left(\omega_{\mathrm{AC2}}t+\varphi_{\mathrm{AC2}}\right) \end{aligned} \tag{5.62}$$

where $\varphi_{\mathrm{DC}} = \varphi_{\mathrm{S}} + \varphi_{\mathrm{AC1}} + \varphi_{\mathrm{AC2}}$.

A non-linear optimization can be used to fit eq. (5.62) to the measured data by minimizing the objective function described by:

$$\min_{x} \sum_{i} \left(F\left(x, x\mathrm{data}_i\right) - y_i\right)^2 \tag{5.63}$$

where y_i is the simulated short-circuit current and $F(x)$ is the proposed solution as described by eq. (5.62).

The mean variance mapping optimization (MVMO) is the non-linear optimization method adapted here and throughout the work. The MVMO is a new population-based stochastic optimization technique, where the mapping function used transforms the uniformly distributed random variation into a new one which is characterized by the variance and mean of the n-best population attained so far. It aims to perform prompt and accurate optimization with a minimum amount of objective function evaluations [99].

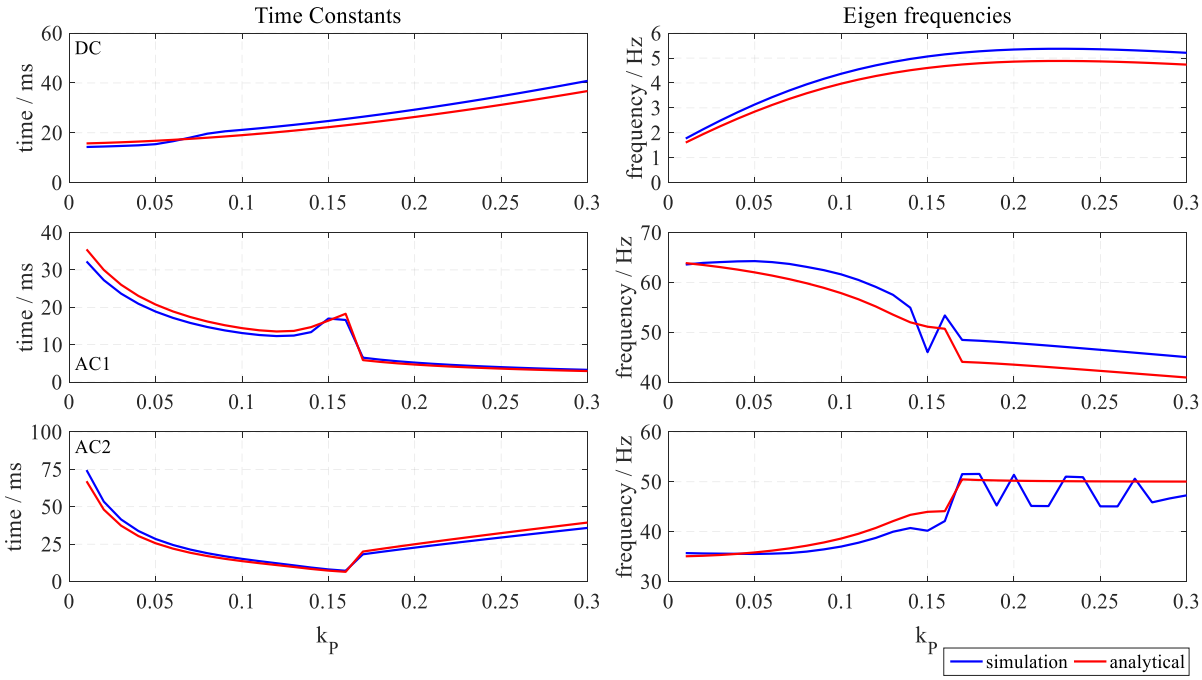

Figure 5-9 Influence of proportional gain on the time constants and eigen frequencies

Figure 5-9 and 5-10 show the influence of the PI-controller's parameters on the time constants and eigen frequencies of the transient currents. A great resemblance between the derived analytical expressions and the extracted values, which prove the validity of the proposed

expressions for time constants and eigen frequencies, can be observed. From these figures it can be concluded that large values of proportional gain do not have a great influence on the eigen frequencies, where for the values $k_P \geq 0.15$ the eigen frequencies tend to be constant. Additionally, the AC time constants are not influenced greatly for high values of integral gain, especially for $k_I \geq 5$.

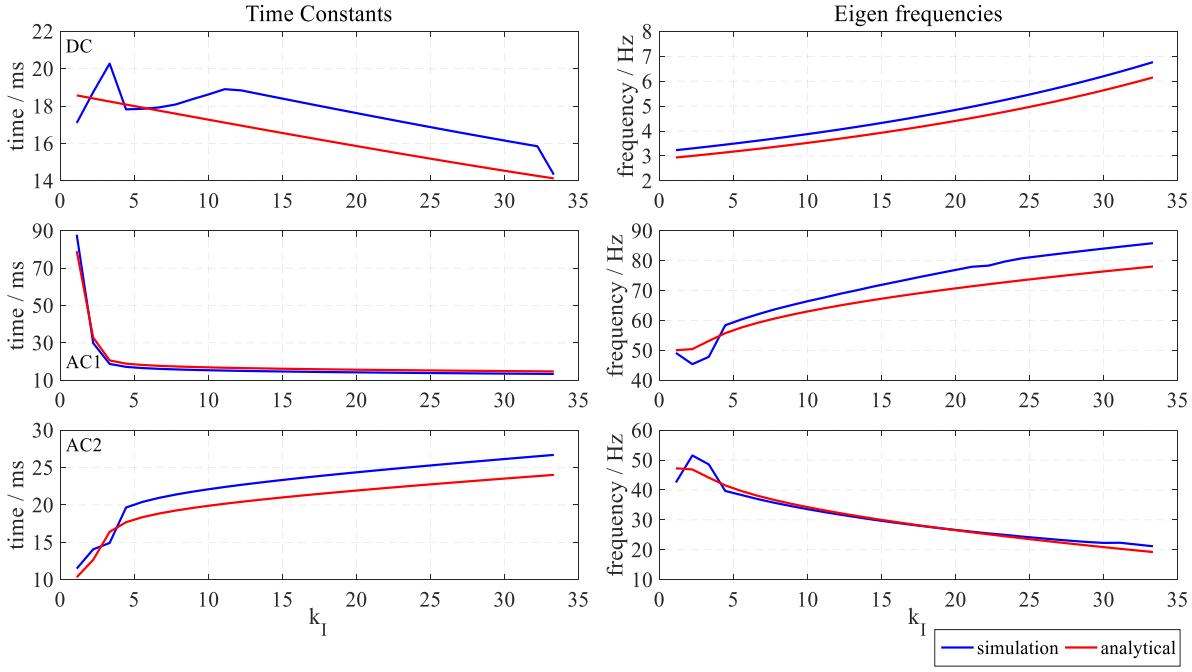

Figure 5-10 Influence of integral gain on the time constants and eigen frequencies

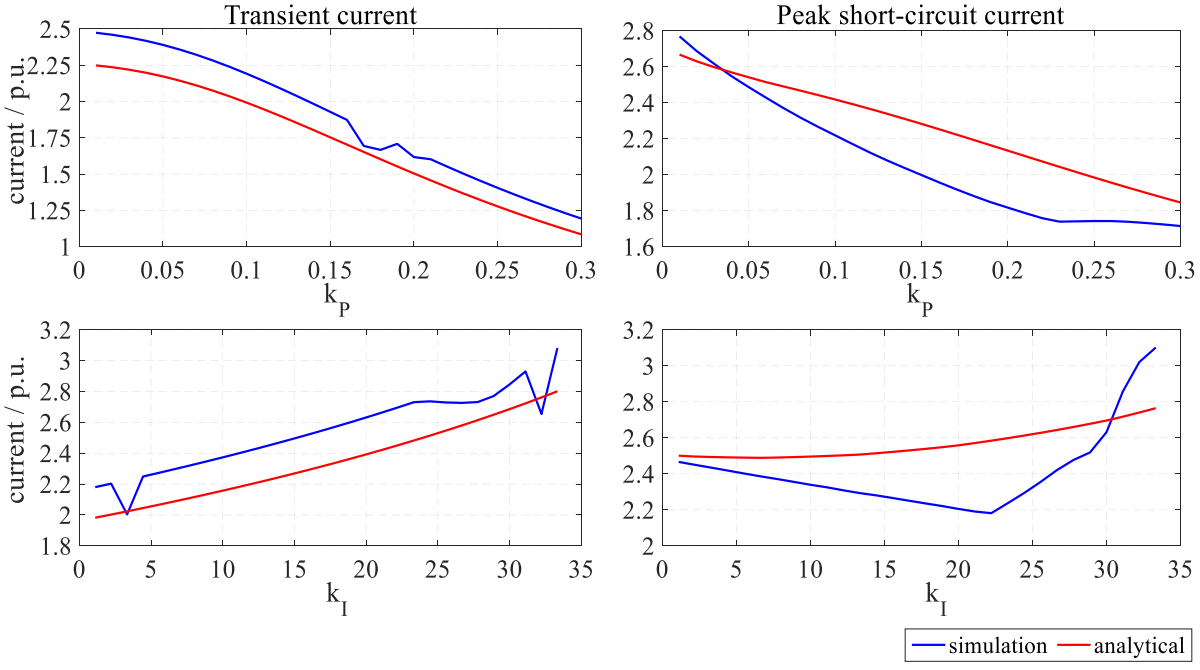

Figure 5-11 Influence of the PI-controller's parameters on the short-circuit current

The influence of the PI-controller's parameters on the short-circuit current is shown in Figure 5-11. Both gains of the PI-controller's parameters greatly influence the transient impedance as described by eq. (5.55). As the proportional gain has a great influence on the AC time constants as shown in Figure 5-9, it will consequently influence the peak value of the short-circuit current as shown. However, the influence of the integral gain on the peak value of the short-circuit current is minor especially in the practical range of values of the integral gain (5-15). This is related to the fact that large values of the integral gain do not greatly influence the time constants as shown in Figure 5-10.

5.2.4 Influence of Magnetic Saturation

During short-circuit periods the value of the main inductance will vary due to the variation of both stator and rotor currents and consequently the magnetizing current. The magnetizing current will tend to decrease during the short-circuit because the DFIG must inject a reactive current into the grid. It will then reduce its active current magnitude as protection of the converter against high currents and to reduce the mechanical stresses on its shaft. Consequently, the main inductance will increase according to the saturation curve shown in Figure 4-42. This fact can be observed in Figure 5-12 which shows the variation of the main inductance for the first cycle after fault initiation.

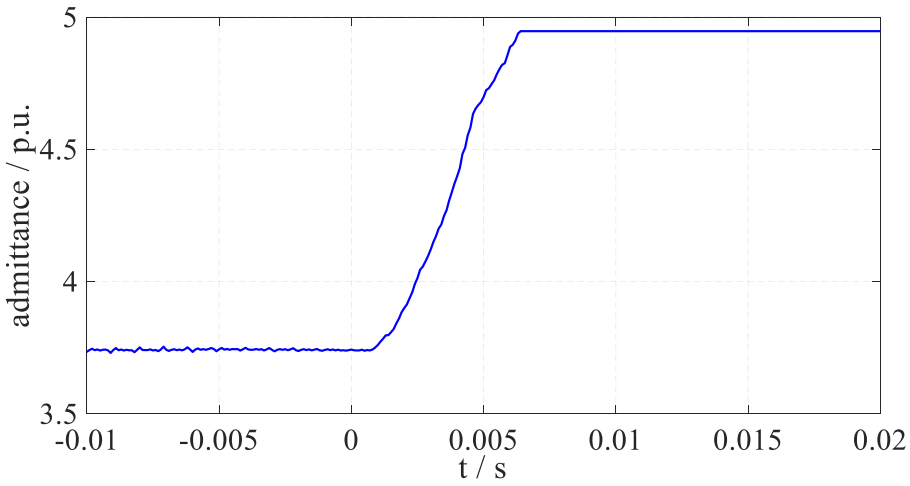

Figure 5-12 Variation of the DFIG's main inductance during short-circuit

It is expected that the fault response of the DFIG will change due to magnetic saturation. However, this is not true because as the machine's inductance increases, it de-saturates due to the reduction of the magnetizing current. The leakage coefficient σ will concurrently decrease as a result of demagnetization. Consequently, the machine's transient impedance as well as the time constants, eigen frequencies and, as a result, the short-circuit current will remain the same.

This fact was also illustrated in the frequency response shown in Figure 4-43, where the magnetic saturation does not have any remarkable influence on the machine's impedances.

5.2.5 Influence of MSC Voltage Limitation

The MSC voltage limitation has a remarkable influence on the fault response of the DFIG because the MSC does not produce the required rotor voltage as demanded by the controller as a result of the voltage limitation.

Analyzing the fault response under such conditions is not an easy task due to the non-linear behavior of the machine because the machine's dynamic state will change whenever a voltage limitation takes place. In order to understand how the machine's dynamic state changes with the voltage limitation, the MVMO is implemented to estimate the equivalent transfer function of the machine during a short-circuit period. This is achieved by minimizing the objective function described in eq. (5.63)[7].

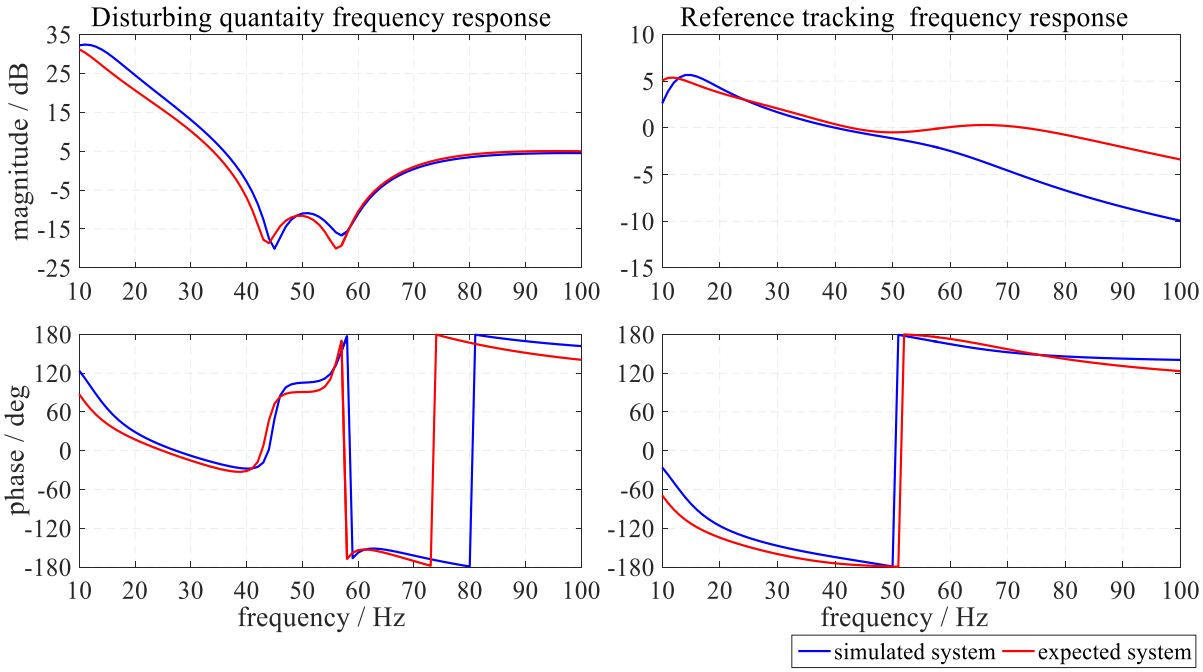

Figure 5-13 Frequency response of the DFIG's stator current during fault considering MSC voltage limitation

The frequency response of the simulated system and the expected system (assuming that the MSC voltage limitation is high enough) are shown in Figure 5-13. In the response to the disturbing quantity the simulated system has a higher gain magnitude than the expected system at low frequencies. Also, it shows a higher rejection gain at the lowest eigen frequency. But a

[7] The proportional gain k_{P} was increased and consequently the integral gain $k_{\mathrm{I}} = k_{\mathrm{P}} / \tau_{\mathrm{I}}$ to generate high rotor voltage

lower rejection gain at the highest eigen frequency. Yet, both responses are almost identical with regard to reference tracking, except for the highest eigen frequency and beyond, where the simulated system retains a higher rejection gain. Furthermore, the gains at the operating frequency for both systems are almost identical, which implies that the voltage limitation only influences the transient components. In addition, both responses almost have the same phase angle at the eigen frequencies while the simulated system has a higher phase angle in the low frequency region.

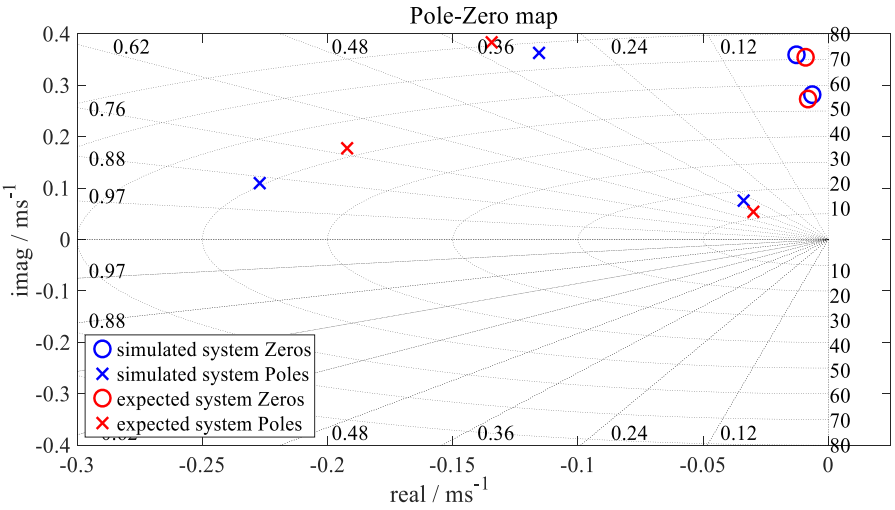

Figure 5-14 Pole-Zero excursion of the DFIG stator current transfer function for the disturbing quantity

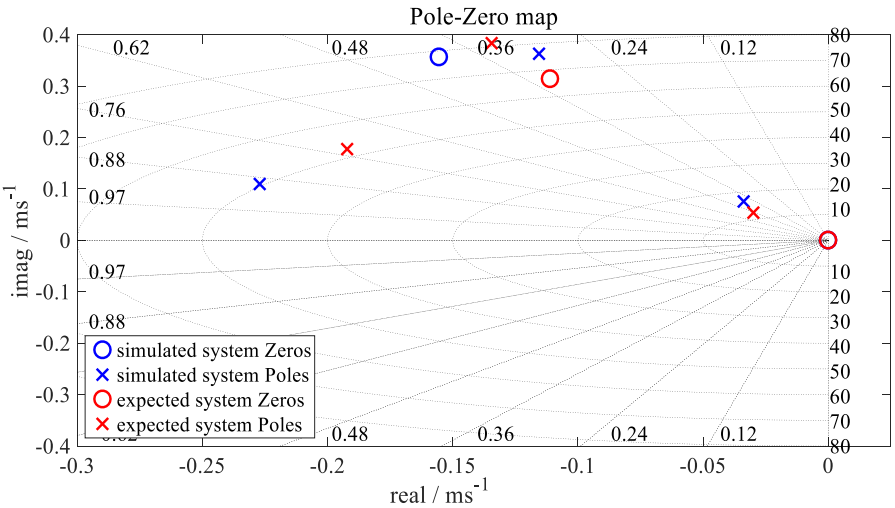

Figure 5-15 Pole-Zero excursion of the DFIG stator current transfer function for reference tracking

From the discussion above it can be concluded that the damping of the DC transient current and the 1st AC transient current (highest eigen frequency) are reduced due to the voltage limitation. Concurrently, their magnitudes are increased, while the damping of the 2nd AC transient current (lowest eigen frequency) increases. As a result, its magnitude is reduced. This can be observed

in the Pole-Zero map shown in Figure 5-14 and 5-15 for the disturbing quantity and the reference tracking quantity respectively.

For the disturbing quantity, the pole of the DC transient current has moved into a higher oscillating mode and a lower damping yielding higher magnitudes. Additionally, the pole of the 1st AC transient current has also moved into a lower oscillating mode and a lower damping while its zero remains almost in the same position yielding a lower magnitude. Furthermore, the pole of the 2nd AC transient current moved into a lower oscillating mode and a higher damping with its zero again remaining in almost the same position and yielding a higher magnitude. For the reference tracking, the conditions for the poles are the same as for the disturbing quantity. The zero of the 1st AC transient current moved into a higher oscillating mode and damping. This yields a lower magnitude as the pole retains a lower oscillating mode and a lower damping. For the 2nd AC transient current the zero remains at the origin. This yields that the magnitude will decrease because the pole is positioned far away from the origin.

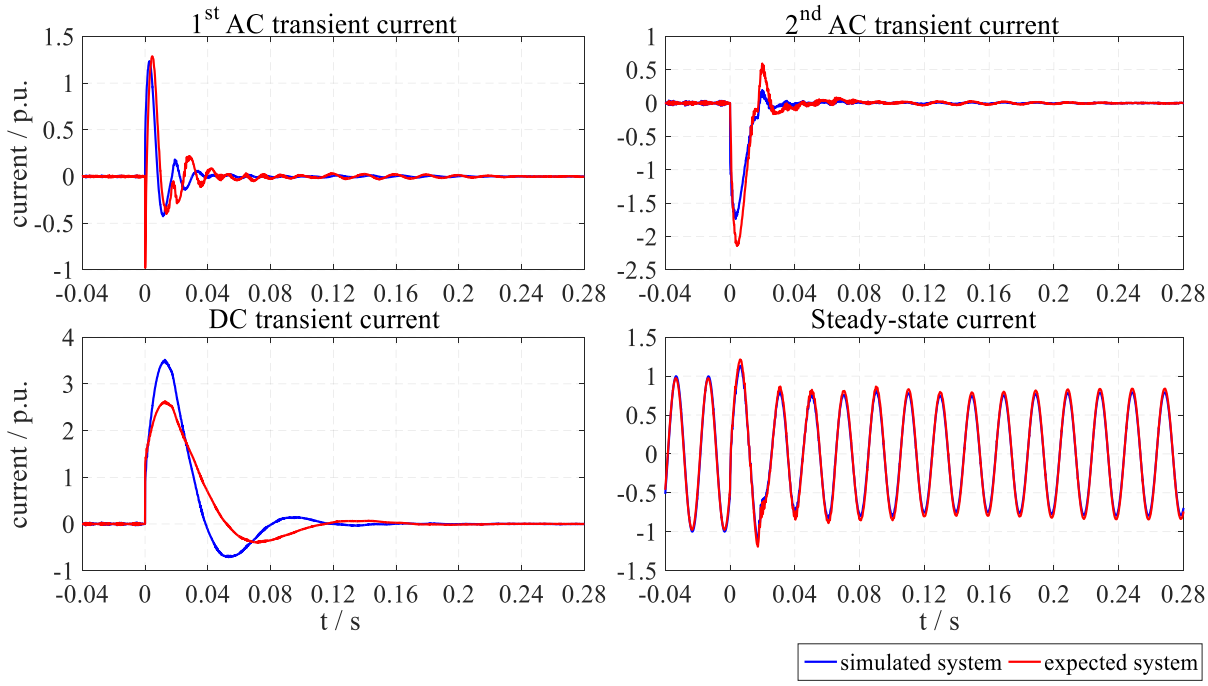

Figure 5-16 Short-circuit current components of the DFIG stator considering MSC voltage limitation

The resultant short-circuit current components are shown in Figure 5-16. It is clear that the most notable difference is in the DC transient component. As already discussed, the high proportional gain as well as the integral gain will lead to a very low transient time constant for the AC components. As a result, their magnitudes will demolish quickly, while the DC time constant will decrease. Still, this decrease is not significant. Consequently, the required transient rotor voltage will be mainly produced by the DC current component. This means that due to the MSC

voltage limitation the MSC will not be able to produce the required transient DC rotor voltage, which leads to the significant difference observed in the DC transient current component.

The short-circuit currents of the DFIG stator under MSC voltage limitation are shown in Figure 5-17. The plotted curves show that the simulated current is almost identical to the expected current for the first cycle. This is related to the fact that the required rotor voltage exceeds the limits after the first cycle as shown in Figure 5-18. Therefore, it can be concluded that the voltage limitation does not influence both the transient current magnitude and the peak current.

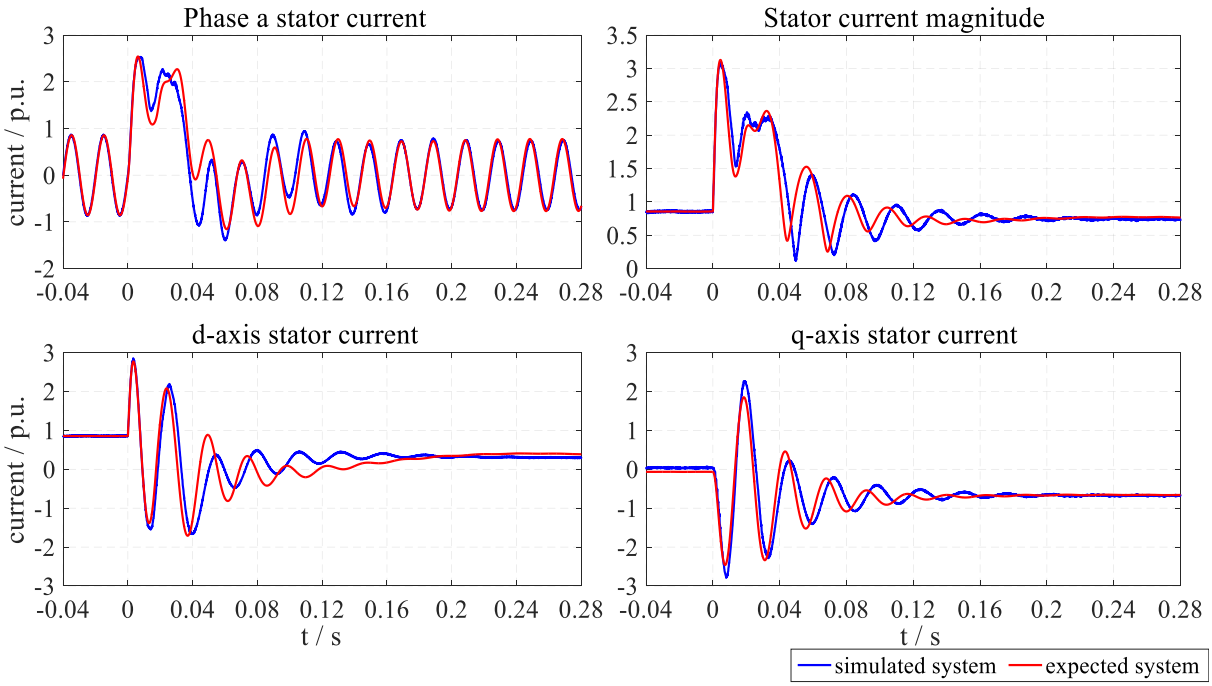

Figure 5-17 Influence of MSC voltage limitation on the DFIG stator short-circuit current

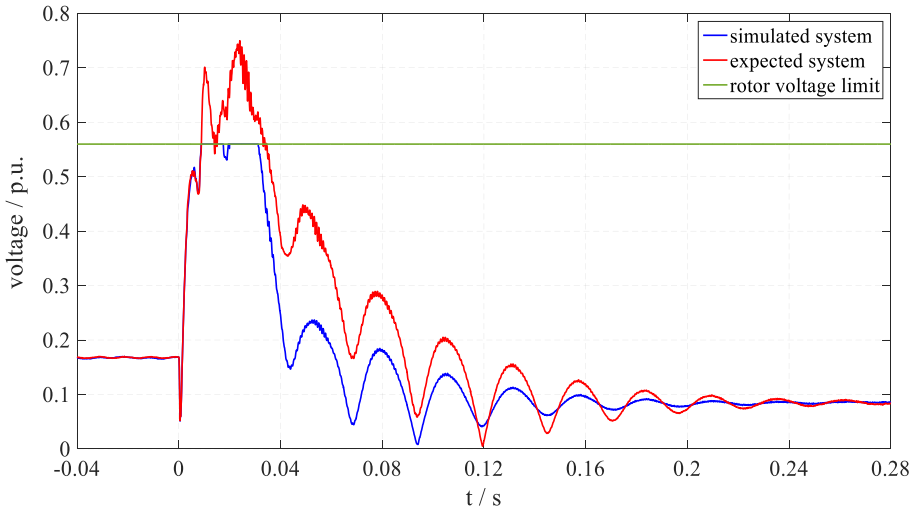

Figure 5-18 Required rotor voltage considering MSC voltage limitation

6 Techniques to Reduce the Peak Short-Circuit Current

It has been shown in the previous chapter that due to the direct connection of the DFIG stator to the grid that any disturbance in the grid voltage will result in high short-circuit current magnitudes and over-voltages in the DC circuit. The semiconductor devices are sensitive to high magnitudes of currents and voltages, which may violate their thermal and voltage limits. Therefore a protection strategy of the converters against such high currents and voltages magnitudes should be implemented. However, the FRT poses a challenge to overcome due to design limitations.

In the early development days, the DFIG-WT was conventionally equipped with a passive crowbar for protection against excessive currents and voltages. The operation period of the passive crowbar lasts for long periods, typically six cycles, and during such long periods of operation the DFIG acts as a conventional induction generator that consumes a considerable amount of reactive power [100]. Naturally, such behaviour is not subjected to the grid codes requirements. Nevertheless upon voltage restoration high over voltages occur in the rotor circuit that may lead to damage of the converter. Several solutions were proposed to enhance the operation of the crowbar circuit. Among these were the restoration of the operation with the currents last measured as a reference current to ensure safe operation during the transition to normal operation [101], or adaption of an active crowbar with strategy to reduce the activation period [102]. However, those solutions are complicated because they require switching between several control passes, which reduces reliability of the controller. Another sophisticated solution to overcome long deactivation periods would be to instead of using a crowbar to block the IGBT and to let the rotor current commutate through the diodes. Meanwhile the chopper is triggered to reduce the DC link voltage as well as the rotor currents [103]. Although this would effectively reduce the deactivation period of the MSC as well as the DC link voltage and rotor currents blocking would still be inventible.

Other solutions would include the installation of extra hardware components in the rotor or stator circuit. Those extra hardware components include one of the following; a saturable core fault current limiter (FCL) [104] [105], a super conducting FCL [106], a combination of resistances and capacitances with a bidirectional switch [107], a series dynamic resistance with a bypass switch [108], a dynamic voltage restorer with a VSC [109], a passive resistance network [110]. Other solutions focus on control adjustment during FRT. The demagnetizing current was added to the reference current to constrain the rotor current to below 2 p.u in [111], while the stator transient voltage was added to the rotor voltage in [112] for the same reason. Although both approaches successfully reduced the currents they both require the existence of

a flux observer and need to operate in over-modulation. Furthermore, they cannot reduce the current if the voltage sag is lower than 0.3 p.u,. and upon voltage restoration high current over-shoots will occur. Two other solutions were proposed in [88]. The first was to add instantly the step change in the stator voltage to the rotor voltage for a limited time frame in order to avoid long periods of operation in over-modulation. The second was to let the first set-point of the reference reactive current be set as under excited for the first half cycle and then to reverse it. Again, both methods were successful with regard to current reduction. Yet, it is still not clear how to set the application time in the first solution. It also prolongs the decaying time. In the second solution it is not clear how to adjust the value of the reference reactive current. Furthermore, in real controller instantaneous application is impossible due to the delays introduced by the measurement and the converter modulation. An improved control strategy was proposed in [113] to limit the DC-link voltage by feedback of the rotor power in the current control loop of the GSC. However, this approach requires elevating the thermal rating of the GSC to withstand the extra transferred power of the rotor circuit during FRT.

Most of the aforementioned hardware based solutions feature either components that should be fully rated or components that are expensive, which will increase the overall cost of the WT unit. Additionally, some of them require a sophisticated control strategy. Also, the control adjustment solutions, even those that were successful in curbing the problems of the high short-circuit current and the DC voltage, had a negative impact on the DFIG. Some of these effects were the operation in over-modulation and the reduction of its feasibility with higher voltage drops.

In this chapter new techniques are developed for the purpose of reducing the peak value of the short-circuit current for FRT enhancement. These new methods utilize the dynamic model of the DFIG to derive the compensation rules while using the available MSC voltage without running into over-modulation. Again, the MVMO is used to optimally tune the parameters relevant for the compensation rules to achieve the highest effectiveness of the proposed techniques.

Some remarks need to be made to ensure clear results. The simple network shown in Figure 6-1 is used for simulation purposes. The simulation model of the DFIG-WT represents a manufacturer based model with real-world parameters so that the results reflect the real dynamic behavior as closely as possible. All the DFIG-WT's parameters are found in the Appendix. A 3-phase fault is applied at a section in the cable so that a 90% voltage drop occurs at the PCC. Prior to the fault the DFIG-WT is operating in the super synchronous mode with an active power set-point equal to 0.95 p.u. and slip equal to -0.18. The timing of the fault is

chosen in such a way that the maximum peak current occurs in phase a. Additionally, the magnetic saturation is considered for the DFIG for all the simulations carried out. Furthermore, the results without any compensation technique but only a PI-controller in the inner current control loop is considered here as a benchmark for comparison.

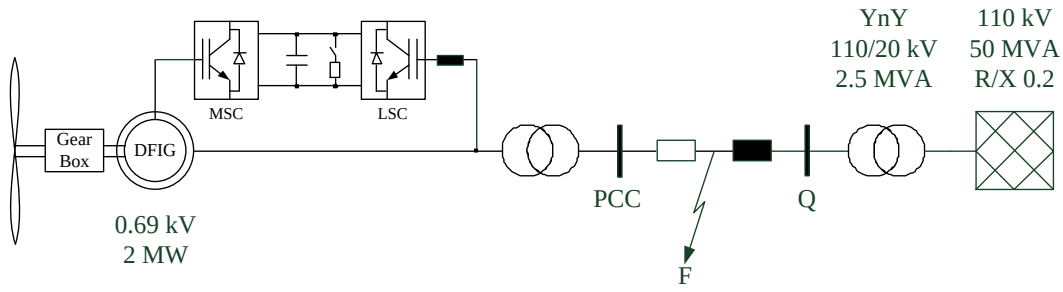

Figure 6-1 Simulation network used for the validation of the proposed peak short-circuit current techniques

6.1 Transient Flux Compensation

The DFIG stator current can be written as:

$$\underline{i}_{\mathrm{S}}^{\angle 0} = -\frac{\underline{v}_{\mathrm{S}}^{\angle 0} + \underline{v}'^{\angle 0}_{\mathrm{int}}}{r_{\mathrm{S}} + s\sigma l_{\mathrm{S}}} \tag{6.1}$$

where $\underline{v}'^{\angle 0}_{\mathrm{int}} = s\frac{l_{\mathrm{M}}}{l_{\mathrm{R}}}\underline{\psi}_{\mathrm{R}}^{\angle 0}$ is the internal transient voltage.

For the step change in the stator voltage the DFIG stator current can be rewritten as:

$$\underline{i}_{\mathrm{S}}^{\angle 0} = \underline{i}_{\mathrm{S,ss}}^{\angle 0} + \Delta\underline{i}_{\mathrm{S,tr}}^{\angle 0} \tag{6.2}$$

where $\underline{i}_{\mathrm{S,ss}}^{\angle 0}$ and $\Delta\underline{i}_{\mathrm{S,tr}}^{\angle 0}$ are the steady-state current and transient current respectively and aredescribed as:

$$\underline{i}_{\mathrm{S,ss}}^{\angle 0} = -\frac{\underline{v}_{\mathrm{S}}^{\angle 0} + \mathrm{j}\omega_{\mathrm{S}}\frac{l_{\mathrm{M}}}{l_{\mathrm{R}}}\underline{\psi}_{\mathrm{R}}^{\angle 0}}{r_{\mathrm{S}} + \mathrm{j}\omega_{\mathrm{S}}\sigma l_{\mathrm{S}}} \tag{6.3}$$

$$\Delta\underline{i}_{\mathrm{S,tr}}^{\angle 0} = -\frac{\Delta\underline{v}_{\mathrm{S}}^{\angle 0} + \Delta\underline{v}'^{\angle 0}_{\mathrm{int}}}{r_{\mathrm{S}} + s\sigma l_{\mathrm{S}}} \tag{6.4}$$

From eq. (6.4) the transient current can be set to zero if $\Delta\underline{v}'^{\angle 0}_{\mathrm{int}}$ is set equal to $-\Delta\underline{v}_{\mathrm{S}}^{\angle 0}$. This is satisfied if the transient rotor voltage is set to:

$$\Delta\underline{v}_{\mathrm{R}}^{\angle 0} = \frac{s^2 + s\left(\frac{r_{\mathrm{S}}}{\sigma l_{\mathrm{S}}} + \frac{r_{\mathrm{R}}}{l_{\mathrm{R}}} - \mathrm{j}\omega_{\mathrm{R}}\right) + r_{\mathrm{S}}\left(\frac{r_{\mathrm{R}}}{\sigma l_{\mathrm{S}} l_{\mathrm{R}}} - \mathrm{j}\frac{\omega_{\mathrm{R}}}{\sigma l_{\mathrm{S}}}\right)}{s\frac{l_{\mathrm{M}}}{l_{\mathrm{R}}}\left(\frac{r_{\mathrm{S}}}{\sigma l_{\mathrm{S}}} + s\right)} \Delta\underline{v}_{\mathrm{S}}^{\angle 0} \tag{6.5}$$

From this it follows that a full dynamic rejection of the disturbing quantity is achieved if the required dynamic rotor voltage described in eq. (6.5) is provided in the controller as a feed-forward to the rotor voltage. However, the existence of a pure integrator would lead to instability due to uncertainties in the values of the parameter. Additionally, the initial dynamic rotor voltage $\Delta\underline{v}_{\mathrm{R,init}}^{\angle 0} = l_{\mathrm{R}}/l_{\mathrm{M}}\,\Delta\underline{v}_{\mathrm{S}}^{\angle 0}$ is more than double the MSC voltage limit. In order to overcome those difficulties the rate of change of the internal transient voltage can be increased by setting $\Delta\underline{\psi}_{\mathrm{R}}^{\angle 0} = 0$. Based on this the required dynamic rotor voltage can be driven either from the open-loop or the closed-loop dynamic response of the DFIG.

6.1.1 Open-Loop Transient Flux Compensation

From the full order model of the DFIG described in chapter 3 the open-loop rotor flux can be derived after some mathematical manipulation as:

$$\underline{\psi}_{\mathrm{R}}^{\angle 0} = \frac{-\frac{r_{\mathrm{R}} l_{\mathrm{M}}}{\sigma l_{\mathrm{S}} l_{\mathrm{R}}}\underline{v}_{\mathrm{S}}^{\angle 0} - \left(\frac{r_{\mathrm{S}}}{\sigma l_{\mathrm{S}}} + s\right)\underline{v}_{\mathrm{R}}^{\angle 0}}{s^2 + s\left(\frac{r_{\mathrm{S}}}{\sigma l_{\mathrm{S}}} + \frac{r_{\mathrm{R}}}{\sigma l_{\mathrm{R}}} - \mathrm{j}\omega_{\mathrm{R}}\right) + \frac{r_{\mathrm{S}}}{\sigma l_{\mathrm{S}} l_{\mathrm{R}}}\left(r_{\mathrm{R}} - \mathrm{j}\omega_{\mathrm{R}} l_{\mathrm{R}}\right)} \tag{6.6}$$

Consequently, the open-loop transient rotor flux is set to zero if the dynamic rotor voltage is set to:

$$\underline{v}_{\mathrm{R,dyn}}^{\angle 0} = \frac{-r_{\mathrm{R}} l_{\mathrm{M}}}{l_{\mathrm{R}}\left(r_{\mathrm{S}} + s\sigma l_{\mathrm{S}}\right)} \Delta\underline{v}_{\mathrm{S}}^{\angle 0} \tag{6.7}$$

Rearranging eq. (6.7) for controller implementation yields:

$$\underline{v}_{\mathrm{R,dyn}}^{\angle 0} = -\frac{r_{\mathrm{R}}\sigma l_{\mathrm{S}} l_{\mathrm{M}}}{l_{\mathrm{R}}\left(r_{\mathrm{S}} + \mathrm{j}\omega_{\mathrm{S}}\sigma l_{\mathrm{S}}\right)} \frac{\left(s - \mathrm{j}\omega_{\mathrm{S}}\right)\sigma\tau_{\mathrm{S}}}{1 + s\sigma\tau_{\mathrm{S}}} \underline{v}_{\mathrm{S}}^{\angle 0} \tag{6.8}$$

Figure 6.2 shows the inner current control loop with an open-loop transient flux compensation.

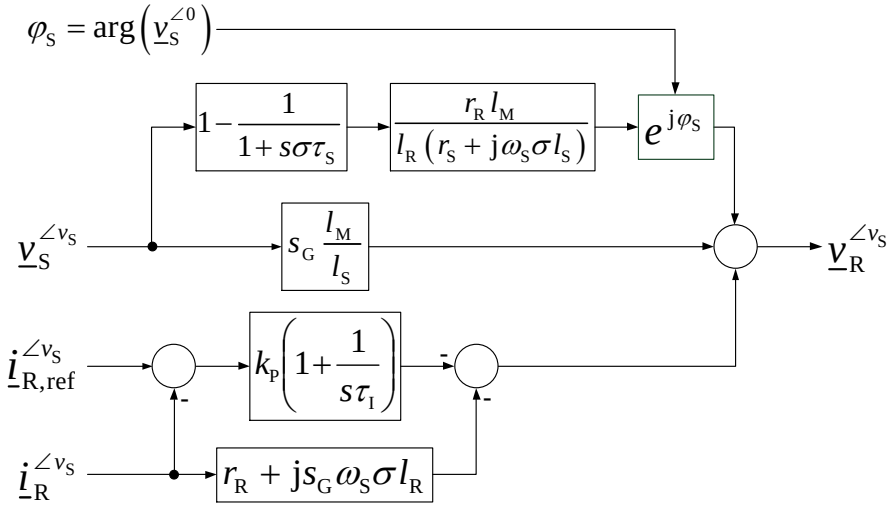

Figure 6-2 MSC inner current control loop with an open-loop transient flux compensation

6.1.2 Closed-Loop Transient Flux Compensation

The compensation of the transient flux can also be driven considering the feed-forward decoupled control of the DFIG. The closed-loop rotor flux can be estimated by equating the rotor voltage described in eq. (4.46) with its value in eq. (6.6), which results after some mathematical manipulation in the following expression of the closed-loop rotor flux:

$$\underline{\psi}_R^{\angle 0} = \frac{\left(b_2 s^2 + \underline{b}_1 s + \underline{b}_0\right)\underline{v}_S^{\angle 0} - \left(r_S + s\sigma l_S\right)\left(k_P\left(s - j\omega_S\right) + k_I\right) l_R \underline{i}_{R,ref}^{\angle 0}}{a_3 s^3 + \underline{a}_2 s^2 + \underline{a}_1 s + \underline{a}_0} \tag{6.9}$$

where a_3 to a_0 are the same as in eq. (5.28)-(5.31) and

$$b_2 = s_G \sigma l_R l_M \tag{6.10}$$

$$\underline{b}_1 = s_G l_R l_M \left(\frac{r_S}{l_S} - j2\omega_S\sigma\right) - k_P l_M \tag{6.11}$$

$$\underline{b}_0 = -k_I + j\omega_S\left(k_P - s_G l_R\left(\frac{r_S}{l_S} - j\omega_S\sigma\right)\right) \tag{6.12}$$

In order to reset the transient closed-loop rotor flux, the dynamic reference current should be set to:

$$\underline{i}_{R,ref,dyn}^{\angle 0} = \frac{\left(b_2 s^2 + \underline{b}_1 s + \underline{b}_0\right)\Delta\underline{v}_S^{\angle 0}}{\left(r_S + s\sigma l_S\right)\left(k_P\left(s - j\omega_S\right) + k_I\right) l_R} \tag{6.13}$$

Rearranging eq. (6.13) for controller implementation yields:

$$\underline{i}_{\mathrm{R,ref,dyn}}^{\angle 0} = \left(\underline{A} \frac{(s - \mathrm{j}\omega_\mathrm{S})\sigma\tau_\mathrm{S}}{1 + s\sigma\tau_\mathrm{S}} + \underline{B} \frac{s\tau_\mathrm{I}}{1 + (s - \mathrm{j}\omega_\mathrm{S})\tau_\mathrm{I}} \right) \underline{v}_\mathrm{S}^{\angle 0} \tag{6.14}$$

where

$$\underline{A} = \frac{l_\mathrm{M}}{l_\mathrm{R}} \frac{\sigma l_\mathrm{S} k_\mathrm{I} - \mathrm{j}\omega_\mathrm{S}\sigma(s_\mathrm{G} l_\mathrm{R} - l_\mathrm{S} k_\mathrm{P})(r_\mathrm{S} + \mathrm{j}\omega_\mathrm{S}\sigma l_\mathrm{S})}{(\sigma l_\mathrm{S} k_\mathrm{I} - k_\mathrm{P}(r_\mathrm{S} + \mathrm{j}\omega_\mathrm{S}\sigma l_\mathrm{S}))(r_\mathrm{S} + \mathrm{j}\omega_\mathrm{S}\sigma l_\mathrm{S})} \tag{6.15}$$

$$\underline{B} = \frac{l_\mathrm{M}}{k_\mathrm{P} l_\mathrm{S} l_\mathrm{R}} \frac{\left(r_\mathrm{S} - \dfrac{\sigma l_\mathrm{S}}{\tau_\mathrm{I}}\right)(s_\mathrm{G} l_\mathrm{R} - l_\mathrm{S} k_\mathrm{P}) + l_\mathrm{S} k_\mathrm{P}}{r_\mathrm{S} + \left(-\dfrac{1}{\tau_\mathrm{I}} + \mathrm{j}\omega_\mathrm{S}\right)\sigma l_\mathrm{S}} \tag{6.16}$$

Figure 6.3 shows the inner current control loop with a closed-loop transient flux compensation.

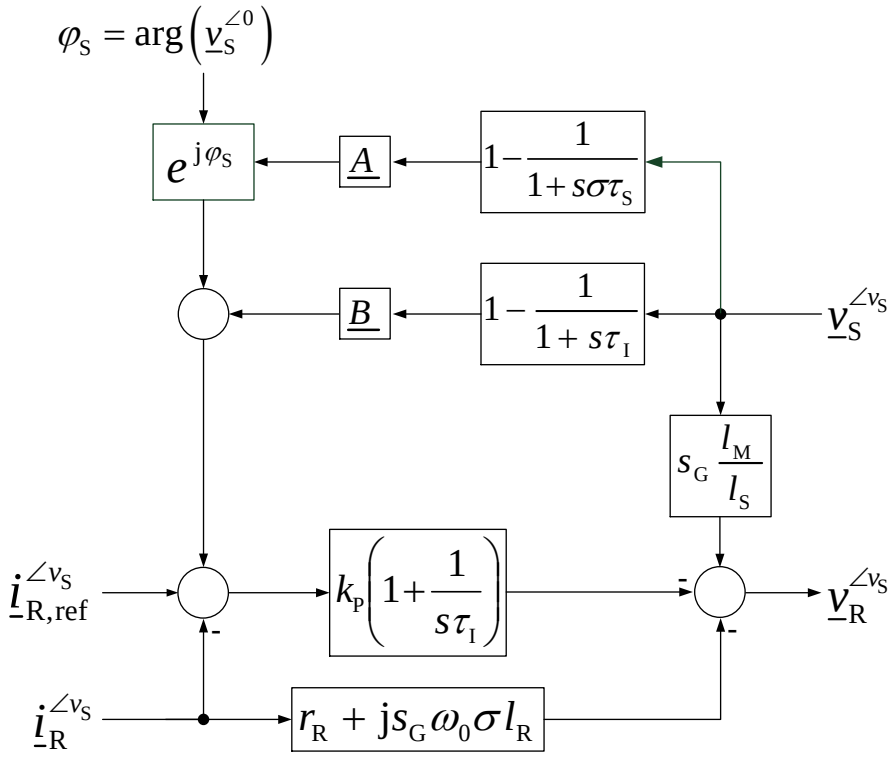

Figure 6-3 MSC inner current control loop with a closed-loop transient flux compensation

6.1.3 Simulation Results For Transient Flux Compensation

The short-circuit current of the DFIG stator is shown in Figure 6-4. The highest peak short-circuit current occurs with the PI-controller after 6 ms from the fault, while the lowest peak occurs with the closed-loop transient flux compensation after 7 ms from the fault. The closed-loop compensation is successful in reducing the peak short-circuit current by 22%, while the open loop reduces the peak value by 5%. After fault clearance no high current over-shoots

occur. The highest magnitude occurs with the PI-controller and the lowest with the closed-loop compensation.

The simulation results of other quantities are shown in Figure 6-5. Upon fault initiation the internal transient voltage will get reduced to match the stator voltage reduction and the new reference current's set points. The internal transient voltage declines rapidly under closed-loop compensation to a value of 0.9 p.u. in 7 ms while it decreases more slowly in the case of PI-controller to 0.96 in 6 ms. That is why the lowest peak value of the short-circuit current occurs with the closed-loop compensation. As a result of the fast change of the internal voltage, the rotor voltage magnitude increases much faster to its highest value in the case of the closed-loop compensation in comparison to the open-loop and PI-controller cases.

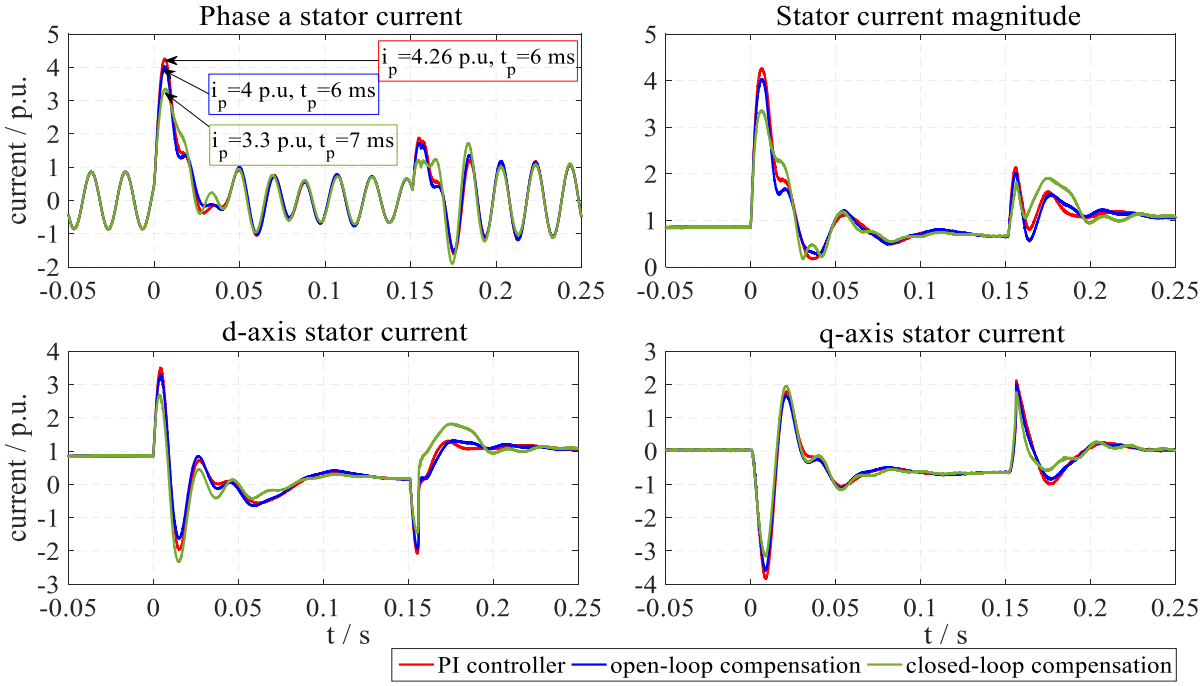

Figure 6-4 DFIG stator short-circuit current with transient flux compensation

However, the rotor voltage does not increase beyond the maximum available MSC voltage, which in the case of the transient is up to 0.56 p.u. Furthermore, the high rotor voltage magnitude results in a higher DC link voltage and consequently increases the activity of the chopper. The fast change decline in the internal voltage and the reduced peak short-circuit current result in lower over-shoot in the electromagnetic torque and faster damping of oscillation in the case of the closed-loop, which results in lower mechanical stresses on the shaft. Provided that the energy stored in the DFIG remains the same and that the peak short-circuit current is dominantly reactive, the responses of the DFIG-WT's active power remain almost the same in all cases. As the current's magnitude in all the cases observed increases with

the same pattern the main inductance value will also de-saturate with the same pattern and reach its highest value at the same time.

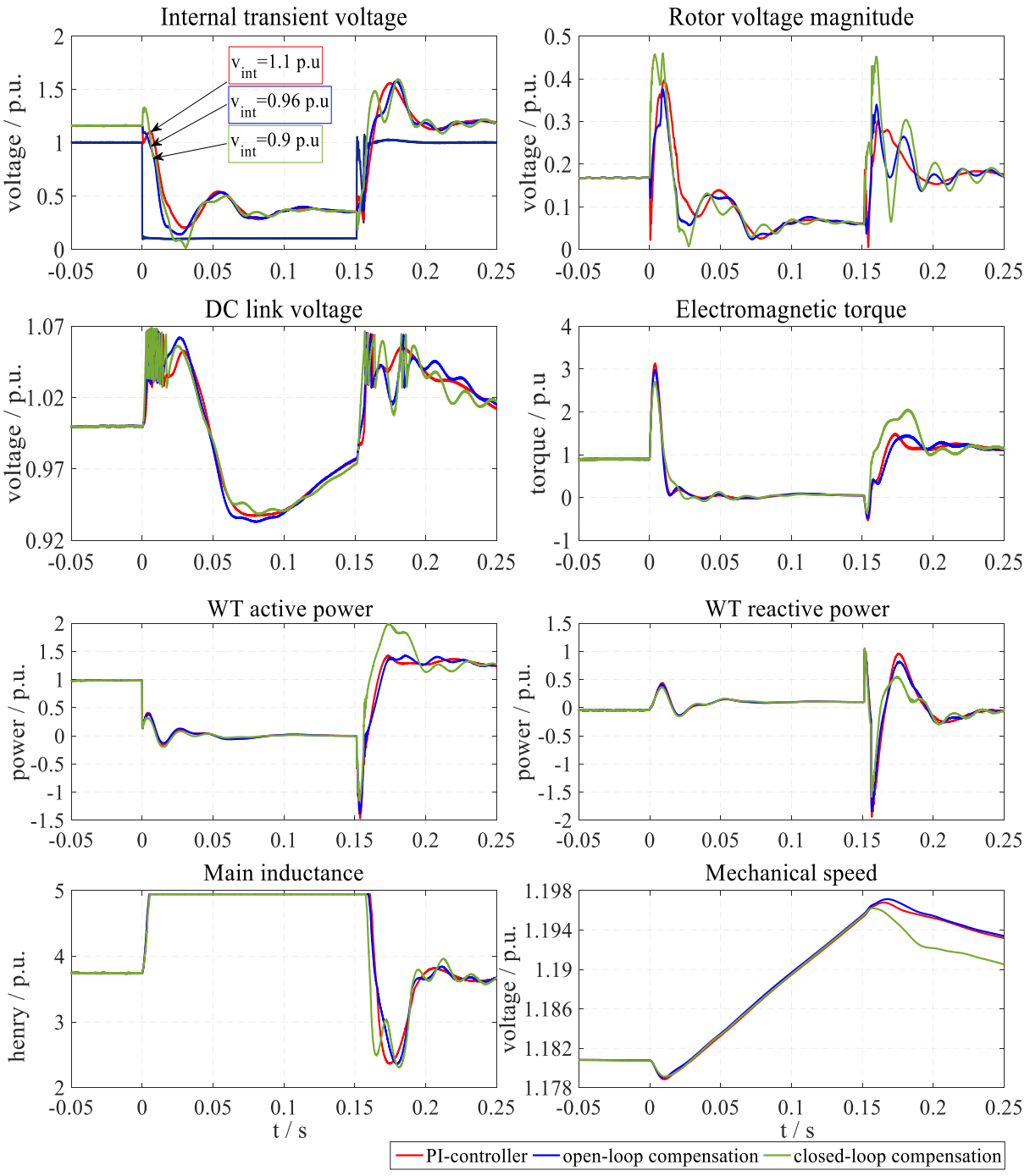

Figure 6-5 Simulation results for transient flux compensation

After fault clearance the same scenario repeats itself again. The internal voltage increases again faster in the case of the closed-loop in comparison to the other cases. This results in a higher rotor voltage magnitude, and consequently in a higher DC link voltage and increased chopper operation. Additionally, the torque over-shoot is lower in the case of closed-loop compensation due to lower current and internal transient voltage peak values. Resulting from the great difference between the terminal voltage and the internal voltage, higher reactive power would

be absorbed by the machine. This reactive power magnitude and rate of change is dependent on how fast the MSC's controller modifies its rotor voltage to its new set point. Therefore, in the case of the PI-controller the amount of reactive power is the highest. This is why the over-shoot in the reactive and active power in the case of closed-loop compensation is the lowest. It is also important to notice that, after the first cycle of the closed-loop compensation the internal voltage shows a sag in its value. This is a consequence of the large sag occurring in the rotor voltage and in response to it the MSC controller increases the d-axis reference current in order to increase the produced power. This is why a higher swell in the active power occurs. The active power swell will damp the mechanical speed and force it to quickly return to its reference value as illustrated. This is beneficial for the transient stability due to a fast damping of the rotor angle.

6.2 Transient Impedance Compensation

According to eq. (6.1) another method to reduce the peak short-circuit current would be to increase the DFIG transient impedance as much as possible. The transient impedance of the DFIG according to eq. (6.1) is described by:

$$\underline{z}'_{\mathrm{S}} = r_{\mathrm{S}} + \mathrm{j}\omega_{\mathrm{S}}\sigma l_{\mathrm{S}} \tag{6.17}$$

The highest value the transient impedance can reach is given by:

$$\underline{z}'_{\mathrm{S}} = r_{\mathrm{S}} + \mathrm{j}\omega_{\mathrm{S}} l_{\mathrm{S}} \tag{6.18}$$

This value represents the transient impedance with an open circuited rotor which can be achieved by setting the rotor current to zero.

6.2.1 Open-Loop Transient Impedance Compensation

From the transfer function of the rotor current described in eq. (3.28) the rotor current can be set to zero by considering the following:

$$\underline{v}_{\mathrm{R}}^{\angle 0} = \frac{(s - \mathrm{j}\omega_{\mathrm{R}})\, l_{\mathrm{M}}}{r_{\mathrm{S}} + s l_{\mathrm{S}}}\, \underline{v}_{\mathrm{S}}^{\angle 0} \tag{6.19}$$

The steady-state value in eq. (6.19) is already given as a feed forward term in the MSC controller. Therefore, it can be excluded and only the dynamic term is considered, which results in the required transient rotor voltage as:

$$\underline{v}_{\mathrm{R,dyn}}^{\angle 0} = \frac{(s - \mathrm{j}\omega_{\mathrm{S}})(r_{\mathrm{S}} + \mathrm{j}\omega_{\mathrm{R}} l_{\mathrm{S}})\, l_{\mathrm{M}}}{r_{\mathrm{S}} + s l_{\mathrm{S}}}\, \Delta\underline{v}_{\mathrm{S}}^{\angle 0} \tag{6.20}$$

Rearranging eq. (6.20) for the implementation of the controller yields:

$$\underline{v}_{\mathrm{R,dyn}}^{\angle 0} = l_{\mathrm{M}}\left(r_{\mathrm{S}} + \mathrm{j}\omega_{\mathrm{R}} l_{\mathrm{S}}\right)\frac{\left(s - \mathrm{j}\omega_{\mathrm{S}}\right)\tau_{\mathrm{S}}}{1 + s\tau_{\mathrm{S}}}\underline{v}_{\mathrm{S}}^{\angle 0} \tag{6.21}$$

The schematic of the inner current control loop with an open-loop transient impedance compensation is shown in Figure 6-6.

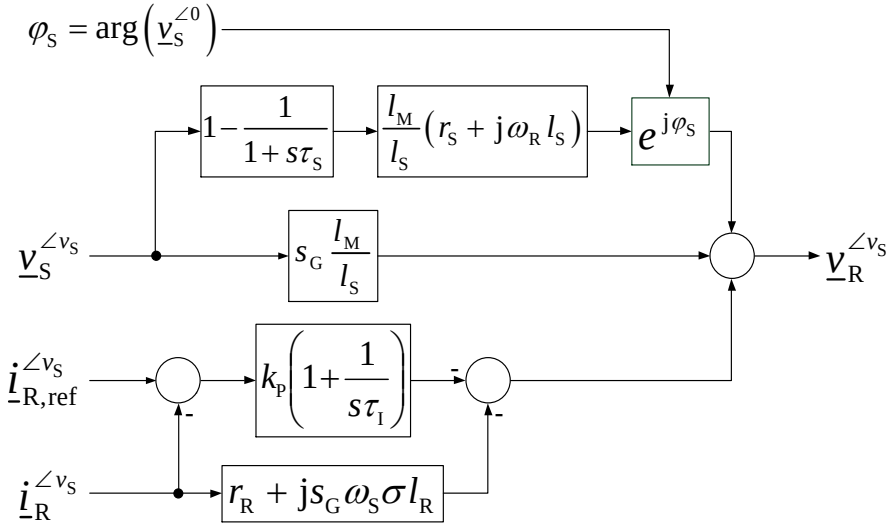

Figure 6-6 MSC inner current control loop with an open-loop transient impedance compensation

6.2.2 Closed-Loop Transient Impedance Compensation

The rotor current's transfer function can also be derived considering the feed-forward decoupled control of the DFIG. Based on the MSC controller shown in Figure 4-33 the rotor current's transfer function excluding both measurement and converter delays is:

$$\underline{i}_{\mathrm{R}}^{\angle 0} = \frac{\left(b_2 s^2 + \underline{b}_1 s + \underline{b}_0\right)\underline{v}_{\mathrm{S}}^{\angle 0} - \left(r_{\mathrm{S}} + s l_{\mathrm{S}}\right)\left(k_{\mathrm{P}}\left(s - \mathrm{j}\omega_{\mathrm{S}}\right) + k_{\mathrm{I}}\right) l_{\mathrm{R}}\, \underline{i}_{\mathrm{R,ref}}^{\angle 0}}{a_3 s^3 + \underline{a}_2 s^2 + \underline{a}_1 s + \underline{a}_0} \tag{6.22}$$

where a_3 to a_0 are the same for the stator current's transfer function other coefficients are defined as follows:

$$b_2 = \left(s_{\mathrm{G}} - 1\right) l_{\mathrm{M}} \tag{6.23}$$

$$\underline{b}_1 = s_{\mathrm{G}}\frac{l_{\mathrm{M}}}{l_{\mathrm{S}}} r_{\mathrm{S}} - \mathrm{j}\left(\omega_{\mathrm{S}}\left(s_{\mathrm{G}} - 1\right) - \omega_{\mathrm{R}}\right) l_{\mathrm{M}} \tag{6.24}$$

$$\underline{b}_0 = -\mathrm{j}\omega_{\mathrm{S}}\left(s_{\mathrm{G}} r_{\mathrm{S}} - \mathrm{j}\omega_{\mathrm{R}} l_{\mathrm{S}}\right)\frac{l_{\mathrm{M}}}{l_{\mathrm{S}}} \tag{6.25}$$

From eq. (6.22) the required dynamic reference current to set the rotor current to zero is described by:

$$\underline{i}_{\mathrm{R,ref,dyn}}^{\angle 0} = \frac{\left(b_2 s^2 + \underline{b}_1 s + \underline{b}_0\right)}{\left(r_\mathrm{S} + s l_\mathrm{S}\right)\left(k_\mathrm{P}\left(s - \mathrm{j}\omega_\mathrm{S}\right) + k_\mathrm{I}\right) l_\mathrm{R}} \Delta \underline{v}_\mathrm{S}^{\angle 0} \tag{6.26}$$

Rearranging eq. (6.26) for the implementation of the controller yields:

$$\underline{i}_{\mathrm{R,ref,dyn}}^{\angle 0} = \left(\underline{A} \frac{\left(s - \mathrm{j}\omega_\mathrm{S}\right)\tau_\mathrm{S}}{1 + s\tau_\mathrm{S}} + \underline{B} \frac{s\tau_\mathrm{I}}{1 + \left(s - \mathrm{j}\omega_\mathrm{S}\right)\tau_\mathrm{I}} \right) \underline{v}_\mathrm{S}^{\angle 0} \tag{6.27}$$

where

$$\underline{A} = -\frac{l_\mathrm{M}}{l_\mathrm{S}} \frac{r_\mathrm{S} + \mathrm{j}\omega_\mathrm{R} l_\mathrm{S}}{k_\mathrm{I} l_\mathrm{S} - k_\mathrm{P}\left(r_\mathrm{S} + \mathrm{j}\omega_\mathrm{S} l_\mathrm{S}\right)} \tag{6.28}$$

$$\underline{B} = -\frac{l_\mathrm{M}}{k_\mathrm{P} l_\mathrm{S}} \frac{s_\mathrm{G} r_\mathrm{S} - \left(s_\mathrm{G} - 1\right)\frac{l_\mathrm{S}}{\tau_\mathrm{I}}}{r_\mathrm{S} + \left(-\frac{1}{\tau_\mathrm{I}} + \mathrm{j}\omega_\mathrm{S}\right) l_\mathrm{S}} \tag{6.29}$$

The schematic of the inner current's control loop with a closed-loop transient impedance compensation is shown in Figure 6-7.

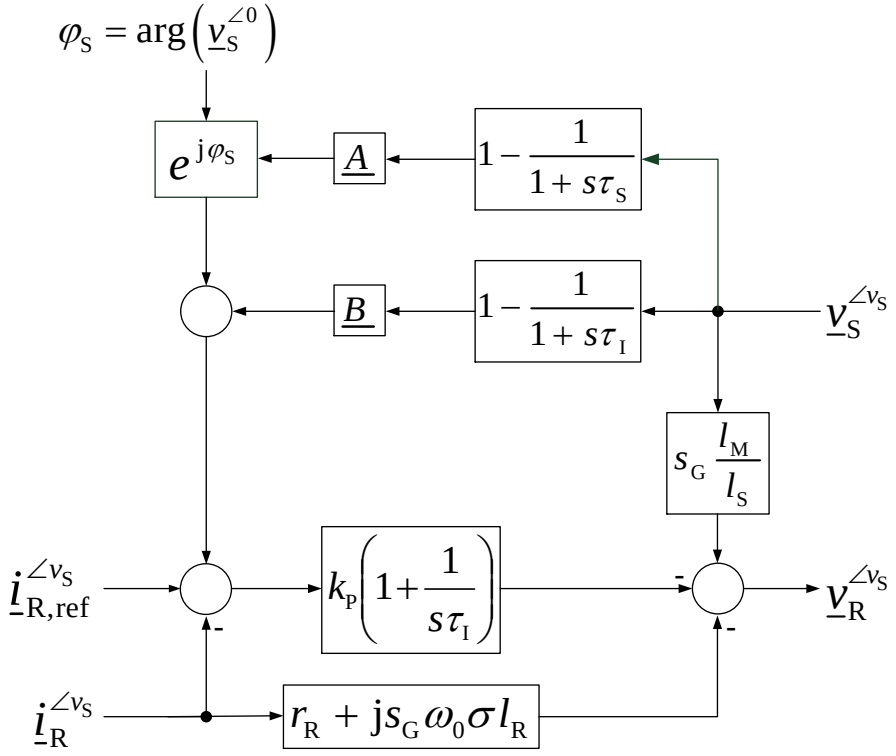

Figure 6-7 MSC inner current's control loop with a closed-loop transient impedance compensation

6.2.3 Optimized Transient Impedance Compensation

According to eq. (6.20) and (6.26) the initially required dynamic rotor voltage is equal to:

Open-loop:

$$\underline{v}_{\mathrm{R,dyn,init}}^{\angle 0} = \frac{l_{\mathrm{M}}}{l_{\mathrm{S}}}\left(r_{\mathrm{S}} + \mathrm{j}\omega_{\mathrm{R}} l_{\mathrm{S}}\right)\Delta\underline{v}_{\mathrm{S}}^{\angle 0} \tag{6.30}$$

Closed-loop

$$\underline{v}_{\mathrm{R,dyn,init}}^{\angle 0} = \frac{l_{\mathrm{M}}}{l_{\mathrm{S}} k_{\mathrm{P}}}\left(s_{\mathrm{G}} - 1\right)\Delta\underline{v}_{\mathrm{S}}^{\angle 0} \tag{6.31}$$

From this it can be concluded that the initially required dynamic rotor voltage is more than twice the available MSC voltage, which means that operation in over modulation is unavoidable. Furthermore, the associated time constants are larger than the natural machine's time constant, which implies that the duration of the over modulation operation will be greater. As a result, high harmonic currents will be generated and will also be sustained for longer periods of time. Consequently, high electrical losses and stresses on the mechanical shaft are unavoidable.

Such a scenario of course is not ideal. Thus, gain parameters and time constants should be rescaled to assure a more efficient compensation. Therefore, the gains and the time constants are extended by gain factors as follows:

Open-loop:

$$\underline{v}_{\mathrm{R,dyn}}^{\angle 0} = k_{\mu} l_{\mathrm{M}}\left(r_{\mathrm{S}} + \mathrm{j}\omega_{\mathrm{R}} l_{\mathrm{S}}\right)\frac{\left(s - \mathrm{j}\omega_{\mathrm{S}}\right)k_{\delta}\tau_{\mathrm{S}}}{1 + s k_{\delta}\tau_{\mathrm{S}}}\underline{v}_{\mathrm{S}}^{\angle 0} \tag{6.32}$$

Closed-loop:

$$\underline{i}_{\mathrm{R,ref,dyn}}^{\angle 0} = \left(k_{\mu 1}\underline{A}\frac{\left(s - \mathrm{j}\omega_{\mathrm{S}}\right)k_{\delta 1}\tau_{\mathrm{S}}}{1 + s k_{\delta 1}\tau_{\mathrm{S}}} + k_{\mu 2}\underline{B}\frac{s k_{\delta 2}\tau_{\mathrm{I}}}{1 + \left(s - \mathrm{j}\omega_{\mathrm{S}}\right)k_{\delta 2}\tau_{\mathrm{I}}}\right)\underline{v}_{\mathrm{S}}^{\angle 0} \tag{6.33}$$

The gain factors k_{μ} and k_{δ} can be tuned empirically. However, this would not lead to optimal performance. Therefore, MVMO is used again for to reliably tune both gains, where the objective function is evaluated as follows:

$$\min\left(i_{\mathrm{S,p}}, \tau_{\mathrm{resp}}\right) \tag{6.34}$$

and subjected to:

$$\left|v_{\mathrm{R}}\right| \le v_{\mathrm{MSC,max}} \;\&\; \left|v_{\mathrm{S}}\right| \ge v_{\mathrm{S,threshold}} \tag{6.35}$$

where $i_{\mathrm{S,p}}$ is the peak value of the stator's short-circuit current, τ_{resp} is the response time required for the rotor's instantaneous currents to perfectly track the reference currents set point

after fault occurrence, $v_{MSC,max}$ is the maximum available MSC voltage and $v_{S,threshold}$ is the stator voltage sag deactivation limit of the converter.

6.2.4 Simulation Results for Transient Impedance Compensation

It becomes clear in Figure 6-8 that the optimized transient impedance compensation successfully manages to reduce the peak short-circuit current by 21% for the open-loop and by 26% for the closed-loop. For both cases the time point occurrence of the peak value was delayed by 1ms in comparison to the PI-controller case. After fault clearance again the current over shoot was minimum with transient impedance compensation. However, a higher swell in the d-axis current component occurred for the closed-loop compensation in comparison to others.

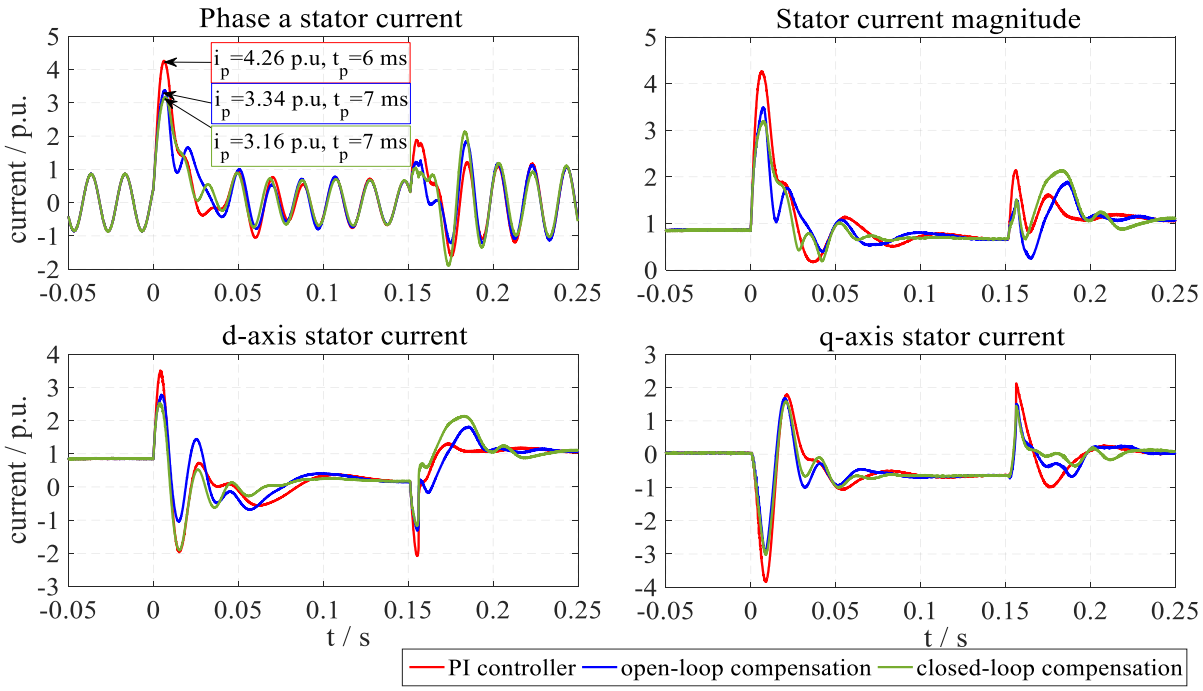

Figure 6-8 DFIG stator short-circuit current with a transient impedance compensation

As shown in Figure 6-9 upon fault occurrence the internal transient voltage decreases much faster with the compensation than with the PI-controller. Although the open-loop compensation results in a higher peak value than the closed-loop does, the value of the internal transient voltage is lower. This arises from the fact that the compensation technique modifies the transient impedance of the machine. This means that the closed-loop results in a slower decline in the transient impedance. The initial rotor voltage magnitude is the same for both cases and equal to 0.52 p.u., which is still lower than the maximum allowable value of 0.56 p.u.. However, the rotor voltage magnitude decreases much faster with the closed-loop compensation than it does with the open-loop compensation or the PI-controller. Generally, the high rotor voltage magnitude in the case of compensation results in a higher DC link voltage and in higher

operation cycles of the chopper circuit. Moreover, the slower decreases of the rotor voltage magnitude with open-loop compensation will result in higher operation cycles of the chopper circuit in comparison to the closed-loop compensation. The much lower internal transient voltage and peak short-circuit current value results in a much lower torque over shoot compared to the case with the PI-controller.

Upon fault clearance the same scenario repeats itself again as it does for the flux compensation. However, the rotor voltage magnitude displays a much deeper sag after the first cycle, which leads to a greater swell in the active power as well as in the electromagnetic torque. Yet, this high swell is beneficial for the rotor stability because it increases damping and, as a result, the speed deviation is limited as seen in Figure 6-9.

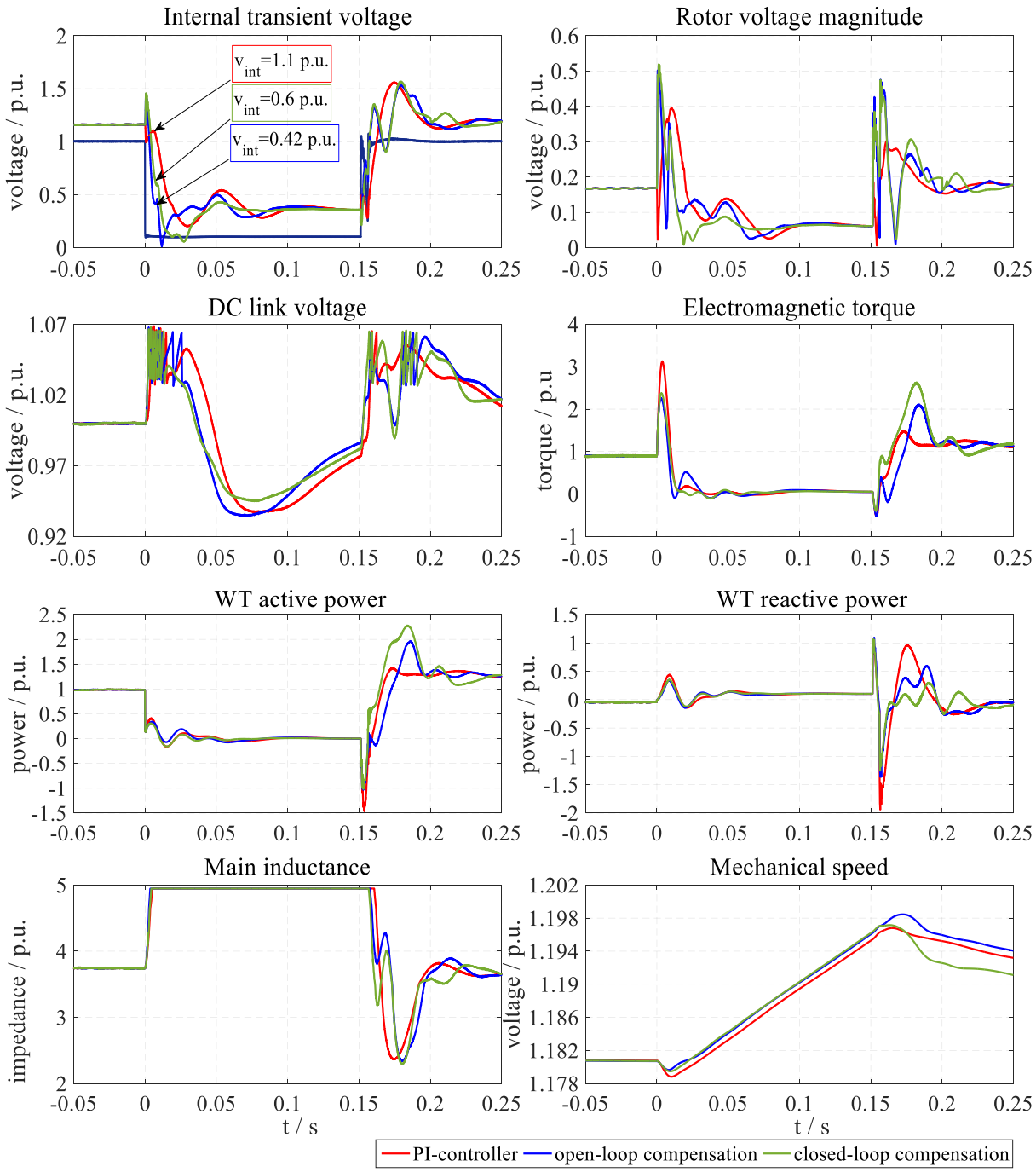

Figure 6-9 Simulation results of the transient impedance compensation

6.3 Pole Shift Method

One of the methods to reduce the peak short-circuit current is to shift the system's poles away from the origin in the left half of the *s*-plane, thus increasing the damping. This can be accomplished by shifting the system poles away from the origin by increasing the proportional gain of the PI-controller, which increases the damping of the AC transient components and consequently reduces the peak short-circuit current. However, the disadvantage of this procedure is that the system's zeros also moves away from the origin in the left half of the *s*-

plane. Therefore, the error voltage produced by the PI-controller increases sharply and may cause the MSC to run into over modulation. Additionally, the damping of the DC transient component is reduced significantly as well with the increase in the proportional gain. This will consequently increase the mechanical stresses on the rotating shaft due to the pulsating torque component as well as elevate heat production in the machine due to the ohmic losses. This fact is illustrated in Figure 6-10, which shows how the magnitude of the rotor voltage increases significantly with the proportional gain and how a sustained oscillation can be found due to the reduced damping of the DC component.

Another method to shift the system's poles without simultaneously shifting the zeros is to decrease the real component value of the rotor current's feed forward term $\mathrm{Re}\{\underline{G}_{\mathrm{FFI}}\}$. By reducing the real component the damping of the AC components will increase without a significant increase in the rotor voltage magnitude. This can be observed in Figure 6-11, which shows how the poles of the AC components shift towards higher damping, while the zeros shift is not that significant.

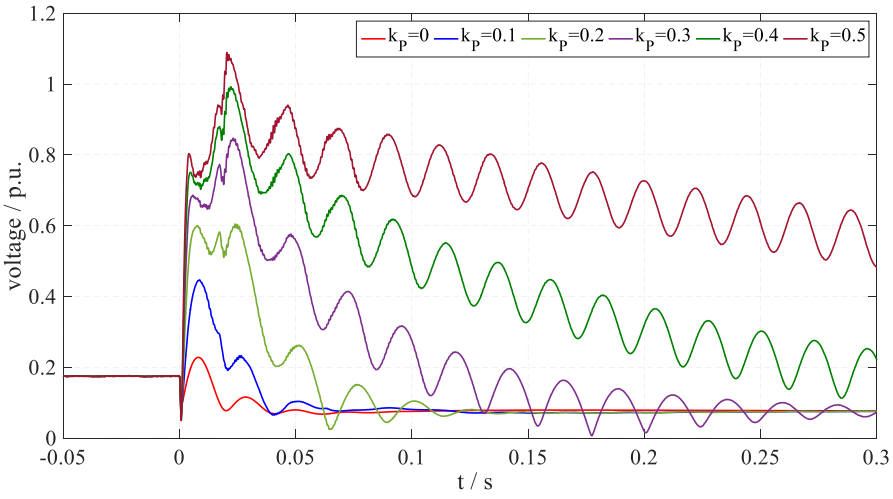

Figure 6-10 Influence of the proportional gain on the required rotor voltage during a deep voltage sag

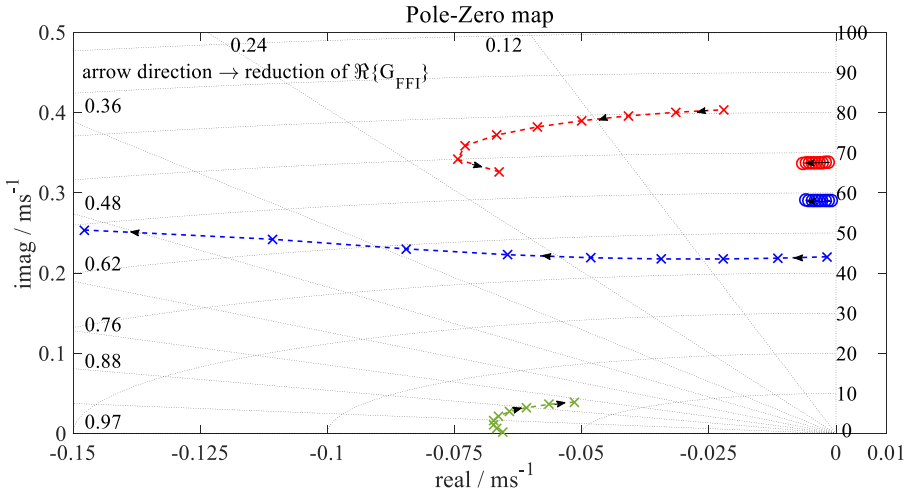

Figure 6-11 Influence of the rotor current's feed forward real component on the system's poles and zeros

The disadvantage of this method is that the controller effort will increase because the PI-controller has to compensate for the error produced by the high value of $\Re\{\underline{G}_{\mathrm{FFI}}\}$. Additionally, if the value $\Re\{\underline{G}_{\mathrm{FFI}}\}$ is too high, the PI-controller will be completely ineffective if the required error voltage is higher than the anti-windup limits. Therefore, choosing the right value of $\Re\{\underline{G}_{\mathrm{FFI}}\}$ is a tradeoff between controllability and FRT enhancement.

Simulation Results for Pole Shift Method

As the value of $\Re\{\underline{G}_{\mathrm{FFI}}\}$ decreases, the peak as well as the magnitude of the short-circuit current declines as shown in Figure 6-12. Additionally, it can be observed that the current's oscillations are damped quickly and the time occurrence of the peak does not change with the decrease of $\Re\{\underline{G}_{\mathrm{FFI}}\}$. This shows that the value of $\Re\{\underline{G}_{\mathrm{FFI}}\}$ has a great influence on the AC time constants of the DFIG stator short-circuit current as has been explained.

The rest of the simulation results are shown in Figure 6-13. Upon fault occurrence the internal transient voltage decreases to its new operating value which is decided on based on the terminal voltage. The rate of change of the internal transient voltages increases significantly with the decrease of the value of $\Re\{\underline{G}_{\mathrm{FFI}}\}$, where the internal transient voltage with the lowest $\Re\{\underline{G}_{\mathrm{FFI}}\}$ value $\left(-3r_{\mathrm{R}}\right)$ is the fastest to reach its new operating point. The same is also valid for the rotor voltage. However, due to the high value of $\Re\{\underline{G}_{\mathrm{FFI}}\}$ the magnitude of the rotor voltage increases to higher values in comparison to other values, but it is still within the limit range. The high rotor voltage magnitude results in a higher DC link voltage and consequently in higher operating cycles of the chopper circuit. The torque over-shoot also decreases with the value of

$\Re\{\underline{G}_{\mathrm{FFI}}\}$ due to the lower current magnitude and the fast reduction of the internal transient voltage. Just as with the other compensation techniques, the peak short-circuit current is dominantly reactive, and the responses of the DFIG-WT active power remain almost the same for all cases. Additionally, the main inductance value also de-saturates in the same pattern and reaches its highest value at the same time.

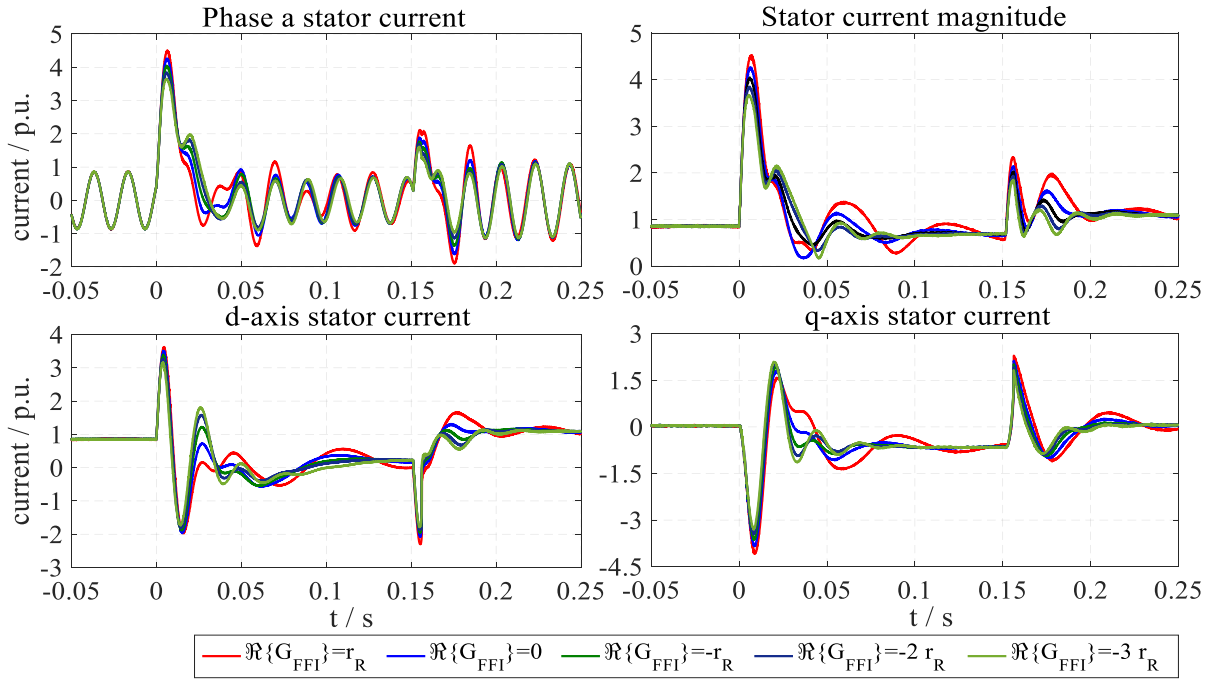

Figure 6-12 DFIG stator short-circuit current with the pole shift method

Upon fault clearance the phenomena is repeated, the internal transient voltage increases faster than in the other cases for the lowest $\Re\{\underline{G}_{\mathrm{FFI}}\}$ value, which results in a higher rotor voltage magnitude, and, consequently, in a higher DC link voltage and increased chopper operation. The torque over-shoot is almost the same for all the values because the differences between the current magnitudes at the peak time as well as the internal transient voltages are the same. Again, high reactive power is absorbed by the machine, which is dependent on the MSC controller due to the difference between the terminal voltage and the internal voltage, and due to the over-shoot in the reactive and active power for the highest $\Re\{\underline{G}_{\mathrm{FFI}}\}$ value in comparison to the other cases. This will then lead to a larger swell in the internal voltage which is followed by a greater swell of the active and reactive powers. Consequently, the speed excursion is lower due to the high active power swell.

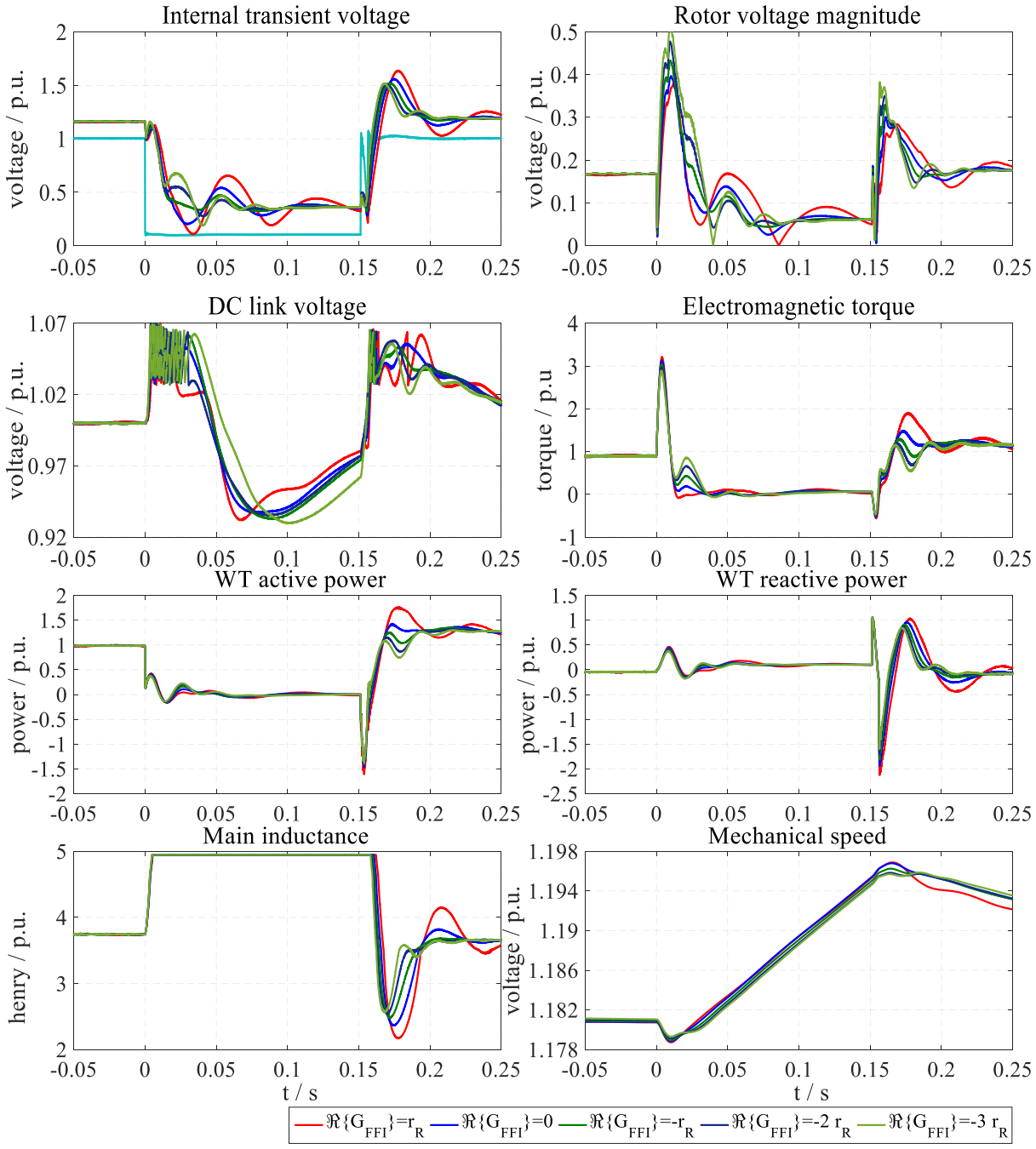

Figure 6-13 Simulation results of the transient pole shift method

7 Analysis of Unsymmetrical Fault Response

Although the probability of unsymmetrical fault types reaches almost 90% for all fault types [114], not a lot of attention is paid to the investigation of the dynamic response of the DFIG-WT during unsymmetrical faults. This might be related to the absence of any clear or specific requirements in the former grid codes [115], [116]. However, in 2015 the VDE established new grid code requirements regarding the connection of private generation facilities to the public high-voltage network [117]. According to these new requirements the generating units must remain connected in the entire operating range as long as the phase-to-phase voltages at the grid connection point within the boundaries of the curve shown in Figure 7-1 exist. Furthermore, the generating units must support the grid voltage by providing a reactive current in accordance to the slope shown in Figure 7-2.

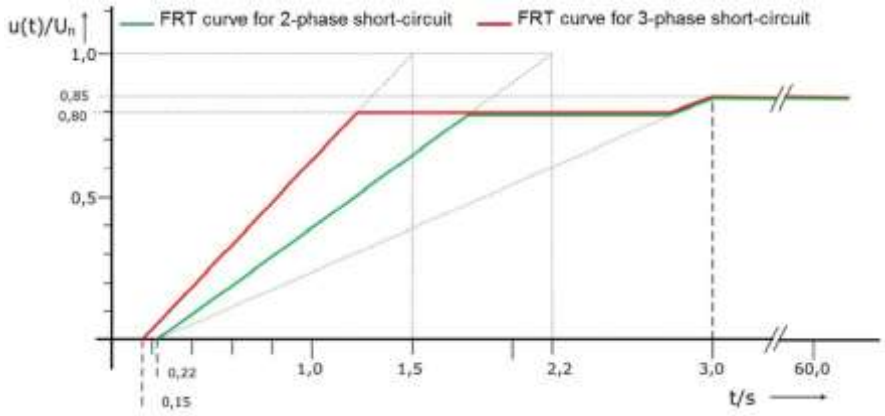

Figure 7-1 New FRT requirements according to VDE [117]

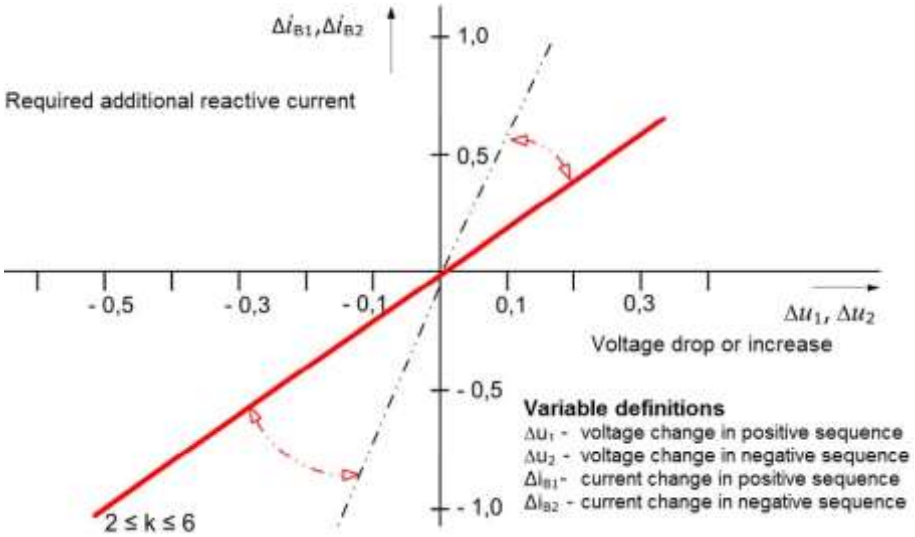

Figure 7-2 Voltage support requirements according to VDE [117]

The occurrence of unsymmetrical voltage at the terminals of the DFIG-WT produces additional torque that increases the core losses. Furthermore, the flow of negative sequence current in the machine's windings leads to a non-uniform distribution of the power losses, which

consequently results in local winding overheating and decrease of machine life expectancy [118]. Additionally, the interaction between the sequence components creates a pulsating torque on the shaft, causing audible noises and extra mechanical stress [119]. Therefore, several control approaches were proposed to solve those problems. However, there are concrete control objectives assigned to the negative sequence control in the DFIG-WT which can be realized one at a time. These are [119]:

For LSC:

1) negative sequence current suppression
2) DC link pulsating voltage suppression

For MSC:

1) no compensation
2) negative sequence current suppression
3) pulsating torque suppression

It could be determined that there is no control objective that results in a better performance than the other. This can be related, but not limited to, the following facts:

- If a full mitigation of the negative sequence currents is achieved, there will be no current left for the protection devices to sense.
- The compensation of the pulsating electromagnetic torque of the DFIG requires prioritization of the negative sequence controller in the MSC, which in that case requires the reduction of the positive sequence voltage that may lead to conflict with the grid code requirements.
- It is preferred to operate the LSC with balanced current to avoid non-uniform power losses. However, high DC link voltage pulsation decreases the service life of the capacitor.

The knowledge about the DFIG-WT dynamic response under unsymmetrical grid faults is crucial for new FRT requirement's compliance verification and for choosing the right settings of the protective devices. However, the dynamic response is solely dependent on the assigned controller objective. Therefore, in this chapter a detailed analysis of the DFIG-WT dynamic response under unsymmetrical grid faults is carried out. The analysis will be carried out for each controller objective and a mathematical interpretation of the results for each objective will be derived for a clear and deep understanding of the dynamic response.

The simulation network in Chapter 6 is used here but with a phase-to-phase fault applied between phase A and B that results in a negative sequence voltage of magnitude 0.2 p.u. at the PCC. Prior to the fault the DFIG-WT was operating at 0.6 p.u. active power set point, -0.1 slip and unity power factor. The operating conditions were chosen to allow for full control of the DFIG-WT under unsymmetrical grid fault.

The negative sequence components of the voltages and currents are separated from the original signal in accordance to eq. (4.3) which is realized through a derivative with one step delay as shown in Figure 7-3, where τ_{p} is the discrete time step of the simulation, that was set to $1\mu s$.

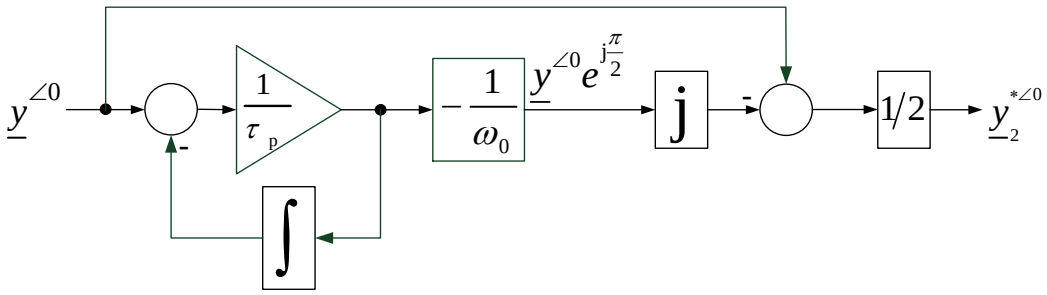

Figure 7-3 Instantaneous separation of the negative sequence component

7.1 LSC Unsymmetrical Fault Response Analysis

The negative sequence voltage equation in a fixed reference frame of the LSC is the same as for the positive sequence. Consequently, the following relations can be directly derived in the same manner as for the positive sequence:

$$\underline{v}_{\mathrm{LSC2}}^{\angle 0} = \underline{v}_{\mathrm{G2}}^{\angle 0} + (r_{\mathrm{LSC}} + sl_{\mathrm{LSC}}) \cdot \underline{i}_{\mathrm{LSC2}}^{\angle 0} \tag{7.1}$$

$$\underline{i}_{\mathrm{LSC2}}^{\angle 0}(t) = \frac{\Delta \underline{v}_{\mathrm{LSC2}}^{\angle 0} - \Delta \underline{v}_{\mathrm{G2}}^{\angle 0}}{r_{\mathrm{LSC}} + \mathrm{j}\omega_0 l_{\mathrm{LSC}}} e^{-\frac{t}{\tau_{\mathrm{LSC}}}} + \underline{i}_{\mathrm{LSC2,ss}}^{\angle 0} \tag{7.2}$$

Eq. (7.2) represents the natural fault response of the LSC under unsymmetrical fault, which resembles the natural response of an RL-circuit, where the magnitude of the transient current is dependent on the step change of both LSC and grid negative sequence voltages and the impedance value of the line choke and decays with the choke time constant.

7.1.1 LSC Response With Current Suppression

In order to suppress the LSC's negative sequence current, the LSC output voltage should be exactly the same as the grid voltage, which is realized as shown in Figure 7-4, where

$$\underline{G}_{\mathrm{meas}}^{*} = \frac{1 - \mathrm{j}\frac{1.3617\omega_0}{\omega_{\mathrm{c}}} - 0.618\left(\frac{\omega_0}{\omega_{\mathrm{c}}}\right)^2}{1 + \frac{1.3617}{\omega_{\mathrm{c}}} s + \frac{0.618}{\omega_{\mathrm{c}}^2} s^2} \tag{7.3}$$

$$\underline{G}_{\mathrm{dt}}^{*} = e^{-(s + \mathrm{j}\omega_0)\tau_{\mathrm{dt}}} \tag{7.4}$$

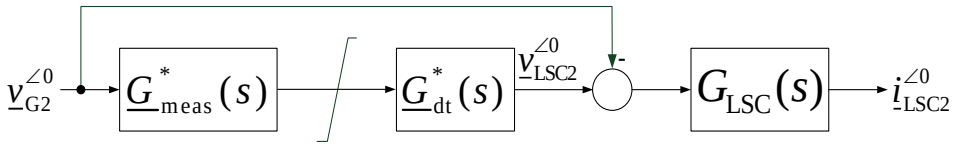

Figure 7-4 LSC controller with negative sequence current suppression

The transfer function of the LSC negative sequence current can then be derived as:

$$\underline{i}_{LSC2}^{\angle 0} = G_{LSC}(s)\left(\underline{G}_{meas}^{*}(s)\cdot\underline{G}_{dt}^{*}(s)-1\right)\underline{v}_{G2}^{\angle 0} \qquad (7.5)$$

Neglecting the delay introduced by the controller would result in a full rejection of the grid voltage and, consequently, the dynamic response can be ignored completely. The resultant LSC negative sequence currents are shown in Figure 7-5. It can be observed that the resultant transient currents decay quickly, while a very small residual/ steady-state current of small magnitude remains. As a result, this residual current is not produced by the negative sequence controller, but rather by the positive sequence controller. This is due to the double grid frequency component superimposed on the DC link due to the interaction between sequence components, where the DC link voltage controller generates a d-axis reference current with this superimposed double grid frequency component. This component will then be reflected as a fundamental and a third harmonic component in the negative sequence as well as in the positive sequence. However, their magnitudes are of negligible value, because the integrator of the PI-controller will attenuate them.

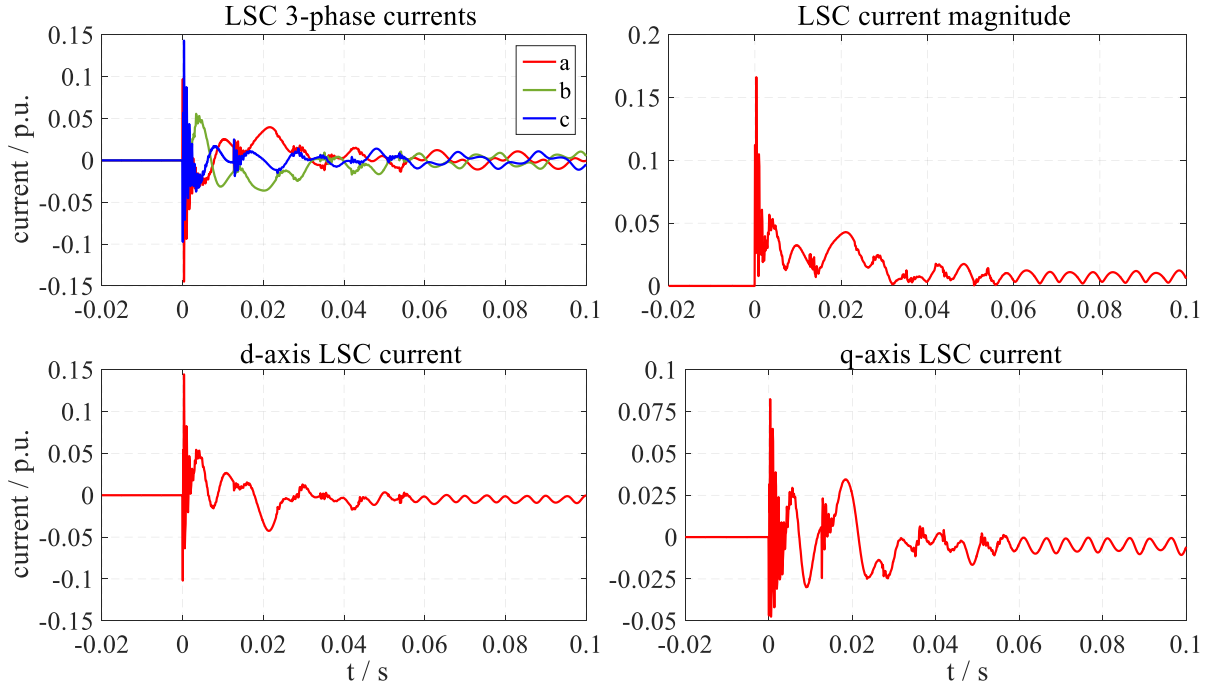

Figure 7-5 LSC negative sequence currents with negative sequence current suppression

7.1.2 LSC Response With Pulsating Voltage Suppression

As a result of unsymmetrical grid faults a pulsating active power component with twice the grid frequency occurs at the MSC and the LSC due to the interaction between sequence components. They are derived from the instantaneous active power as follows:

$$\begin{aligned}\underline{p}_{\mathrm{MSC}} &= \mathrm{Re}\left\{\left(\underline{v}_{\mathrm{MSC1}}^{\angle 0}+\underline{v}_{\mathrm{MSC2}}^{*\angle 0}\right)\cdot\left(\underline{i}_{\mathrm{MSC1}}^{*\angle 0}+\underline{i}_{\mathrm{MSC2}}^{\angle 0}\right)\right\}\\ &= \mathrm{Re}\left\{\underbrace{\underline{v}_{\mathrm{MSC1}}^{\angle 0}\cdot\underline{i}_{\mathrm{MSC1}}^{*\angle 0}}_{p_{\mathrm{MSC1}}}+\underbrace{\underline{v}_{\mathrm{MSC2}}^{*\angle 0}\cdot\underline{i}_{\mathrm{MSC2}}^{\angle 0}}_{p_{\mathrm{MSC2}}^{*}}+\underbrace{\underline{v}_{\mathrm{MSC1}}^{\angle 0}\cdot\underline{i}_{\mathrm{MSC2}}^{\angle 0}+\underline{v}_{\mathrm{MSC2}}^{*\angle 0}\cdot\underline{i}_{\mathrm{MSC1}}^{*\angle 0}}_{\tilde{p}_{\mathrm{MSC}}}\right\}\end{aligned} \tag{7.6}$$

$$\begin{aligned}\underline{p}_{\mathrm{LSC}} &= \mathrm{Re}\left\{\left(\underline{v}_{\mathrm{LSC1}}^{\angle 0}+\underline{v}_{\mathrm{LSC2}}^{*\angle 0}\right)\cdot\left(\underline{i}_{\mathrm{LSC1}}^{*\angle 0}+\underline{i}_{\mathrm{LSC2}}^{\angle 0}\right)\right\}\\ &= \mathrm{Re}\left\{\underbrace{\underline{v}_{\mathrm{LSC1}}^{\angle 0}\cdot\underline{i}_{\mathrm{LSC1}}^{*\angle 0}}_{p_{\mathrm{LSC1}}}+\underbrace{\underline{v}_{\mathrm{LSC2}}^{*\angle 0}\cdot\underline{i}_{\mathrm{LSC2}}^{\angle 0}}_{p_{\mathrm{LSC2}}^{*}}+\underbrace{\underline{v}_{\mathrm{LSC1}}^{\angle 0}\cdot\underline{i}_{\mathrm{LSC2}}^{\angle 0}+\underline{v}_{\mathrm{LSC2}}^{*\angle 0}\cdot\underline{i}_{\mathrm{LSC1}}^{*\angle 0}}_{\tilde{p}_{\mathrm{LSC}}}\right\}\end{aligned} \tag{7.7}$$

The pulsating power components can be written in a reference frame that rotates at twice the grid frequency as follows [48], [88]:

$$\begin{aligned}\tilde{p}_{\mathrm{MSC}}^{\angle -2\omega_0} &= \left(v_{\mathrm{MSC1,d}}^{\angle \omega_0}\cdot i_{\mathrm{MSC2,d}}^{\angle -\omega_0}-v_{\mathrm{MSC1,q}}^{\angle \omega_0}\cdot i_{\mathrm{MSC2,q}}^{\angle -\omega_0}+v_{\mathrm{MSC2,d}}^{\angle -\omega_0}\cdot i_{\mathrm{MSC1,d}}^{\angle \omega_0}-v_{\mathrm{MSC2,q}}^{\angle -\omega_0}\cdot i_{\mathrm{MSC1,q}}^{\angle \omega_0}\right)\\ &\quad -\mathrm{j}\left(v_{\mathrm{MSC1,d}}^{\angle \omega_0}\cdot i_{\mathrm{MSC2,q}}^{\angle -\omega_0}+v_{\mathrm{MSC1,q}}^{\angle \omega_0}\cdot i_{\mathrm{MSC2,d}}^{\angle -\omega_0}+v_{\mathrm{MSC2,d}}^{\angle -\omega_0}\cdot i_{\mathrm{MSC1,q}}^{\angle \omega_0}+v_{\mathrm{MSC2,q}}^{\angle -\omega_0}\cdot i_{\mathrm{MSC1,d}}^{\angle \omega_0}\right)\end{aligned} \tag{7.8}$$

$$\begin{aligned}\tilde{p}_{\mathrm{LSC}}^{\angle -2\omega_0} &= \left(v_{\mathrm{LSC1,d}}^{\angle \omega_0}\cdot i_{\mathrm{LSC2,d}}^{\angle -\omega_0}-v_{\mathrm{LSC1,q}}^{\angle \omega_0}\cdot i_{\mathrm{LSC2,q}}^{\angle -\omega_0}+v_{\mathrm{LSC2,d}}^{\angle -\omega_0}\cdot i_{\mathrm{LSC1,d}}^{\angle \omega_0}-v_{\mathrm{LSC2,q}}^{\angle -\omega_0}\cdot i_{\mathrm{LSC1,q}}^{\angle \omega_0}\right)\\ &\quad -\mathrm{j}\left(v_{\mathrm{LSC1,d}}^{\angle \omega_0}\cdot i_{\mathrm{LSC2,q}}^{\angle -\omega_0}+v_{\mathrm{LSC1,q}}^{\angle \omega_0}\cdot i_{\mathrm{LSC2,d}}^{\angle -\omega_0}+v_{\mathrm{LSC2,d}}^{\angle -\omega_0}\cdot i_{\mathrm{LSC1,q}}^{\angle \omega_0}+v_{\mathrm{LSC2,q}}^{\angle -\omega_0}\cdot i_{\mathrm{LSC1,d}}^{\angle \omega_0}\right)\end{aligned} \tag{7.9}$$

Due to the power imbalance between the MSC and LSC, this pulsating power components will be superimposed on the DC link. The relationship between the pulsating power and the DC voltage, neglecting the converter losses, is given by:

$$\frac{d}{dt}\tilde{\underline{v}}_{\mathrm{DC}}^{\angle 0}=\frac{\tilde{p}_{\mathrm{MSC}}+\tilde{p}_{\mathrm{LSC}}}{v_{\mathrm{DC}}} \tag{7.10}$$

where

$$\tilde{\underline{v}}_{\mathrm{DC}}^{\angle 0}=\tilde{v}_{\mathrm{DC}}^{\angle -2\omega_0}e^{-\mathrm{j}2\omega_0 t} \tag{7.11}$$

In order to fully suppress the DC link voltage oscillation the following needs to be satisfied:

$$\tilde{p}_{\mathrm{MSC}}+\tilde{p}_{\mathrm{LSC}}=0 \tag{7.12}$$

This is realized by letting the LSC negative sequence current be equal to:

$$\underline{i}_{\mathrm{LSC2}}^{\angle -\omega_0}=\frac{\underline{i}_{\mathrm{LSC1}}^{\angle \omega_0}\underline{v}_{\mathrm{G2}}^{\angle -\omega_0}+\tilde{p}_{\mathrm{MSC}}}{\underline{v}_{\mathrm{G1}}^{\angle \omega_0}} \tag{7.13}$$

Another approach to realize eq. (7.12) and to avoid the computational effort associated with eq. (7.13) can be chosen to extract the pulsating voltage component via a resonance filter and force it to zero via a PI-controller. This generates the required LSC negative sequence reference currents. A fast resonance filter that is based on a Lê filter is described in detail in [88], in which also a more sophisticated controller which guarantees a faster response is examined. The full schematic of the LSC controller with DC link voltage oscillation suppression is shown in Figure 7-6.

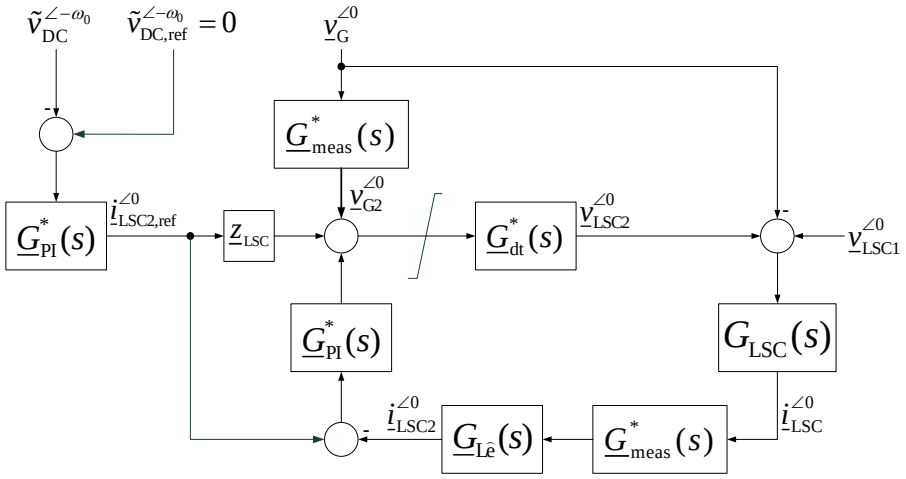

Figure 7-6 LSC controller with DC voltage pulsation suppression

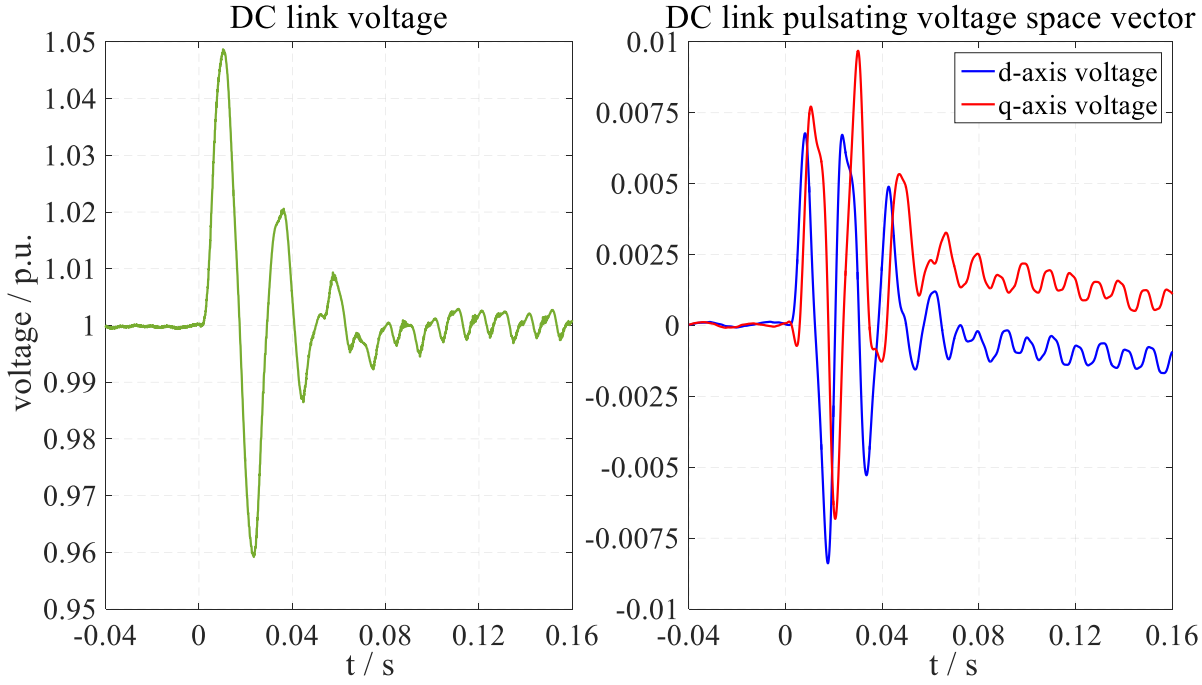

Figure 7-7 DC link voltage response under phase-to-phase fault with pulsating components suppression

The response of the DC link with the proposed controller under unsymmetrical fault ($|v_{G2}| = 0.2$) is shown in Figure 7-7. After fault initiation high over shoots occur that decay after two cycles.

These over-shoots occur in the space vector component of the pulsating components which are then gradually reduced to zero.

The pulsating voltage component is dependent on the dynamic behavior of the DFIG. For a full dynamic response analysis of the LSC negative sequence current the DFIG dynamics should be considered. However, this would lead to a highly complex analysis. Still, if the LSC inner current control loop is considered on its own, disregarding the measurement and converter delays as before, the transfer function of the LSC negative sequence current can be expresses as:

$$\frac{\underline{i}_{\mathrm{LSC2}}^{\angle 0}}{\underline{i}_{\mathrm{LSC2,ref}}^{\angle 0}} = \frac{G_{\mathrm{LSC}}(s)(\underline{G}_{\mathrm{PI}}^{*}(s) + \underline{z}_{\mathrm{LSC}})}{1 + \underline{G}_{\mathrm{LSC}}(s)\underline{G}_{\mathrm{L\hat{e}}}(s)\underline{G}_{\mathrm{PI}}^{*}(s)} \tag{7.14}$$

Substituting for each transfer function yields a characteristic polynomial of the third order. From this the time constants and eigen frequencies are derived as:

$$-\frac{1}{\tau_{\mathrm{DC}}} + \mathrm{j}\omega_{\mathrm{DC}} = -\frac{r_{\mathrm{LSC}} + k_{\mathrm{P}}}{2l_{\mathrm{LSC}}} - \mathrm{j}\frac{\omega_0}{2} - \sqrt{\left(\frac{r_{\mathrm{LSC}} + k_{\mathrm{P}}}{2l_{\mathrm{LSC}}} - \mathrm{j}\frac{\omega_0}{2}\right)^2 - \frac{l_{\mathrm{LSC}}}{k_{\mathrm{I}}}} \tag{7.15}$$

$$-\frac{1}{\tau_{\mathrm{AC1,2}}} + \mathrm{j}\omega_{\mathrm{AC1,2}} \approx -\frac{r_{\mathrm{LSC}} + 0.5k_{\mathrm{P}}}{2l_{\mathrm{LSC}}} \pm \sqrt{\left(\frac{r_{\mathrm{LSC}} + 0.5k_{\mathrm{P}}}{2l_{\mathrm{LSC}}}\right)^2 - \frac{k_{\mathrm{P}}\left(1 + \mathrm{j}k_2\left(k_1 - 1\right)\right)}{l_{\mathrm{LSC}}\tau_{\mathrm{L\hat{e}}}}} \tag{7.16}$$

As in the case of the positive sequence, the PI-controller is tuned to result in an overdamped system. With the time constant of the Lê filter being too small ($k_2 = 2$), the dynamic response of the LSC can be disregarded. This can be observed in Figure 7-8 which shows the LSC negative sequence transient currents, where it is clear that the magnitudes of the transient currents are too small and decay fast. Consequently, the LSC again can be considered as a current source with the negative sequence reference currents as set-points. Figure 7-9 shows the tracking behavior of the LSC negative sequence currents, where in the first half cycle after fault occurrence there are remarkable differences between the reference currents and the measured currents. However, after the first half cycle those differences are not of significance anymore.

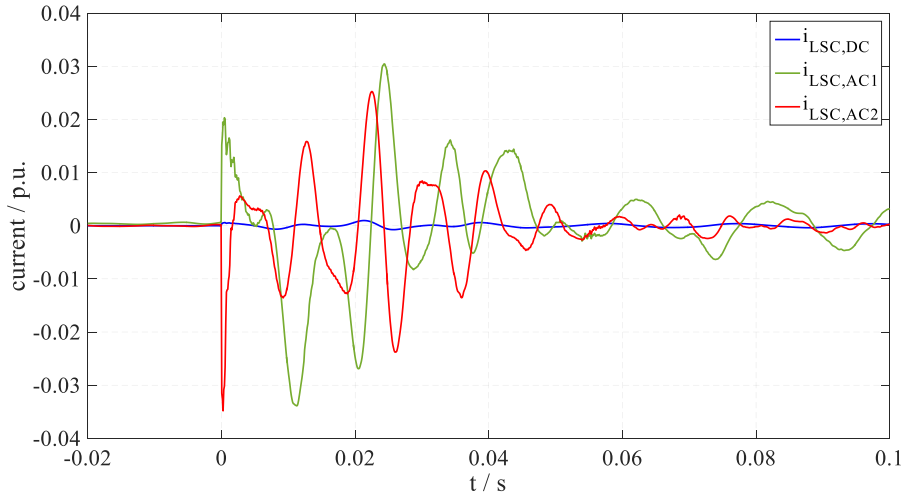

Figure 7-8 LSC negative sequence transient currents with pulsating component suppression

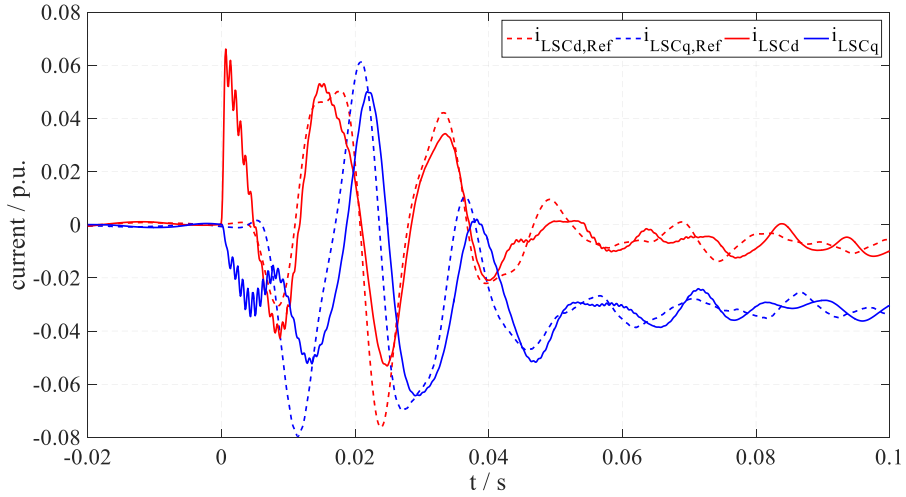

Figure 7-9 LSC negative sequence current tracking behavior with pulsating component suppression

7.2 DFIG Unsymmetrical Fault Response Analysis

From the DFIG negative sequence stator current transfer function described in eq. (3.28) the dynamic response can be also separated into fast and slow responses in the negative sequence as follows:

$$\underline{i}_{\mathrm{S2,DC}}^{\angle 0} = \frac{-\left(r_{\mathrm{R}} + \mathrm{j}\omega_{\mathrm{R}} l_{\mathrm{R}}\right)\underline{v}_{\mathrm{S2}}^{\angle 0} + s l_{\mathrm{M}}\underline{v}_{\mathrm{R2}}^{\angle 0}}{s l_{\mathrm{S}}\left(r_{\mathrm{R}} + \mathrm{j}\omega_{\mathrm{R}}\sigma l_{\mathrm{R}}\right) + r_{\mathrm{S}}\left(r_{\mathrm{R}} + \mathrm{j}\omega_{\mathrm{R}} l_{\mathrm{R}}\right)} \tag{7.17}$$

$$\underline{i}_{\mathrm{S2,AC}}^{\angle 0} = \frac{-\left(r_{\mathrm{R}} + \left(s + \mathrm{j}\omega_{\mathrm{R}}\right) l_{\mathrm{R}}\right)\underline{v}_{\mathrm{S}}^{\angle 0} + \mathrm{j}\omega_{\mathrm{S}} l_{\mathrm{M}}\underline{v}_{\mathrm{R}}^{\angle 0}}{s l_{\mathrm{R}}\left(r_{\mathrm{S}} + \mathrm{j}\omega_{\mathrm{S}}\sigma l_{\mathrm{S}}\right) + \mathrm{j}\omega_{\mathrm{R}} l_{\mathrm{R}}\left(r_{\mathrm{S}} + \mathrm{j}\omega_{\mathrm{S}}\sigma l_{\mathrm{S}}\right) + r_{\mathrm{R}}\left(r_{\mathrm{S}} + \mathrm{j}\omega_{\mathrm{S}} l_{\mathrm{S}}\right)} \tag{7.18}$$

Based on eq. (7.17) and (7.18) the time constants and eigen frequencies characterizing the negative sequence transient current are found to be:

$$\frac{1}{\tau_{\mathrm{DC}}}+\mathrm{j}\omega_{\mathrm{DC}}\approx\frac{r_{\mathrm{S}}\left(r_{\mathrm{R}}+\mathrm{j}\omega_{\mathrm{R}}l_{\mathrm{R}}\right)}{l_{\mathrm{S}}\left(r_{\mathrm{R}}+\mathrm{j}\omega_{\mathrm{R}}\sigma l_{\mathrm{R}}\right)} \tag{7.19}$$

$$\frac{1}{\tau_{\mathrm{AC}}}+\mathrm{j}\omega_{\mathrm{AC}}\approx\frac{r_{\mathrm{R}}\left(r_{\mathrm{S}}+\mathrm{j}\omega_{\mathrm{S}}l_{\mathrm{S}}\right)}{l_{\mathrm{R}}\left(r_{\mathrm{S}}+\mathrm{j}\omega_{\mathrm{S}}\sigma l_{\mathrm{S}}\right)}+\mathrm{j}\omega_{\mathrm{R}} \tag{7.20}$$

It can be seen that the values in eq. (7.19) and (7.20) are the conjugate of the values describing the time constants and eigen frequencies of the positive sequence transient currents described in eq. (5.18) and (5.19). This is a general conclusion because the negative sequence space vector is rotating in the opposite direction of the positive sequence space vector.

The transient current components constituting the total response of the DFIG stator negative sequence short-circuit current are consequently expressed as:

DC transient current:

$$\Delta\underline{i}_{\mathrm{S2,DC}}^{\angle 0}\left(t\right)=\underline{y}_{\mathrm{S2,DC}}\left(\Delta\underline{v}_{\mathrm{S2}}^{\angle 0}+\frac{l_{\mathrm{M}}r_{\mathrm{S}}}{l_{\mathrm{S}}\left(r_{\mathrm{R}}+\mathrm{j}\omega_{\mathrm{R}}\sigma l_{\mathrm{R}}\right)}\Delta\underline{v}_{\mathrm{R2}}^{\angle 0}\right)e^{-\left(\frac{1}{\tau_{\mathrm{DC}}}+\mathrm{j}\omega_{\mathrm{DC}}\right)t} \tag{7.21}$$

where,

$$\underline{y}_{\mathrm{S2,DC}}=\frac{\left(r_{\mathrm{R}}+\mathrm{j}\omega_{\mathrm{R}}l_{\mathrm{R}}\right)}{r_{\mathrm{S}}\left(r_{\mathrm{R}}+\mathrm{j}\omega_{\mathrm{R}}l_{\mathrm{R}}\right)+\mathrm{j}\omega_{\mathrm{S}}l_{\mathrm{S}}\left(r_{\mathrm{R}}+\mathrm{j}\omega_{\mathrm{R}}\sigma l_{\mathrm{R}}\right)} \tag{7.22}$$

AC transient current:

$$\Delta\underline{i}_{\mathrm{S2,AC}}^{\angle 0}\left(t\right)=\underline{y}_{\mathrm{S2,AC}}\left(\Delta\underline{v}_{\mathrm{S2}}^{\angle 0}-\frac{\mathrm{j}\omega_{\mathrm{S}}l_{\mathrm{M}}\left(r_{\mathrm{S}}+\mathrm{j}\omega_{\mathrm{S}}\sigma l_{\mathrm{S}}\right)}{\mathrm{j}\omega_{\mathrm{S}}\left(\sigma-1\right)r_{\mathrm{R}}l_{\mathrm{S}}}\Delta\underline{v}_{\mathrm{R2}}^{\angle 0}\right)e^{-\left(\frac{1}{\tau_{\mathrm{AC}}}+\mathrm{j}\omega_{\mathrm{AC}}\right)t} \tag{7.23}$$

where,

$$\underline{y}_{\mathrm{S2,AC}}=\frac{r_{\mathrm{R}}\left(1-\dfrac{\left(r_{\mathrm{S}}+\mathrm{j}\omega_{\mathrm{S}}l_{\mathrm{S}}\right)}{\left(r_{\mathrm{S}}+\mathrm{j}\omega_{\mathrm{S}}\sigma l_{\mathrm{S}}\right)}\right)}{r_{\mathrm{R}}\left(r_{\mathrm{S}}+\mathrm{j}\omega_{\mathrm{S}}l_{\mathrm{S}}\right)+\mathrm{j}\left(\omega_{\mathrm{S}}+\omega_{\mathrm{R}}\right)l_{\mathrm{R}}\left(r_{\mathrm{S}}+\mathrm{j}\omega_{\mathrm{S}}\sigma l_{\mathrm{S}}\right)} \tag{7.24}$$

Steady-state current:

$$\underline{i}_{\mathrm{S2,SS}}^{\angle 0}=\frac{-\left(r_{\mathrm{R}}+\mathrm{j}\left(\omega_{\mathrm{S}}+\omega_{\mathrm{R}}\right)l_{\mathrm{R}}\right)\underline{v}_{\mathrm{S}}^{\angle 0}+\mathrm{j}\omega_{\mathrm{S}}l_{\mathrm{M}}\underline{v}_{\mathrm{R}}^{\angle 0}}{r_{\mathrm{R}}\left(r_{\mathrm{S}}+\mathrm{j}\omega_{\mathrm{S}}l_{\mathrm{S}}\right)+\mathrm{j}\left(\omega_{\mathrm{S}}+\omega_{\mathrm{R}}\right)l_{\mathrm{R}}\left(r_{\mathrm{S}}+\mathrm{j}\omega_{\mathrm{S}}\sigma l_{\mathrm{S}}\right)} \tag{7.25}$$

Finally, the DFIG stator short-circuit space vector current is given by:

$$\underline{i}_{\mathrm{S2}}^{\angle 0}\left(t\right)=\Delta\underline{i}_{\mathrm{S2,DC}}^{\angle 0}\left(t\right)+\Delta\underline{i}_{\mathrm{S2,AC}}^{\angle 0}\left(t\right)+\underline{i}_{\mathrm{S2,SS}}^{\angle 0} \tag{7.26}$$

and the phase current will be given by:

$$i_{\mathrm{S2a}}\left(t\right)=\Re\left\{\Delta\underline{i}_{\mathrm{S2,DC}}^{\angle 0}\left(t\right)+\Delta\underline{i}_{\mathrm{S2,AC}}^{\angle 0}\left(t\right)+\underline{i}_{\mathrm{S2,SS}}^{\angle 0}\right\} \tag{7.27}$$

7.2.1 DFIG Response Without Compensation

If no control objective was assigned, the negative sequence rotor voltage would be kept at zero. Consequently, the dynamic response of the DFIG stator negative sequence current will be resultant from the step change in the stator's negative sequence voltage. Accordingly, the dynamic response of the current is described by eq. (7.26). However, due to the delays introduced by measurement delays and converter sampling as well as the delays introduced by the Lê filter, a residual rotor voltage will be measurable, which will slightly modify the dynamic response of the current. Figure 7-10 shows the resultant rotor voltage which is of a very low magnitude. Therefore, the resultant residual current will also be of a small magnitude as shown in Figure 7-11. For the sake of simplicity it will be ignored in the further analysis.

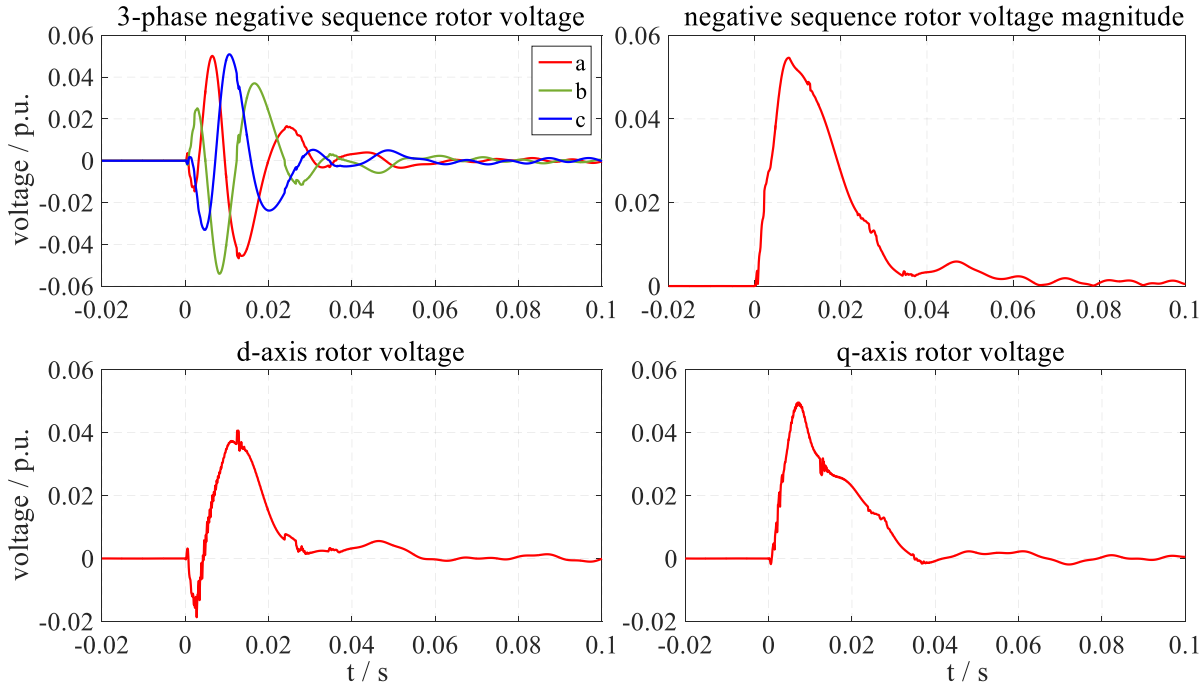

Figure 7-10 Residual negative sequence rotor voltage

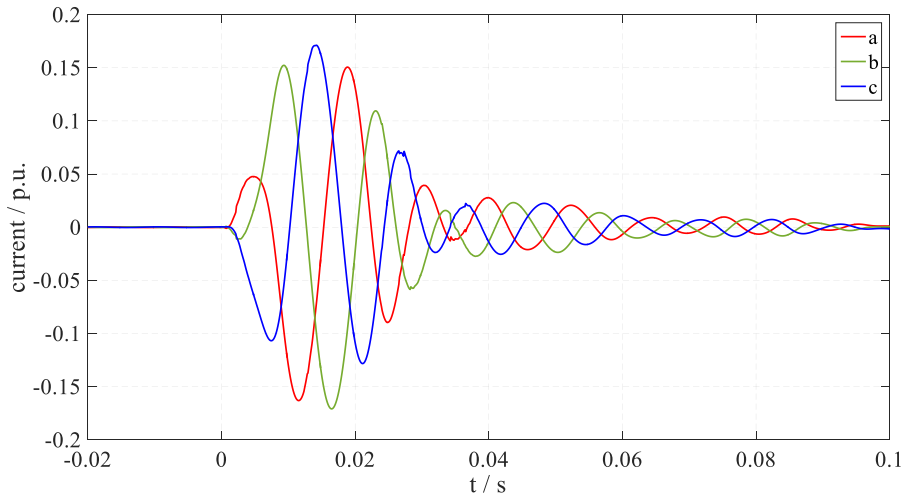

Figure 7-11 Resultant residual negative sequence stator current

The negative sequence current'S response is shown in Figure 7-12 with its transient current components shown in Figure 7-13. There are differences between the actual simulated result and the analytical result based on eq. (7.26) and (7.27) because of the residual rotor voltage. However, there is still a great resemblance between both signals, which proves the validity of the derived analytical equations. From the transient current components it can be concluded that the DFIG behaves exactly like an RL-circuit with the transient current component resultant from the rotation of a very low magnitude. It can be ignored completely. This is related to the high impedance associated with this current component and is characterized by the high value of the negative slip.

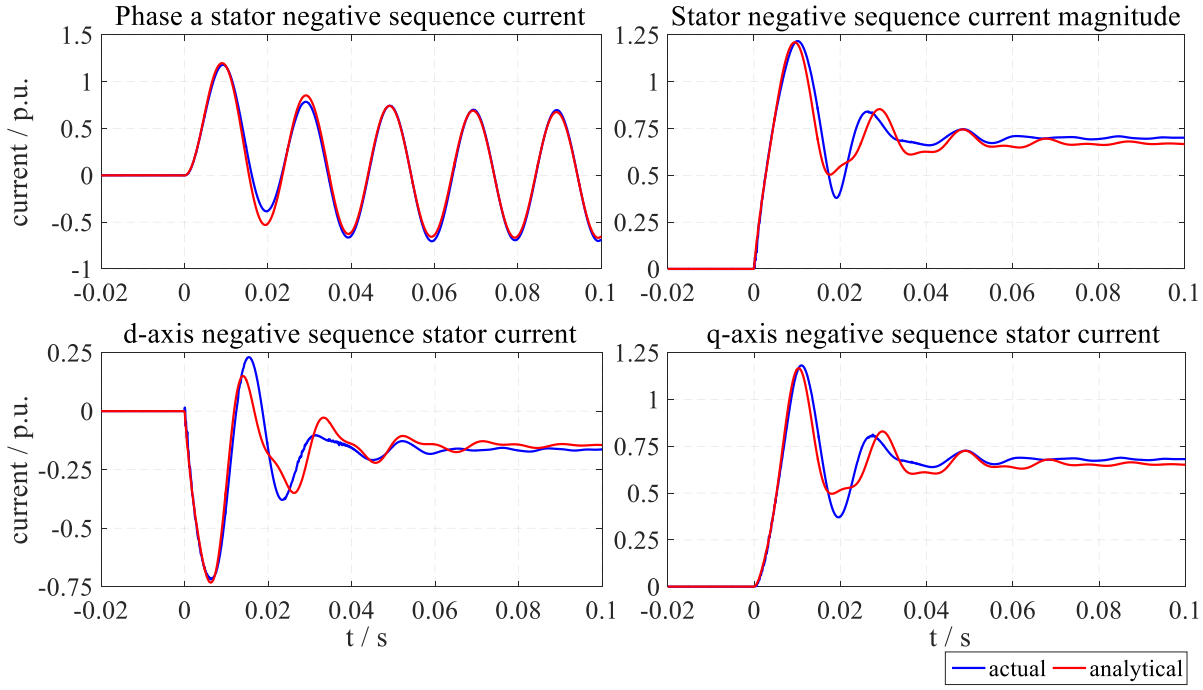

Figure 7-12 DFIG stator negative sequence current's response without compensation

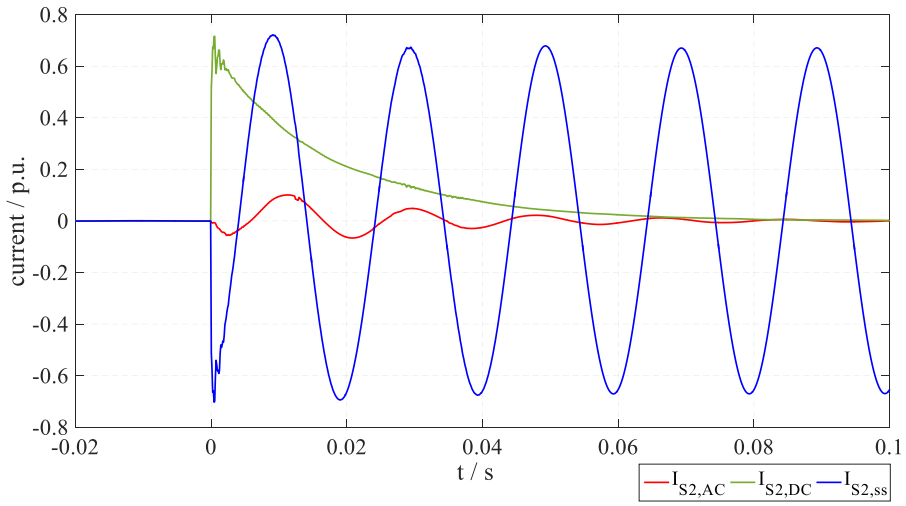

Figure 7-13 Negative sequence transient current's components without compensation

Therefore, the negative sequence current can be then described by:

$$\underline{i}_{\mathrm{S2}}^{\angle 0}(t)=\frac{\underline{v}_{\mathrm{S2}}^{\angle 0}}{\underline{z}'_{\mathrm{S2}}}\left(1-e^{-\left(\frac{1}{\tau_{\mathrm{DC}}}+\mathrm{j}\omega_{\mathrm{DC}}\right)t}\right) \tag{7.28}$$

where $\underline{z}'_{\mathrm{S2}}$ is the negative sequence transient impedance described by:

$$\underline{z}'_{\mathrm{S2}}=r_{\mathrm{S}}+\mathrm{j}\omega_{\mathrm{S}}l_{\mathrm{S}}\frac{\left(r_{\mathrm{R}}+\mathrm{j}\omega_{\mathrm{R}}\sigma l_{\mathrm{R}}\right)}{\left(r_{\mathrm{R}}+\mathrm{j}\omega_{\mathrm{R}}l_{\mathrm{R}}\right)} \tag{7.29}$$

7.2.2 DFIG Response With Negative Sequence Currents Suppression

Here, the negative sequence rotor voltage is set to minimize the required negative sequence current, which can either be the rotor current or the stator current. In this work only the suppression of the rotor's negative sequence current is discussed. However, the analysis would yield the same result if the stator's current suppression was chosen. From the space vector model of the DFIG, the required rotor negative sequence voltage for rotor negative sequence current suppression under quasi stationary conditions is given by :

$$\underline{v}_{\mathrm{R2}}^{\angle -\omega_{\mathrm{S}}}\approx s_{\mathrm{G2}}\frac{l_{\mathrm{M}}}{l_{\mathrm{S}}}\underline{v}_{\mathrm{S2}}^{\angle -\omega_{\mathrm{S}}} \tag{7.30}$$

Due to the uncertainties in the parameters' measurement the required rotor voltage is extended by a standard PI-controller and the rotor current feed forward term as follows:

$$\underline{v}_{\mathrm{R2}}^{\angle -\omega_{\mathrm{S}}}\approx s_{\mathrm{G2}}\frac{l_{\mathrm{M}}}{l_{\mathrm{S}}}\underline{v}_{\mathrm{S2}}^{\angle -\omega_{\mathrm{S}}}-\mathrm{j}s_{\mathrm{G2}}\omega_{\mathrm{S}}\sigma l_{\mathrm{R}}\underline{i}_{\mathrm{R2}}^{\angle -\omega_{\mathrm{S}}}-\left(k_{\mathrm{P}}+\frac{k_{\mathrm{I}}}{s}\right)\cdot\left(\underline{i}_{\mathrm{R2,ref}}^{\angle -\omega_{\mathrm{S}}}-\underline{i}_{\mathrm{R2}}^{\angle -\omega_{\mathrm{S}}}\right) \tag{7.31}$$

The MSC negative sequence controller will be a facsimile of the positive sequence controller but with the reference currents set to zero as shown in Figure 7-14.

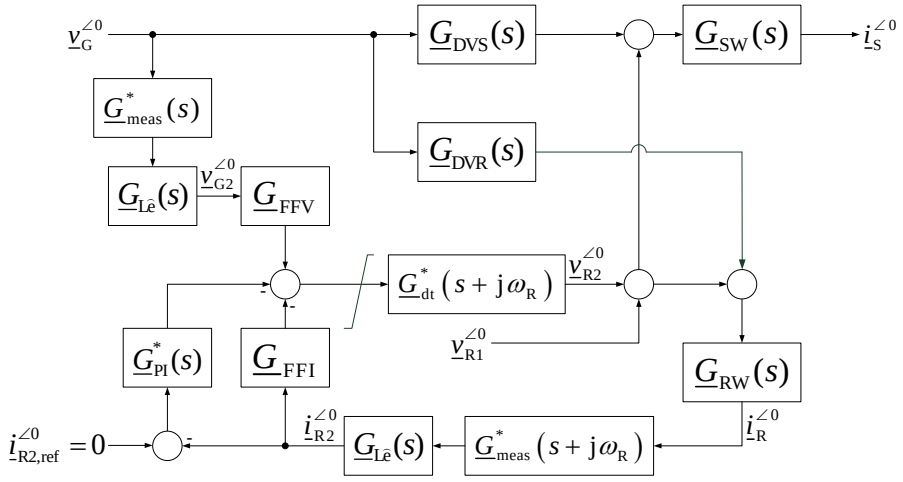

Figure 7-14 MSC negative sequence current controller

Based on Figure 7-14 the transfer function of the DFIG stator negative sequence current is found to be:

$$\underline{i}_{\mathrm{S2}}^{\angle 0} = \frac{\left(\underline{N}_{\mathrm{S}}(s) - \underline{D}_{\mathrm{S}}(s)\cdot\left(\underline{G}_{\mathrm{DVS}}(s) - \underline{G}_{\mathrm{DVR}}(s)\right)\right)\underline{v}_{\mathrm{S2}}^{\angle 0} + G_{\mathrm{PI}}^{*}(s)\cdot G_{\mathrm{dt}}^{*}\left(s+\mathrm{j}\omega_{\mathrm{R}}\right)\cdot\underline{G}_{\mathrm{SW}}(s)\underline{i}_{\mathrm{R2,ref}}^{\angle 0}}{1-\underline{D}_{\mathrm{S}}(s)} \qquad (7.32)$$

where

$$\underline{N}_{\mathrm{S}}(s) = \underline{G}_{\mathrm{SW}}(s)\cdot\left(\underline{G}_{\mathrm{DVS}}(s) + \underline{G}_{\mathrm{L\hat{e}}}(s)\cdot\underline{G}_{\mathrm{meas}}^{*}(s)\cdot\underline{G}_{\mathrm{dt}}^{*}\left(s+\mathrm{j}\omega_{\mathrm{R}}\right)\cdot\underline{G}_{\mathrm{FFV}}\right) \qquad (7.33)$$

$$\underline{D}_{\mathrm{S}}(s) = \underline{G}_{\mathrm{L\hat{e}}}(s)\cdot\underline{G}_{\mathrm{dt}}^{*}\left(s+\mathrm{j}\omega_{\mathrm{R}}\right)\cdot\underline{G}_{\mathrm{meas}}^{*}\left(s+\mathrm{j}\omega_{\mathrm{R}}\right)\cdot\underline{G}_{\mathrm{RW}}(s)\cdot\left(\underline{G}_{\mathrm{PI}}^{*}(s) - \underline{G}_{\mathrm{FFI}}\right) \qquad (7.34)$$

$$\underline{G}_{\mathrm{FFV}} = s_{\mathrm{G2}}\frac{l_{\mathrm{M}}}{l_{\mathrm{S}}}, \underline{G}_{\mathrm{FFI}} = \mathrm{j}s_{\mathrm{G2}}\omega_{\mathrm{S}}\sigma l_{\mathrm{R}} \qquad (7.35)$$

$$\underline{G}_{\mathrm{DVS}}(s) = \frac{\underline{G}_{\mathrm{SZ2}}}{\underline{G}_{\mathrm{SW2}}}, \underline{G}_{\mathrm{DVR}}(s) = \frac{\underline{G}_{\mathrm{RZ2}}}{\underline{G}_{\mathrm{RW2}}} \qquad (7.36)$$

The characteristic polynomial of the negative sequence current transfer function is of 14$^{\mathrm{th}}$ order, which impair any effort done to find an adequate mathematical interpretation of the short-circuit parameters. Therefore, again and for the sake of simplicity, the delays introduced by the measuring filters and converter sampling are neglected. The frequency response of the transfer function with and without consideration of measurement and sampling delays is shown in Figure 7-15. From the disturbing quantity response can be concluded that exclusion of both G_{meas}^{*} and G_{dt}^{*} has only minor influence on the magnitude and phase angle of the current. Yet, the responses of the reference tracking are identical in the frequency range up to 100 Hz. However, beyond this frequency the phase angle tends to be constant without measurement delays while it keeps its descending with measurement delays. Although the phase angels differ in the range beyond 100 Hz, this difference will not have any remarkable influence on the dynamic response because there are no poles or zeros beyond this frequency except for the poles and zeros of the grid filters. Accordingly, the transfer function can be further reduced to:

$$\underline{i}_{\mathrm{S2}}^{\angle 0} = \frac{\left(\underline{N}_{\mathrm{S}}(s) - \underline{D}_{\mathrm{S}}(s)\cdot\left(\underline{G}_{\mathrm{DVS}}(s) - \underline{G}_{\mathrm{DVR}}(s)\right)\right)\underline{v}_{\mathrm{S2}}^{\angle 0} + \underline{G}_{\mathrm{PI}}^{*}(s)\cdot\underline{G}_{\mathrm{SW}}(s)\underline{i}_{\mathrm{R2,ref}}^{\angle 0}}{1-\underline{D}_{\mathrm{S}}(s)} \qquad (7.37)$$

where

$$\underline{N}_{\mathrm{S}}(s) = \underline{G}_{\mathrm{SW}}(s)\cdot\left(\underline{G}_{\mathrm{DVS}}(s) + \underline{G}_{\mathrm{L\hat{e}}}(s)\cdot\underline{G}_{\mathrm{FFV}}\right) \qquad (7.38)$$

$$\underline{D}_{\mathrm{S}}(s) = \underline{G}_{\mathrm{L\hat{e}}}(s)\cdot\underline{G}_{\mathrm{RW}}(s)\cdot\left(\underline{G}_{\mathrm{PI}}^{*}(s) - \underline{G}_{\mathrm{FFI}}\right) \qquad (7.39)$$

Figure 7-16 shows the negative sequence phase currents of the DFIG stator with and without consideration of measurement and sampling delays. Even though there is a difference between

both signals, it is not great and it is mainly related to the inflected third order harmonic component produced by the superimposed double grid frequency component on the DC link. This component has a greater magnitude when measurement and sampling delays are considered due to the extra delays in the system.

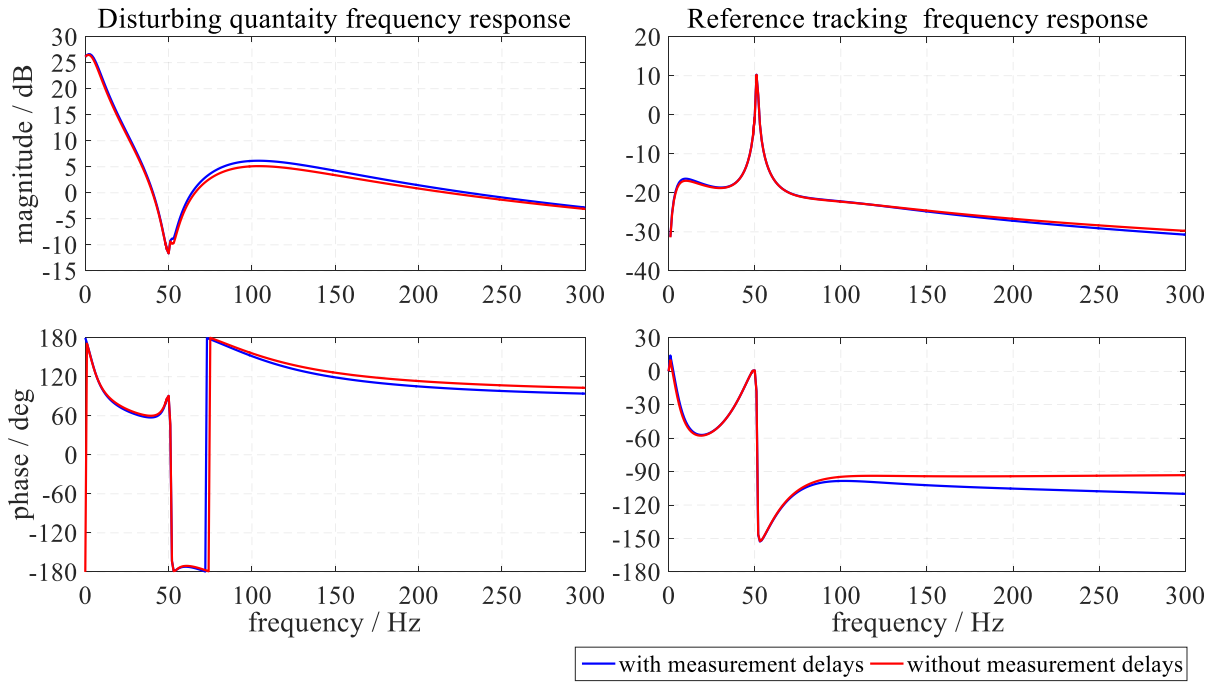

Figure 7-15 Influence of measurement delays' exclusion on DFIG stator's negative sequence current frequency response

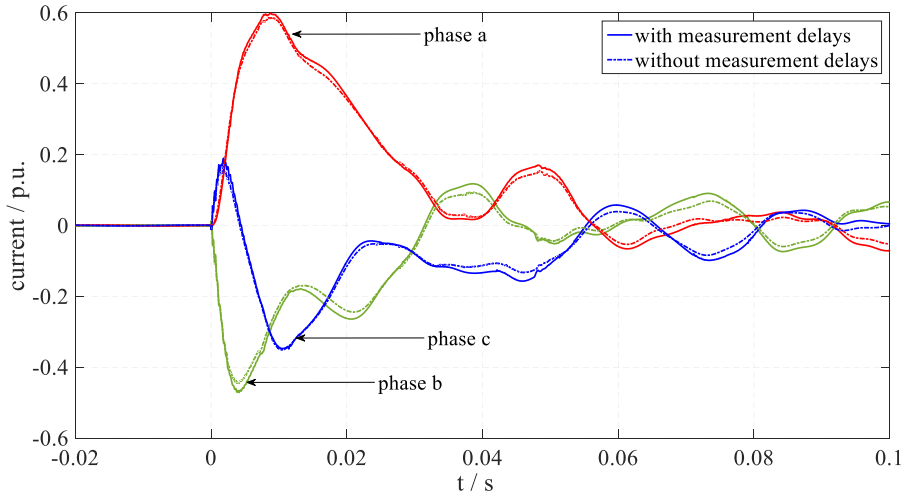

Figure 7-16 DFIG stator's negative sequence phase currents with and without measurement delays

The characteristic polynomial of the simplified transfer function derived in eq. (7.37) is of 5th order, which is again difficult to analyze. However, taking a closer look at Figure 7-17, this shows the negative sequence short-circuit current in the simulation and in the analytical result based on eq. (7.37). From this it can be deduced that the analytical result resembles the actual simulated signal and only a small difference exists resulting from the inflected third harmonic

component produced by the superimposed double grid frequency component on the DC link. It should be noted that it is very difficult to account for such a component analytically. That is why it is excluded from the analysis. Based on the analytical interpretation the different transient currents are shown in Figure 7-18.

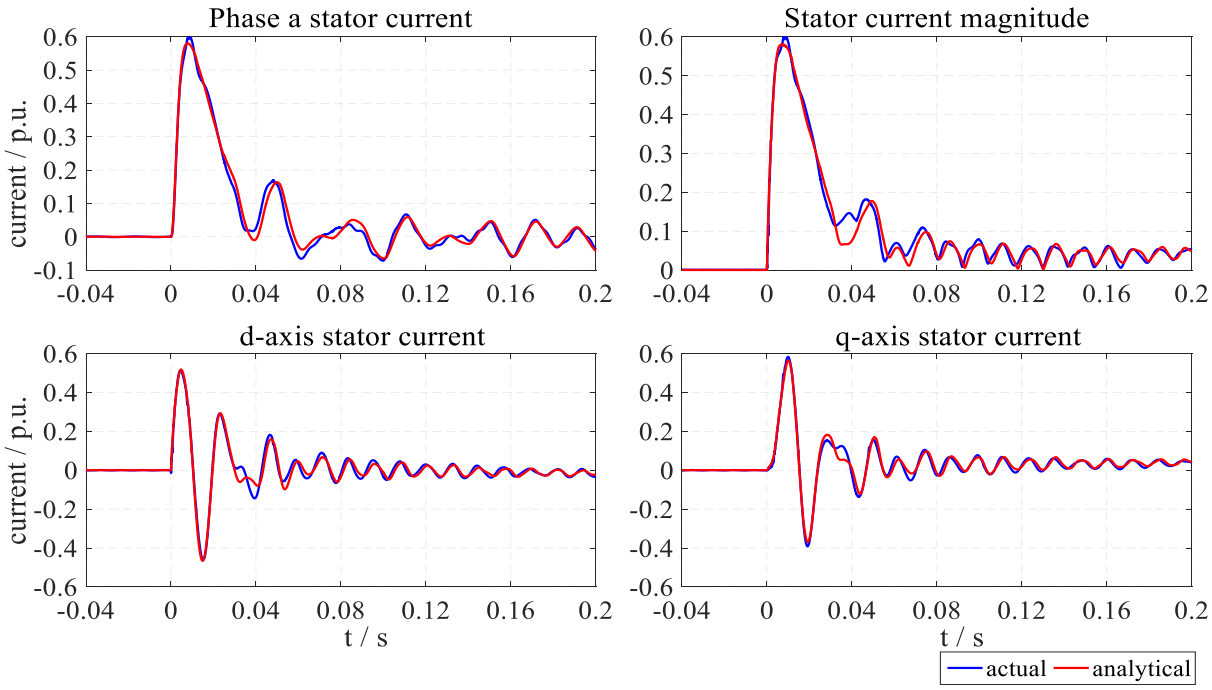

Figure 7-17 DFIG stator's negative sequence short-circuit current with rotor current suppression control

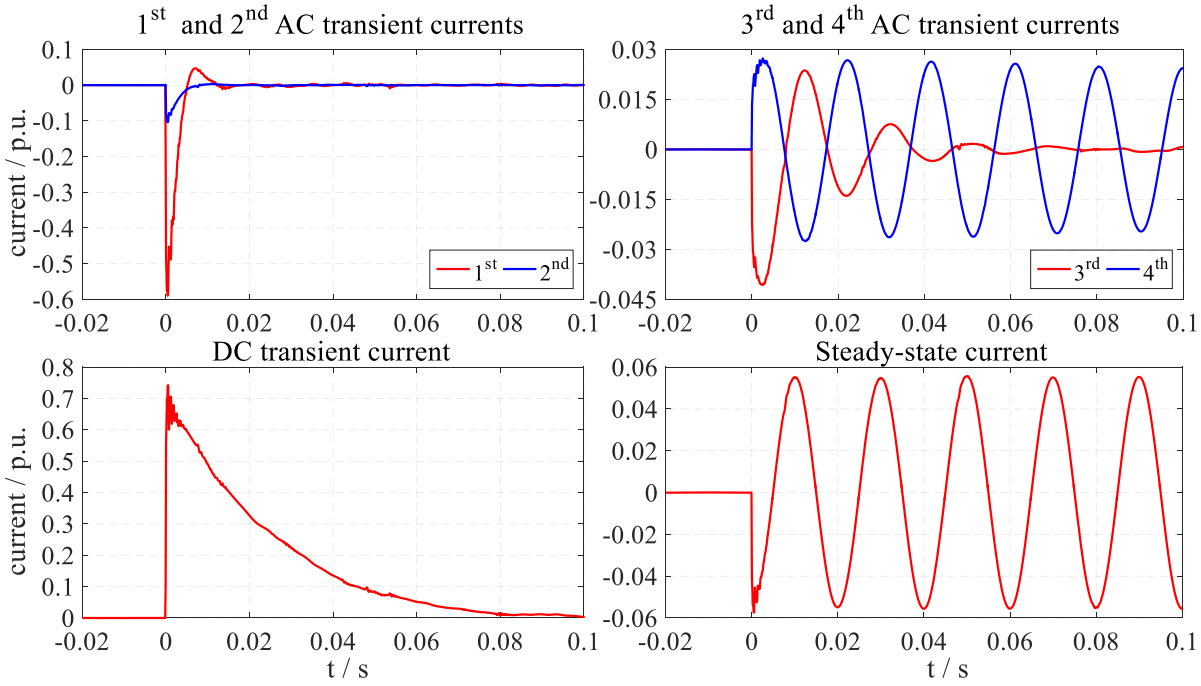

Figure 7-18 DFIG stator's negative sequence transient current components with rotor current suppression control

There are four different AC transient currents, a DC transient current and a steady-state short-circuit current. The first two AC transient currents are mainly characterized by the Lê filter's

time constants, while the third and fourth are characterized by the machine electrical parameters and the PI-controller's parameters. The DC transient current is characterized by a combination dominated by the machine's electrical parameters and partially influenced by the Lê filter's time constants and the PI-controller's parameters. The steady-state fault current can be easily described by:

$$\underline{i}_{\mathrm{S2,SS}}^{\angle 0} = \frac{\underline{v}_{\mathrm{S2}}^{\angle 0}}{r_{\mathrm{S}} + \mathrm{j}\omega_{\mathrm{S}} l_{\mathrm{S}}} \tag{7.40}$$

With the same procedure as for the symmetrical fault the DFIG dynamic response is separated into fast and slow. Thus, the resultant transfer functions are:

$$\underline{i}_{\mathrm{S2,DC}}^{\angle 0} = \frac{0.5\dfrac{1+\mathrm{j}(k_1-1)k_2}{1-\mathrm{j}\omega_{\mathrm{S}}\tau_{\mathrm{L\hat{e},2}}}\left(\underline{G}_{\mathrm{FFV}} l_{\mathrm{M}} s - k_{\mathrm{P}} - \mathrm{j}\dfrac{k_{\mathrm{I}}}{\omega_{\mathrm{S}}} - \underline{G}_{\mathrm{FFI}}\right) - r_{\mathrm{R}} - \mathrm{j}\omega_{\mathrm{R}} l_{\mathrm{R}}}{\underline{a}_1 s + \underline{a}_0} \underline{v}_{\mathrm{S2}}^{\angle 0} \tag{7.41}$$

where

$$\underline{a}_1 = l_{\mathrm{S}}\left(r_{\mathrm{R}} + \mathrm{j}\omega_{\mathrm{R}}\sigma l_{\mathrm{R}} + \underline{G}_{\mathrm{L\hat{e}}}\left(k_{\mathrm{P}} + \mathrm{j}\frac{k_{\mathrm{I}}}{\omega_{\mathrm{S}}} + \underline{G}_{\mathrm{FFI}}\right)\right) \tag{7.42}$$

$$\underline{a}_0 = r_{\mathrm{S}}\left(r_{\mathrm{R}} + \mathrm{j}\omega_{\mathrm{R}} l_{\mathrm{R}} + \underline{G}_{\mathrm{L\hat{e}}}\left(k_{\mathrm{P}} + \mathrm{j}\frac{k_{\mathrm{I}}}{\omega_{\mathrm{S}}} + \underline{G}_{\mathrm{FFI}}\right)\right) \tag{7.43}$$

while

$$\underline{i}_{\mathrm{S2,AC}}^{\angle 0} = \frac{\underline{N}_{\mathrm{S}}(s) - \underline{D}_{\mathrm{S}}(s)\cdot\left(\underline{G}_{\mathrm{DVS}}(s) - \underline{G}_{\mathrm{DVR}}(s)\right)}{1-\underline{D}_{\mathrm{S}}(s)} \underline{v}_{\mathrm{S2}}^{\angle 0} \tag{7.44}$$

where $\underline{N}_{\mathrm{S}}(s)$ and $\underline{D}_{\mathrm{S}}(s)$ are the same as in eq. (7.32) and (7.33) but with the RMS representation for $\underline{G}_{\mathrm{DVS}}(s)$, $\underline{G}_{\mathrm{DVR}}(s)$, $\underline{G}_{\mathrm{RW}}(s)$ and $\underline{G}_{\mathrm{SW}}(s)$.

From eq. (7.41) the DC time constant and eigen frequency are found to be:

$$-\frac{1}{\tau_{\mathrm{DC}}} + \mathrm{j}\omega_{\mathrm{DC}} = -\frac{r_{\mathrm{S}}}{l_{\mathrm{S}}} \frac{r_{\mathrm{R}} + \mathrm{j}\omega_{\mathrm{R}} l_{\mathrm{R}} + 0.5\dfrac{1+\mathrm{j}(k_1-1)k_2}{1-\mathrm{j}\omega_{\mathrm{S}}\tau_{\mathrm{L\hat{e},2}}}\left(k_{\mathrm{P}} + \mathrm{j}\left(\dfrac{k_{\mathrm{I}}}{\omega_0} + (\omega_{\mathrm{S}} + \omega_{\mathrm{R}})\sigma l_{\mathrm{R}}\right)\right)}{r_{\mathrm{R}} + \mathrm{j}\omega_{\mathrm{R}}\sigma l_{\mathrm{R}} + 0.5\dfrac{1+\mathrm{j}(k_1-1)k_2}{1-\mathrm{j}\omega_{\mathrm{S}}\tau_{\mathrm{L\hat{e},2}}}\left(k_{\mathrm{P}} + \mathrm{j}\left(\dfrac{k_{\mathrm{I}}}{\omega_0} + (\omega_{\mathrm{S}} + \omega_{\mathrm{R}})\sigma l_{\mathrm{R}}\right)\right)} \tag{7.45}$$

which for practical parameters of the PI-controller can be further reduced to:

$$-\frac{1}{\tau_{DC}}+\mathrm{j}\omega_{DC}\approx-\frac{r_S}{\sigma l_S}\frac{2\omega_R+(\omega_S+\omega_R)\sigma\dfrac{1+\mathrm{j}(k_1-1)k_2}{1-\mathrm{j}\omega_S\tau_{L\hat{e},2}}}{2\omega_R+(\omega_S+\omega_R)\dfrac{1+\mathrm{j}(k_1-1)k_2}{1-\mathrm{j}\omega_S\tau_{L\hat{e},2}}} \tag{7.46}$$

while the transient impedance is found to be:

$$\underline{z}'_{S2}=r_S+\mathrm{j}\omega_S l_S\left(\frac{r_R+\mathrm{j}\omega_R\sigma l_R+0.5\dfrac{1+\mathrm{j}(k_1-1)k_2}{1-\mathrm{j}\omega_S\tau_{L\hat{e},2}}\left(k_P+\mathrm{j}\left(\dfrac{k_I}{\omega_S}+(\omega_S+\omega_R)\sigma l_R\right)\right)}{r_R+\mathrm{j}\omega_R l_R+0.5\dfrac{1+\mathrm{j}(k_1-1)k_2}{1-\mathrm{j}\omega_S\tau_{L\hat{e},2}}\left(k_P+\mathrm{j}\left(\dfrac{k_I}{\omega_S}+(\omega_S+\omega_R)\sigma l_R\right)\right)}\right) \tag{7.47}$$

which again can be further reduced to:

$$\underline{z}'_{S2}=r_S+\mathrm{j}\omega_S\sigma l_S\left(\frac{2\omega_R+(\omega_S+\omega_R)\dfrac{1+\mathrm{j}(k_1-1)k_2}{1-\mathrm{j}\omega_S\tau_{L\hat{e},2}}}{2\omega_R+(\omega_S+\omega_R)\sigma\dfrac{1+\mathrm{j}(k_1-1)k_2}{1-\mathrm{j}\omega_S\tau_{L\hat{e},2}}}\right) \tag{7.48}$$

The characteristic polynomial of the transfer function in eq. (7.44) is still of fourth order and any mathematical interpretation of the time constants and eigen frequencies would yield a very complex equation. However, some procedures can be employed to help in finding a reasonable mathematical representation of the time constants and eigen frequencies. Firstly, by taking a closer look at the transient components one can realize that the third and fourth transient currents are of a very small magnitude. The real reason behind this is that the Lê filter impedes a fast-decoupled control achieved by the feed-forward terms. Consequently, at the beginning of the fault the error voltage produced by the PI-controller experiences a very high transient impedance of the rotor circuit described by:

$$\underline{z}'_{R2}\approx\left.\frac{1}{\underline{G}_{RW}}\right|_{s\to\mathrm{j}\omega_S}\approx r_R+\mathrm{j}s_{G2}\omega_S l_R\frac{r_S+\mathrm{j}\omega_S\sigma l_S}{r_S+\mathrm{j}\omega_S l_S} \tag{7.49}$$

Secondly, the fourth transient current which represents the rotating component's response to the fault is too small. This implies that it can be ignored. Finally, the time constant of the Lê filter $\tau_{L\hat{e},1}$ is too small compared to others and it can also be ignored. Both the first and second AC transient currents can be represented by one equivalent AC transient current. Based on the proposed procedures the following mathematical interpretation is derived:

$$-\frac{1}{\tau_{\mathrm{AC1\&2}}}+\mathrm{j}\omega_{\mathrm{AC1\&2}}\approx-\frac{\omega_{\mathrm{R}}\tau_{\mathrm{L\hat{e},2}}+s_{\mathrm{G}2}\omega_{\mathrm{S}}\left(1-\mathrm{j}k_2\right)\tau_{\mathrm{L\hat{e},1}}-\mathrm{j}\left(1-\mathrm{j}\omega_{\mathrm{S}}\tau_{\mathrm{L\hat{e},2}}\right)\left(1+\mathrm{j}\omega_{\mathrm{R}}\tau_{\mathrm{L\hat{e},1}}\right)}{\tau_{\mathrm{L\hat{e},1}}\tau_{\mathrm{L\hat{e},2}}\left(s_{\mathrm{G}2}\omega_{\mathrm{S}}-\mathrm{j}\left(\frac{1}{\tau_{\mathrm{L\hat{e},2}}}+\frac{1}{\tau_{\mathrm{L\hat{e},1}}}-\mathrm{j}\omega_{\mathrm{S}}\right)\right)}+\mathrm{j}\omega_{\mathrm{S}} \tag{7.50}$$

$$-\frac{1}{\tau_{\mathrm{AC3}}}+\mathrm{j}\omega_{\mathrm{AC3}}\approx-\frac{\left(r_{\mathrm{S}}+\mathrm{j}\omega_0 l_{\mathrm{S}}\right)}{\left(r_{\mathrm{S}}+\mathrm{j}\omega_0\sigma l_{\mathrm{S}}\right)l_{\mathrm{R}}}\left(r_{\mathrm{R}}+k_{\mathrm{P}}+\mathrm{j}s_{\mathrm{G}2}\omega_{\mathrm{S}}\sigma l_{\mathrm{R}}\right)+\mathrm{j}\omega_{\mathrm{S}} \tag{7.51}$$

$$-\frac{1}{\tau_{\mathrm{AC4}}}+\mathrm{j}\omega_{\mathrm{AC4}}\approx\mathrm{j}\omega_{\mathrm{S}}\frac{\left(r_{\mathrm{S}}+\mathrm{j}\omega_{\mathrm{S}}l_{\mathrm{S}}\right)\left(r_{\mathrm{R}}+k_{\mathrm{P}}+\mathrm{j}\frac{k_{\mathrm{I}}}{\omega_{\mathrm{S}}}+\mathrm{j}s_{\mathrm{G}2}\omega_{\mathrm{S}}\sigma l_{\mathrm{R}}\right)+\mathrm{j}\omega_{\mathrm{R}}l_{\mathrm{R}}\left(r_{\mathrm{S}}+\mathrm{j}\omega_{\mathrm{S}}\sigma l_{\mathrm{S}}\right)}{\left(r_{\mathrm{S}}+\mathrm{j}\omega_{\mathrm{S}}l_{\mathrm{S}}\right)\left(r_{\mathrm{R}}+k_{\mathrm{P}}+\mathrm{j}s_{\mathrm{G}2}\omega_{\mathrm{S}}\sigma l_{\mathrm{R}}\right)+\mathrm{j}\omega_{\mathrm{R}}l_{\mathrm{R}}\left(r_{\mathrm{S}}+\mathrm{j}\omega_{\mathrm{S}}\sigma l_{\mathrm{S}}\right)} \tag{7.52}$$

It is clear that the expressions of the time constants and eigen frequencies characterizing the AC transient currents are complicated. Therefore, in order to reduce the computational effort to calculate the negative sequence short-circuit current, the third and fourth AC transient currents can be ignored. Then, the equivalent time constant and eigen frequency representing the first two AC transient currents can be expressed by:

$$-\frac{1}{\tau_{\mathrm{AC}}}+\mathrm{j}\omega_{\mathrm{AC}}\approx-0.5\left(\frac{1}{\tau_{\mathrm{L\hat{e},2}}}+\frac{1}{\tau_{\mathrm{L\hat{e},1}}}\right)-\mathrm{j}\omega_{\mathrm{S}} \tag{7.53}$$

Consequently, the negative sequence short-circuit current can be expressed as:

$$\underline{i}_{\mathrm{S2}}^{\angle 0}\left(t\right)=\frac{\underline{v}_{\mathrm{S2}}^{\angle 0}}{\underline{z}'_{\mathrm{S2}}}\left(e^{-\left(\frac{1}{\tau_{\mathrm{DC}}}+\mathrm{j}\omega_{\mathrm{DC}}\right)t}-\frac{\underline{z}'_{\mathrm{S2}}}{\underline{z}'_{\mathrm{S2}}-\underline{z}_{\mathrm{S2,ss}}}e^{-\left(\frac{1}{\tau_{\mathrm{AC}}}+\mathrm{j}\omega_{\mathrm{AC}}\right)t}\right)-\underline{i}_{\mathrm{S2,SS}}^{\angle 0} \tag{7.54}$$

Figure 7-19 shows the difference between the actual simulated negative sequence current and the proposed approximate mathematical interpretation of it. It becomes clear that the proposed equation gives a very good representation of the actual current.

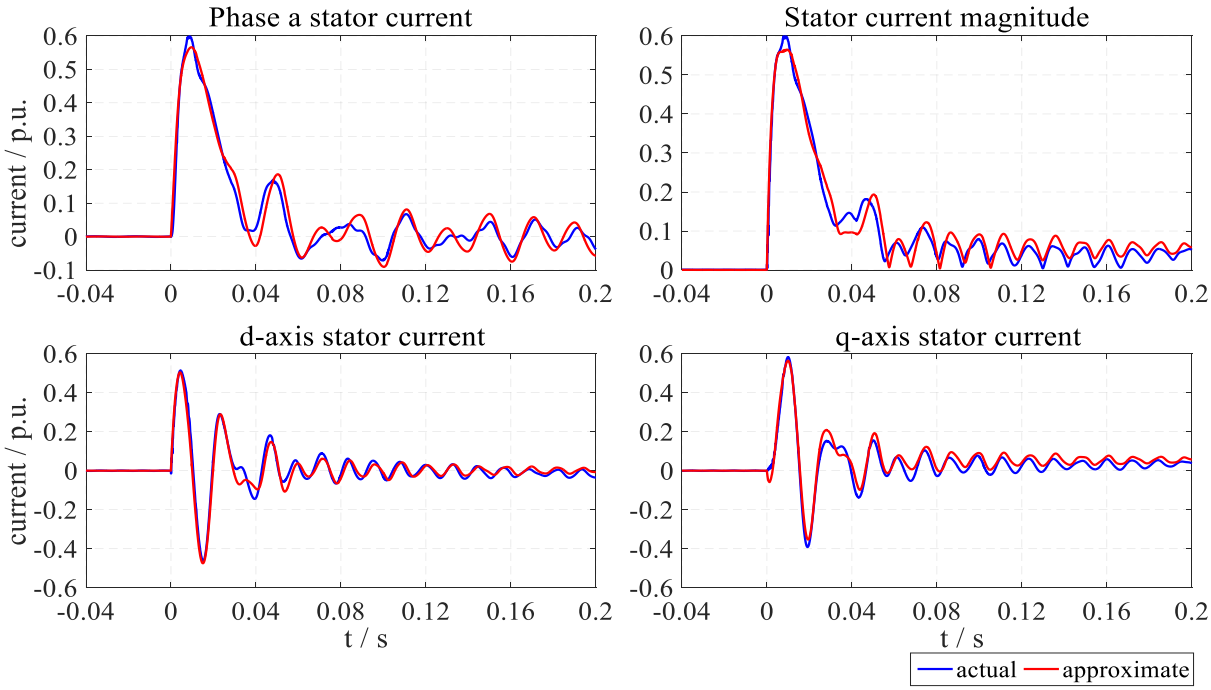

Figure 7-19 Approximate representation of the DFIG stator's negative sequence short-circuit current with rotor current suppression control

7.2.3 DFIG Response With Pulsating Torque Suppression

The pulsating electromagnetic torque is given by:

$$\tilde{t}_{\mathrm{el}}(t) = \mathrm{Im}\left\{\underline{\psi}_{\mathrm{S1}}^{\angle 0}\,\underline{i}_{\mathrm{S2}}^{\angle 0} + \underline{\psi}_{\mathrm{S2}}^{*\angle 0}\,\underline{i}_{\mathrm{S1}}^{*\angle 0}\right\} \tag{7.55}$$

The pulsating torque can be rewritten in a rotating reference frame as follows [119]:

$$\tilde{t}_{\mathrm{el}}(t) = \mathrm{Im}\left\{\underline{\psi}_{\mathrm{S1}}^{\angle\omega_{\mathrm{S}}}\,\underline{i}_{\mathrm{S2}}^{\angle-\omega_{\mathrm{S}}} e^{\mathrm{j}2\omega_{\mathrm{S}}t} + \left(\underline{\psi}_{\mathrm{S2}}^{\angle-\omega_{\mathrm{S}}}\,\underline{i}_{\mathrm{S1}}^{\angle\omega_{\mathrm{S}}} e^{\mathrm{j}2\omega_{\mathrm{S}}t}\right)^{*}\right\} \tag{7.56}$$

Substituting for the stator voltages and neglecting the stator resistances yields:

$$\tilde{t}_{\mathrm{el}}(t) \approx \frac{1}{\omega_{\mathrm{S}}}\,\mathrm{Re}\left\{\underline{v}_{\mathrm{S1}}^{\angle\omega_{\mathrm{S}}}\,\underline{i}_{\mathrm{S2}}^{\angle-\omega_{\mathrm{S}}} e^{\mathrm{j}2\omega_{\mathrm{S}}t} - \left(\underline{v}_{\mathrm{S2}}^{\angle-\omega_{\mathrm{S}}}\,\underline{i}_{\mathrm{S1}}^{\angle\omega_{\mathrm{S}}} e^{\mathrm{j}2\omega_{\mathrm{S}}t}\right)^{*}\right\} \tag{7.57}$$

In order to suppress the pulsating torque the following needs to be satisfied:

$$\underline{v}_{\mathrm{S1}}^{\angle\omega_{\mathrm{S}}}\,\underline{i}_{\mathrm{S2}}^{\angle-\omega_{\mathrm{S}}} = \underline{v}_{\mathrm{S2}}^{\angle-\omega_{\mathrm{S}}}\,\underline{i}_{\mathrm{S1}}^{\angle\omega_{\mathrm{S}}} \tag{7.58}$$

From this follows:

$$\underline{i}_{\mathrm{S2}}^{\angle-\omega_{\mathrm{S}}} = \frac{\underline{v}_{\mathrm{S2}}^{\angle-\omega_{\mathrm{S}}}}{\underline{v}_{\mathrm{S1}}^{\angle\omega_{\mathrm{S}}}}\,\underline{i}_{\mathrm{S1}}^{\angle\omega_{\mathrm{S}}} \tag{7.59}$$

The required negative sequence rotor reference current is then derived by substituting for it. This yields the following relationship:

$$\underline{i}_{\mathrm{R2,ref}}^{\angle -\omega_\mathrm{S}} = \left(-\frac{l_\mathrm{S}}{l_\mathrm{M}} \frac{\underline{i}_{\mathrm{S1}}^{\angle \omega_\mathrm{S}}}{\underline{v}_{\mathrm{S1}}^{\angle \omega_\mathrm{S}}} + \mathrm{j}\frac{1}{\omega_0 l_\mathrm{M}} \right) \underline{v}_{\mathrm{S2}}^{\angle -\omega_\mathrm{S}} \tag{7.60}$$

It should be noted that the real operator in eq. (7.57) was eliminated in the further procedure. However, the influence of this elimination will be discussed at a later point.

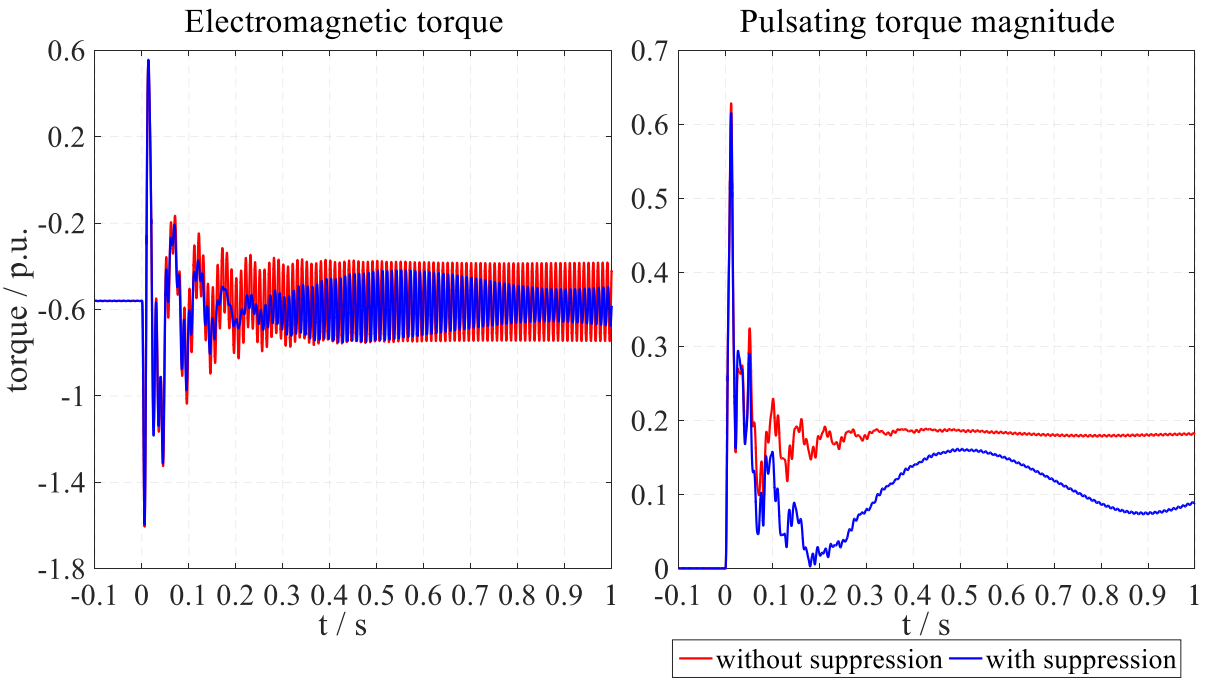

Figure 7-20 DFIG electromagnetic response with pulsating torque suppression control

Figure 7-20 shows the influence of pulsating torque suppression control on the DFIG electromagnetic torque. It is clear that the magnitude of the pulsating torque is reduced. However, it is also plain that the controller was too slow. Again, as discussed earlier, the error voltage output of the PI-controller experiences a high rotor transient impedance. The resulting time constant of the produced transient current is too great, as described in eq. (7.52). This shows that it takes too long for the rotor negative sequence current to track its reference value. Additionally, the reference currents are dependent on the dynamic response of the stator current, which is also influenced by several transient components as has been discussed earlier. An alternative method will be proposed at the end of this chapter that will increase the speed of response of the machine.

The controller configuration will be exactly the same as in Figure 7-14. However, the rotor reference current will be set as in eq. (7.60). Accordingly, the stator's negative sequence transfer function, excluding measurement and sampling delays, is found to be:

$$\underline{i}_{\mathrm{S2}}^{\angle 0} = \frac{\underline{N}_\mathrm{S}(s) - \underline{D}_\mathrm{S}(s)\cdot\left(\underline{G}_{\mathrm{DVS}}(s) - \underline{G}_{\mathrm{DVR}}(s)\right) - \dfrac{G_{\mathrm{PI}}^{*}(s)\cdot\underline{G}_{\mathrm{SW}}(s)}{\mathrm{j}\omega_0 l_\mathrm{M}} \left(1 + \mathrm{j}\omega_0 l_\mathrm{S} \left(\dfrac{\underline{i}_{\mathrm{S1}}^{\angle 0}}{\underline{v}_{\mathrm{S1}}^{\angle 0}} \right)^{*} \right)}{1 - \underline{D}_\mathrm{S}(s)} \underline{v}_{\mathrm{S2}}^{\angle 0} \tag{7.61}$$

From eq. (7.61) it is obvious that the dynamic response of the positive sequence components influences the dynamic response of the negative sequence components. Furthermore, the positive sequence components lead to moving zeros during the fault period. In other words, the positive sequence component will keep on changing the position of the zeros of eq. (7.61) during the transient period because the stator's positive sequence currents as well as the voltages do not jump directly to their steady-state values. If the positive sequence stator current is replaced by its transfer function as described in eq. (7.28), including the Lê filter for positive sequence separation, it will inflict five additional pole-zero pairs on the negative sequence transfer function.

As a result, the zeros' movement will be mainly influenced by the variation of the positive sequence rotor reference currents. This movement can be observed in Figure 7-21. It is clear that only the original zeros of the negative sequence current transfer function are in movement and not the inflicted ones. Additionally, the movement of the zeros is not sparse and it occurs mainly near to its start position. This is related to the fact that the rotor's positive sequence reference currents do not experience any dynamics and just jump following an expected pattern to their new set values.

According to eq. (7.61) the negative sequence short-circuit current contains ten transient current components. Five of them are mainly related to the negative sequence parameters, while the other five are introduced by the positive sequence dynamics. Figure 7-22 shows the difference between the actually measured current and the analytical one derived from eq. (7.61)[8]. Of course the exclusion of measurement and sampling delays is the main reason for the very small difference between the two signals.

[8] The applied short-circuit impedance was selected to result in a negative sequence voltage magnitude of 0.15 p.u. at the PCC. This is in order to avoid any voltage limitation during the transient period.

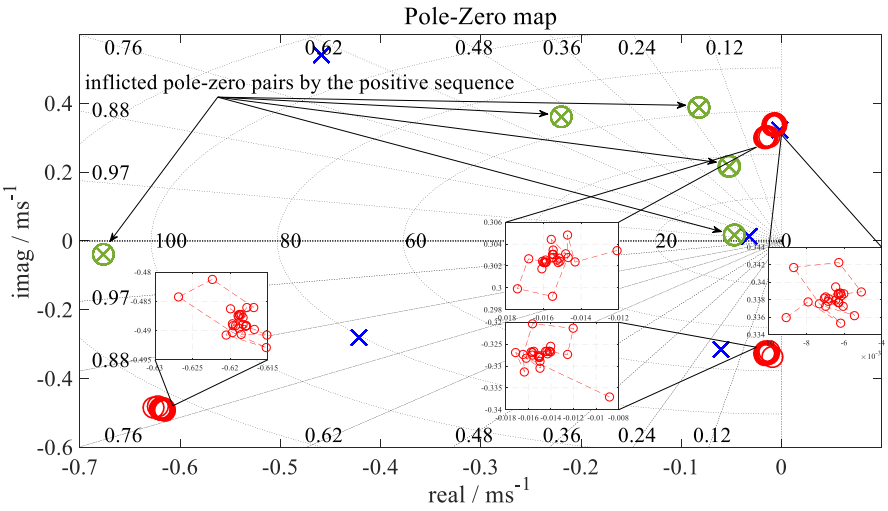

Figure 7-21 Zeros' movement of the negative sequence current transfer function for the first cycle influenced by the dynamic response of the positive sequence components

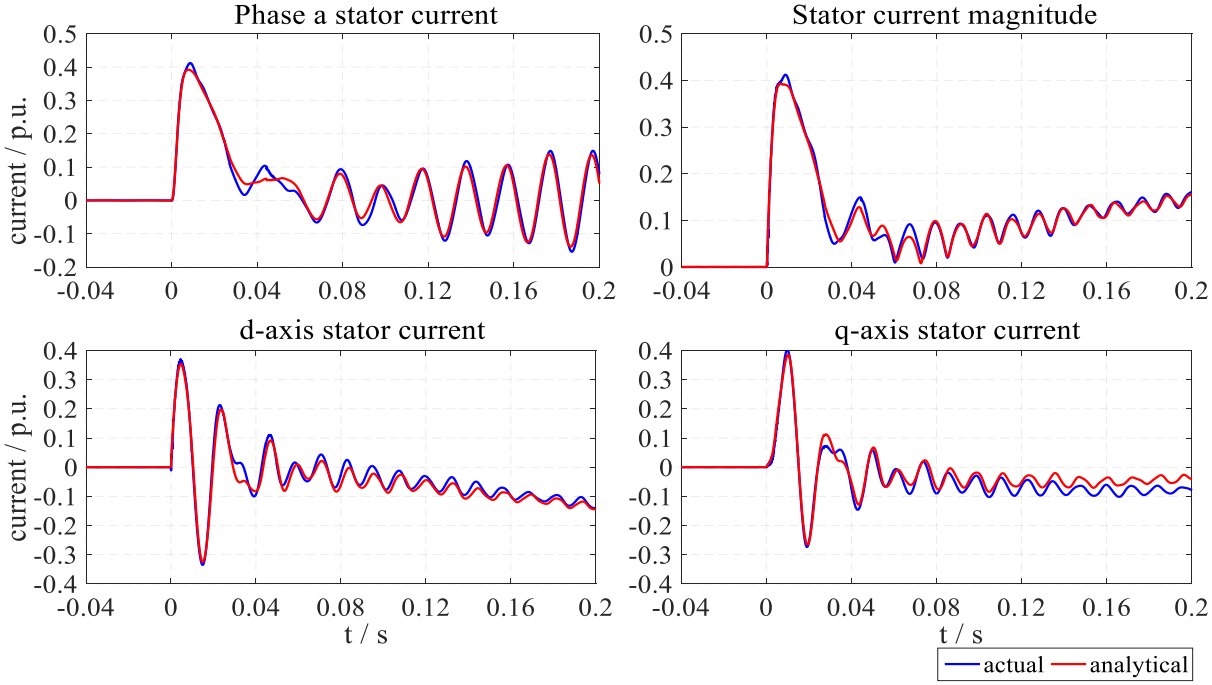

Figure 7-22 DFIG stator's negative sequence short-circuit current with pulsating torque suppression control

As already mentioned the positive sequence dynamics will produce five semi-coherent pole-zero pairs as illustrated in Figure 7-21. This implies that the associated transient currents will have a very small magnitude. Consequently, these currents can be ignored for the sake of simplicity without losing accuracy. Figure 7-22 shows the total transient currents, while Figure 7-23 and 7-24 show the transient currents produced by the positive sequence dynamics and by the change in the reference currents, respectively.

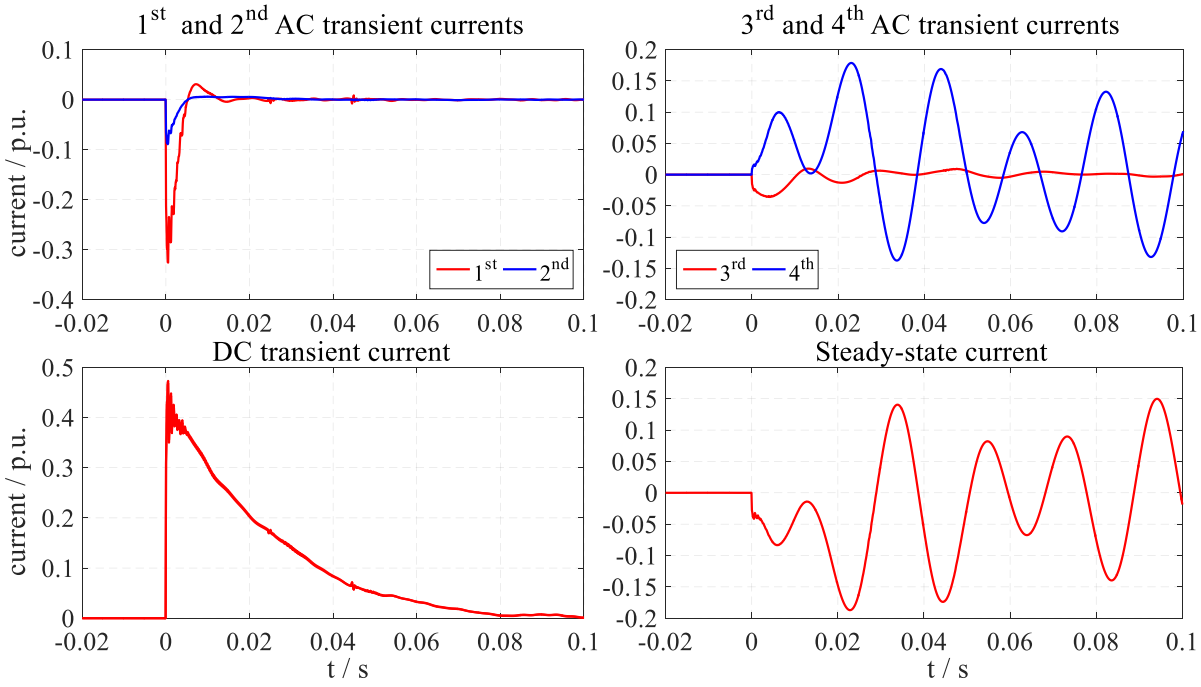

Figure 7-23 DFIG stator's negative sequence transient current components with pulsating torque suppression control

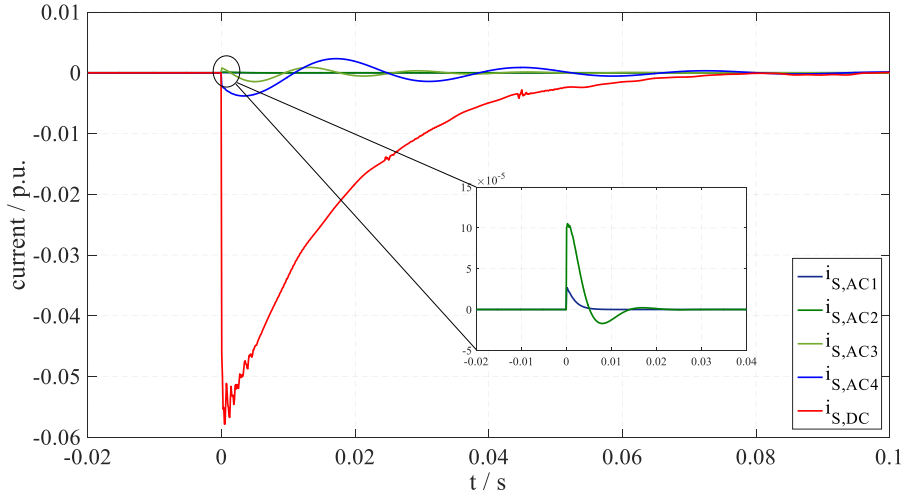

Figure 7-24 Transient currents inflicted by the positive sequence's dynamic response

The reference currents do not change instantaneously, as they are basically dependent on the transient behavior of the stator currents. Therefore, the produced transient currents in response to the change in the reference currents are not that critical. However, the new values of the reference currents force the corresponding zero produced by the PI-controller to shift away from its respective pole as displayed in Figure 7-25, which shows the final position of that zero. This shift modifies the negative sequence impedance to result in the required steady-state current. Thus, the magnitude of the transient current associated with this pole-zero pair will increase, as the zero shifts away from the pole, in order to counter the instantaneous change of the steady-state current to maintain a constant flux linkage in accordance with the law of constant flux.

Consequently, the transient currents produced in response to the change in the reference currents can be ignored except for the current defined by the aforementioned pole-zero pole.

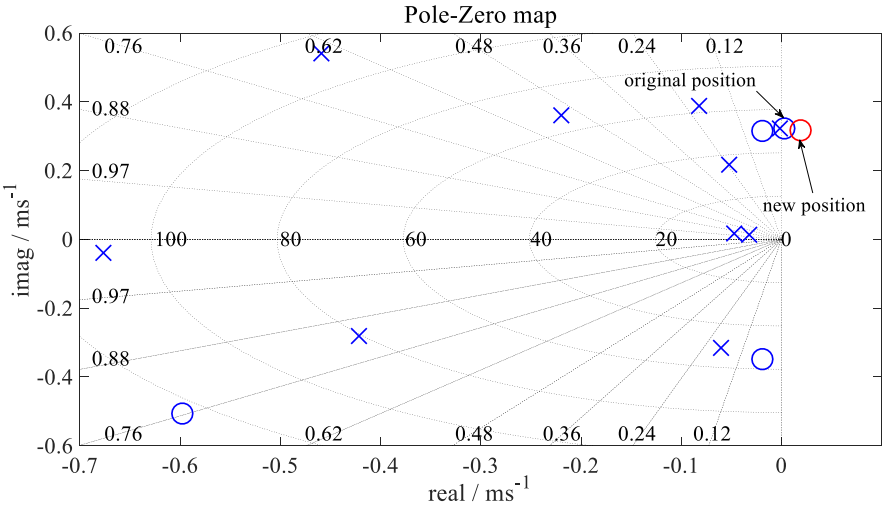

Figure 7-25 Zero shift away from the respective pole in response to the change in the reference currents

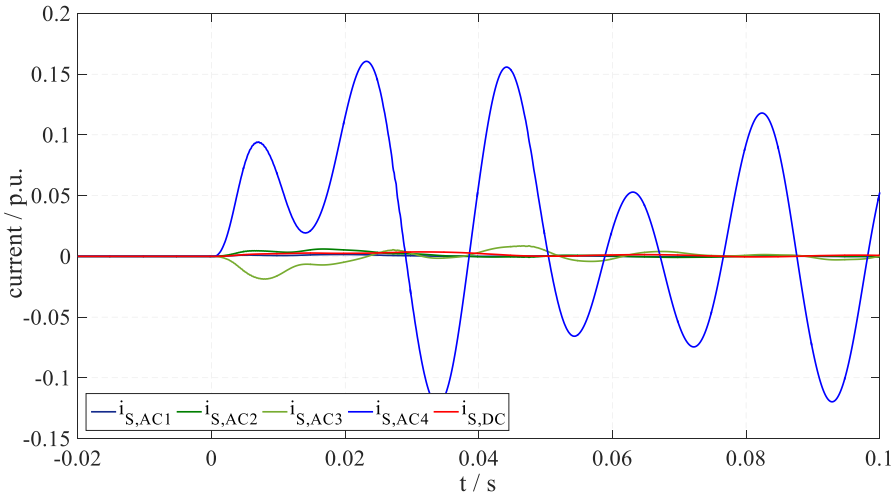

Figure 7-26 Transient currents generated in response to the change in the rotor's negative sequence reference currents

Figure 7-26 shows the transient currents produced in response to the change in the reference currents. It becomes clear that all of them have a very small magnitude except for the fourth AC transient current. Finally, it can be assumed, based on the previous discussion, that all of the transient currents are produced in response to the step change in the stator's negative sequence voltage, except for the fourth AC transient current. They are characterized by the same time constants and eigen frequencies as described in the previous section. Therefore, the negative sequence transient current can be expressed, following the same assumptions made in the previous section without ignoring the fourth AC transient current, as:

$$\underline{i}_{\mathrm{S2}}^{\angle 0}(t)=\frac{\underline{v}_{\mathrm{S2}}^{\angle 0}}{\underline{z}'_{\mathrm{S2}}}\left(e^{-\left(\frac{1}{\tau_{\mathrm{DC}}}+\mathrm{j}\omega_{\mathrm{DC}}\right)t}-e^{-\left(\frac{1}{\tau_{\mathrm{AC}}}+\mathrm{j}\omega_{\mathrm{AC}}\right)t}\right)-\underline{i}_{\mathrm{S2,SS}}^{\angle 0}\left(1-e^{-\left(\frac{1}{\tau_{\mathrm{AC4}}}+\mathrm{j}\omega_{\mathrm{AC4}}\right)t}\right) \tag{7.62}$$

where the new steady-state fault current is given by:

$$\underline{i}_{\mathrm{S2,SS}}^{\angle 0}=\frac{\underline{v}_{\mathrm{S2}}^{\angle 0}-\mathrm{j}\omega_{\mathrm{S}}l_{\mathrm{M}}\underline{i}_{\mathrm{R2,Ref}}^{\angle 0}}{r_{\mathrm{S}}+\mathrm{j}\omega_{\mathrm{S}}l_{\mathrm{S}}}=\underline{v}_{\mathrm{S2}}^{\angle 0}\frac{1+\mathrm{j}\omega_{\mathrm{S}}l_{\mathrm{M}}\left(\frac{\underline{i}_{\mathrm{R1,Ref}}^{\angle 0}}{\underline{v}_{\mathrm{S1}}^{\angle 0}}\right)^{*}}{r_{\mathrm{S}}+\mathrm{j}\omega_{\mathrm{S}}l_{\mathrm{S}}} \tag{7.63}$$

The approximate short-circuit currents based on eq. (7.62) are shown in Figure 7-27. Despite the clear difference between the actual current signals and the approximate ones, the approximate currents still maintain great similarity with the actual currents. They are accurate enough to represent the short-circuit behavior of the DFIG in this case.

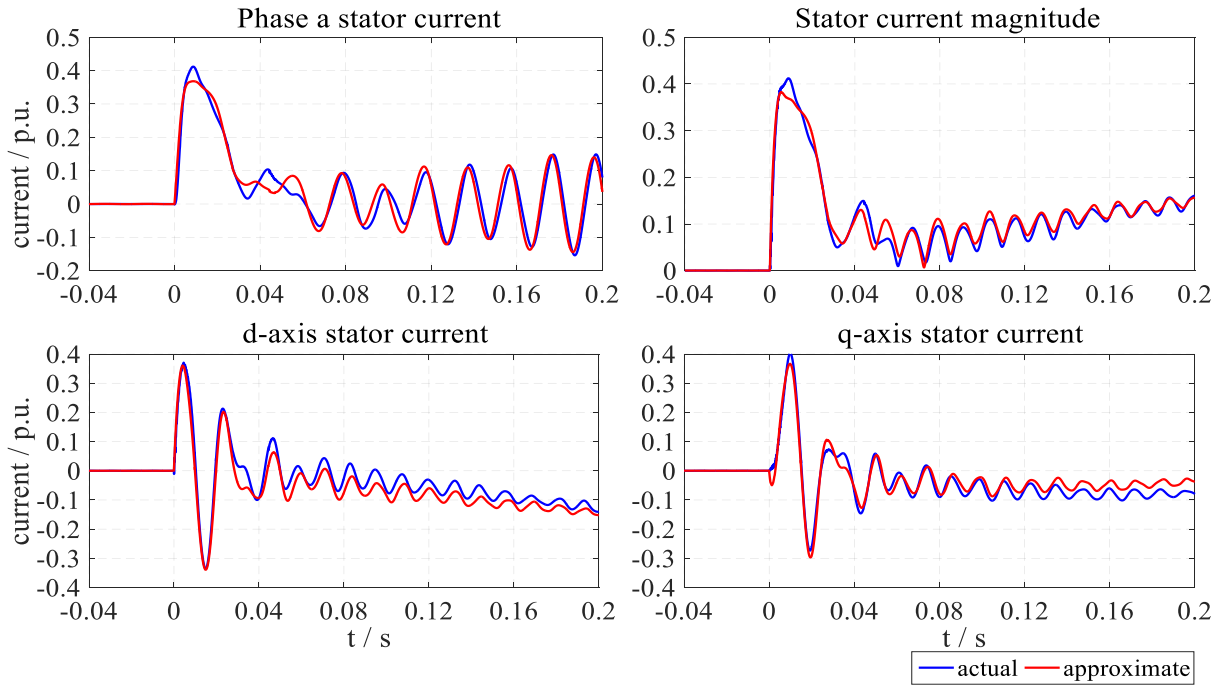

Figure 7-27 Approximate representation of the DFIG stator's negative sequence short-circuit current with pulsating torque suppression control

7.2.3.1 Modified Pulsating Torque Suppression Controller

As shown in the previous analysis, the DFIG negative sequence circuit is characterized by a large time constant influenced by electric characteristics of the machine and the PI-controller's parameters. This large time constant inhibits the fast suppression of the pulsating torque. In order to overcome this, the parameters of the PI-controller need to be enlarged. However, if the positive sequence current in eq. (7.54) is replaced by its steady-state value described in eq. (5.59), this yields:

$$\underline{i}_{\mathrm{R2,ref}}^{\angle -\omega_\mathrm{S}} = -\frac{\underline{i}_{\mathrm{R1,ref}}^{\angle \omega_\mathrm{S}}}{\underline{v}_{\mathrm{S1}}^{\angle \omega_\mathrm{S}}} \underline{v}_{\mathrm{S2}}^{\angle -\omega_\mathrm{S}} \tag{7.64}$$

Therefore, it is far better to use the rotor reference currents rather than the measured positive sequence stator current, because this does not modify the pole-zero pairs' position of the transfer function of the negative sequence stator current. Furthermore, the estimate of the required negative sequence rotor reference currents in eq. (7.64) does not require the same knowledge of the machine's parameters as the one before. Another modification can be applied by considering the real operator that was ignored in eq. (7.57). This is beneficial because the imaginary part of the reference currents has absolutely no influence on the pulsating torque, but rather leads to an unjustified increase in the magnitude of the negative sequence MSC voltage as well as of the negative sequence current. This may consequently lead to over modulation, especially during the transient period. A final modification can be applied by replacing the rotor's negative sequence currents by the reference current in the feed-forward term. This will significantly reduce the time constant introduced by the fourth transient AC current. It allows for a fast feed-forward decoupled control by the fast generation of the required voltage drop across the rotor's negative sequence impedance by the MSC as there is no separation filter in the path of the reference current the way it is in the measured current.

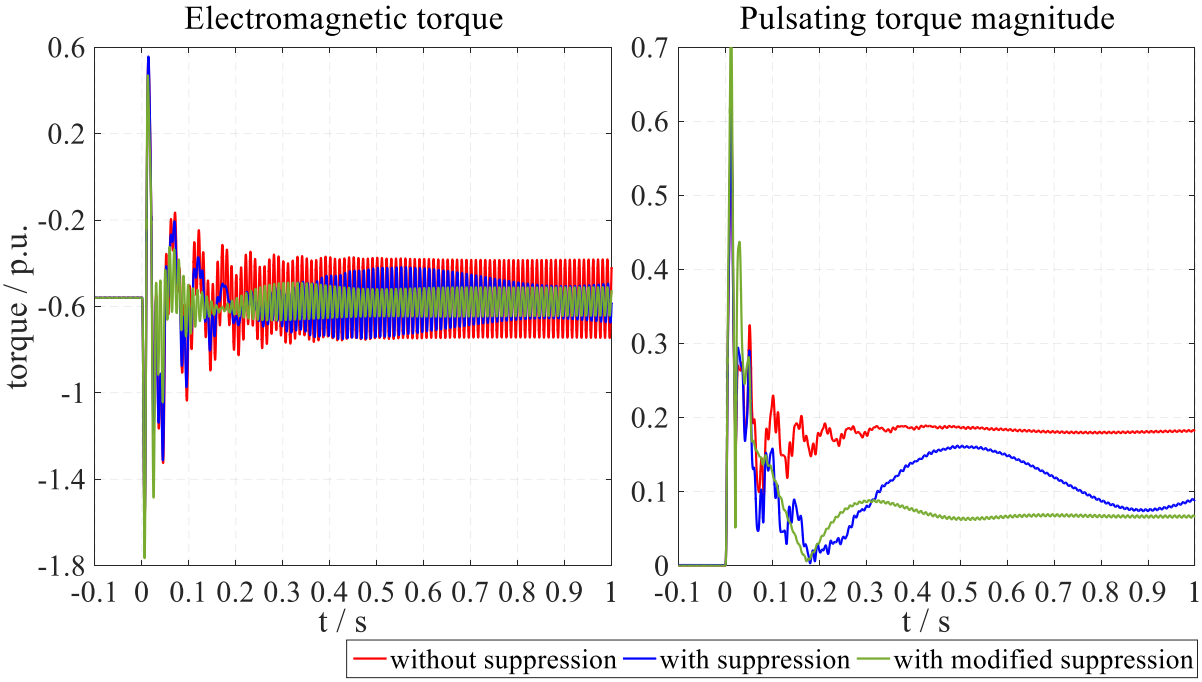

Figure 7-28 DFIG electromagnetic response with pulsating torque suppression modified control

Figure 7-28 shows the behavior of the DFIG electromagnetic torque during a phase-to-phase short-circuit. It becomes clear how fast the pulsating torque is damped with the modified control

and how quickly it reaches its steady-state value in comparison to the normal suppression control.

7.2.4 DFIG Response During Voltage Limitation

It is more likely for the MSC to run into over-modulation during the occurrence of an unsymmetrical type of faults, especially with pulsating torque suppression control. In this case two modes of operation are likely, either the MSC runs into over-modulation in the first cycle during the transient period, or it does so during the whole fault's period, meaning during the transient and the steady-state period. In the first case the required negative sequence rotor voltage's magnitude exceeds the maximally allowed value only for a few milliseconds during the transient period and more likely after the first half cycle. In other words, this happens after the occurrence of the maximum peak current. In the second case the required negative sequence rotor voltage's magnitude exceeds the maximally allowed value for the total fault period and also after the first half cycle. Figure 7-29 shows the voltage profile for both cases. In the first case the unsymmetrical fault resulted in a negative sequence voltage magnitude of 0.225 p.u at the PCC, while in the second case it resulted in 0.277 p.u.

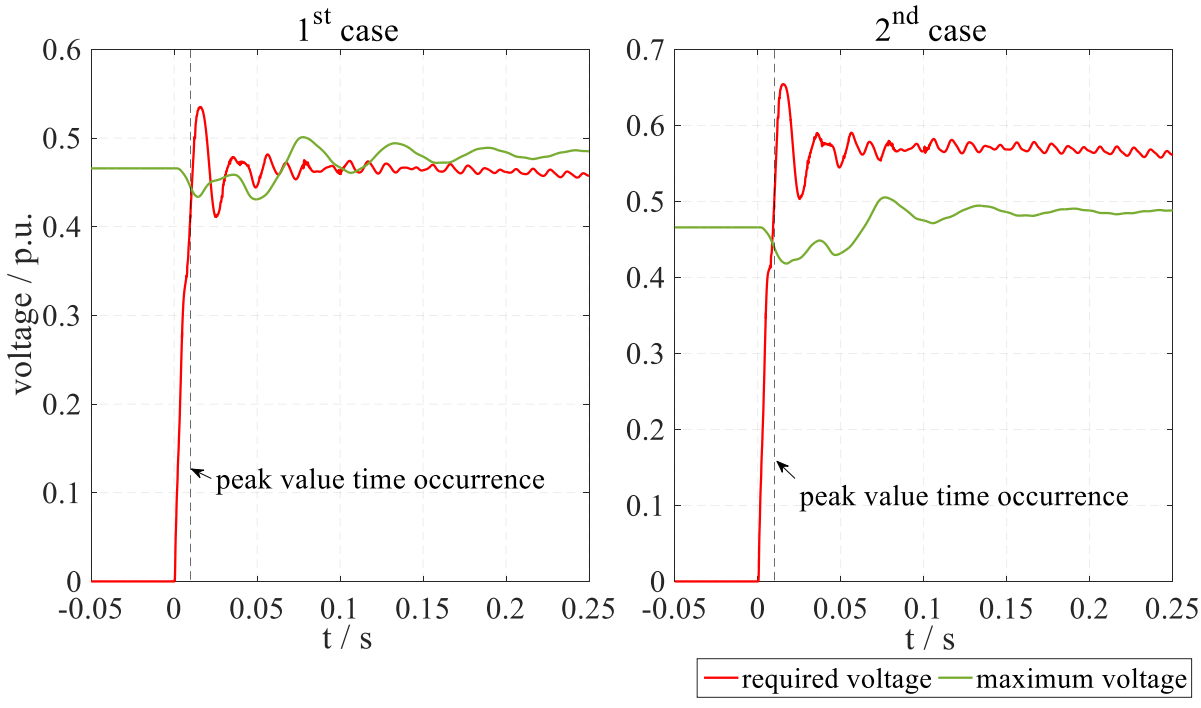

Figure 7-29 Required negative sequence rotor voltage profile for the two cases

In the first case the negative sequence rotor voltage's magnitude exceeds the limits only by 0.01 p.u. for a half cycle. Furthermore, this increased value takes place after the occurrence of the peak value of the short-circuit current. For most of the cases where the required steady-state negative sequence rotor voltage is lower or equal to the MSC negative sequence voltage limits,

this scenario is more likely to repeat itself. Accordingly, there will be no remarkable influence on the dynamic response of the negative sequence short-circuit current except in the time period in which the high value occurs. However, in this time period the current's magnitude will be post the peak descending to its minimum value as the rotor voltage is ascending to its maximum value. This conclusion can be clearly observed in Figure 7-30, which shows the difference between the simulated system and the expected one when the MSC negative sequence voltage limits are high enough. Based on this, eq. (7.54) and (7.62) can still be used for short-circuit current calculation without any change in their values.

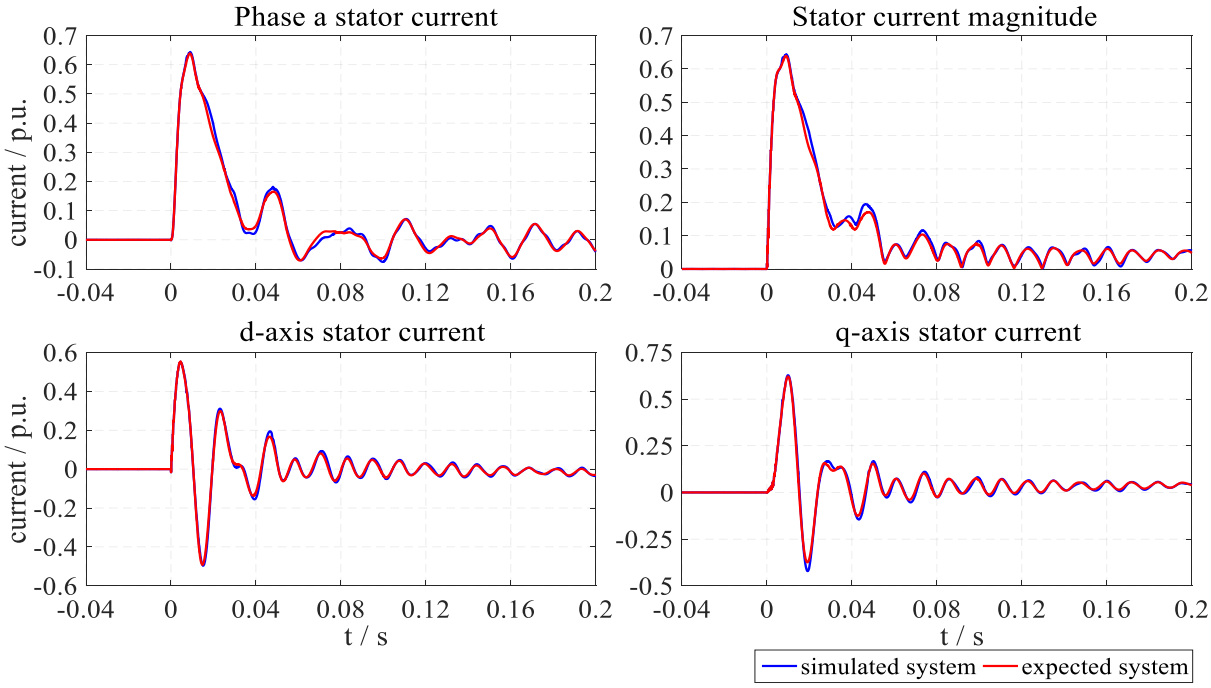

Figure 7-30 Influence of voltage limitation on DFIG stator negative sequence short-circuit current: 1st case

In the second case, the negative sequence rotor voltage's magnitude exceeds the limits almost by 0.1 p.u. for a half cycle. This increased value can be measured after the occurrence of the peak value of the short-circuit current as well as for the whole short-circuit period. This implies that there will be a change in the negative sequence current's response, especially with regard to the steady-state value. However, again the peak value will be the same as the exceeding of the limit was after its occurrence. Figure 7-31 shows the difference between the simulated system and the expected one when the MSC negative sequence voltage's limits are high enough. By observing the two currents it can be seen that the difference mostly occurs in the steady-state period in the q-axis current, where the steady-state current is usually reactive representing the magnetizing current absorbed by the stator in case of unsymmetrical fault and rotor current suppression control.

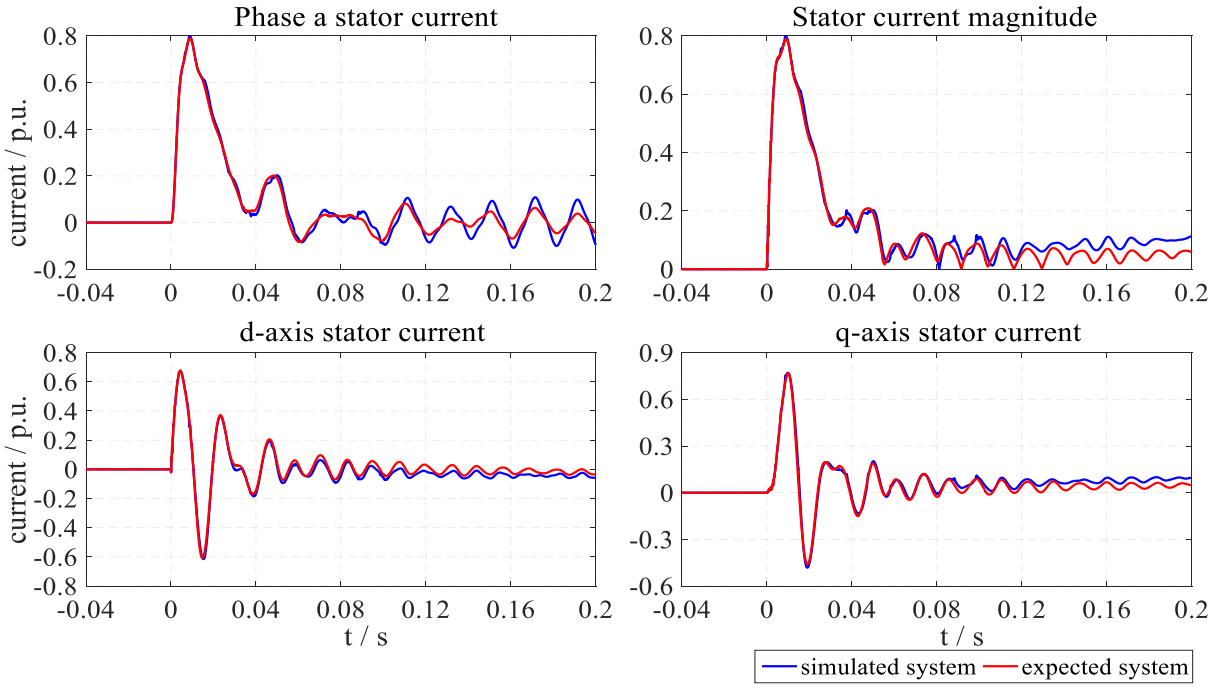

Figure 7-31 Influence of voltage limitation on DFIG stator's negative sequence short-circuit current: 2nd case

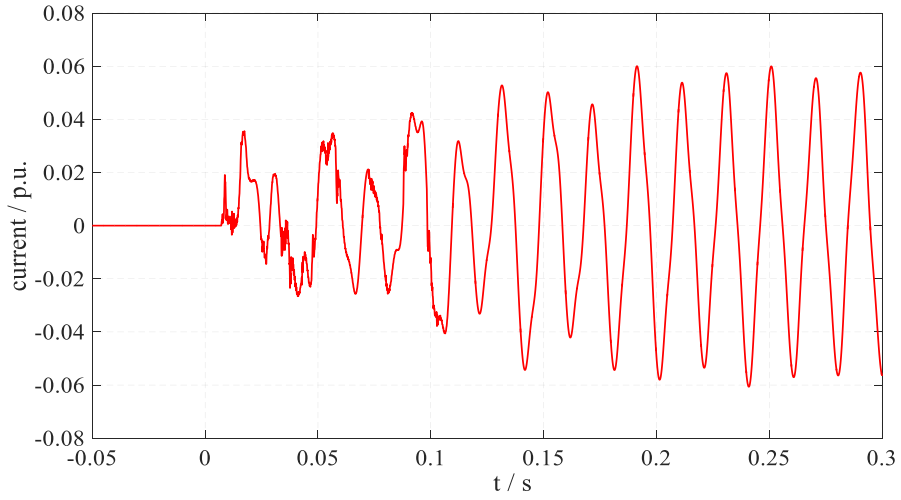

Figure 7-32 Current difference between the simulated and expected short-circuit negative sequence current

The change in the steady-state current will of course be accompanied by a transient current generation to oppose this instantaneous . By analyzing the current difference between the two current signals shown in Figure 7-32, it is found to contain two main current components illustrated in Figure 7-33. The first component is a steady-state current representing the sustained difference between the two signals, while the second is an AC transient current component, which is found to have almost the same time constant and eigen frequency as the fourth AC transient current described by eq. (7.52).

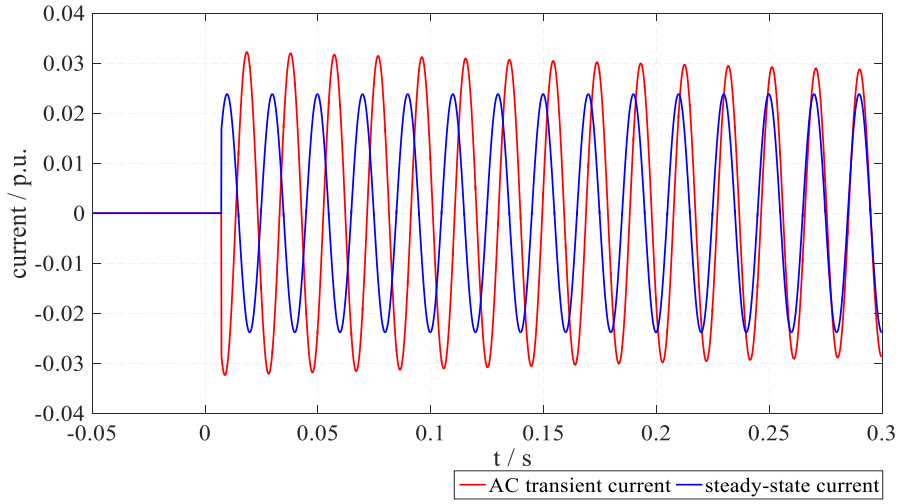

Figure 7-33 Components of the current difference

This is an expected result because, as already discussed in the previous section, any change in the steady-state currents through the alteration of the reference current will be countered by an AC transient current, i.e. the fourth AC transient current, characterized by time constants and eigen frequency described by eq. (7.52). Since the limitation of the rotor voltage yields a change in the steady-state current, it can be modeled as a change in the reference currents, because the rotor voltage's magnitude is reduced by generating a reactive reference current as discussed in chapter 4. Consequently, again, both eq. (7.54) and (7.62) can also be used for short-circuit current calculation only if the value of the steady-state current is changed as follows:

$$\underline{i}_{\mathrm{S2,ss}}^{\angle 0} \approx \underline{v}_{\mathrm{S2}}^{\angle 0} \frac{1-\alpha \dfrac{l_{\mathrm{M}}^2}{l_{\mathrm{S}} l_{\mathrm{R}}}}{\sigma\left(r_{\mathrm{S}} + \mathrm{j}\omega_0 l_{\mathrm{S}}\right)} \tag{7.65}$$

where $\alpha \approx \left|v_{\mathrm{S2}}\right| / \left|v_{\mathrm{S2,max}}\right|$ represents the ratio between the stator's negative sequence voltage magnitude and the maximum stator negative sequence that results in the maximally allowable rotor negative sequence voltage.

8 Standard Calculation of Fault Current Contribution

As presented in the last chapters, the short-circuit current of the DFIG-WT is not only dependent on the machine electrical parameters but it is rather dictated by a combination of factors, including the machine electrical parameters and the controller configuration and parameters. This makes a simple and reliable method to estimate the fault current contribution of the DFIG-WT with sufficient accuracy is nearly impossible, because this requires a full knowledge of the DFIG-WT configuration. However, this information is usually not accessible and in most of the time unavailable for any grid operator as it consider from the intellectual property of the WT manufacturer. On the other hand the knowledge of the fault current contribution is essential for any grid operator or owner for proper rating and setting of the protective devices and relays. Furthermore, in the early design stage the WT manufacturer needs an initial estimation about the fault levels of his WT to roughly estimate the initial costs in a matter that allow him to be competitive with other WT manufacturers.

Usually the IEC-60909 is applied to estimate the fault current contribution of the generation units. IEC-60909 offers simplified and reliable procedures based on equivalent voltage source calculation and correction factors for short-circuit current quantities calculation with sufficient accuracy. However, it is no more adequate for this purpose when it comes to DFIG-WT, because it only consider the generation unit electrical parameters. Therefore, in this chapter new methods is introduced to estimate an equivalent parameters of the DFIG-WT, which allows it to be used for fault current calculation using IEC-60909 and consequently leads to better accuracy in the results.

8.1 Procedures For Fault Current Calculation According to IEC-60909

Considering the simple network shown in Figure 8-1 the fault current flowing into the short-circuit is calculated by introducing an equivalent voltage source at the short-circuit location, where it represents the only active voltage of the system with all network feeders, synchronous and asynchronous machines are replaced by their internal impedances as illustrated in Figure 8-2.

Accordingly the initial symmetrical short-circuit current I''_{k} is calculated using the eq. (8.1) with the equivalent voltage source $cV_{\mathrm{n}}/\sqrt{3}$ at the short-circuit location and the short-circuit impedance Z_{k} [120].

$$I''_{\mathrm{k}} = \frac{cV_{\mathrm{n}}}{\sqrt{3}Z_{\mathrm{k}}} \tag{8.1}$$

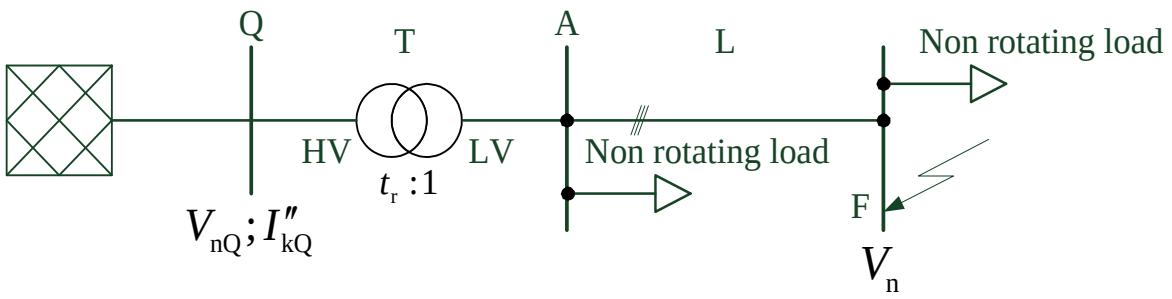

Figure 8-1 System diagram

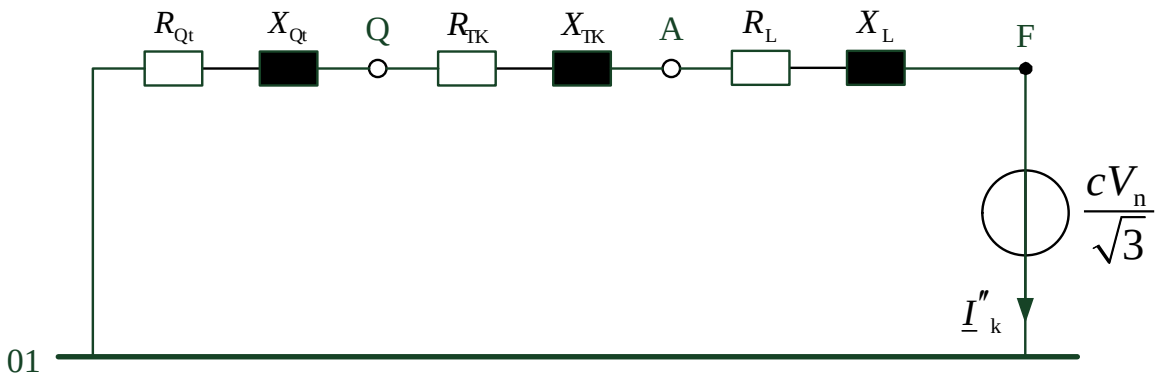

Figure 8-2 Equivalent circuit diagram of the positive-sequence system

The voltage factor *c* is a used for calculation of the minimum and maximum short-circuit currents, while Z_{k} is the short-circuit impedance of the electrical equipment and is multiplied with the impedance correction factors KG, KT and KS or KSO for generators (G), network transformers (T) and power station units (S) respectively.

The peak short circuit current i_{p} is then calculated using the initial symmetrical current as follows:

$$i_{\mathrm{p}} = \kappa\sqrt{2}I''_{\mathrm{k}} \tag{8.2}$$

The factor κ accounts for the aperiodic DC component. The derivation of the factor κ can be found in [121] and is given by:

$$\kappa = 1.02 + 0.98e^{-3R/X} \tag{8.3}$$

According to IEC-60909 there are three different methods for R/X ratio calculation in meshed network, they are:

1) Uniform R/X ratio (Method A)

2) R/X ratio at short circuit location (Method B)

3) Equivalent frequency f_c (Method C)

Method A

The factor κ is calculated based on eq. (8.3) taking the smallest ratio of R/X in all branches.

Method B

The R/X ratio is calculated from the equivalent impedance seen from the short-circuit location. A correction value 1.15 modifies the factor κ to cover inaccuracies caused by using R_k/X_k ratio from network reduction with complex impedances.

Method C

The equivalent impedance seen from short-circuits location is calculated assuming $f_c = 20Hz$, then the R/X ratio is calculated accordingly:

$$\frac{R}{X} = \frac{R_c}{X_c}\frac{f_c}{f} \tag{8.4}$$

8.2 Equivalent Short-Circuit Parameters Of DFIG-WT

According to the IEC TR 60909-1 the total short-circuit current is described by:

$$i_k = i_{k,AC} + i_{k,DC} = \sqrt{2}I_k''\left[\sin\left(\omega t + \varphi_U - \gamma\right) + e^{-\frac{R}{X}\omega t}\sin\left(\gamma - \varphi_U\right)\right] = \kappa\sqrt{2}I'' \tag{8.5}$$

where γ is the impedance angle and φ_U is the voltage angle at the beginning of the short-circuit, which is considered to be zero for the maximum value of i_p.

Consequently, the equivalent parameters of the DFIG-WT for fault current calculation is found by fitting the equation describing the total short-circuit current of the DFIG-WT described by eq. (5.62) to eq. (8.5), with the replacement of the subtransient current notation with the transient current notation.

One can conclude from the analysis introduced in chapter 5 that for practical value, the integral gain part of the PI-controller do not influence the peak short circuit current significantly. This fact can be observed in Figure 8-3. Therefore, this current component can be ignored and the resultant time constant and eigen frequency of the equivalent AC transient currents becomes:

$$-\frac{1}{\tau_{AC}} + j\omega_{AC} \approx -\frac{\left(k_P - js_G\omega_0\sigma l_R\right)\left(r_S + j\omega_0 l_S\right)}{\left(r_S + j\omega_0\sigma l_S\right)l_R} + j\omega_R \tag{8.6}$$

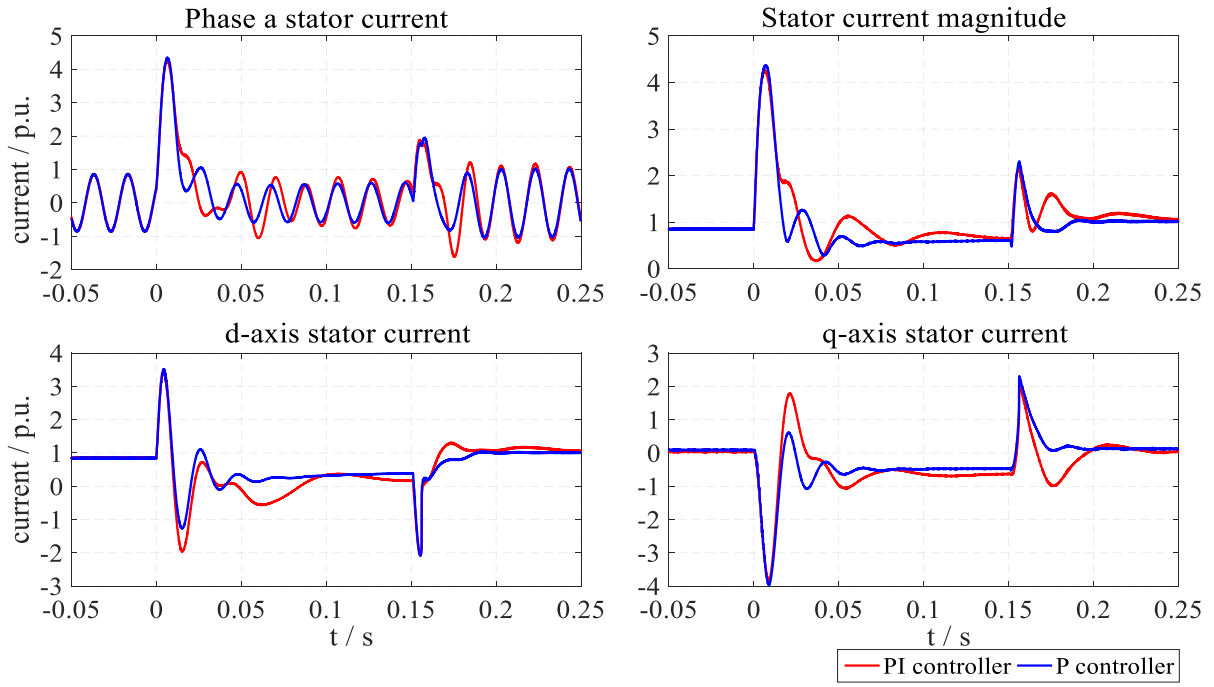

Figure 8-3 DFIG stator short-circuit current with P controller

Equating eq. (5.62) with eq. (8.5) with the assumption that the short-circuit occurred at the zero crossing yields:

$$\sin(-\gamma)+e^{-\frac{R}{X}\omega t}\sin(\gamma)=\frac{\left|i_{\mathrm{S,ss}}+i_{\mathrm{LSC,ss}}\right|\sin(-\varphi_{\mathrm{S}})+\left|i_{\mathrm{AC}}\right|e^{-\frac{t}{\tau_{\mathrm{AC}}}}\sin(-\varphi_{\mathrm{AC}})}{i'_{\mathrm{k}}}+e^{-\frac{t}{\tau_{\mathrm{DC}}}}\sin(\varphi_{\mathrm{DC}}) \qquad (8.7)$$

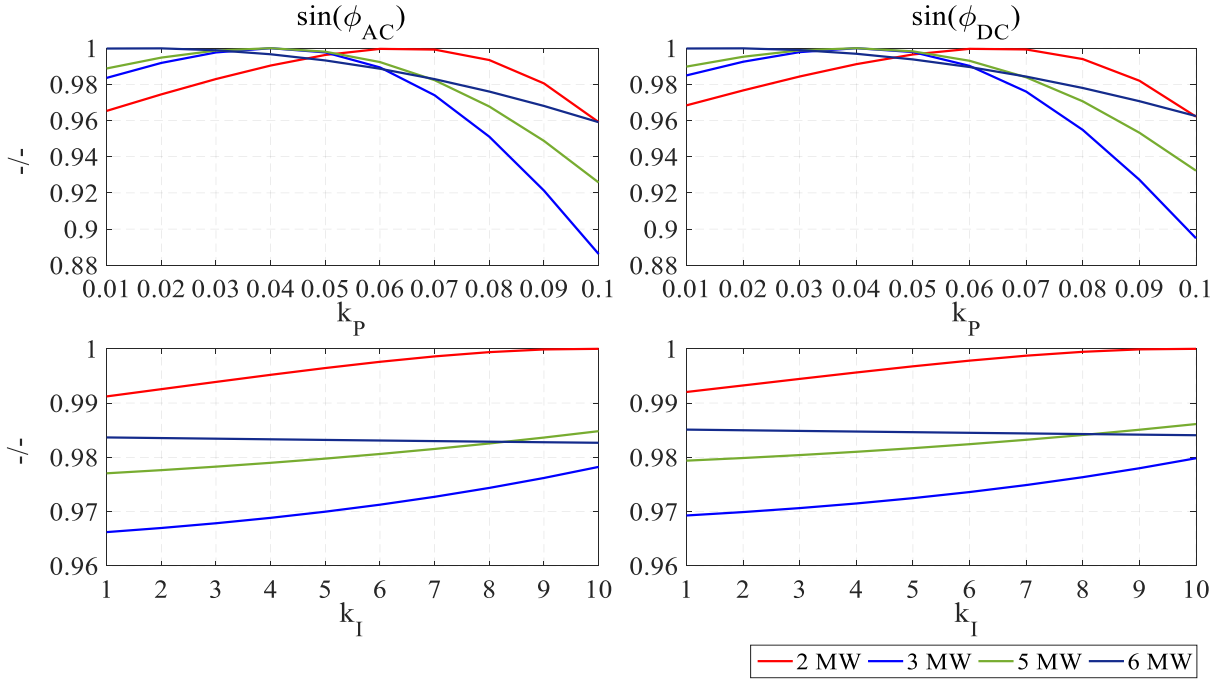

Figure 8-4 Influence of the PI controller parameters on the impedance angle

Figure 8-4 shows the influence of the PI controller parameters on the angles sin values for different machines ratings. As it is shown the values varies between 0.88 and 1. Therefore, in eq. (8.7) all the values can be replaced by one. This replacement would not have remarkable influence on the peak value and it would lead of course to a simpler derivation of the equivalent parameters without losing of accuracy. Furthermore, this is the same procedure followed in deriving the factor κ in the IEC-60909. Consequently, eq. (8.7) is further reduced to:

$$-1+e^{-\frac{R}{X}\omega t}=-\frac{\left|i_{\mathrm{WT,ss}}\right|}{i'_{\mathrm{k}}}\left(1-e^{-\frac{t}{\tau_{\mathrm{AC}}}}\right)-e^{-\frac{t}{\tau_{\mathrm{AC}}}}+e^{-\frac{t}{\tau_{\mathrm{DC}}}} \tag{8.8}$$

where $\left|i_{\mathrm{AC}}\right|=i'_{\mathrm{k}}-\left|i_{\mathrm{S,ss}}+i_{\mathrm{LSC,ss}}\right|$ as given in eq. (5.9) and (5.56) and $\left|i_{\mathrm{WT}}\right|=\left|i_{\mathrm{S,ss}}+i_{\mathrm{LSC,ss}}\right|$.

linearizing the exponential terms in eq. (8.8) using Taylor series yields:

$$\begin{aligned}-\frac{R}{X}\omega t+\frac{\left(\frac{R}{X}\omega t\right)^2}{2!}-\frac{\left(\frac{R}{X}\omega t\right)^3}{3!}+\ldots=-\frac{\left|i_{\mathrm{WT,ss}}\right|}{i'_{\mathrm{k}}}\Bigg(&\frac{t}{\tau_{\mathrm{AC}}}-\frac{\left(\frac{t}{\tau_{\mathrm{AC}}}\right)^2}{2!}+\frac{\left(\frac{t}{\tau_{\mathrm{AC}}}\right)^3}{3!}-\ldots\\&+\frac{t}{\tau_{\mathrm{AC}}}-\frac{\left(\frac{t}{\tau_{\mathrm{AC}}}\right)^2}{2!}+\frac{\left(\frac{t}{\tau_{\mathrm{AC}}}\right)^3}{3!}-\ldots\\&-\frac{t}{\tau_{\mathrm{DC}}}+\frac{\left(\frac{t}{\tau_{\mathrm{DC}}}\right)^2}{2!}-\frac{\left(\frac{t}{\tau_{\mathrm{DC}}}\right)^3}{3!}+\ldots\Bigg)\end{aligned} \tag{8.9}$$

With the R/X value is lower than zero the peak value time occurrence would be lower than 10 ms ($t_{\mathrm{p}}<10ms$). Therefore, the high order values can be ignored and the final equivalent R/X ratio is given by:

$$\frac{R}{X}\approx\frac{1}{\omega\tau_{\mathrm{DC}}}-\frac{1}{\omega\tau_{\mathrm{AC}}}\left(1-\frac{\left|i_{\mathrm{WT,ss}}\right|}{i'_{\mathrm{k}}}\right) \tag{8.10}$$

The steady-state current in eq. (8.10) is mainly dependent on how the reference currents for both the LSC and MSC are set during the short-circuit, which varies from manufacturer to another. Therefore, it is better to represent eq. (8.10) as follows:

$$\frac{R}{X}\approx c_{\mathrm{cont}}\frac{1}{\omega\tau_{\mathrm{DC}}} \tag{8.11}$$

where c_{cont} is a factor that represent the influence of the controller behavior on the value of the peak short-circuit current and it can be calculated from the FRT tests as follows:

$$c_{cont} = \frac{1}{3}\frac{X_{DC}}{R_{DC}}\ln\left(\frac{i'_k}{i_{p,meas} - i'_k}\right) \tag{8.12}$$

where X_{DC}/R_{DC} are found from the machine electrical parameters and $i_{p,meas}$ is the measured peak current values from the FRT test, while i'_k is the initial transient current which is calculated rather by using the transient impedance value given in eq. (5.55) or from fitting the measured short-circuit current under no load condition with the proposed mathematical interpretation in eq. (5.62) excluding the second AC transient current based on what has been made in this chapter.

8.3 New Method For Estimation of The R/X ratio in Meshed Networks

Considering the network shown in Figure 8-5, the total value of the aperiodic decaying DC current flowing through the fault is given by, assuming p.u. values:

$$I''e^{-\frac{t}{\tau}} = I''_1 e^{-\frac{t}{\tau_1}} + I''_2 e^{-\frac{t}{\tau_2}} + I''_3 e^{-\frac{t}{\tau_3}} + ... \tag{8.13}$$

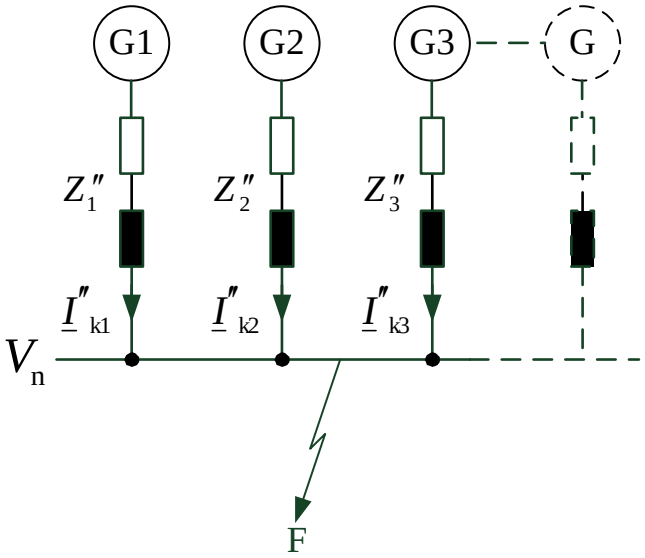

Figure 8-5 Sample meshed network

Applying linearization yields:

$$I''\left(1-\frac{t}{\tau}+\frac{\left(\frac{t}{\tau}\right)^2}{2!}-\ldots\right)=I_1''\left(1-\frac{t}{\tau_1}+\frac{\left(\frac{t}{\tau_1}\right)^2}{2!}-\ldots\right)+I_2''\left(1-\frac{t}{\tau_2}+\frac{\left(\frac{t}{\tau_2}\right)^2}{2!}-\ldots\right)+ I_4''\left(1-\frac{t}{\tau_3}+\frac{\left(\frac{t}{\tau_3}\right)^2}{2!}-\ldots\right).....\tag{8.14}$$

With $I''=I_1''+I_2''+I_3''+.....,\ I_{1\to3}''=V_{\mathrm{n}}/Z_{1\to3}''$ and $t=t_{\mathrm{p}}$ the equivalent R/X is found to be:

$$\frac{R_{\mathrm{eq}}}{X_{\mathrm{eq}}}=c_{\mathrm{eq}}\frac{Y_1''\frac{R_1}{X_1}+Y_2''\frac{R_2}{X_2}+Y_3''\frac{R_3}{X_3}+.....}{Y_1''+Y_2''+Y_3''+\ldots}\tag{8.15}$$

and the factor κ is calculated as follows:

$$\kappa=1.02+0.98e^{-3R_{\mathrm{eq}}/X_{\mathrm{eq}}}\tag{8.16}$$

where the factor c_{eq} is to compensate for the high order terms and peak time variation. Consequently, there would be no need for the correction value 1.15, instead it is assigned for the factor c_{eq} .

From eq (8.15) the equivalent R/X ratio is calculated based on the ratio of each individual branch to the total admittance. The new method gives a better interpretation of the meaning of the R/X ratio and it is much simpler and straight forward to calculate in comparison to the methods presented in the IEC-60909.

8.4 Fault Current Contribution Case Study

A case study with the proposed calculation methods will be performed in this section. The results with proposed method for estimating the equivalent R/X and the new given expression for the transient impedance will be compared to the results from the IEC-60909, firstly with methods B and C and secondly with the new proposed method for R/X calculation in meshed networks which will be referred to as method D.

The network in Figure 8-6 will be used in this study case, where a three phase fault is applied at three different places consecutively, they are K11, K12 and K13. For each fault location the simulation results will be compared against the results from the new proposed methods and

IEC-60909 to determine which method offers better accuracy. The data of the network elements are as follow:

Transformer T1: $S_{rT1} = 1500\,\text{kVA}$; $V_{rT1HV} / V_{rT1LV} = 20\,\text{kV} / 0{,}69\,\text{kV}$; $u_{krT1} = 6\,\%$; $u_{RrT1} = 1\,\%$

Transformer T2: $S_{rT2} = 16\,\text{MVA}$; $V_{rT2HV} / V_{rT2LV} = 110\,\text{kV} / 20\,\text{kV}$; $u_{krT2} = 12\,\%$; $u_{RrT2} = 0{,}6\,\%$

110-kV-Feeder: $S''_{kQ} = 2000\,\text{MVA}$; $R_Q / X_Q = 0{,}1$

Cabel L1 to L10, NA2XS2Y 150 mm²: $R' = 0.211\,\Omega/\text{km}$; $X' = 0.122\,\Omega/\text{km}$

Cabel L11, NA2XS2Y 500 mm²: $R' = 0.0681\,\Omega/\text{km}$; $X' = 0.0681\,\Omega/\text{km}$

DFIG-WT (P1): $I_{LR} / I_{rG} = 4.3412$; $R_G / X_G = 0.29933$.

According to the new method proposed here the required DFIG-WT values for short-circuit current calculation are:

DFIG-WT (P2): $I_{LR} / I_{rG} = 4.116$; $R_G / X_G = 0.5311$.

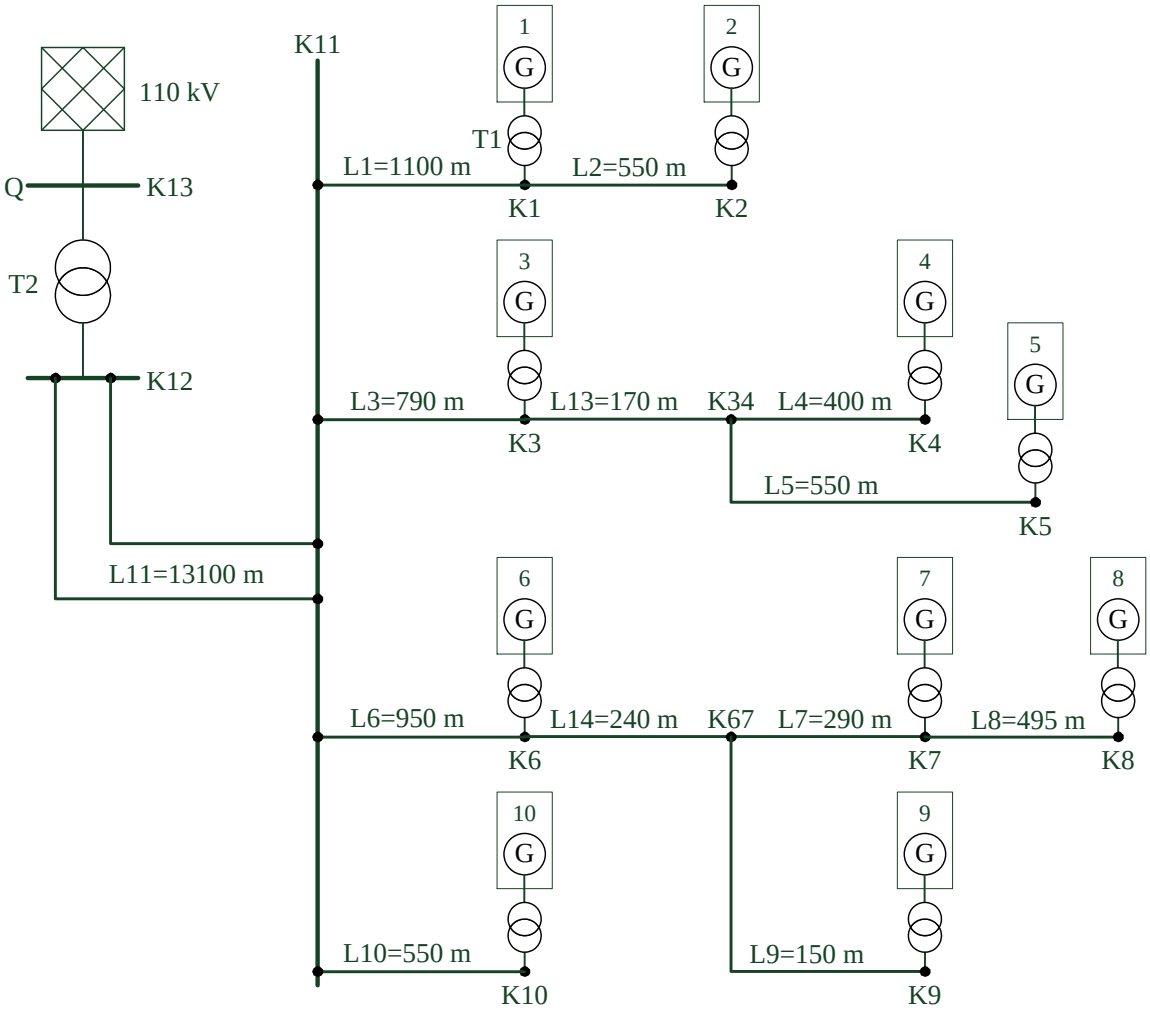

Figure 8-6 Study case Network with nodes and cables numbering (The symbol G stands for DFIG-WT)

Short-circuit calculation

Table 8-1 states the values of the equivalent grid impedances as well as the initial symmetrical short-circuit currents for the different fault locations, while the values of the equivalent R/X are found in Table 8-2 as seen from the fault location and the peak short-circuit current values for the same faults are found in Table 8-3.

Table 8-1 Initial symmetrical short-circuit currents

Initial symmetrical short-circuit currents in kA	P1	P2
Fault location at K11		
$V_n = 20\text{kV}$	$\lvert\underline{Z}_{eq}\rvert = 2.34\,\Omega$	$\lvert\underline{Z}_{eq}\rvert = 2.4\,\Omega$
L1	0.43	0.41
L3	0.65	0.62
L6	0.86	0.82
L10	0.22	0.21
L11	3.29	3.29
K11	5.42	5.28
Fault location at K12		
$V_n = 20\text{kV}$	$\lvert\underline{Z}_{eq}\rvert = 2.16\,\Omega$	$\lvert\underline{Z}_{eq}\rvert = 2.21\,\Omega$
L11	1.898	1.83
T2	4.039	4.04
K12	5.869	5.74
Fault location at K13		
$V_n = 110\text{kV}$	$\lvert\underline{Z}_{eq}\rvert = 6.51\,\Omega$	$\lvert\underline{Z}_{eq}\rvert = 6.51\,\Omega$
Q	10.497	10.497
T2	0.243	0.239
K13	10.736	10.73

Table 8-2 R/X ratio as seen from the fault location

Fault location	Method B		Method C		Method D	
	P1	P2	P1	P2	P1	P2
K11	0.24	0.3	0.22	0.25	0.254	0.3769
K12	0.16	0.2	0.12	0.13	0.172	0.267
K13	0.1	0.11	0.1	0.1	0.119	0.1229

Table 8-3 Peak short-circuit currents

Peak short-circuit currents in kA	Method B		Method C		Method D		Simulation
	P1	P2	P1	P2	P1	P2	
Fault location at K11 $V_n = 20\text{kV}$							
L1	0.91	0.83	0.93	0.87	0.87	0.84	0.83
L3	1.37	1.25	1.39	1.31	1.3	1.26	1.24
L6	1.81	1.65	1.84	1.73	1.7	1.66	1.6
L10	0.46	0.42	0.47	0.44	0.43	0.42	0.42
L11	6.97	6.6	7.08	6.92	7.06	6.49	6.65
K11	11.47	10.6	11.66	11.11	11.4	10.68	10.4
Fault location at K12 $V_n = 20\text{kV}$							
L11	4.37	4.04	4.55	4.352	3.69	3.59	3.62
T2	9.31	8.93	9.68	9.616	9.7	8.8	9.29
K12	13.52	12.68	14.07	13.66	13.39	12.4	12.25
Fault location at K13 $V_n = 110\text{kV}$							
Q	25.788	26.72	25.821	26.36	25.9	25.9	25.6
T2	0.597	0.59	0.598	0.59	0.51	0.5	0.511
K13	26.38	26.29	24.41	26.36	26.14	26	26

From Table 8-3 it can be seen that both Method B (P2) and D (P2) give the highest accuracy higher accuracy for the fault location at K11, followed by Method C (P2) and D (P1) for the second highest accuracy at the same location, while Method B (P1) and C (P1) give the lowest accuracy. On the other hand Method D (P2) and (P1) give the highest accuracy for both fault locations K12 and K13. The second highest accuracy achieved for the fault locations K12 and K13 is achieved by Method B (P2) and C (P2) and the lowest is achieved by Method B(P1) and C (P1). Consequently, it can be concluded from the given results that the new proposed method

for estimating the DFIG-WT values for short-circuit calculation as well as the new method for estimation of the R/X value in meshed network (D) yield higher accuracy when compared to any other methods. This is evident in Table 8-4 which shows the error in the calculation according to the different methods compared to the values from the simulation, where on the average error sum Method D (P2) gives the lowest error followed by Method B (P2) and Method D (P1).

Table 8-4 Peak short-circuit current calculation error

Calculation error in %	Method B		Method C		Method D	
	P1	P2	P1	P2	P1	P2
Fault location at K11						
L1	9.64	0.00	12.05	4.82	4.82	1.20
L3	10.48	0.81	12.10	5.65	4.84	1.61
L6	13.13	3.12	15.00	8.12	6.25	3.75
L10	9.52	0.00	11.90	4.76	2.38	0.00
L11	4.81	-0.75	6.47	4.06	6.17	-2.41
K11	10.29	1.92	12.12	6.83	9.62	2.69
Fault location at K12						
L11	20.72	11.60	25.69	20.22	1.93	-0.83
T2	0.22	-3.88	4.20	3.51	4.41	-5.27
K12	10.37	3.51	14.86	11.51	9.31	1.22
Fault location at K13						
Q	0.73	4.37	0.86	2.97	1.17	1.17
T2	16.83	15.46	17.03	15.46	-0.20	-2.15
K13	1.46	1.12	-6.12	1.38	0.54	0.00
Average sum error $\sum\|error\|/12$						
$\sum$	9.0167	3.8783	11.533	7.4408	4.3033	1.8583

9 Summary and Conclusion

A detailed analysis of the transient behaviour of the DFIG-WT during symmetrical and unsymmetrical faults has been performed taking into consideration the system nonlinearities that might influence the transient response. A new set of mathematical interpretations of the dynamic behaviour based on the performed analysis were provided and concurrently validated. The new mathematical interpretations help in the deep understanding of the machine dynamic behaviour, and thus help in assessing the machine stability when connected to any type of networks and in estimating the fault current limits under various disturbances. Furthermore, new control methods for FRT capability enhancement are proposed based on the newly developed mathematical interpretation.

A detailed modelling of the DFIG-WT components considering the DFIG nonlinearities and the switching dynamics of the semiconductor devices. However, neither the leakage saturation and the skin effect of the DFIG were modelled due to the lack of information, but methods of modelling them were provided. It was shown that the switching dynamics of the semiconductor devices are very fast in the 1-2 μs range and it would slightly influence the harmonic spectrum of the output voltages and currents. Therefore, it was replaced by a switch model, which was proven to be much faster and accurate enough.

The modelling process allowed for an independent controller design for each of the turbine, MSC and LSC. The turbine power-speed control allows for maximum energy yield through maximum power point tracking, while the pitch controller allows for speed limitation beyond the rated one. To allow for independent fast decoupled control of the MSC and LSC for the positive and negative sequence components a fast separation algorithm based on Lê filter was introduced and was later modified to reduce the gain in the high frequency range as well as the dynamic over-shoots. The decoupled feed-forward control augmented with a PI-controller to cover for measurement uncertainties as well as parameter variations during different operating conditions allows for fast and accurate tracking of the reference values. However, for reliable and safe operation the voltage and the current magnitudes should be limited to the rated values to guarantee continuous operation of the converters. In this essence the highest priority was set to the positive sequence active current followed by the positive sequence reactive current then negative sequence current and finally the harmonic currents, while for the voltage the highest priority was set to the negative sequence voltage to fulfill the required control objective, followed by the positive sequence and finally the harmonic voltages.

The stability analyses of gird connected converter based renewable energy sources is performed by the impedance-based stability criterion. However, with the feed-forward decoupled control

the grid connected inverter behave as a current source and applying such stability criterion may lead to misleading results. Therefore, another two stability criterion that investigate the stability of the inverter output current and voltages in both the floating mode and stand-alone mode. For the LSC it was shown that the stability margin for the output current increases as the grid SCR increases and when the grid filters were implemented the phase margins decreases as the grid SCR increases, while the stability margin for the output voltage is not influenced by the grid SCR or by the grid filters. With active damping the phase margin increases for some selected harmonics. On the contrary the voltage limitation has considerably reduced the gain margins for the output current in some high frequency bands. For MSC the grid stiffness does not has remarkable influence on the machine stability as well as the magnetic saturation. However, the stator filter is critical for the stability of the stator current, where the phase margins were very small for different grid SCR beyond 750 Hz. On the other hand, the voltage limitation tend to increase the phase margins in the this range because it limits the current magnitudes in this range.

With the full DFIG-WT system being provided a detailed an accurate analysis of the fault response is performed. It was shows through a step by step analysis that the dynamic response of the LSC to voltage drops are fast and yields small current magnitudes and full dynamic rejection of the disturbing quantity could be assumed. This yields that the LSC could be considered as a current source with the reference currents as the internal set points. On the contrary the DFIG suffers from a very high short-circuit current magnitudes in response to the stator voltage drops. It was shown that the DFIG stator short-circuit current contains two decaying AC transient currents and one DC decaying transient current. The transient currents are found to be characterized by the electrical parameters of the machine as well as the parameters of the PI-controller, where an approximate expressions describing the time constants and eigen frequencies of each transient component were provided and validated. The influence of the non-linarites on the short-circuit behavior were then examined. It was shown that the magnetic saturation did not have any influence on the short-circuit current and the main reason was that the variation of the leakage coefficient forced by the variation of the main inductance has led to a counter variation in the total inductance. On the other hand the voltage limitation had forced the system poles and zeros to navigate to another positions leading to a totally different response to the expected one. However, the voltage limitation occurred after the first half cycle, which means that the peak value remains the same.

The deep knowledge and understanding of the DFIG dynamics allowed then to propose five new methods to reduce the high peak short-circuit current it suffers from in order to enhance

the FRT capability as well as to protect the semiconductor devices against them. The first four methods were driven in way either to increase the rate of change of the internal transient voltage or to virtually increase the transient impedance. Additionally, they were designed once considering open-loop configuration and second considering the closed-loop configuration. However, for the methods to be practically applicable the gains should be designed in a way that would result in highest peak reduction without running into over modulation or to lead to disconnection. Therefore, the MVMO were used to optimally tune the gains of the transient impedance compensation method which satisfy the given criteria. The last proposed method were designed in a way that would result in a high decaying rate of the AC transient current components through the modification of the feed forward term of the rotor currents. It was shown that all the proposed methods were able to reduce the peak short-circuit current significantly, this is without violating the safety boundaries of the converter.

The occurrence of unsymmetrical voltage at the DFIG-WT terminals has a series of negative consequences on both the DFIG and the LSC, like pulsating torque and voltages in the DC link, power loss, overheating, etc... Therefore a dedicated controller should be designed to overcome such consequences. However, there are concrete control objectives assigned for negative sequence control in the DFIG-WT, which can be fulfilled one at a time. The analysis of the unsymmetrical fault response of the DFIG and LSC for each control objective were provided, and again as before an approximate expressions describing the short-circuit current as well as the time constants and eigen frequency were provided and validated. From the analysis again the LSC dynamics can be totally ignored and it could be considered either as an open circuit in case of current suppression control or as a current source with the reference currents as internal set-points in case of pulsating voltage suppression control. Without compensation the DFIG can be considered as a RL circuit and the rotating components can be totally ignored due to the very high rotor transient impedance resulted from the high negative slip. When negative sequence rotor current suppression is set as controller objective, the stator short-circuit current will contain five different transient currents which are characterized by combination of the machine electrical parameters, PI-control parameters and the parameters of the Lê filter. However, not all of the transient currents of a significant magnitude, and the short-circuit current can be approximated with only one AC and DC decaying transient current. This approximated mathematical interpretation of the negative sequence short-circuit current were proven to be adequate and holds high resemblance to the actual behavior. It was shown that the positive sequence dynamics influence the zeros position of the stator current with pulsating torque suppression control, where the zeros keep on changing their positions during the

transient period. However, the zeros excursion are not sparse and the short-circuit current under this condition contains ten decaying transient currents, which again can be approximated only by three; two AC and one DC decaying transient currents in addition to of course the steady-state current. Again the provided approximate short-circuit current expression were proven to be accurate enough to represent the actual behavior. One of the two AC transient currents under this controller objective is characterized with a very large time constant. This large time constant impede the fast suppression of the pulsating torque. Therefore, a modified structure of the controller was provided in order to overcome such behavior and to guarantee fast suppression of the pulsating torque. The new controller structure were proven to be much faster than the original one and would not result in extra transient current components but rather in lower number. It is more likely for the MSC to run into over-modulation during unsymmetrical type of faults, which may result in two operating modes; either to run into over-modulation in the first cycle during the transient period, or in the whole duration of the fault meaning during the transient and steady-state period. In the first case the negative sequence rotor voltage magnitude exceeds the limits after the first half cycle and for a limited time window. Consequently, the peak value of the short-circuit current will remain and the current wave will almost retain the same behavior. Therefore, the pre provided short-circuit current expressions is still valid and need no reformation. In the second case the voltage limitation is represented as a variation in the value of the reference current dependent on the amount of the required rotor voltage. In this case the expression of the steady-state current is only modified with a factor that represents the ratio between the required rotor voltage and the maximum value.

From the analysis provided throughout this thesis it is clear that the short-circuit current of the DFIG-WT is dictated by a combination of factors, including the machine electrical parameters as well as the controller parameters. Unfortunately, any information of the controller structure or configuration is obscured, because it is considered as an intellectual property of the manufacturer. However, its knowledge is inevitable for the calculation of the fault current contribution of the individual generation set. Therefore, a very simple and direct forward method is provided to estimate an equivalent parameters of the DFIG-WT, which later helps in calculating its fault current contribution is the same manner as in IEC-60909. The new method is dependent on firstly representing the short-circuit current with only three current components and from the FRT tests with no-load conditions an equivalent R/X and locked rotor current ratios are estimated. Furthermore, a new method to estimate the R/X of meshed networks, which is based on the linearization of the exponential decaying term, were provided. The new method is an easy and direct method and gives a better interpretation of the R/X ratio in comparison to the methods provided in the IEC-60909. A study case was performed to prove the adequacy of the new

methods and from comparing the results to the one from the simulation it was shown that the new method gives the highest accuracy with an average error of 1.85% compared to all other method of the IEC-60909.

10 References

[1] "Vital Signs: Carbon Dioxide," Climate Change: Vital Signs of the Planet. Available: http://climate.nasa.gov/vital-signs/carbon-dioxide.

[2] "Industrial Revolution," Wikipedia, the free encyclopedia.

[3] N. US Department of Commerce, "ESRL Global Monitoring Division - Global Greenhouse Gas Reference Network." Available: http://www.esrl.noaa.gov/gmd/ccgg/trends/graph.html.

[4] N. Oreskes, "The Scientific Consensus on Climate Change," *Science*, vol. 306, no. 5702, pp. 1686–1686, Mar. 2004.

[5] "Climate change evidence: How do we know?," Climate Change: Vital Signs of the Planet. Available: http://climate.nasa.gov/evidence.

[6] "Climate Change: Vital Signs of the Planet: Global Temperature." Available: http://climate.nasa.gov/vital-signs/global-temperature/.

[7] J. Hansen, M. Sato, and R. Ruedy, "Public Perception of Climate Change and the New Climate Dice," *SciRate*, Apr. 2012.

[8] "Data.GISS: GISS Surface Temperature Analysis: Analysis Graphs and Plots." Available: http://data.giss.nasa.gov/gistemp/graphs_v3/.

[9] C. Mora *et al.*, "The projected timing of climate departure from recent variability," *Nature*, vol. 502, no. 7470, pp. 183–187, Oct. 2013.

[10] "Office of Planning and Research - List of Organizations." Available: http://opr.ca.gov/s_listoforganizations.php.

[11] "Shale oil: the next energy revolution," PwC. Available: http://www.pwc.com/gx/en/industries/energy-utilities-mining/oil-gas-energy/publications/shale-oil-changes-energy-markets.html.

[12] "Global climate talks | Environment," the Guardian. Available: http://www.theguardian.com/environment/global-climate-talks.

[13] "Paris Climate Change Conference - November 2015." Available: http://unfccc.int/meetings/paris_nov_2015/meeting/8926.php.

[14] G. Kieffer and T. D. Couture, "Renewable Energy Target Setting," International Renewable Energy Agency (IRENA), Jun. 2015.

[15] F. Blaabjerg and K. Ma, "Future on Power Electronics for Wind Turbine Systems," *IEEE J. Emerg. Sel. Top. Power Electron.*, vol. 1, no. 3, pp. 139–152, Sep. 2013.

[16] J. L. Sawin, F. Sverrisson, and W. Rickerson, "RENEWABLES 2015 GLOBAL STATUS REPORT," REN21, Paris.

[17] "GLOBAL WIND ENERGY OUTLOOK 2014 - GWEC." .

[18] W. Sousa de Oliveira and A. J. Fernandes, "Global Wind Energy Market, Industry and Economic Impacts," *Energy Environ. Res.*, vol. 2, no. 1, May 2012.

[19] X. Lu, M. B. McElroy, and J. Kiviluoma, "Global potential for wind-generated electricity," *Proc. Natl. Acad. Sci.*, vol. 106, no. 27, pp. 10933–10938, Jul. 2009.

[20] C. L. Archer and M. Z. Jacobson, "Evaluation of global wind power," *J. Geophys. Res. Atmospheres*, vol. 110, no. D12, p. D12110, Jun. 2005.

[21] "World Wind Energy Market Update 2015," *Navigant Research*. .

[22] *Yearbook Wind Energy 2015 WIND ENERGY MARKET*, vol. 25. Berlin: German Wind Energy Association (BWE).

[23] "Wind in power: 2014 European statistics," THE EUROPEAN WIND ENERGY ASSOCIATION, 6.

[24] H. Polinder, "Overview of and trends in wind turbine generator systems," in *2011 IEEE Power and Energy Society General Meeting*, 2011, pp. 1–8.

[25] F. Sulla, "Fault Behavior of Wind Turbines," Lund University, Sweden, 2012.

[26] H. Li and Z. Chen, "Overview of different wind generator systems and their comparisons," *IET Renew. Power Gener.*, vol. 2, no. 2, pp. 123–138, Jun. 2008.
[27] C. Feltes, "Advanced Fault Ride-Through Control of DFIG based Wind Turbines including Grid Connection via VSC-HVDC," Duisburg-Essen, Duisburg, 2012.
[28] A. D. Hansen, F. Iov, F. Blaabjerg, and L. H. Hansen, "Review of Contemporary Wind Turbine Concepts and their Market Penetration," *J. Wind Eng. Ind. Aerodyn.*, vol. 28, no. 3, 2004.
[29] "South Baltic Offshore Wind Energy Regions." Available: http://www.southbaltic-offshore.eu/regions-denmark.html.
[30] "History of wind power," *Wikipedia, the free encyclopedia*. 21-Oct-2015.
[31] M. Vestas, "V164-8.0 MW® breaks world record for wind energy production," *MHI Vestas Offshore*. [Online]. Available: http://www.mhivestasoffshore.com/v164-8-0-mw-breaks-world-record-for-wind-energy-production/. [Accessed: 03-Nov-2015].
[32] A. EL-Naggar, "Brushless Double Fed Machine Wind Turbine Modeling and Control," Brandenburg Technical University, Cottbus, 2011.
[33] M. Tsili and S. Papathanassiou, "A review of grid code technical requirements for wind farms," *IET Renew. Power Gener.*, vol. 3, no. 3, pp. 308–332, Sep. 2009.
[34] "Grid code: high and extra high voltage," E.ON Netz GmbH, Bayreuth, Germany, Aug. 2003.
[35] "Grid code: high and extra high voltage," E.ON Netz GmbH, Bayreuth, Germany, Apr. 2006.
[36] I. Erlich, W. Winter, and A. Dittrich, "Advanced grid requirements for the integration of wind turbines into the German transmission system," in *IEEE Power Engineering Society General Meeting, 2006*, 2006, p. 7 pp.-.
[37] "Requirements for offshore grid connections in the E.ON Netz Network," E.ON Netz GmbH, Bayreuth, Germany, Apr. 2008.
[38] G. Michalke, "Variable Speed Wind Turbines - Modelling, Control, and Impact on Power Systems," phd, TU Darmstadt, Darmstadt, 2008.
[39] T. Sant, "Improving BEM-based Aerodynamic Models in Wind Turbine Design Codes," phd, Delft University, Delft, Netherland, 2007.
[40] G. Abad, J. Lopez, M. Rodriguez, L. Marroyo, and G. Iwanski, *Doubly Fed Induction Machine: Modeling and Control for Wind Energy Generation*, 1 edition. Hoboken, NJ: Wiley-IEEE Press, 2011.
[41] J. Fortmann, "Modeling of wind turbines with doubly fed generator system," phd, Universität Duisburg-Essen, Duisburg, Germany, 2015.
[42] M. Ragheb and Ragheb, A. M., "Wind Turbines Theory - The Betz Equation and Optimal Rotor Tip Speed Ratio," in *Fundamental and Advanced Topics in Wind Power*, R. Carriveau, Ed. InTech, 2011.
[43] E. Kulunk, "Aerodynamics of Wind Turbines," in *Fundamental and Advanced Topics in Wind Power*, R. Carriveau, Ed. InTech, 2011.
[44] J. F. Manwell, J. G. McGowan, and A. L. Rogers, *Wind Energy Explained: Theory, Design and Application*, 2. Auflage. Chichester, U.K: John Wiley & Sons, 2009.
[45] N. W. Miller, W. W. Price, and J. J. Sanchez-Gasca, "Dynamic Modeling of GE 1.5 and 3.6 Wind Turbine-Generators," GE-Power Systems Energy Consulting, Oct. 2003.
[46] A. Petersson, "Analysis, Modeling and Control of Doubly-Fed Induction Generators for Wind Turbines," phd, Chalmers University of Technology, Götberg, Sweden, 2003.
[47] A. Perdana, "Dynamic Models of Wind Turbines," phd, Chalmers University of Technology, Götberg, Sweden, 2008.
[48] S. Engelhardt, "Direkte Leistungsregelung einer Windenergieanlage mit doppelt gespeister Asynchronmaschine," Ph. D Dissertation, Dept. Electrical Engineering and Information, Univ. Duisburg-Essen, Duisburg, Germany, 2011.

[49] O. Anaya-Lara, N. Jenkins, J. Ekanayake, P. Cartwright, and M. Hughes, *Wind Energy Generation: Modelling and Control*, 1. Auflage. Chichester, U.K: John Wiley & Sons, 2009.
[50] M. H. Hansen, A. D. Hansen, T. J. Larsen, S. Øye, P. Sørensen, and P. Fuglsang, "Control design for a pitch-regulated, variable speed wind turbine," Risø National Laboratory, Roskilde, Denmark, 87-550-3409–8, Jan. 2005.
[51] G. Ramtharan, N. Jenkins, O. Anaya-Lara, and E. Bossanyi, "Influence of rotor structural dynamics representations on the electrical transient performance of FSIG and DFIG wind turbines," *Wind Energy*, vol. 10, no. 4, pp. 293–301, Jul. 2007.
[52] M. Z. B. Sujod, "Advanced Converter Control Techniques for Improving the Performances of DFIG based Wind Turbines," Wissenschaftliche Abschlussarbeiten » Dissertation, Universität Duisburg-Essen, Fakultät für Ingenieurwissenschaften » Elektrotechnik und Informationstechnik, 2014.
[53] M. Hiller, R. Sommer, and M. Beuermann, "Converter Topologies and Power Semiconductors for Industrial Medium Voltage Converters," in *IEEE Industry Applications Society Annual Meeting, 2008. IAS '08*, 2008, pp. 1–8.
[54] A. Wintrich, U. Nicolai, W. Tursky, and T. Reiman, *Application Manual Power Semiconductors*, 2nd ed. Nuremberg, Germany: SEMIKRON International GmbH, 2015.
[55] N. Mohan, T. M. Undeland, and W. P. Robbins, *Power Electronics: Converters, Applications, and Design*, 3. Auflage. Hoboken, NJ: John Wiley & Sons, 2002.
[56] A. M. Hava, R. J. Kerkman, and T. A. Lipo, "A high-performance generalized discontinuous PWM algorithm," *IEEE Trans. Ind. Appl.*, vol. 34, no. 5, pp. 1059–1071, Sep. 1998.
[57] *The Induction Machines Design Handbook, Second Edition*, 2 edition. Boca Raton, FL: CRC Press, 2009.
[58] *Power System Stability and Control*, 1st edition. New York: McGraw-Hill Education, 1994.
[59] H. M. Jabr and N. C. Kar, "Leakage flux saturation effects on the transient performance of wound-rotor induction motors," *Electr. Power Syst. Res.*, vol. 78, no. 7, pp. 1280–1289, Jul. 2008.
[60] T. Tuovinen, M. Hinkkanen, and J. Luomi, "Modeling of Saturation Due to Main and Leakage Flux Interaction in Induction Machines," *IEEE Trans. Ind. Appl.*, vol. 46, no. 3, pp. 937–945, May 2010.
[61] G. J. Rogers and D. S. Benaragama, "An induction motor model with deep-bar effect and leakage inductance saturation," *Arch. Für Elektrotechnik*, vol. 60, no. 4, pp. 193–201, Jul. 1978.
[62] C. Gerada, K. J. Bradley, M. Sumner, and P. Sewell, "Evaluation and Modeling of Cross Saturation Due to Leakage Flux in Vector-Controlled Induction Machines," *IEEE Trans. Ind. Appl.*, vol. 43, no. 3, pp. 694–702, May 2007.
[63] J. O. Ojo, A. Consoli, and T. A. Lipo, "An improved model of saturated induction machines," *IEEE Trans. Ind. Appl.*, vol. 26, no. 2, pp. 212–221, Mar. 1990.
[64] J. M. Aller, D. Delgado, A. Bueno, J. C. Viola, and J. A. Restrepo, "Model of the induction machine including saturation," in *2013 15th European Conference on Power Electronics and Applications (EPE)*, 2013, pp. 1–8.
[65] P. Maki-Ontto and J. Luomi, "Induction motor model for the analysis of capacitive and induced shaft voltages," in *2005 IEEE International Conference on Electric Machines and Drives*, 2005, pp. 1653–1660.
[66] E. Zhong and T. A. Lipo, "Improvements in EMC performance of inverter-fed motor drives," *IEEE Trans. Ind. Appl.*, vol. 31, no. 6, pp. 1247–1256, Nov. 1995.
[67] L. Ran, S. Gokani, J. Clare, K. J. Bradley, and C. Christopoulos, "Conducted electromagnetic emissions in induction motor drive systems. I. Time domain analysis and

identification of dominant modes," *IEEE Trans. Power Electron.*, vol. 13, no. 4, pp. 757–767, Jul. 1998.
[68] Y. Xu and D. C. Aliprantis, "Wound-rotor induction machine model with saturation and high-frequency effects," in *2014 International Conference on Electrical Machines (ICEM)*, 2014, pp. 1838–1844.
[69] A. Boglietti, A. Cavagnino, and M. Lazzari, "Experimental High-Frequency Parameter Identification of AC Electrical Motors," *IEEE Trans. Ind. Appl.*, vol. 43, no. 1, pp. 23–29, Jan. 2007.
[70] Y. Xu, "Advanced wound-rotor machine model with saturation and high-frequency effects," *Grad. Theses Diss.*, Jan. 2014.
[71] F. Zare, J. Adabi, and A. Ghosh, "Different approaches to reduce shaft voltage in AC generators," in *13th European Conference on Power Electronics and Applications, 2009. EPE '09*, 2009, pp. 1–9.
[72] I. Erlich, Z. Kasztel, and P. Schegner, "Enhanced modal based Technique for Construction of Power System Dynamic Equivalents," *PSCC Proc. Fourteenth Power Syst. Comput. Conf. Seville June 24-28 2002*, pp. 1–7, 2002.
[73] J. M. Undrill, J. A. Casazza, E. M. Gulachenski, and L. K. Kirchrnayer, "Electromechanical Equivalent for Use in Power System Stability Studies," *IEEE Trans. Power Appar. Syst.*, vol. PAS-90, no. 5, pp. 2060–2071, Sep. 1971.
[74] B. Moore, "Principal component analysis in linear systems: Controllability, observability, and model reduction," *IEEE Trans. Autom. Control*, vol. 26, no. 1, pp. 17–32, Feb. 1981.
[75] P. M. M. Bongers, "Modeling and Identification of Flexible Wind Turbines and A Factorizational Approach to Robust Control Design," Dissertation, TU Delft, Delft University of Technology, 1994.
[76] M. Kalantar and M. Sedighizadeh, "Reduced order model for doubly output induction generator in wind park using integral manifold theory," *Iran. J. Electr. Electron. Eng.*, vol. 1, no. 1, pp. 41–48, 2005.
[77] R. M. G. Castro and J. M. F. de Jesus, "A wind park reduced-order model using singular perturbations theory," *IEEE Trans. Energy Convers.*, vol. 11, no. 4, pp. 735–741, Dec. 1996.
[78] S. Ahmed-Zaid, P. Sauer, M. Pai, and M. Sarioglu, "Reduced order modeling of synchronous machines using singular perturbation," *IEEE Trans. Circuits Syst.*, vol. 29, no. 11, pp. 782–786, Nov. 1982.
[79] I. Erlich, J. Kretschmann, J. Fortmann, S. Mueller-Engelhardt, and H. Wrede, "Modeling of Wind Turbines Based on Doubly-Fed Induction Generators for Power System Stability Studies," *IEEE Trans. Power Syst.*, vol. 22, no. 3, pp. 909–919, Aug. 2007.
[80] E. Istvan, P. Hans, and D. Sascha, "A new synchronous generator model for power system stability analysis," presented at the Power Systems Computation Conference (PSCC), Dresden, Germany, 1996.
[81] J. Kretschmann, H. Wrede, S. Mueller-Engelhardt, and I. Erlich, "Enhanced Reduced Order Model of Wind Turbines with DFIG for Power System Stability Studies," in *Power and Energy Conference, 2006. PECon '06. IEEE International*, 2006, pp. 303–311.
[82] N. Hoffmann, R. Lohde, M. Fischer, F. W. Fuchs, L. Asiminoaei, and P. B. Thøgersen, "A review on fundamental grid-voltage detection methods under highly distorted conditions in distributed power-generation networks," in *2011 IEEE Energy Conversion Congress and Exposition (ECCE)*, 2011, pp. 3045–3052.
[83] T.-N. Le, "Kompensation schnell veränderlicher Blindströme eines Drehstromverbrauchers," *ETZ-Arch.*, vol. 11, no. 8, pp. 249–253, 1989.
[84] C. L. Fortescue, "Method of Symmetrical Co-Ordinates Applied to the Solution of Polyphase Networks," *Trans. Am. Inst. Electr. Eng.*, vol. XXXVII, no. 2, pp. 1027–1140, Jul. 1918.

[85] J. Sun, "Impedance-Based Stability Criterion for Grid-Connected Inverters," *IEEE Trans. Power Electron.*, vol. 26, no. 11, pp. 3075–3078, Nov. 2011.
[86] M. Liserre, R. Teodorescu, and F. Blaabjerg, "Stability of photovoltaic and wind turbine grid-connected inverters for a large set of grid impedance values," *IEEE Trans. Power Electron.*, vol. 21, no. 1, pp. 263–272, Jan. 2006.
[87] K. Ogata, *Modern Control Engineering*. Prentice Hall, 2010.
[88] C. Feltes, "Advanced Fault Ride Through Control of DFIG Based Wind Turbines Including Grid Connection Via VSC-HVDC," Ph. D Dissertation, Electrical Power System, Duisburg-Essen, Duisburg, Germany, 2012.
[89] C. T. Lee, C. W. Hsu, and P. T. Cheng, "A Low-Voltage Ride-Through Technique for Grid-Connected Converters of Distributed Energy Resources," *IEEE Trans. Ind. Appl.*, vol. 47, no. 4, pp. 1821–1832, Jul. 2011.
[90] T. F. Coleman and Y. Li, "An Interior Trust Region Approach for Nonlinear Minimization Subject to Bounds," Cornell University, Ithaca, NY, USA, 1993.
[91] S. Schostan, K. D. Dettmann, T. D. Thanh, and D. Schulz, "Harmonic propagation in a doubly fed induction generator of a wind energy converter," in *2009 Compatibility and Power Electronics*, 2009, pp. 101–108.
[92] J. Morren and S. W. H. de Haan, "Short-Circuit Current of Wind Turbines With Doubly Fed Induction Generator," *IEEE Trans. Energy Convers.*, vol. 22, no. 1, pp. 174–180, Mar. 2007.
[93] M. Vajta, "Some remarks on pade'-approximations," presented at the 3rd TEMPUS-INTCOM Symposioum, Veszprém , Hungary, 2000, pp. 1–6.
[94] F. Klein, *Lectures on the ikosahedron and the solution of equations of the fifth degree*. London : Trübner & Co., 1888.
[95] D. S. Dummit, "Solving Solvable Quintics," *Math. Comput.*, vol. 57, no. 195, pp. 387–401, 1991.
[96] V. S. Adamchik and D. J. Jeffrey, "Polynomial Transformations of Tschirnhaus, Bring and Jerrard," *SIGSAM Bull*, vol. 37, no. 3, pp. 90–94, Sep. 2003.
[97] W. H. Press, S. A. Teukolsky, W. T. Vetterling, and B. P. Flannery, *Numerical Recipes 3rd Edition: The Art of Scientific Computing*, 3 edition. Cambridge, UK ; New York: Cambridge University Press, 2007.
[98] M. L. Crow, *Computational Methods for Electric Power Systems, Second Edition*, 2 edition. Boca Raton: CRC Press, 2009.
[99] I. Erlich, G. K. Venayagamoorthy, and N. Worawat, "A Mean-Variance Optimization algorithm," in *IEEE Congress on Evolutionary Computation*, 2010, pp. 1–6.
[100] J. J. Justo, F. Mwasilu, and J.-W. Jung, "Doubly-fed induction generator based wind turbines: A comprehensive review of fault ride-through strategies," *Renew. Sustain. Energy Rev.*, vol. 45, pp. 447–467, May 2015.
[101] J. Morren and S. W. H. de Haan, "Ridethrough of wind turbines with doubly-fed induction generator during a voltage dip," *IEEE Trans. Energy Convers.*, vol. 20, no. 2, pp. 435–441, Jun. 2005.
[102] G. Pannell, D. J. Atkinson, and B. Zahawi, "Minimum-Threshold Crowbar for a Fault-Ride-Through Grid-Code-Compliant DFIG Wind Turbine," *IEEE Trans. Energy Convers.*, vol. 25, no. 3, pp. 750–759, Sep. 2010.
[103] I. Erlich, H. Wrede, and C. Feltes, "Dynamic Behavior of DFIG-Based Wind Turbines during Grid Faults," in *Power Conversion Conference - Nagoya, 2007. PCC '07*, 2007, pp. 1195–1200.
[104] F. Moriconi, F. D. L. Rosa, A. Singh, B. Chen, M. Levitskaya, and A. Nelson, "An innovative compact saturable-core HTS Fault Current Limiter - development, testing and application to transmission class networks," in *IEEE PES General Meeting*, 2010, pp. 1–8.

[105] D. Sarkar, D. Roy, A. B. Choudhury, and S. Yamada, "Performance analysis of saturated iron core superconducting fault current limiter using Jiles–Atherton hysteresis model," *J. Magn. Magn. Mater.*, vol. 390, pp. 100–106, Sep. 2015.

[106] W. Guo, L. Xiao, and S. Dai, "Enhancing Low-Voltage Ride-Through Capability and Smoothing Output Power of DFIG With a Superconducting Fault-Current Limiter #x2013;Magnetic Energy Storage System," *IEEE Trans. Energy Convers.*, vol. 27, no. 2, pp. 277–295, Jun. 2012.

[107] W. Guo *et al.*, "LVRT Capability Enhancement of DFIG With Switch-Type Fault Current Limiter," *IEEE Trans. Ind. Electron.*, vol. 62, no. 1, pp. 332–342, Jan. 2015.

[108] J. Yang, J. E. Fletcher, and J. O'Reilly, "A Series-Dynamic-Resistor-Based Converter Protection Scheme for Doubly-Fed Induction Generator During Various Fault Conditions," *IEEE Trans. Energy Convers.*, vol. 25, no. 2, pp. 422–432, Jun. 2010.

[109] C. Wessels, F. Gebhardt, and F. W. Fuchs, "Fault Ride-Through of a DFIG Wind Turbine Using a Dynamic Voltage Restorer During Symmetrical and Asymmetrical Grid Faults," *IEEE Trans. Power Electron.*, vol. 26, no. 3, pp. 807–815, Mar. 2011.

[110] X. Yan, G. Venkataramanan, Y. Wang, Q. Dong, and B. Zhang, "Grid-Fault Tolerant Operation of a DFIG Wind Turbine Generator Using a Passive Resistance Network," *IEEE Trans. Power Electron.*, vol. 26, no. 10, pp. 2896–2905, Oct. 2011.

[111] D. Xiang, L. Ran, P. J. Tavner, and S. Yang, "Control of a doubly fed induction generator in a wind turbine during grid fault ride-through," *IEEE Trans. Energy Convers.*, vol. 21, no. 3, pp. 652–662, Sep. 2006.

[112] J. Liang, D. F. Howard, J. A. Restrepo, and R. G. Harley, "Feedforward Transient Compensation Control for DFIG Wind Turbines During Both Balanced and Unbalanced Grid Disturbances," *IEEE Trans. Ind. Appl.*, vol. 49, no. 3, pp. 1452–1463, May 2013.

[113] D. Xie, Z. Xu, L. Yang, J. Østergaard, Y. Xue, and K. P. Wong, "A Comprehensive LVRT Control Strategy for DFIG Wind Turbines With Enhanced Reactive Power Support," *IEEE Trans. Power Syst.*, vol. 28, no. 3, pp. 3302–3310, Aug. 2013.

[114] X. Yan, G. Venkataramanan, P. S. Flannery, and Y. Wang, "Evaluation the effect of voltage sags due to grid balance and unbalance faults on DFIG wind turbines," in *International Conference on Sustainable Power Generation and Supply, 2009. SUPERGEN '09*, 2009, pp. 1–10.

[115] "TransmissionCode 2007," Verband der Netzbetreiber - VDN – e.V. beim VDEW, Berlin, 1.1, Aug. 2007.

[116] VDE-AR-N 4105, "Technical minimum requirements for the connection to and parallel operation with low-voltage distribution networks," VDE Verlag GmbH, Berlin, Aug. 2011.

[117] VDE-AR-N 4120:2015-01, "Technical requirements for the connection and operation of customer installations to the high-voltage network (TCC High-Voltage)," VDE Verlag GmbH, Berlin, Oct. 2015.

[118] P. Gnacinski, "Windings Temperature and Loss of Life of an Induction Machine Under Voltage Unbalance Combined With Over- or Undervoltages," *IEEE Trans. Energy Convers.*, vol. 23, no. 2, pp. 363–371, Jun. 2008.

[119] S. Engelhardt, J. Kretschmann, J. Fortmann, F. Shewarega, I. Erlich, and C. Feltes, "Negative sequence control of DFG based wind turbines," in *2011 IEEE Power and Energy Society General Meeting*, 2011, pp. 1–8.

[120] IEC 60909-0:2001, *Short-circuit currents in three-phase a.c. systems Part 0: Calculation of currents*. 2001.

[121] IEC TR 60909-1, *Short-circuit currents in three-phase a.c. systems – Part 1: Factors for the calculation of short-circuit currents according to IEC 60909-0*. 2002.

Publications

A. El-Naggar, A.; Erlich, I. “Short-circuit current reduction techniques of the doubly-fed induction generator based wind turbines for fault ride through enhancement”, IET Renewable Power Generation , April 2017 , accepted and awaiting assignment to an issue.
B. El-Naggar, A.; Erlich, I. “Control approach of three-phase grid connected PV inverters for voltage unbalance mitigation in low-voltage distribution grids”, IET Renewable Power Generation, vol. 10, issue: 10, pp. 1577-1586, 2016
C. El-Naggar, A. “Standard Calculation of Fault Current Contribution of Doubly-Fed Induction Generator Based Wind Turbine” in Wind Turbine - Design, Control and Application, Chapter: 12, Jul. 2016, A. Aissaoui, Ed. InTech.
D. El-Naggar, A.; Erlich, I. “Analysis of Fault Current Contribution of Doubly-Fed Induction Generator Wind Turbines under Unbalanced Grid Faults”, Renewable Energy, vol. 91, pp. 137-146, Jun. 2016.
E. El-Naggar, A.; Erlich, I. “Using MVMO for Optimal Tuning of Linear Quadratic Regulators for DFIG-WT” IFAC-Pap., vol. 48, no. 30, pp. 479–484, 2015 (selected from the best 20 publications and nominated for publishing in “Control Engineering Practice” Journal).
F. El-Naggar, A.; Erlich, I. “Fault Current Contribution Analysis of Doubly-Fed Induction Generator Based Wind Turbines”, IEEE Transactions on Energy Conversion, vol. PP, issue: 99, pp. 1-9, 2015.
G. El-Naggar, A.; Feltes, C.; Erlich, I. “R/X Ratio Influence on Short Circuit Current of Doubly-Fed Induction Generator Based Wind Turbines”, Power and Energy Society General Meeting (PES), 2013 IEEE, pp. 1-5.
H. El-Naggar, A.; Rueda, J.L.; Erlich, I. “Comparison of Short-circuit Current Contribution of Doubly-Fed Induction Generator based Wind Turbines and Synchronous Generator”, PowerTech (POWERTECH), 2013 IEEE Grenoble, pp. 1-6.

Appendix

A.1. DFIG Parameters

Parameter	Symbol	Value
Rated voltage	V_r	690 V
Rated frequency	f_r	50 Hz
Rated power	P_r	2000 kW
Stator resistance	r_s	0.017 p.u.
Stator leakage inductance	$l_{\sigma s}$	0.135 p.u.
Rotor resistance	r_R	0.02 p.u.
Rotor leakage inductance	$l_{\sigma R}$	0.08 p.u.
Magnetizing inductance	l_M	3.35 p.u.
Nominal speed	n_r	1500 min^{-1}
Generator inertia	J_R	1.25 p.u.
Wind rotor inertia	J_W	5.5 p.u.
Shaft stiffness	k_{sh}	455 p.u./rad
Shaft damping	d_{sh}	3.15 p.u.
MSC maximum current	i_{MSC_max}	1.11 p.u.
MSC maximum voltage	v_{MSC_max}	0.45 p.u.
LSC inductance	l_{LSC}	0.15 p.u.
LSC resistance	r_{LSC}	0.0015 p.u.
LSC maximum current	i_{LSC_max}	0.21 p.u.
LSC maximum voltage	v_{LSC_max}	1.14 p.u.

A.2. Space Vectors

The quantities of a three-phase system like voltage, current and flux linkage can be described by a space vector, which consists of two orthogonal components and the zero sequence. The space vector can be calculated by the Clarke transformation as follows:

$$\begin{bmatrix} y_\alpha(t) \\ y_\beta(t) \\ y_0(t) \end{bmatrix} = \frac{2}{3} \begin{bmatrix} 2 & -\frac{1}{2} & -\frac{1}{2} \\ 0 & \frac{\sqrt{3}}{2} & -\frac{\sqrt{3}}{2} \\ \frac{1}{2} & \frac{1}{2} & \frac{1}{2} \end{bmatrix} \begin{bmatrix} y_a(t) \\ y_b(t) \\ y_c(t) \end{bmatrix} \qquad (A.1)$$

The zero sequence component can be disregarded, if there is no neutral connection of the three phase systems. This was the case for the DFIG and the converters in this thesis. Accordingly, the space vector component can be described in stationary reference frame by:

$$\underline{y}^{\angle 0} = y_\alpha + \mathrm{j}y_\beta \tag{A.2}$$

The space vector can be transformed into a rotating reference frame with a frequency corresponding to the measured three phase system. This will result in a DC quantities (dq components), that allows the control with PI-controllers. The space vector can be transformed into this rotating reference frame by the following transformation:

$$\underline{y}^{\angle \omega_0} = y_\mathrm{d}^{\angle \omega_0} + \mathrm{j}y_\mathrm{q}^{\angle \omega_0} = \underline{y}^{\angle 0} e^{-\mathrm{j}\omega_0 t} \tag{A.3}$$

In order to transform back the space vector into three phase system the inverse Clarke transformation is applied:

$$\begin{bmatrix} y_a(t) \\ y_b(t) \\ y_c(t) \end{bmatrix} = \begin{bmatrix} 1 & 0 \\ -\frac{1}{2} & \frac{\sqrt{3}}{2} \\ -\frac{1}{2} & -\frac{\sqrt{3}}{2} \end{bmatrix} \begin{bmatrix} y_\alpha(t) \\ y_\beta(t) \end{bmatrix} \tag{A.4}$$